Notes on the 1976
Summer Study Program
in
GEOPHYSICAL FLUID DYNAMICS
at
THE WOODS HOLE OCEANOGRAPHIC INSTITUTION

Reference No. 76-81

CONTENTS OF THE VOLUME

Course Lectures on Global Climatology

Abstracts of Seminars

Symposium on Planetary Boundary Layers
(Abstracts)

Fellowship Lectures

Staff Members

Howard, Louis N.	Massachusetts Institute of Technology
Huppert, Herbert E.	Cambridge University, England
Ingersoll, Andrew P.	California Institute of Technology, Pasadena
Keller, Joseph B.	Courant Institute of Mathematical Sciences
Malkus, Willem V.R.	Massachusetts Institute of Technology
North, Gerald R.	University of Missouri-St. Louis
Pedlosky, Joseph	University of Chicago
Rhines, Peter B.	Woods Hole Oceanographic Institution
Rooth, Claes	University of Miami, Florida
Somerville, Richard C.	NCAR, Boulder, Colorado
Stern, Melvin E.	University of Rhode Island
Veronis, George	Yale University
Whitehead, John A., Jr.	Woods Hole Oceanographic Institution

Visiting Lecturers

Birchfield, Gene E.	Northwestern University, Evanston
Broecker, Wallace S.	Lamont-Doherty Geological Observatory
Bunker, Andrew F.	Woods Hole Oceanographic Institution
Gierasch, Peter	Cornell University
Imbrie, John	Brown University
Lindzen, Richard S.	Harvard University
Oort, Abraham H.	Princeton University
Saltzman, Barry	Yale University
Vonder Haar, Thomas	Fort Collins, Colorado
Welander, Pierre	University of Washington

Post-doctoral Participants

Gammelsrød, Tor	University of Bergen, Norway
Proctor, Michael R.E.	Massachusetts Institute of Technology

Pre-doctoral Participants

Ashe, Steven M.	Atmos.Dynamics	Yale University
Davey, Michael K.	Appl.Math.	Univ.of Cambridge,England (Australia)
Kells, Lawrence C.	Appl.Math.	Massachusetts Institute of Technology
McDougall, Trevor J.	Mech.Engineering	Univ.of Cambridge,England (Australia)
Pollard, David	Geol.Planet.Sci.	California Institute of Technology
Røed, Lars P.	Appl.Math.	University of Oslo, Norway
Romea, Richard D.	Geophys.Fl.Dyn.	University of Chicago
White, Glenn H.	Atmos.Sci.	State Univ.of N.Y. at Albany
Wielicki, Bruce A.	Appl.Math.Eng.Phys.	Scripps Inst.of Oceanography
Yamagata, Toshio	Geophys.,Oceanog.	Kyushu University, Japan

Visitors to Planetary and Benthic Boundary Layer Symposium

Armi, Laurence D.	Woods Hole Oceanographic Institution
Biscaye, Pierre	Lamont-Doherty Geological Observatory
Corcos, Giles	University of California at Berkeley
Csanady, Gabriel T.	Woods Hole Oceanographic Institution
Flood, Roger D.	Woods Hole Oceanographic Institution
Niiler, Pearn P.	Oregon State University
Panofsky, Hans	Penn. State University
Sarachik, Edward	Harvard University
Sarmiento, Jorge	Lamont-Doherty Geological Observatory
Tochko, John S.	Woods Hole Oceanographic Institution
Weatherly, Georges	Florida State University
Wimbush, Mark	Nova University
Wyngaard, John	N.O.A.A., Boulder, Colorado

Editor's Preface

Global climatology was the principal theme of the eighteenth summer program in Geophysical Fluid Dynamics at the Woods Hole Oceanographic Institution. This single volume contains course lectures, abstracts of seminars and lectures by summer fellows.

As in previous years, the summer fellows were responsible for preparing a first draft of the course lectures on the principal theme. In most cases, the lecturer has been able to re-work the material further. The course lecturers, all of whom contributed so much to the program, are Richard S. Lindzen, Wallace S. Broecker, Abraham H. Oort, John Imbrie, Thomas Vonder Haar, Gerald R. North, Claes Rooth, Gene E. Birchfield, and Richard C. Somerville.

The abstracted seminars cover a broad range of topics, including a one-week symposium on planetary and benthic boundary layers. Much valuable material is referred to in these abstracts.

The major creative products of the summer are the lectures of the ten fellows. These lectures have not been edited or reviewed in the manner appropriate for published papers, and should be regarded as unpublished manuscripts. Readers who would like to quote or use the material should write directly to the authors.

As in previous years, much of the ultimate value of this summer's activities is likely to appear as published papers during the next year or two. In this sense, the material in this volume is simply a report of an ongoing research effort.

We all express our thanks to the National Science Foundation, which provided the bulk of the financial support, the Office of Naval Research, which supported the Boundary Layer Symposium and some of the staff participation, and to Mary C. Thayer, who managed the program and prepared this volume.

Andrew P. Ingersoll

Andrew P. Ingersoll.

Back row: Howard, Veronis, Oort, Proctor, Gammelsrød, Pedlosky, White. Middle row: Malkus, Somerville, Keller, Ingersoll, Thayer, Whitehead, Stern, Weilicki, Rooth, Yamagata. Front row: Kells, McDougall, North, Rød, Ashe, Pollard, Romea.

CONTENTS

Page No.

Course Lectures

Problems of Climate Modeling: A Zonally Symmetric Model 1
Richard S. Lindzen

Problems of Climate Modeling: Steady Axially Symmetric Atmospheric Motions 6
Richard S. Lindzen

Problems of Climate Modeling: Climate Models 9
Richard S. Lindzen

Problems of Climate Modeling 12
Richard S. Lindzen

Paleoclimatic Data (I) 15
Wallace S. Broecker

Paleoclimatic Data (II) 18
Wallace S. Broecker

The Fluid Transports (I) 19
Abraham H. Oort

Global Angular Momentum and Water Vapor Balance 26
Abraham H. Oort

The Fluid Transports (II) 30
Abraham H. Oort

Paleoclimatic Data 37
John Imbrie

Modeling Ice Caps 40
Gene E. Birchfield

The Earth's Radiation Balance (I) 42
Thomas H. Vonder Haar

The Earth's Radiation Balance (II) 44
Thomas H. Vonder Haar

Analytical Behavior of Climate Models (I) 46
Gerald North

Analytical Behavior of Climate Models (II) 50
Gerald North

Water Mass Analysis and the Deep Ocean Circulation (I). . . . 56
Claes Rooth

Information from Some Chemical Tracers (II) 58
Claes Rooth

Water Mass Analysis and the Deep Ocean Circulation (III) . . . 60
Claes Rooth

GeneralCirculation Models and Climate 65
Richard C. Somerville

Page No.

Abstracts of Seminars

Energy Exchange over the North and South Atlantic Oceans 69
Andrew F. Bunker

Recycling Rotating Flow over Varying Bottom Topography 70
Michael K. Davey

Upwelling Near an Ice Edge 71
Tor Gammelsrød and Lars P. Røed

Martian Climatology 71
Peter J. Gierasch

Stability of the Jovian General Circulation 72
Peter J. Gierasch

Variations in the Earth's Orbit: Pacemaker of the Ice Ages . . . 72
John Imbrie

Dynamics of Jupiter's Atmosphere 73
Andrew P. Ingersoll

The Global Energetics of Ice-Age Oscillations: Inferences based on a Statistical-Dynamical Model of Climate 73
Barry Saltzman

Interaction of a Uniform Wind Stress with Inertia-Gravity Waves . . 74
Melvin E. Stern

World Ocean Circulation 74
George Veronis

Thermal Oscillations in a Fluid heated from Below and cooled to Freezing from Above 75
Pierre Welander

Circulation induced by Eddies and Waves 76
Peter B. Rhines

On Trajectories of Rossby Wave Packets released in a Lateral Shear Flow 76
Toshio Yamagata

Symposium on Planetary and Benthic Boundary Layers

Abstracts of Seminars

The Bottom Boundary Layer of the Deep Ocean 78
Laurence Armi and Robert C. Millard, Jr.

Radon and Radium as Geochemical Tracers of Abyssal Mixing Processes . 78
Pierre E. Biscaye and Jorge L. Sarmiento

The Dynamics of Sheared Thermoclines 80
Giles M. Corcos

Turbulent Interface Layers 80
Gabriel T. Csanady

Page No.

Near-bottom Currents and the Genesis of Sea-Floor Waves and Furrows 81
Roger D. Flood

Time-dependent Development of Flow over Bottom Topography . . 82
Herbert E. Huppert

Kolmogorov in the Boundary Layer 82
Willem V.R. Malkus

Tests of Numerical Models of the Seasonal Thermocline . . . 83
Pearn P. Niiler

One-point and Two-point Statistics in the Atmospheric Surface Layer 83
Hans A. Panofsky

Transport Processes in Sloping Side Wall Boundary Layers . . 84
Claes Rooth

Boundary Layer and Large Scale Dynamics 85
Edward S. Sarachik

On the Importance of Density Stratification to the Bottom Boundary Layer on the West Florida Continental Shelf 86
George Weatherly

An Acoustic Sensor of Velocity for Benthic Boundary Layer Studies 86
Albert J. Williams, 3rd and John S. Tochko

The Benthic Boundary Layer and its Interaction with the Bottom Sediment 87
Mark Wimbush

Turbulence Constitutive Equation and Boundary-layer Modeling . 88
John C. Wyngaard

Fellowship Lectures

On Dynamic Feedback Effects in Axially Asymmetric Atmospheric Models 89
Steven M. Ashe

Geostrophic Baroclinic Instability in a Fluid with Three Layers . 108
Michael H. Davey

Stochastic Analogies to Diffusive Climate Models 121
Lawrence C. Kells

Some Aspects of Rotating Weir Flows 127
Trevor J. McDougall

A Functional for Energy Balance Climate Models 137
David Pollard

Some Aspects of Steady, Rotating Channel Flow 149
Lars Petter Røed

A Study of the Formation of Bottom Water in the Western Mediterranean Sea 160
Richard D. Romea

Page No.

Climatic Feedbacks Calculated from Satellite Observations 168
Glenn H. White

Clouds and Climate 190
Bruce A. Wielicki

A Preliminary Study of Flows Generated by a Cylinder Moving on a Beta-Plane 199
Toshio Yamagata

PROBLEMS OF CLIMATE MODELING: A ZONALLY SYMMETRIC MODEL

Richard S. Lindzen

1. INTRODUCTION

The understanding of climate entails a collective understanding of both meteorology and oceanography. As a loose definition, climate can be considered the state of the atmosphere averaged over a sufficiently long time interval to exclude the details of unwanted phenomena (e.g. 'weather').

The great span of time scales encompassed by atmospheric motions considerably complicates our picture of climate. For statistical equilibrium the radiative time scale of the atmosphere is about 30 days for example, whereas that for turbulent convection may be orders-of-magnitude shorter. And the upper atmosphere has a number of 'exotic' time scales, such as in internal cycle of 26 months.

The oceans compound these difficulties. Surface phenomena have scales in years, compared to hundreds of years for the deep ocean.

The unsettling possibility of the atmosphere being a nonunique function of its external parameters may also be considered, but will be avoided here.

Shall we include seasonal dependencies, or average over longer periods? (For instance, ice ages may be dependent on warmer summers to inhibit annual ice accumulation.) This question too will be avoided; henceforth only annual averages will be considered.

Three topics now present themselves: why is the atmosphere as it is at present (and can our insights be incorporated into the modeling)? how are its heat and momentum budgeted (and those of the ocean, about which we know little)?, and how can these be effectively modeled?

Diagnostic approaches to these problems are usually divorced from theoretical treatments. One common methodology is to relate the statistical budgets to external parameters. Another, which may give less ambiguous results, is to start with the equations of motion and 'build up', attempting to deduce a circulation. In this latter category are the general circulation models (GCM's), which entail a sequence of 'doable' calculations. It is also possible to describe hydrodynamical states, perturb them, and study their stability.

In general, we note that the more comprehensive the model (the more physical effects it encompasses), the more compromises must be made to solve it.

2. A ZONALLY SYMMETRIC MODEL

The remainder of this lecture concerns the axisymmetric circulation of the atmosphere.

The cross section of zonally averaged temperature below reveals certain basic phenomena which a symmetric model should seek to reproduce: the lapse rate in the troposphere is uniformly about 6 K/km, although there is an inversion over the winter pole; the equator-to-pole temperature difference is about 40 K at the surface; at the tropical tropopause ($\sim$100 mb) the temperature begins increasing with height, while at the midlatitude tropopause (~ 200 mb) the temperature becomes isothermal, the net effect being a reversal in pole-to-equator gradient in the upper atmosphere.

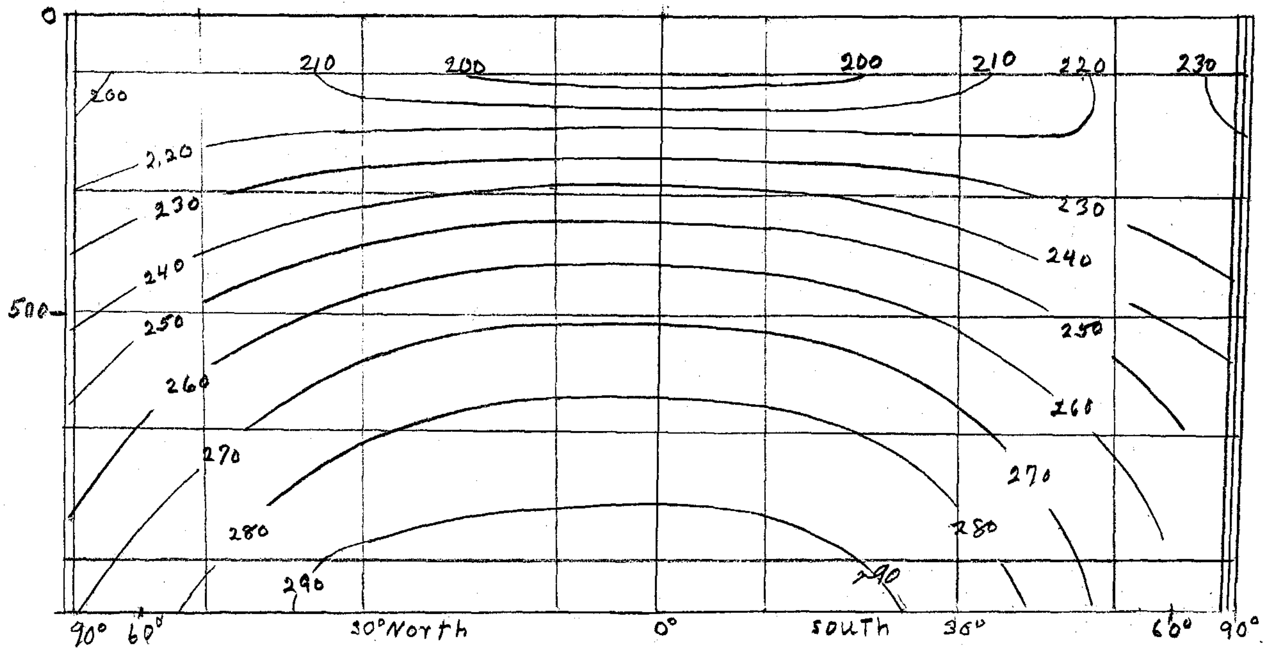

The time-and-longitude averaged temperature $(\overline{T})$ in January as estimated by Palmén and Newton (1967). Values are in degrees K.

The next figure is a cross section of the July zonal wind. Because this is a time average of a meandering jet whose instantaneous magnitude is several times the average, the strength of the winds shown varies ~ 5-10 m/sec between years.

Symmetric models in general overestimate the surface westerlies. Consideration of any of these models brings us back to a basic discussion of what processes maintain the symmetric circulation. The so-called 'conventional wisdom' of the past twenty years dates to Jeffreys. He estimated the horizontal momentum transport due to mean meridional winds $(\rho \tilde{u} \tilde{v})$ using surface values, $\tilde{u} \sim u' \sim v' \approx 10$ m/sec, (he was unaware of the existence of the jet stream with $u \approx 100$ m/sec) and hence concluded that eddy fluxes from the asymmetric circulation were necessary to achieve a balanced angular momentum budget in a latitude belt. Nor was he aware of any mechanism for large-scale vertical transport of momentum.

It is these deficiencies that motivate Ed Schneider's model of the steady symmetric circulation, which will now be considered. The relevant governing equations are:

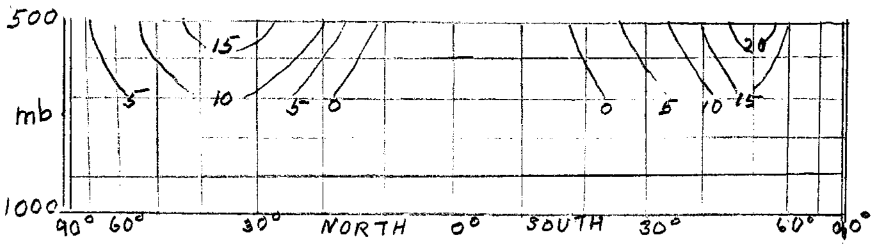

The time-and-longitude averaged zonal wind ($\bar{u}$) in January as estimated by Heastie and Stephenson (1958). Values are in m/sec^{-1}.

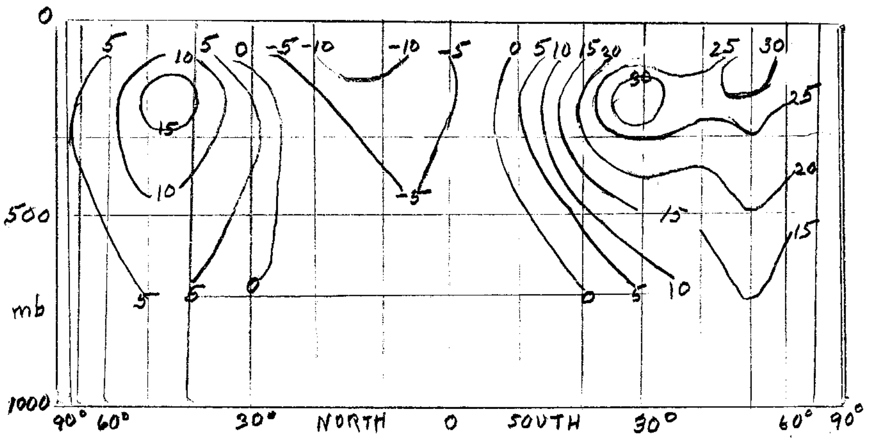

The time-and-longitude averaged zonal wind ($\bar{u}$) in July as estimated by Heastie and Stephenson (1958). Values are in m/sec^{-1}.

hydrostatic balance: $\frac{\partial\phi}{\partial\xi} = \frac{RT}{H_0}$

continuity: $\frac{1}{a\cos\theta}\frac{\partial v\cos\theta}{\partial\theta} + e^{\xi/H_0}\frac{\partial}{\partial\xi}\left(e^{-\xi/H_0}w\right) = 0$

momentum:
$$\begin{cases} \frac{v}{a\cos\theta}\frac{\partial u\cos\theta}{\partial\theta} + w\frac{\partial u}{\partial\xi} - 2\Omega v\sin\theta = F_x \\ \frac{v}{a}\frac{\partial v}{\partial\theta} + w\frac{\partial v}{\partial\xi} + 2\Omega\sin\theta + \frac{u^2}{a}\tan\theta = -\frac{1}{a}\frac{\partial\phi}{\partial\theta} + F_y \end{cases}$$

energy: $\frac{v}{a\cos\theta}\frac{\partial T}{\partial\theta} + w\left(\frac{\partial T}{\partial\xi} + \Gamma\frac{T}{T_0}\right) = \frac{Q}{C_p}$

where $\xi \equiv -H_0\ln\left(\frac{p}{p_0}\right)$.

The frictional and diabatic heating terms, F_x, F_y, and Q, are in reality the 'playmakers' for this problem. This precludes our following traditional GFD modeling approaches (i.e., neglecting these terms to first order, or replacing them by eddy diffusivities) since the physics contained in them is crucial to the nature of the solutions. In particular, solar energy goes largely into evaporation of surface water, and much of the heating of the atmosphere is due to the resultant latent heat release, a process which clearly is <u>not</u> diffusive.

Let us consider two types of clouds in the tropics and subtropics. First are the cumulonimbus which rise from cloud base clear to the tropopause. Second are the shallow 'trade cumulus', extending from the top of the mixed layer ($\sim$ 600 m) to the top of the 'trade-inversion' ($\sim$ 2 km).

The latent heat release due to cumulus will be parameterized by the following scheme. Presuming the vertical velocity in the clouds is larger than that of the ambient air, and that the area of cloud coverage is small (typically about 1%), we can write (following Arakawa & Shubert, 1974) $\frac{Q}{c_p} = \frac{M_c}{\rho}\left(\frac{\partial T}{\partial \xi} + \Gamma \frac{T}{T_0}\right)$ where M_c is the vertical mass flux in the cloud. Also $w = \tilde{w} + w_{cloud}$ so that $\rho w = \rho \tilde{w} + M_c$ where w is the ambient vertical velocity. Shown below is a representative profile of $M_c(z)$.

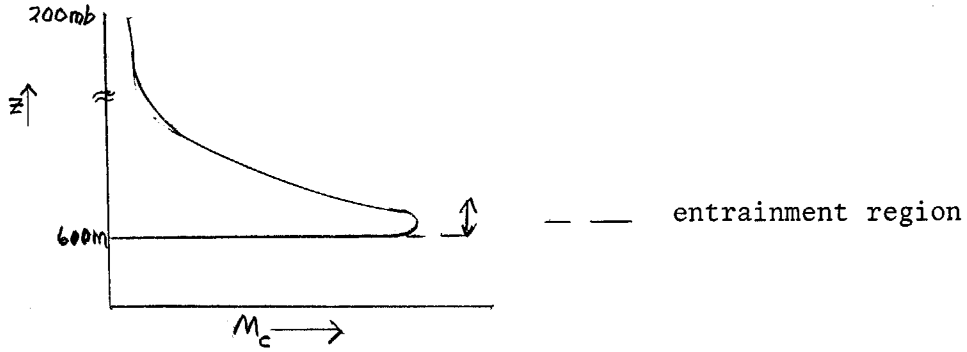

The water-vapor budget at the cloud base is expressed by $M_c = \frac{1}{q}\left[E + \begin{matrix}\text{convergence}\\ \text{of moisture}\end{matrix}\right]$ were E is the surface evaporation (per unit area per unit time) and q is the mixing ratio (mass water vapor/mass air); $\left(\begin{matrix}\text{convergence}\\ \text{of moisture}\end{matrix}\right) = q\,\rho w_{\text{trade-inversion}}$. Latent heat adds to the clouds' buoyancy: the air in the cloud appears to rise without cooling adiabatically.

Boundary layer friction is expressed using an eddy diffusion coefficient: $F_x = \frac{1}{\rho}\frac{\partial}{\partial \xi}\left(\mu \frac{\partial u}{\partial \xi}\right)$, where $\frac{\mu}{\rho}$ = 50 cm^2/sec at the surface and 10^4 at 1.1 km, which should adequately model mixed-layer turbulence. Above 1.1 km, the mixed-layer friction is set to zero, and momentum exchange due to cumulus takes over. This is expressed by

$$F_{x_c} = \frac{1}{\rho}\frac{\partial}{\partial \xi}\left(M_c\left[u - u_c\right]\right)$$

where u_c is a typical velocity in the cloud, which as a crude approximation, is taken equal to u at the cloud base.

Lastly, the portion of Q due to radiative heating is given by

$\frac{Q_{rad}}{c_p} = \frac{T_e(\theta, \xi) - T}{\tau(\xi)}$ where $\tau(\xi)$ is a relaxation time and T_e is the radiational equilibrium temperature.

3. FINAL COMMENTS FOR LECTURE #1.

A number of approaches have been taken to solving the problem just outlined, and these will be considered in more detail in the subsequent lectures.

Initially Q from latent heat release is derived from observed precipitation (note that although the ITCZ is about 200 km wide, it migrates, and its time-averaged effect shows up as a band of precipitation about 1000 km wide centered near the equator). Using this Q, M_c is derived, and hence F_x, the overall goal being to compute $\frac{\partial T}{\partial \theta}$ and $\frac{\partial T}{\partial \xi}$ which will be compared to observations.

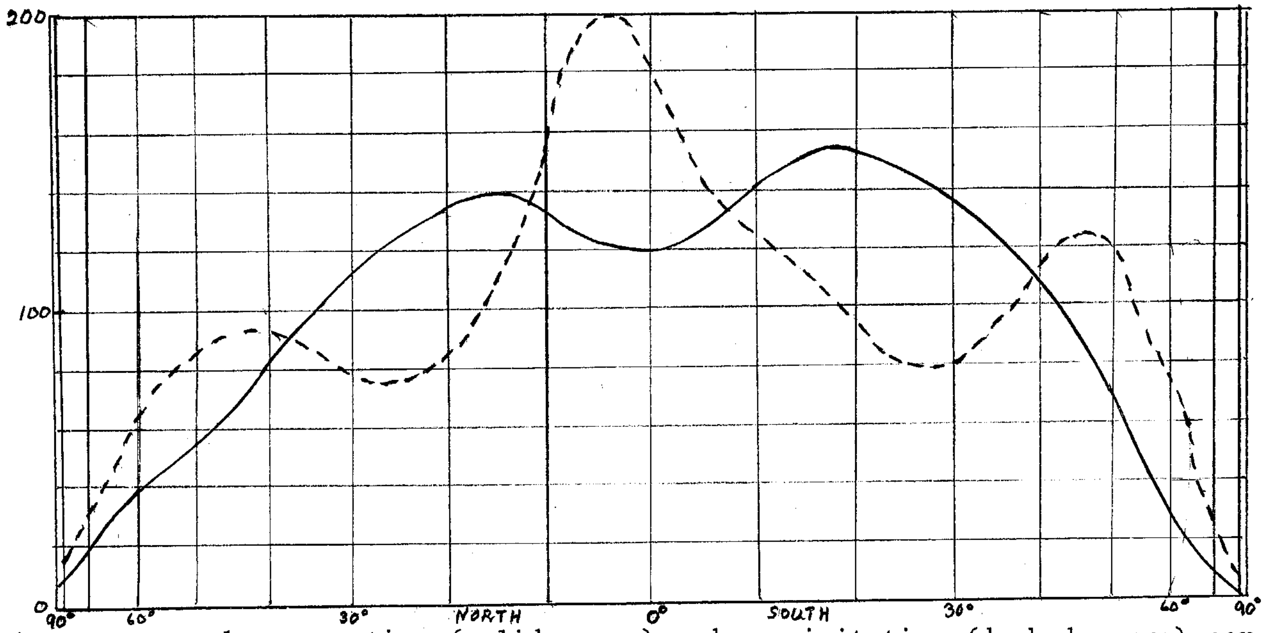

The Processes which Maintain the Circulation

Average annual evaporation (solid curve) and precipitation (dashed curve) per unit area as given by Sellers (1966). Values are in centimeters of water per year, or g cm^{-3} $year^{-1}$.

References

Arakawa. A. and W.H.Shubert 1974 Interaction of a cumulus cloud ensemble with a large scale environment, Part I. J.Atmos.Sci. 31: 674.

Jeffreys, H. 1933 The function of cyclones in the general circulation, in Selected Papers on the Theory of Thermal Convection with Special Application to the Earth's Planetary Atmosphere. Ed. by B. Saltzman, Dover Pub., New York. 1962.

Lorenz, E. 1967 The Nature and Theory of the General Circulation of the Atmosphere, WMO-No.218.TP.115.

Schneider, E. and E. Lindzen (submitted for publication) Linearized models of steady axisymmetric motions of the earth's atmosphere driven by radiation and cumulus convection.

Notes submitted by
Steven M. Ashe

PROBLEMS OF CLIMATE MODELING: STEADY AXIALLY SYMMETRIC ATMOSPHERIC MOTIONS

Richard S. Lindzen

We continue our study of steady axially symmetric atmospheric motions. The bulk of the results here are based on and treated comprehensively in Schneider and Lindzen 1976C, hereinafter referenced as SL, and Schneider 1976.

Define a meridional stream function ψ such that

$$V = \frac{e^{\xi/H_0}}{\cos\theta}\frac{\partial\psi}{\partial\xi} \qquad W = -\frac{e^{\xi/H_0}}{a\cos\theta}\frac{\partial\psi}{\partial\theta}$$

where a = earth's radius, θ = latitude and $\frac{\xi}{H_0} = -\ln\frac{p}{p_0}$. In the viscosity terms we assume $\rho \propto e^{-\xi/H_0}$; elsewhere we do not restrict $p(\xi)$.

We nondimensionalize the equations by assigning the following scales:

$$\xi \sim H_0 \quad y \equiv a\sin\theta \sim aT,\ T_0 \sim (\Delta T)_v = \Delta T \qquad \mu = \mu_{surface} = \nu$$

$$u, u_c \sim U = \frac{R\Delta T}{2\Omega a} \quad \Gamma \sim \frac{\Delta T}{H_0} \quad \tau \sim t$$

$M_c \sim \frac{\rho\psi}{a} \quad \psi \sim EUH_0$ where $(\Delta T)_v$ is a vertical temperature contrast imposed by the boundary condition and ν is the eddy viscosity at the surface. The nondimensional parameters are $E = \frac{\nu}{2\Omega H_0^2}$ the Ekman number; $R_o = \frac{U}{2\Omega a}$, the Rossby number; $\lambda = \frac{1}{2\Omega E t}$ a radiative-diffusive number.

This yields the equations:

$$R_0\underline{\left[\frac{1}{\sqrt{1-y^2}}\frac{\partial\psi}{\partial\xi}\frac{\partial}{\partial y}\left(u\sqrt{1-y^2}\right) - \frac{\partial\psi}{\partial y}\frac{\partial u}{\partial\xi}\right]} - \frac{Y}{\sqrt{1-y^2}}\frac{\partial\psi}{\partial} = \frac{\partial}{\partial\xi}\left(u\frac{\partial u}{\partial\xi}\right) + R_0\frac{\partial}{\partial\xi}\left(M_c(u-u_c)\right) \tag{1}$$

$$\underline{E^2R_0\frac{\partial}{\partial\xi}\left[e^{2\xi}\frac{\partial\psi}{\partial\xi}\frac{\partial}{\partial y}\left(\frac{1}{\sqrt{1-y^2}}\frac{\partial\psi}{\partial\xi}\right) - e^{\xi}\frac{\partial\psi}{\partial y}\frac{\partial}{\partial\xi}\left(\frac{e}{\sqrt{1-y^2}}\frac{\partial\psi}{\partial\xi}\right)\right]} +$$

$$+y\frac{\partial u}{\partial\xi} + \underline{R_0\frac{y}{\sqrt{1-y^2}}\frac{\partial}{\partial\xi}(u^2)} = \sqrt{1-y^2}\frac{\partial T}{\partial y} + \frac{E^2}{\sqrt{1-y^2}}\frac{\partial}{\partial\xi}\left(e^{\xi}\frac{\partial}{\partial\xi}\left(\mu\frac{\partial}{\partial\xi}\left(e^{\xi}\frac{\partial\psi}{\partial\xi}\right)\right)\right) \tag{2}$$

$$R_0\left[\underline{\frac{\partial\psi}{\partial\xi}\frac{\partial T}{\partial y}} - \frac{\partial\psi}{\partial y}\left(\frac{\partial T}{\partial\xi} + \Gamma\frac{T}{T_0}\right)\right] = \frac{\partial}{\partial\xi}\left(\mu\left(\frac{\partial T}{\partial\xi} + \Gamma\right)\right) + \lambda e^{-\xi}\frac{T_e - T}{\tau} + R_0M_c\left(\frac{\partial T}{\partial\xi} + \Gamma\frac{T}{T_0}\right) \tag{3}$$

$$R_o\left[\underline{\frac{\partial\psi}{\partial\xi}\frac{\partial T}{\partial y}} - \frac{\partial\psi}{\partial y}\left(\frac{\partial T}{\partial\xi}+\Gamma\frac{T}{T_o}\right)\right] = \frac{\partial}{\partial\xi}\left(\mu\left(\frac{\partial T}{\partial\xi}+\Gamma\right)\right)+\lambda e^{-\xi}\frac{T_e-T}{\tau}+R_oM_c\left(\frac{\partial T}{\partial\xi}+\Gamma\frac{T}{T_o}\right) \qquad (3)$$

We set the radiative equilibrium temperature $T_e=\frac{1}{2}\left[(T_o(y)-\Gamma\xi)+|T_o(y)-\Gamma\xi|\right]$ where we have scaled the temperature down by 200° K, so that the stratispheric temperature is 0°. This field is shown in Fig.3c of SL. It becomes isothermal at sufficiently high altitude.

In the linearized model we drop all (underlined) nonlinear terms, set $\sigma\equiv\frac{\partial T}{\partial\xi}+\Gamma\frac{T}{T_o}$, *a priori*, and specify M_c from observed precipitation.

For the boundary conditions we set zero motion across the top, bottom and poles:

The top is stress-free: $\frac{\partial u}{\partial\xi}=\frac{\partial}{\partial\xi}\left(e^{\xi}\frac{\partial\psi}{\partial\xi}\right)=0$ at $\xi=\xi_T$

$T=0$ at $\xi=\xi_T$. The surface temperature is set.

$$T=T_o(y) \text{ at } \xi=0.$$

We apply the geophysical boundary condition, that the turbulent momentum flux is proportional to and in the same direction as the surface stress:

$$\frac{\mu}{\rho_o}\frac{\partial u}{\partial\xi}=C_D u|\underline{V}|,\quad \frac{\mu}{\rho_o}\frac{\partial v}{\partial\xi}=C_D v|\underline{V}| \text{ at } \xi=0.$$

where C_D is a drag coefficient. This condition is linearized by setting $|\underline{V}|$ constant.

This is an eighth order equation in ξ, a non-separable partial differential equation in ξ and y. To solve, it was written in finite differences and solved by Gaussian elimination. Motion occurs because of the latitudinal dependence of heating through $T_e(y,\xi)$ and $M_c(y,\xi)$. (The solution is non-singular at the equator despite Ekman-layer type dynamics.)

Case 1 omits M_c so that the system is driven by variations in T_e only. If σ is taken as observed then T is close to T_e and the zonal wind is close to the thermal wind (maximum of 30 m/sec near 20°N) (See Figs. 3a, b, c in SL). The meridional wind is slight; it arises because of thermal wind vertical shear in the surface friction layer (below 800 mb). It becomes important when you include moisture and boundary layer convergence. The static stability computed is much less than that which was specified -- an internal inconsistency.

Case 2 puts in the cumulus heating term due to M_c but leaves out cumulus friction. (The M_c curve used follows the precipitation curve in Fig.1 of SL except that it drops continually from its value at 30°N to zero at 90°N. Also $M_c = 0$ at 900 mb and has its maximum at 800 mb.) You get very large $\frac{\partial T}{\partial y}$ and u reaching 300 m/sec at 20°N (see Figs.7a, b in SL). This violates angular momentum conservation; the linear equations cannot transport angular momentum latitudinally.

Case 3 restores cumulus friction to Case 2. The solution is in Fig.8 a-c of SL. Note that the maximum zonal wind speed is 140 m/sec at 35°N (much more realistic!) and the upper level temperature gradients are almost zero below 30°N, but then become steep; the tropopause is discontinuous between 30-40°N. Although u is still too large, its maximum value is smaller than in Case 2 because cumulus friction limits u at low latitudes and the Coriolis parameter is greater at the more northerly maximum. The stream function shows three direct meridional cells: a frictionally-driven Hadley cell with a smaller thermally-driven bottom cell, and a weak upper cell in the stratosphere.

We note that Charney (1971) formulated a model called C.I.S.K. (Conditional Instability of the Second Kind) which is based on the idea that a saturated atmosphere may be unstable due to the release of latent heat as an air parcel is raised, even if Γ is subadiabatic. Charney's model predicts growing instability increasing from the equator while SL predicts growing instability towards the equator.

In the nonlinear model we reinstate the term shown in dashed underline in (1), representing the advection of zonal momentum. The other solid underlined nonlinear terms are still omitted because they are found to be smaller in effect.

We redefine $\hat{u} = -\frac{y^2}{2} + R_0(1-y^2)^{1/2}\, u$, which is the angular momentum of a ring of fluid or a latitude circle. This permits the first equation to be written,

$$R_0\left[\frac{\partial \hat{u}}{\partial y}\frac{\partial \psi}{\partial \xi} - \frac{\partial \hat{u}}{\partial \xi}\frac{\partial \psi}{\partial y}\right] = \frac{\partial}{\partial \xi}\left(\mu \frac{\partial \bar{u}}{\partial \xi}\right) + R_0 \frac{\partial}{\partial \xi}\left(M_c\left(\hat{u}-\hat{u}_e\right)\right)$$

(R. Hide (1969) used this equation to argue that there cannot be an extremum of angular momentum in the fluid, if only diffusive friction is considered $(M_c = 0)$. The only extremum can be at the equator at the surface.)

To solve this nonlinear system we use an iterative scheme on u and ψ in (1), substituting the previously found u to linearize the equation, by which ψ is computed, and vice versa. The first approximation is $u = 0$, which reduces to the linear equation discussed previously.

This method is found to converge provided friction (diffusive + cumulus) dominates nonlinear meridional advection of angular momentum.

References

Charney, J. G. 1971 Tropical cyclogenesis and the formation of the intertropical convergence zone. In: Reid, W.H., ed.: Mathematical Problems in Geophysical Fluid Dynamics (Lectures in Applied Mathematics, Vol.13) Providence: American Mathematical Society: 355-368.

Hide, R. 1969 Dynamics of the atmospheres of the major planets with an appendix on the viscous boundary layer at the rigid bounding surface of an electrically-conducting rotating fluid in the presence of a magnetic field. J.Atmos.Sci. 26: 841-853.

Schneider, E.K., and R.S.Lindzen 1976a: A discussion of the parameterization of momentum exchange by cumulus convection. J.Geophys.Res.(Green), in press.

-------- and R.S.Lindzen 1976b: On the influence of stable stratification on the thermally-driven tropical boundary layer. J.Atmos.Sci., in press.

-------- and R.S.Lindzen 1976c: Linearized models of steady axisymmetric motions of the earth's atmosphere driven by radiation and cumulus convection. J.Atmos.Sci., submitted for publication.

-------- , 1976 Nonlinear model of steady axisymmetric motion of the earth's atmosphere driven by radiation and cumulus convection. J.Atmos.Sci.,submitted for publication.

Notes submitted by
Lawrence C. Kells

PROBLEMS OF CLIMATE MODELLING

Richard S. Lindzen

This lecture:

(1) reviews the motivation for this study of zonally symmetric models;

(2) reviews features of the linearized and non-linearized model results;

(3) presents a simple one-dimensional analysis for the tropical static stability and height of the tropical tropopause as a function of the surface evaporation rate;

(4) presents a simple two-dimensional analysis for the lateral extent of the Hadley cell as a function of the cumulus convective heating.

(1) The motivation for this study is to see to what extent a time independent zonally symmetric model can simulate the atmosphere's observed (time and longitudinal mean) flows; this steady state can then be regarded as the basic state upon which (time and/or longitudinally dependent) eddies occur, (e.g., baroclinic instabilities and stationary orographically forced eddies). This is contrary to the more accepted concept that the baroclinic eddies themselves transport momentum up-gradient to main the mean jet stream; however, it may be that much of the observed 'transient eddy' and 'stationary eddy' transports (rf. Oort's lectures) is really due to essentially steady symmetric circulations which meander slightly over the time period or longitudinal extent of the observations.

(2) Linearized Model: (Schneider and Lindzen, 1976)

Although the linearized results are fairly close to the nonlinear results, (since the nonlinear terms remain small in the nonlinear analysis), the linearized model has a few drawbacks.

The velocity of the linearized zonal jet is too large (105 m/s at 35° 1st.). This large a velocity implies that the total zonal angular momentum, $(u+\Omega a\cos\phi)a\cos\phi$, has a local maximum in the interior of the fluid, (near the center of the zonal jet). This is impossible in nonlinear theory (Hide (1969), Schneider (1976)) and occurs here because the linearized theory neglects advection of relative angular momentum by the meridional circulation.

Also, the linearized model cannot predict the surface zonal wind velocities. These must be zero since there can be no net advection of planetary angular momentum into a vertically integrated column to balance any frictional torque at the surface.

Nonlinear Model: (Schneider, 1976)

The temperature fields are much the same as the linearized case; nearly flat from 0 - 35° lat. with a sharp transition to radiative equilibrium at 40° lat. However, the nonlinear results show the effect of advective meridional transports which now must satisfy conservation of zonal angular momentum and produce a temperature field in geostrophic balance with the zonal wind.

The Hadley cell is slightly broader and the zonal jet is pushed slightly poleward to 40° lat., with a zonal velocity of 120 m/s. Surface winds are easterly, 5 m/s, from 0° - 30° lat. and westerly, 10 m/s, at midlatitudes. The Hadley cell is centered at $\sim 15°$ lat., with a total mass flux of $\sim 70\%$ of the observed annual mean. A weak Ferrel cell occurs in the model, frictionally driven by the high latitude surface westerlies.

(3) In the equations, the value of the static stability is specified *a priori* and the results are only considered valid if the computed temperature field has a static stability of approximately the specified value. It is an important climatological problem to theoretically predict the atmospheric static stability. We can do this for Hadley cell regions with a simple one-dimensional calculation, using concepts and approximations borne out by the present numerical results.

In the Hadley cell, radiative cooling is balanced by downwelling due to cumulus heating, and meridional gradients and horizontal advection are small. Thus we can consider a one-dimensional vertical model in which:

$$\langle m_c \rangle \frac{1}{cp} \frac{\partial s}{\partial z} = \rho \langle Q_R \rangle \qquad (1)$$

where $\langle m_c \rangle$ is the vertical mass flux of the cumulus heating, at any level, horizontally averaged over the Hadley cell

$\langle Q_R \rangle$ is the radiative cooling, horizontally averaged

$\frac{1}{cp} \frac{\partial s}{\partial z}$ is the static stability

$\rho = \rho_0 e^{-\zeta}$ density at level ζ .

Also,

$$\langle Q_R \rangle \simeq \frac{T - T_e(z)}{\tau(z)} \qquad (2)$$

where T is the temperature

T_e is the radiative equilibrium temperature

$\tau(z)$ is a radiative time constant

The cumulus clouds rise through a height Δz such that the increase in ambient potential temperature Δs is equal to the latent heat gained by condensation of water vapor. This is known since the evaporation rate from the ocean is specified. With this constraint, we can substitute (2) into (1), integrate vertically, and find Δs and Δz , and thus the static stability $\frac{1}{cp} \frac{\Delta s}{\Delta z}$. The results are

$$\Delta z \sim 14\text{-}16 \text{ km}$$

$$\frac{1}{cp} \frac{\Delta s}{\Delta z} \sim 2.2^{\circ}\mathrm{K/km}^{-1}$$

(4) The numerical results show that the Hadley cell smears the cumulus heating and flattens out the horizontal temperature field to 40° lat. where the temperature suddenly adjusts to radiative equilibrium.

The nonlinear numerical method of solution used could not solve the case of a very latitudinally narrow cumulus heat source, but it is felt that the lateral extent of the Hadley cell depends only on the total amount of cumulus heating, and not on its latitudinal distribution. This is shown by the following calculation: -

Since friction is small, and the equatorial zonal velocity is nearly zero, the zonal wind field in the upper troposphere is approximately that of a ring moved frictionlessly from rest at the equator:

$$u \simeq \frac{y^2}{2R_0} \qquad (3)$$

where

y = sin (latitude)
R_0 = a global Rossby number

This velocity occurs at a height Δz, the vertical extent of the Hadley cell (here in units of scale heights), which is found from the specified net cumulus heating as in section (3) above.

The heat equation, when integrated latitudinally from the equator to the outer edge of the Hadley cell at $y = y_1$, gives

$$\int_0^{y_1} Q_c \cdot dy = \frac{e^{-\zeta}}{\tau(\zeta)} \cdot \int_0^{y_1} (T_e(\zeta) - T(y,\zeta)) \cdot d\zeta \qquad (4)$$

where $Q_c(y,\zeta)$ is the specified heat source due to cumulus convection (other symbols defined above). Assuming u varies linearly with height everywhere, equation (3) and the thermal wind relation give the horizontal variation of temperature. The temperature field is then obtained using the boundary condition that $T = T_e(\zeta)$, the radiative equilibrium temperature, at $y = y_1$.

Substituting for $T - T_e$ in Eq. (4), we find

$$\frac{e^{-\zeta}}{\tau(\zeta)} \cdot \frac{y_1^5}{10 \cdot \Delta z \cdot R_0} = \int_0^{y_1} Q_c \cdot dy$$

Thus the latitudinal extent of the Hadley cell, y_1, depends only on the integrated cumulus heating Q_c and not on its latitudinal distribution.

References

Hide, R. 1969 J.Atmos.Sci., 26: 841-853.

Schneider, E.K. and R. S. Lindzen 1976 Linearized models of steady axisymmetric motions of the earth's atmosphere driven by radiation and cumulus convection. Submitted for publication.

Schneider, E.K. 1976 Nonlinear model of the steady axisymmetric motion of the earth's atmosphere driven by radiation and cumulus convection. Submitted for publication.

Notes submitted by
David Pollard

PROBLEMS IN CLIMATE MODELING: CLIMATE MODELS

Richard S. Lindzen

We have discussed a tentative reassessment of the general circulation. Continuing on an *ad hoc* plane, we will now talk about climate models, especially the so-called 'simple albedo feedback models'. The albedo feedback mechanism is important due to the large contrast in albedo between ice-covered and ice-free areas. Small changes in the solar constant might induce a large change in global climate due to this feedback.

Hereafter we adopt the following assumptions:

1) the surface temperature T depends on latitude θ and time t.

2) the latitude of snow line θ_s depends on the surface temperature only.

3) the albedo α has the step function form:

$$\alpha(\theta) = \begin{cases} 0.6\ (\theta > \theta_s, & \text{ice-covered)} \\ 0.3\ (\theta < \theta_s, & \text{ice-free)} \end{cases}$$

The value in considering these simplified models is to develop an intuitive understanding for use in the more complex models. Our next assumptions are:

a) all elements in the energy budget can be expressed in terms of surface temperature T (although this is obviously wrong),

b) the atmosphere (with a time scale of one month), oceans (with time scales from 5 to 1000 years) and cryosphere (with a time scale of 10,000 years) are in equilibrium with each other and the sun.

For albedo feedback, notice that the snow and sea ice are more important than glaciers because the former has a much shorter time constant than the latter.

In a time-dependent form, the energy balance equation may be written as follows:

$$C\frac{\partial T}{\partial t} = Q\cdot S(\theta)\cdot a(T) - I + div.\vec{F}$$

where C denotes the heat capacity, Q denotes the solar constant divided by four. $S(\theta)$ denotes the normalized mean annual meridional distribution of solar radiation.

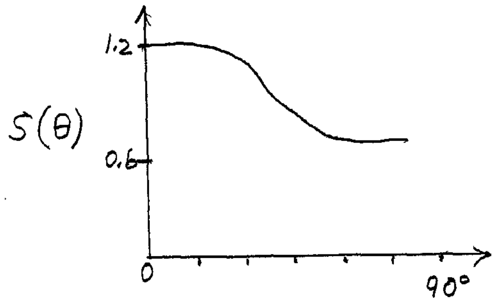

$a(T)$ denotes the absorption function defined as $1 - \alpha(\theta)$, I denotes the outgoing infrared radiation flux and F means the poleward heat flux in both atmosphere and oceans.

Adopting the empirical formula: $I = A + BT$ steady-state equilibrium implies:

$$Q\cdot S(\theta)\cdot a(I)-I+\underbrace{div.\vec{F}}_{\mathcal{J}(I)}=0.$$

The model becomes complete by specifying how the ice-sheet edge θ_s or $X_s (=\sin\theta_s)$ is determined. As the prescription for this, we adopt the condition

$T > -10^{\circ}C$, no ice present

$T < -10^{\circ}C$, ice present.

In terms of the radiation flux I, -10°C is expressed as

$$I(X_s) = I_s$$

which in turn gives the ice-sheet edge θ_s (or X_s).

In order to solve the problem, we choose X_s first and specify $a(X, X_s)$ then solve for Q.

When we plot the results on a $(Q/I_s, X_s)$ plane, the climate that has a positive slope is stable (and intuitively what one would expect) and the one that has a negative slope is unstable (and not what one would expect). These situations are shown in the figure schematically.

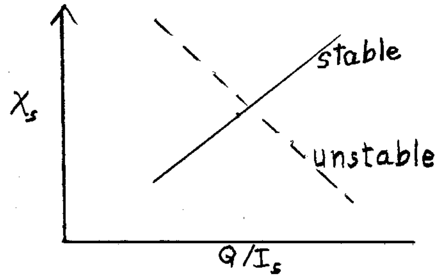

Next we review the results of some earlier models.

i) No heat flux: $\mathcal{J} \equiv 0$.

In this model $Q\cdot S\cdot a = I$. We have two curves corresponding to the upper and lower limits on albedo:

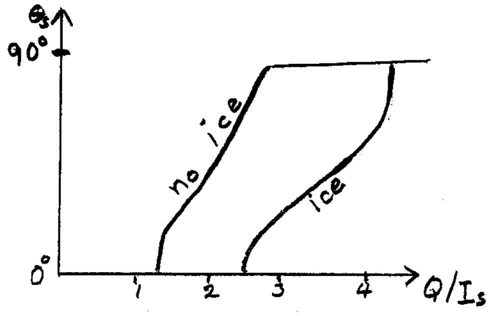

All possible climates lie in between the two curves. We find this model is stable.

ii) Budyko's model: $\mathcal{J} = \gamma(I-\bar{I})$

The result is shown in the figure.

This model is unstable because heat is transported latitudinally; as the ice cap advances, the region it covers absorbs less sunlight, hence the rest of the earth loses more heat by horizontal transfer to the poles and cools, hence the ice advances further. This model informs us of the necessity of latitudinal heat transport for instability.

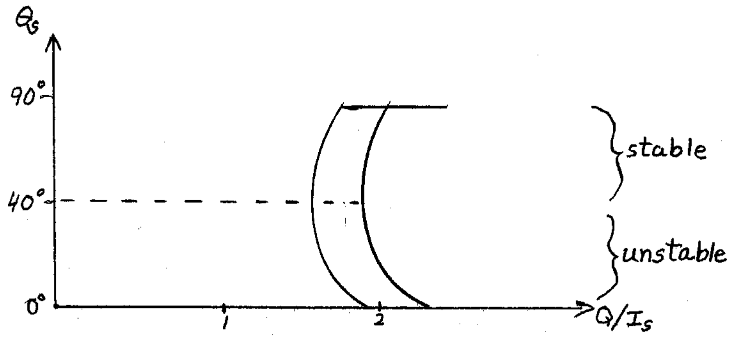

iii) Sellers' model: $\mathcal{F} = -\frac{d}{dx}\left\{(1-x^2)D\,\frac{dT}{dx}\right\}$

Now there is only one curve because the temperature is continuous across the snow line in this model. The result is shown in the figure.

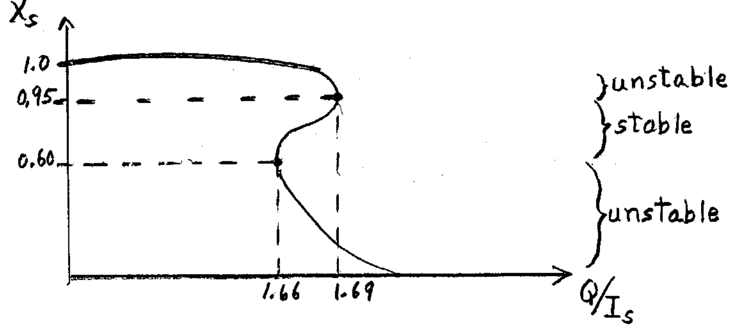

There is an unstable region for $1.0 > X_s > 0.95$, but this has no physical meaning. According to the figure, we are now in delicate equilibrium, only 2% away from disaster, a completely ice-covered earth !!

How could we incorporate the Hadley cell into these models?

Recall from Lecture #3 that the Hadley cell homogenizes temperature between 0° and 30° latitude. Therefore replace the radiation forcing between the latitudes 0° to 30° with its average. Otherwise, we use Budyko's model. The result is shown in the figure.

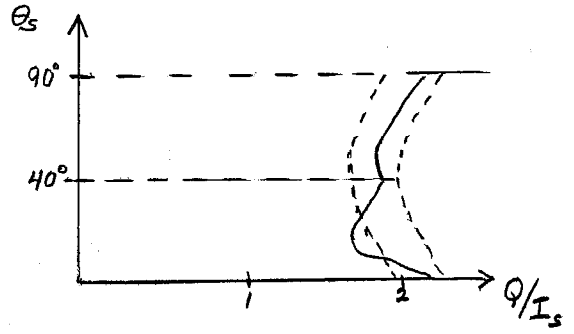

Specifically allowing for the Hadley cell enhances stability. Making this assumption in Sellers' model gives little change from Sellers' results, because his diffusive transport dehomogenizes the temperature in the tropics.

Finally we can use these to discuss the past ice age. At 18,000 years B.P. the ice line was 60° lat. instead of 72°, yet the tropical temperatures were almost the same as today's. If we let the heat transfer coefficient (γ in Budyko's model) go almost to zero poleward of the pack ice limit (because $\vec{F}$ may be due to oceans, not atmosphere), then the equator maintains its present temperature. Then we must re-define $\bar{I}$ such that the integral of div.$\vec{F}$ is still zero over whole earth. The system becomes much more stable, because there is little transport of heat into the polar region north of the ice line. It now takes a 20% decrease in the solar constant to have an ice-covered earth.

Notes submitted by
Toshio Yamagata and
Glenn H. White

PALEOCLIMATIC DATA

Wallace S. Broecker

In the next 100 years, it is expected that the CO_2 content of the atmosphere will double. According to Manabe and Wetherald, this will raise the Earth's average temperature (T_{av}) by 2.5°C. Eleven thousand (11K) years ago, in the most recent glacial age, T_{av} was only 5°C colder, so a 2.5°C increase could have a big effect. The nature of this effect is not known - the effects of clouds, albedo and other feedback mechanisms are unknown.

There is one known forcing function - changes in the Earth's orbital parameters. The Earth's orbit is precessing with a 22K period (years) (currently northern summers occur at greatest sun-earth separation), the Earth's tilt has a 40K period (which affects seasonal contrasts in amount of radiation received at a point on the Earth's surface), and the eccentricity of the orbit has a 90K period. Milankovitch (1958) produced a theory relating changes in climate to these parameters.

Measurements of the 'extent of glaciation' in the past show a 100K period

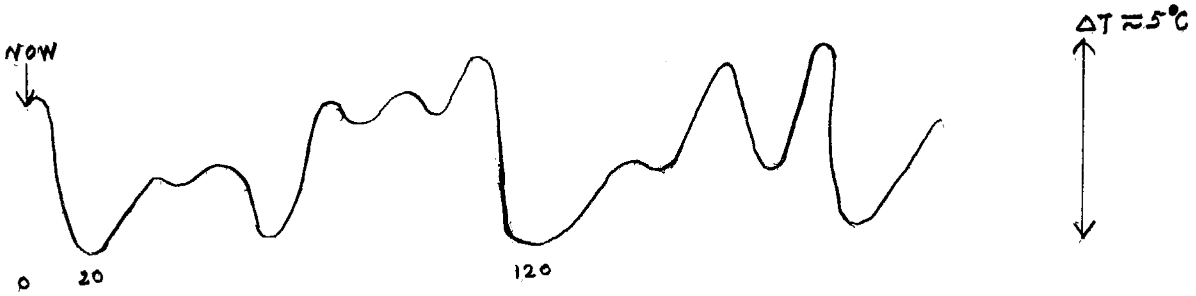

Thousand years before present
Diagram 1.

(see Diagram (1)). (The change is measured by δO^{18} - see later.) There was little glaciation up to 2500K years ago, since then there has been a quasi-periodic fluctuation.

Temperature change from glacial to interglacial periods - (air temperatures)

global av.	5°C	polar icecaps	6°
ocean	3°C	continents	10° (inferred)

Continental ice-coverage evidence in the United States of America indicates that successive glaciations were comparable in extent. About 3 - 5% of Earth was ice-covered, with corresponding sea-level decrease of 100 m. There is evidence of glaciation in South America and New Zealand, probably synchronous with Northern Hemisphere glaciation (Flint, 1947).

Isotope methods applied to deep-sea sedimentation cores are used to find temperatures in the past (Emiliani, 1955).

The ratio O^{18}/O^{16} in oxygen, deposited in $CaCO_3$ in fossils found in cores, for example, can be measured. The change in the ratio is caused by changes in the global ice volume. In H_2O, the lighter isotope evaporates slightly faster than the hearier one, leading to precipitation over the poles which is depleted in O^{18} by about 30 ^{o}/oo. If more ice forms, then the ocean ratio of O^{18}/O^{16} increases.

Fluctuations in the ratio if 1.6 ^{o}/oo are observed (see Diagram 2). The ice storage effect accounts for about 1 ^{o}/oo of this. A temperature effect of -2 ^{o}/oo/^{o}C also has to be taken into account.

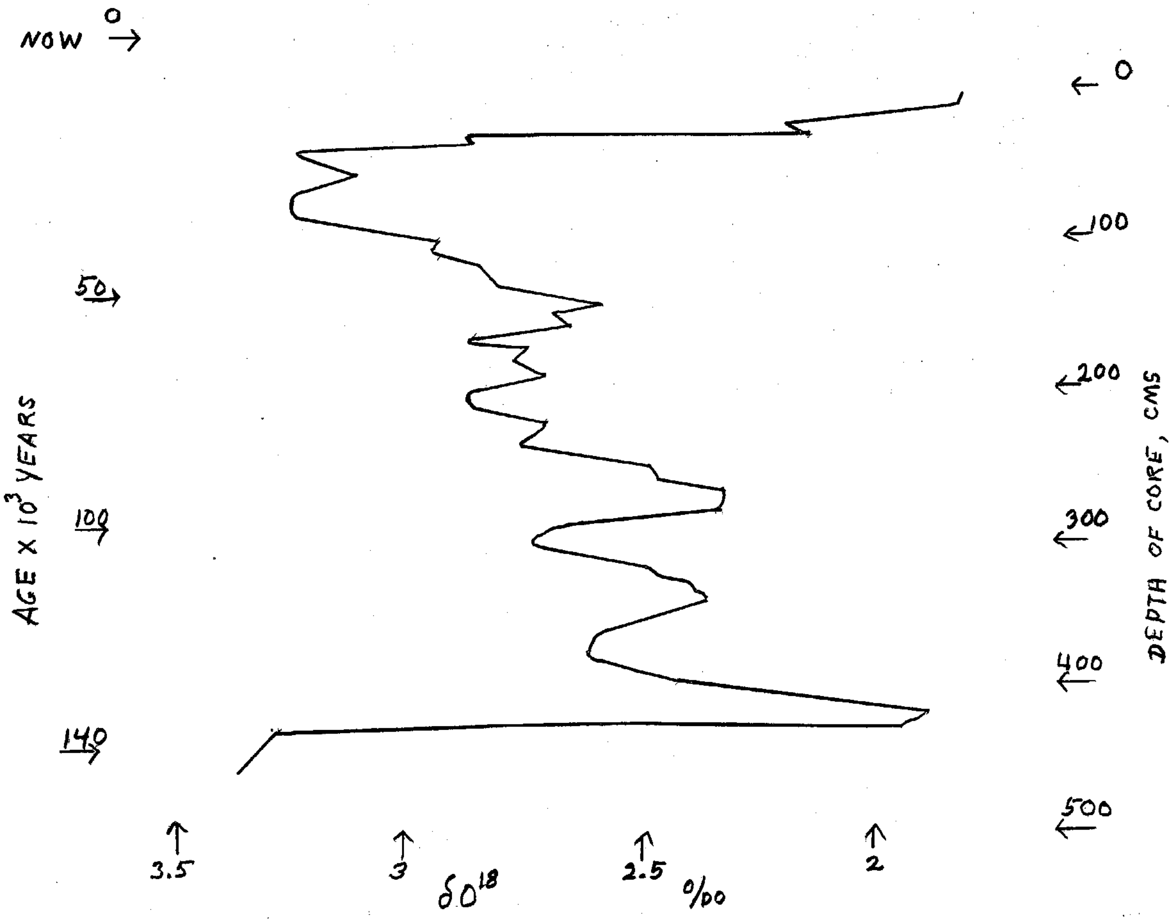

A DEEP-SEA CORE δO18 RECORD

Diagram 2.

Fossils of both surface and benthic origin are analyzed, and the same T change is observed in both. The deep ocean can only cool by about 3°C (or it would freeze), hence the tropical ocean surface was no more than 3° colder in a glacial period than now. (Shackleton 1967)

The usefulness of this method is that many deep-sea cores show the same effects.

To interpret the records, a means of dating the cores is needed.

(a) C^{14} dating is accurate for about 25K years;

(b) can reliably spot the magnetic reversal 700K years ago, and interpolate by assuming constant sedimentation rates;

(c) U^{238} and U^{235} series can be used,

Pa^{231} has 34K years half-life,

Th^{230} has 75K half-life,

U content of ocean constant;

(d) can fix lowest ice volume times by dates of highest stand of oceans, at 82, 103 and 124K years.

Models have been produced to account for the 100K cycle in terms of orbital parameters by using assumptions about glacier growth and melting. However, northern and southern hemisphere glacial periods apparently occur at the same time, which conflicts with seasonal-contrast-in-insolation theories. Broecker thinks that there is no good explanation of the cycle at present.

References

Milankovitch, M. 'Die chronologie des Pleistocans'. Bull.Acad.Sci.Math.Nat. Belgrade 4. 1938.

Flint, R.F. 'Glacial geology and the Pleistocene epoch'. Wiley & Sons,N.Y. 1947.

Emiliani, C. 'Pleistocene temperatures'. J.Geol. 63. 1955.

Shackleton, N. 'Oxygen isotope analyses and Pleistocene temperatures re-assessed'. Nature, 215. 1967.

general reference:

Broecker, W.S. and J. van Donk 'Insolation changes, ice volumes, and the O^{18} record in deep-sea cores'. Rev.Geophys.Space Phys. 8. 1970.

Notes submitted by
Michael K. Davey.

PALEOCLIMATIC DATA

Wallace S. Broecker

ESTIMATES OF PAST ICE VOLUMES AND SEA LEVELS

The ice which makes up the ice sheets of the earth has been formed from water vapour which has been evaporated from the sea surface. Of the two isotopes of oxygen, O^{18} and O^{16}, the lighter O^{16} if favoured by the process of evaporation and so there should be a direct correlation between the O^{18}/O^{16} ratio of the sea, and the degree of glaciation (or sea-level). The best record of the O^{18}/O^{16} ratio is that due to Shackleton who has analyzed this ratio in the shells of little organisms which have lived on the sea bed (see Figure below). These organisms appropriate different amounts of O^{18} and O^{16}, depending on the ratio present in the sea water, and also on the temperature of their environment.

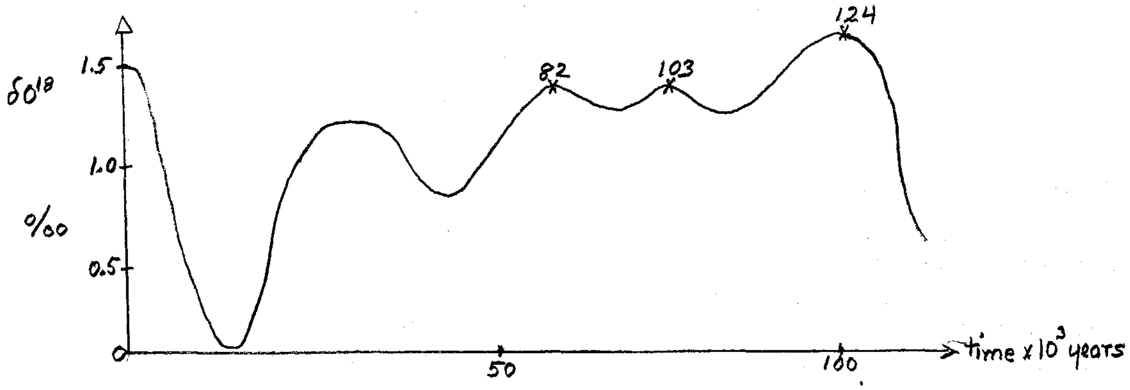

It is assumed that the temperature of the water on the sea bed has only changed by -1 ± 2°C over the last 150,000 years and this leads to an uncertainty in the δO^{18} values of only -0.2 ‰ ± 0.4 ‰. A total variation of 1.5 ‰ is observed over this period, so this leaves 1.3 ‰ ± 0.4 ‰ which is due to the global change in ice volume. The δO^{18} curve which is shown above is reproducible for many samples taken from the world's oceans.

The peaks in the δO^{18} curve at 82, 103 and 124 thousand years, are also evident in the levels of past coral reefs on islands which have been tectonically uplifted (e.g. Barbados, Timor and New Guinea). When allowance is made for the amount of uplifting of these islands (~ 0.3 m/year), the estimates of sea level are as follows:

Sea level (rel.to present)	Years before present
-15 m	82,000
-15 m	103,000
+ 6 m	124,000

The sea level 18,000 years ago can be estimated by several different methods. If it is assumed that the measured δO^{18} is equal to the present difference in O^{18} concentration upon evaporation, multiplied by the volume of the ice, then a sea level of -70 m is obtained. If a direct proportionality between the sea level and the δO^{18} curve is assumed, then using the values in the above table a sea level of -150 m is obtained. The sea level can also be deduced by a direct estimate of the extent and depth of the ice-cover at the time. In this case, the ice thickness is hart to estimate, but a sea level of -120 m is obtained.

OTHER WAYS OF ESTIMATING PAST CLIMATE

The remains of past vegitation provide a good indication of the local climate, providing the samples can be reliably dated. Different types of trees and plants flourish in different environments and a knowledge of this is useful in interpreting the data obtained from pollen samples.

Imbrie has analyzed plankton which lived at the ocean surface, and he has obtained the ocean sea-surface temperatures in the past (see lecture by Imbrie).

The O^{18}/O^{16} ratio in Greenland ice cores also contains information on the average sea-surface temperature.

LONG AND SHORT TIME SCALES

The analysis of benthic forams shows that 70 million years ago, the deep sea was 15°C warmer than it is today. The implications of this are complicated by the fact that the ocean basins were drastically different to what they are today.

On shorter time scales, analysis of Greenland ice cores shows that there have been no dramatic climatic trends in the last 7,000 years.

Notes submitted by
Trevor J. McDougall

THE FLUID TRANSPORTS

Abraham H. Oort

1. INTRODUCTION

The central theme of the three lectures will be the role of the atmosphere and oceans in transporting angular momentum, water vapor and energy.* The climatic picture may be described and to some extent "understood" through the study of the balance equations for these three basic quantities. From real data as well as from model generated data we may diagnose the present climate. We shall concentrate in these lectures on the zonally averaged picture of the climate for the present, while not disregarding the zonal anomalies so far as they are important in maintaining the zonal mean state. The stationary east-west asymmetries generally are thought to be of secondary importance, with the notable exception of the Asian summer monsoon circulation. I intend to discuss in the three lectures:

(1) the nature of the large-scale atmospheric and oceanographic data available to us;

(2) the hemispheric angular momentum, and the water vapor balance as derived from observations;

(3) the global energy balance as derived from observations.

---

*General references are Lorenz (1967), Newell *et al.*(1972, 1974), Oort and Rasmusson (1971), and Starr (1968).

2. NATURE OF LARGE-SCALE ATMOSPHERIC AND OCEANOGRAPHIC DATA

2.1 Atmosphere

It may be of interest to first investigate the dominant scales of motion in the atmosphere as revealed by spectra taken both in time and space. Kinetic energy time spectra near the ground are the easiest to obtain since they only require prolonged measurements at one location. They (Vander Hoven, 1957; Oort and Taylor, 1969; Hwang, 1970) give the following results:

(1) Most energy is contained in waves of two to ten days (baroclinic and long planetary waves).

(2) There is often a spectral gap between 20 minutes and several hours.

(3) There are large diurnal and weaker but still important annual cycles. (The latter are dominant in the case of temperature spectra.)

In the free atmosphere (above 3 km) cyclone waves are much more dominant (Vinnichenko (1970)). The high frequency (~ five minutes) maximum generally present near the ground only occurs intermittently (e.g. during clear air turbulence).

Spatial spectra are more difficult to obtain in general because of the observational network requirements. From hemisphere analyses (Kao and Wendell, 1970; Kao and Sagendorf, 1970; Kao *et al.*, 1970) the importance of the baroclinic and long planetary waves (~ 2000 km. and longer) becomes very clear. Transient eddies seem to have greater importance than stationary eddies in the heat and momentum fluxes.

In general circulation studies total transports of, e.g., sensible heat are frequently broken down into those due to mean meridional overturnings (MMC), transient eddies lasting a few minutes to the longest interval studied (TE), and standing or quasistationary eddies (SE). (Here the word "eddy" means a departure from a zonal, vertical or time mean).

The time mean of north-south sensible heat transport is given by:

$$\overline{vT} = \overline{(\bar{v}+v')(\bar{T}+T')} = \bar{v}\,\bar{T} + \overline{v'T'},$$

where ' denotes the departure of the instantaneous value of a quantity from the time average of that quantity.

The zonal mean heat transport is given by:

$$[vT] = [v]\,[T] + [v^{*}T^{*}],$$

where * denotes the departure of the local value of a quantity from its zonal mean.

The vertical mean heat transport is given by:

$$\widehat{vT} = \hat{v}\,\hat{T} + \widehat{v''T''}$$

where " denotes the departure of a quantity from its vertical mean.

Combining these three operations gives us the total north-south sensible heat transport across a latitude circle:

$$[\widehat{\overline{vT}}] = [\hat{\bar{v}}][\hat{\bar{T}}] + \underbrace{\widehat{[\bar{v}]''[\bar{T}]''}}_{MMC} + \underbrace{[\widehat{\overline{v'T'}}]}_{TE} + \underbrace{[\widehat{\bar{v}^{*}\bar{T}^{*}}]}_{SE}$$

The first term on the right is the heat transport due to the net mass flow across the latitude, which is generally very, very small.

A hemispheric picture of the relative intensity of zonal mean flow, transient and standing eddies in the kinetic energy of the atmosphere is given in Fig. 1 as a function of latitude and pressure. The Mean Kinetic Energy (MKE) is, of course, concentrated near the steady subtropical jet stream while the Transient Eddy Kinetic Energy (TEKE) is more uniformly distributed with respect to latitude and dominates away from the mean jet.

Let us now consider the global distribution of radiosonde stations where the actual atmospheric observations are taken. There are more than 700 stations in the Northern Hemisphere and only about 120 in the Southern Hemisphere. Considering zonal averages, the hemisphere midlatitudes are well-covered, but

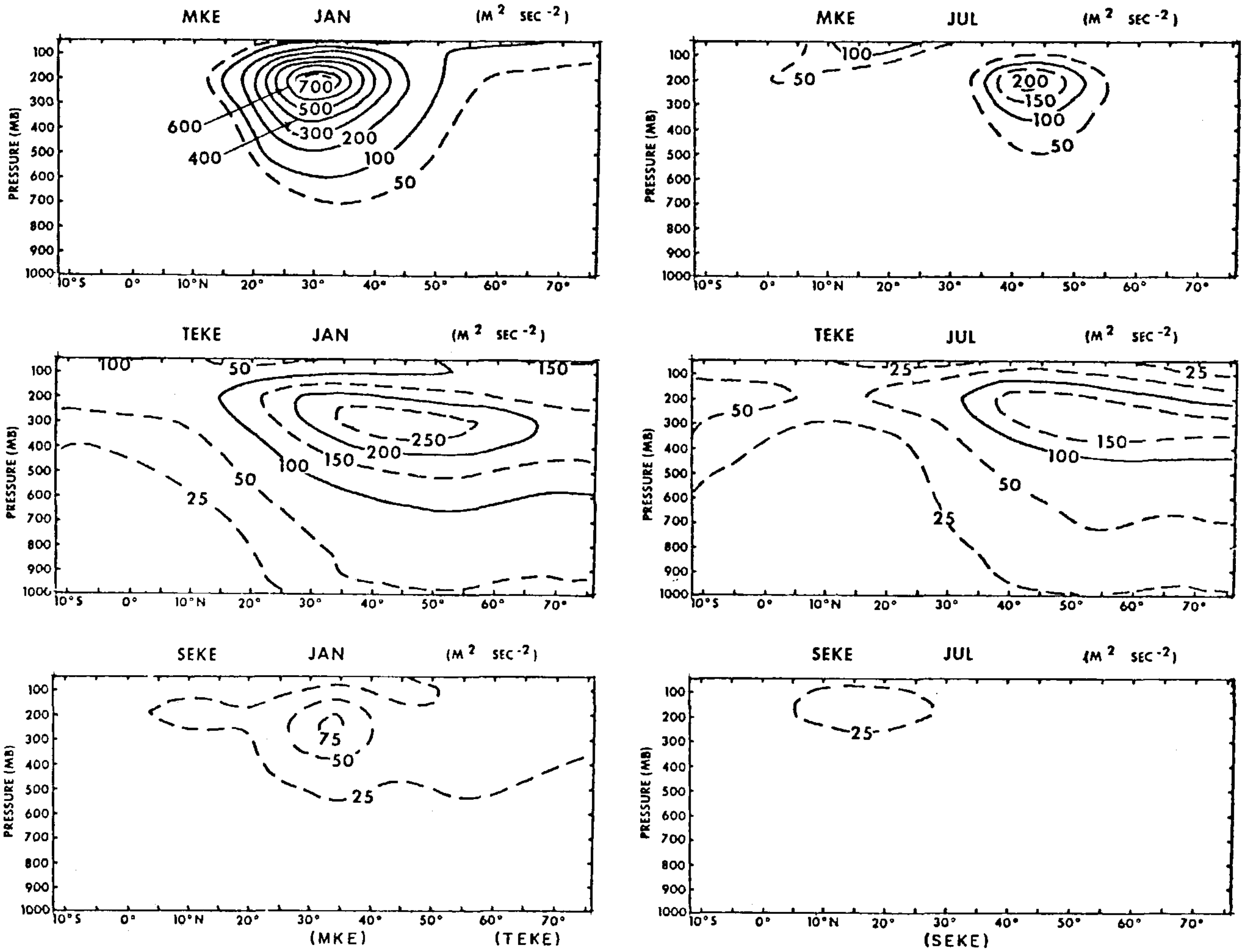

Fig. 1. The mean, transient eddy and standing (or stationary) eddy kinetic energy for January and July. (Oort & Rasmusson, 1971).

coverage is much poorer near the equator and throughout the Southern Hemisphere. There are no stations in the latitude band from 55°S to 65°S. Longitudinally, there are very clear gaps over the oceans. The error in our calculations due to these spatial gaps is worse than any due to instrumentation error in measuring the quantities.

To estimate the effect of these errors on the general circulation statistics, we used Manabe's ZODIAC general circulation model, which gives results fairly like the real atmosphere (except in Antarctica). We compared the results of calculating general circulation statistics from the model using each grid point and from the model using only grid points near each radiosonde station while employing the objective analysis scheme used on real data, to fill in. (Hayashi and Golder, 1976; Oort, 1976).

The mean zonal wind is reproduced fairly well, with some discrepancies in January in the Southern Hemisphere, between the two cases. Figure 2 shows one of the worst cases, the variance in the east-west stationary wind component. Overall, one may conclude that the radiosonde network is generally adequate in the Northern Hemisphere, except for certain parameters near the equator, and fair in the Southern Hemisphere, except for the mean meridional circulation and standing eddies, which cannot be measured with the current network.

We have to consider other data systems especially in the Southern Hemisphere, for example satellite soundings of temperature, humidity, and cloud winds. These have their own problems due to less accuracy.

2.2 Oceans

Time spectra in the oceans look quite different from those in the atmosphere with a large peak near the inertial frequency. Long term subsurface records are available only near the coasts and at the ocean station vessels for the construction of the low frequency part of the spectrum. Thus the data situation is quite different from the one in the atmosphere. The ocean is infrequently being sampled, and only for temperature, salinity, oxygen and some other chemical constitutuents.

Not only are spatial gaps between data points a problem, but so is the unrepresentativeness of the data points themselves. In many one-degree squares one finds none, or only one or two observations. Moreover, because of the existence of so-called MODE eddies as well as of inertial gravity waves, the long-term average may not be measured correctly by a few observations. Thus even the mean fields of temperature, salinity, and oxygen are not known well over the globe. The situation is much worse for the variances in time and the fluxes. Near the surface many ship drift reports show that the bulk of the kinetic energy, in Figs.3 and 4, is in the eddies, 20 to 40 times the mean over the open ocean and two times in the western boundary currents, (Wyrtki, 1976). Below the surface current data are practically non-existent. Transports have to be inferred by geostrophic calculations or from models. This is a very serious problem, because as we will show in the third lecture, heat balance considerations lead to the expectation of a very important meridional heat flux in the oceans, especially at low latitudes. This flux could be accomplished by mean meridional overturnings, transient or stationary eddies or any combination of them. One of the unanswered, but crucial climatic questions is what are the actual magnitude and predominant modes of transfer of energy by the oceans.

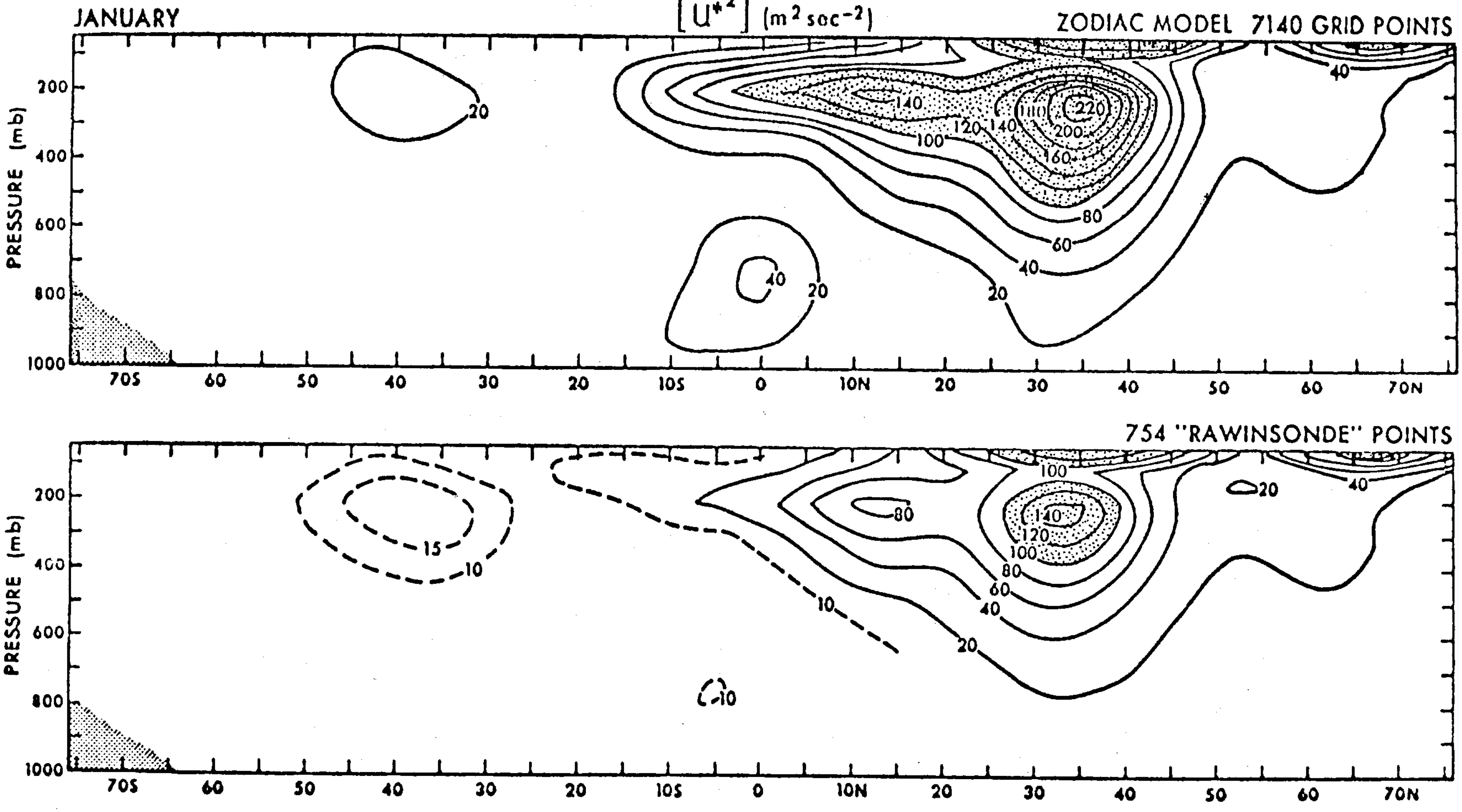

Fig.2 Comparison of the model and "simulated" model analysis of the variance in the east-west stationary wind component, $[\bar{u}^{*2}]$, in January.

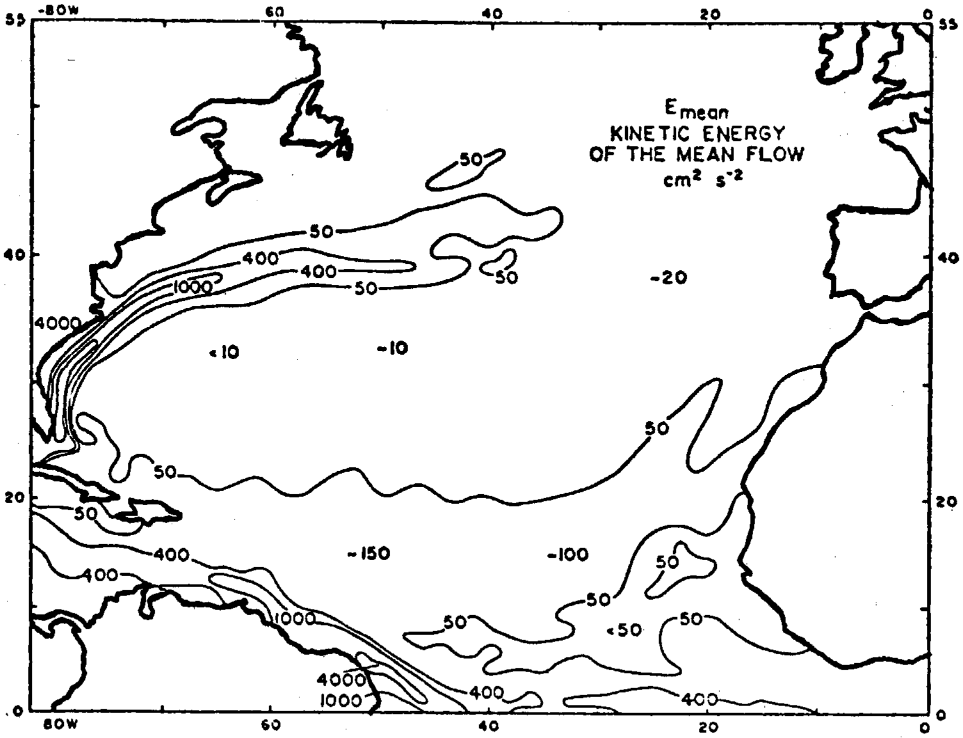

Fig.3 Kinetic energy per unit mass of the mean surface flow for the North Atlantic Ocean based on 1^{0} averages (Wyrtki, 1976).

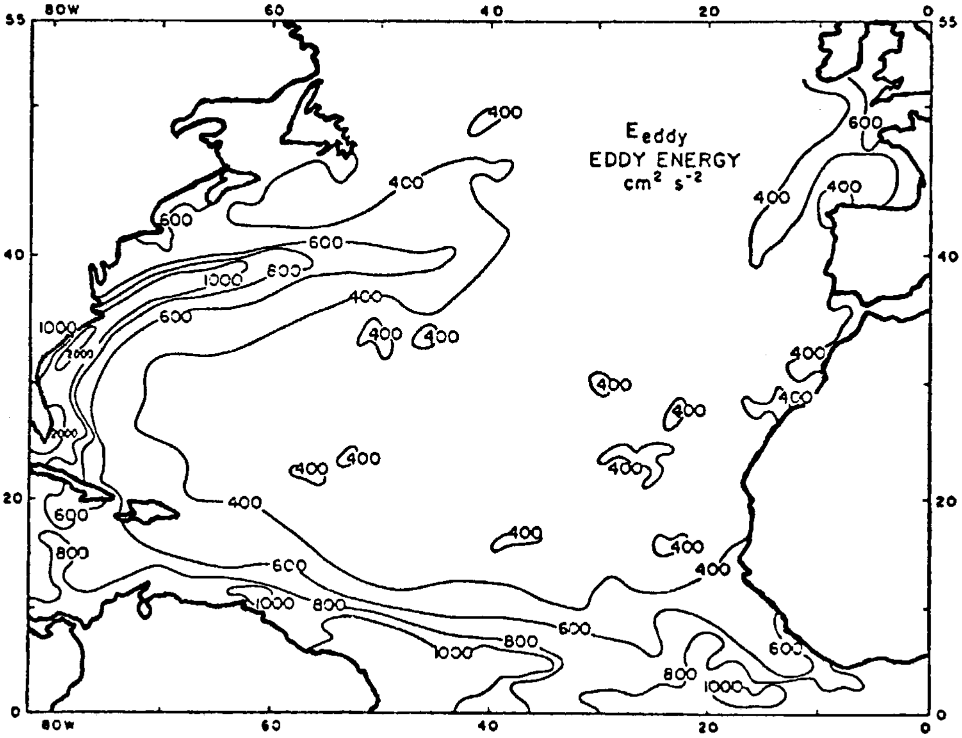

Fig.4 Eddy kinetic energy at the surface per unit mass for the North Atlantic Ocean based on 1^{0} averages (Wyrtki, 1976).

References

Hayashi, Y. and D.G.Golder 1976 Space-time spectral analysis of mid-latitude disturbances appearing in a GFDL general circulation model. J.Atmos.Sci. (submitted for publication).

Hwang, H.J. 1970 Power density spectrum of surface wind speed on Palmyra Island. Monthly Weather Rev., 98: 70-74.

Kao, S.K. and L.L.Wendell 1970 The kinetic energy of the large-scale atmospheric motion in wavenumber-frequency space: I. Northern Hemisphere. J.Atmos.Sci., 27: 359-375.

Kao, S.K. and J. Sagendorf 1970 The large-scale meridional transport of sensible heat in wavenumber-frequency space. Tellus, 22: 172-185.

Kao, S.K., C.Y.Tsay and L.L.Wendell 1970 The meridional transport of angular momentum in wavenumber-frequency space. J.Atmos.Sci. 27: 614-626.

Lorenz, E.N. 1967 The Nature and Theory of the General Circulation of the Atmosphere. WMO Publication No.218, T.P. 115, World Meteorological Organization, Geneva, Switzerland, 161 pp.

Newell, R.E., J.W.Kidson, D.G.Vincent and G.J.Boer 1972 and 1974 The general circulation of the tropical atmosphere and interactions with extratropical latitudes. Vols.1 and 2. The MIT Press, Cambridge, Mass. 258 and 371 pp.

Oort, A.H. and A.Taylor 1969 On the kinetic energy spectrum near the ground. Monthly Weather Rev. 97: 623-636.

Oort, A.H. and E.M.Rasmusson 1971 Atmospheric Circulation Statistics. NOAA Professional Paper 5, U.S.Government Printing Office, Washington, D.C. 323 pp.

Oort, A.H. 1976 Tests of adequacy rawinsonde network for global studies using numerical model output (in preparation)

*Starr, V.P. 1968 Physics of Negative Viscosity Phenomena, McGraw-Hill Book Co., New York City, N.Y. 256 pp.

Van der Hoven 1957 Power spectrum of horizontal wind speed in the frequency range from 0.0007 to 900 cycles per hour. J.Meteor., 14: 160-164.

Vinnichenko, N.K. 1970 The kinetic energy spectrum in the free atmosphere - 1 second to 5 years. Tellus, 22: 158-166.

Wyrtki, K., L.Magaard and J.Hager 1976 Eddy energy in the oceans. J.Geophys.Res. 81: 2641-2646.

Notes submitted by
Glenn H. White

---

[*] Recommended as basic text book.

GLOBAL ANGULAR MOMENTUM AND WATER VAPOR BALANCES

Abraham H. Oort

3. ANGULAR MOMENTUM BALANCE

The angular momentum (M) around the earth's axis of rotation is the sum of the relative and planetary components:

$$M = M_r + M_e$$
$$= u a \cos\phi + \Omega a^2 \cos^2\phi$$

where M_r is the relative component and M_e is the planetary component. ϕ is latitude, a is the earth's radius, and u is the zonal velocity. Integrated values for the angular momentum are:

solid earth: 591,000 x 10^{35} gm cm^2 sec^{-1}

atmosphere (solid body rotation): 1.01 x 10^{35} gm cm^2 sec^{-1}

atmosphere (relative, annual mean): 0.01 x 10^{35} gm cm^2 sec^{-1}.

For the northern hemisphere atmosphere, the relative angular momentum is 1.0 x 10^{33} gm cm^2 sec^{-1} in winter and -.1 x 10^{33} gm cm^2 sec^{-1} in summer. The southern hemisphere has very little seasonal variation, maintaining a constant value of about 10^{33} gm cm^2 sec^{-1}. The effect of the momentum variation on the solid earth is typically a 0.5 x 10^{-3} sec change in the length of the day per day, a quantity which is measurable by astronomers.

The balance equations for angular momentum can be developed, following Starr (1948, 1968). The statement is that the total time derivative of the angular momentum is equal to the sum of the torques:

$$\rho \frac{dM}{dt} = \left(\frac{1}{a\cos\phi}\frac{\partial p}{\partial\lambda}\right) a\cos\phi + F_x a\cos\phi,$$

where the first term on the right-hand side is the pressure torque and the second term represents the frictional torque. λ is the longitude. Making use of the equation of mass continuity, the expression can be rewritten:

$$\frac{\partial \rho M}{\partial t} = -\vec{\nabla}\cdot(\rho M \vec{v}) - \frac{\partial p}{\partial\lambda} + F_x a\cos\phi,$$

where $\vec{v}$ is the three-dimensional velocity. If the equation is integrated over the entire volume of the atmosphere, the divergence term will disappear, and the pressure term will generally give zero contribution, except when topography is considered. If this so-called mountain torque is present, the zonal integral of the pressure term can have discontinuities, giving rise to a contribution.

Since the long time average of the change in the angular momentum will presumably be zero, the frictional and mountain torque must balance. In a general sense, this implies that the area of the surface easterlies must be comparable to the area of the surface westerlies. The mountain torque, which is generally within 10% of the frictional torque, can work either in the same sense as the frictional effect (the usual case) or against it. The pressure torque is mostly associated with synoptic scales of motion, while the frictional torque is associated with smaller scales of motion, such as turbulent fluxes of momentum.

The transport of angular momentum in the atmosphere can be decomposed to examine the various processes. Using the same notation as last time:

$$\widehat{[\overline{Mv}]} = \underset{\substack{\text{net mass}\\ \text{flow}\\ \text{(seasonal)}}}{\widehat{[M]}\,\widehat{[\bar{v}]}} + \underset{\substack{\text{mean meridional}\\ \text{circulation}\\ \text{MMC}}}{\widehat{[\bar{M}]''\,[\bar{v}]''}} + \underset{\substack{\text{stationary}\\ \text{eddies}\\ \text{SE}}}{\widehat{[\bar{M}^{*}\ \bar{v}^{*}]}} + \underset{\substack{\text{transient}\\ \text{eddies}\\ \text{TE}}}{\widehat{[\overline{M'\,v'}]}}$$

The earth's angular momentum can become important for the first term on the right-hand side, while the remaining terms involve only relative angular momentum transport. Transient eddies are defined to have time scales of less than the period of record studied.

Graphs of annual flux of angular momentum (Fig.5) show a poleward flux across 30°-40° north latitude, mainly due to TE. The mechanism of angular momentum transport by eddy processes is tilting of the streamlines, giving rise to

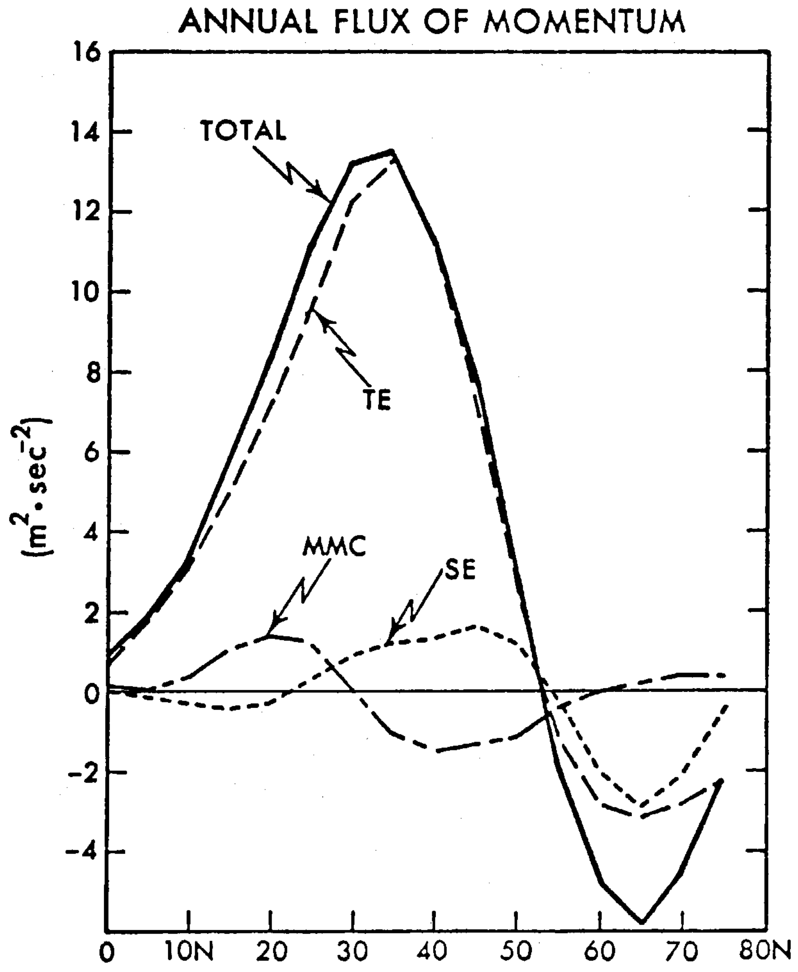

Fig.5. Mechanisms of poleward flux of momentum for annual mean conditions.

u'v' correlations. At high latitudes, there is some southward transport due to TE and SE. Most of the transport is accomplished by TE. However, this does not include only cyclones, as permanent eddies that vary seasonally are included in TE (i.e., variations in the Hadley cell, or monsoons). Some of these seasonal patterns would be included in SE on a winter or summer curve.

Angular momentum can also be transported vertically at certain latitudes, when terms like $[\rho\omega][\Omega a^2\cos^2\phi]$ are large in the MMC, or when there are $\overline{[\rho\omega]'[u]'}$ correlations. Examples of these processes are mean overturning or gravity waves.

Generally, at low latitudes, angular momentum is added to the atmosphere due to the frictional torque on the surface easterlies. At high latitudes, angular momentum is lost by frictional torque on the surface westerlies. There is a corresponding poleward transport at 30° north.

4. WATER BALANCE

On the average, there are 2-3 $\mathrm{gm/cm^2}$ of water in an atmospheric column. The amount is greatest between ±10° latitude, reaching a minimum over the land deserts and over the poles.

Water balance equations can be formulated for both water vapor and for liquid water plus ice (see Peixóto, 1973). For water vapor, the balance is:

$$\rho\frac{dq}{dt} = \text{source of water vapor} = e - c$$

where q is the specific humidity, e is the evaporation, and c is the condensation.

For ice and liquid water, the equation is

$$\rho\frac{dq_c}{dt} = c - e$$

If the total derivatives are expanded and the two equations are added, the result is:

$$\frac{\partial\rho q}{\partial t} + \vec{\nabla}_2\cdot\rho q\vec{v} + \frac{\partial}{\partial z}(\rho q\omega) + \frac{\partial\rho q_c}{\partial t} + \vec{\nabla}_2\cdot\rho q_c\vec{v} + \frac{\partial}{\partial z}(\rho q_c\omega_c) = 0,$$

where $\vec{\nabla}_2$ is the horizontal divergence, ω_c is the vertical velocity of falling condensation, and the equation of mass continuity has been used. This equation can be integrated vertically, from the surface to the top of the water vapor:

$$\frac{\partial W}{\partial t} + \vec{\nabla}_2\cdot\vec{Q} - E + \left(\frac{\partial W_c}{\partial t} + \vec{\nabla}_2 + \vec{Q}_c + P\right) = 0,$$

where $W = \int \rho q\, dz$ = water vapor in a column, E and P are the evapotranspiration and precipitation at the surface, and $\vec{\nabla}_2\cdot\vec{Q}$ and $\vec{\nabla}_2\cdot\vec{Q}_c$ are the vertically averaged horizontal fluxes of water vapor and liquid water plus ice, respectively, W_c, the total amount of liquid water and ice in a vertical column, is very small ($W_c \leq 0.1\text{-}0.3\ \mathrm{gm/cm^2}$), and the horizontal divergence of liquid water flux is very small, so we can approximate the balance by

$$\frac{\partial W}{\partial t} = -\vec{\nabla}_2\cdot\vec{Q} + (E - P).$$

This is the atmospheric branch of the hydrologic cycle.

The terrestrial branch of the hydrologic cycle can be represented by

$$S = -(E-P) - \vec{\nabla}\cdot\vec{R}_o - \vec{\nabla}\cdot\vec{R}_u$$

where S is the rate of ground water storage. The first divergence term represents the divergence of the runoff (due to rivers etc.), and the second divergence term represents the divergence of the subsurface runoff. This last term is usually small and is generally neglected.

The term (E-P) is the link between the atmospheric and terrestrial branches of the hydrologic cycle. It is difficult to measure (E-P) directly. It is often computed as a residual after measurements of $\frac{\partial w}{\partial t}$ and $\vec{\nabla}\cdot\vec{Q}$ are made.

Maps of $\overline{w}(\lambda,\varphi)$ and $\vec{\nabla}\cdot\vec{Q}(\lambda,\phi)$, from Peixóto (1970) show that $\frac{\partial w}{\partial t}$ is very small, and that, for the annual mean, strong convergence of water vapor occurs over the equatorial region in the Intertropical Convergence Zone, over Brazil, India, and over the cyclone belts of the Atlantic and Pacific Oceans. Divergences occur over the polar regions, in the subtropics, and over the land deserts. The fact that $\vec{\nabla}\cdot\vec{Q} > 0$ over deserts implies that there should be an excess of evaporation over precipitation in those areas. Subsurface convergences can be invoked to maintain a water balance in desert regions.

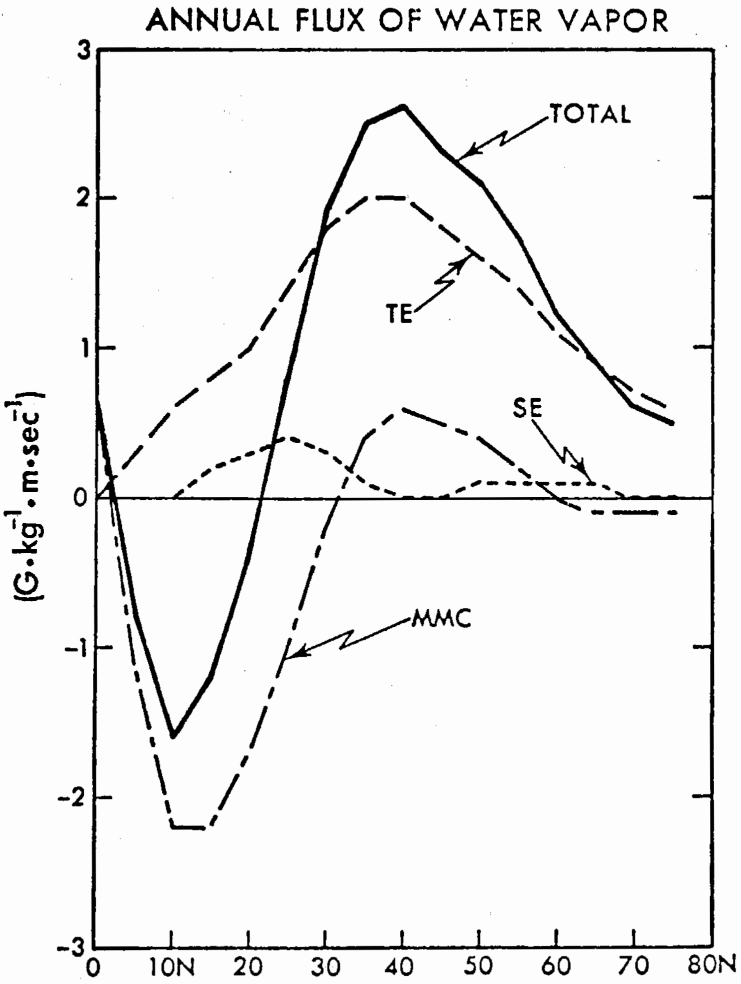

Fig.6. Mechanisms of poleward flux of water vapor for mean conditions.

Graphs of the annual flux of water vapor (Fig.6) indicate that the MMC is important at low latitudes, relative to TE. The water vapor is transported toward the equator by the MMC at low latitudes, and toward the poles by TE at high latitudes.

Graphs of (P-E) (Sellers, 1965, p.84) show:

$(P - E) > 0$	-5°S to 10°N
$(P - E) < 0$	-5°S to -40°S
$(P - E) < 0$	10°N to 40°N
$(P - E) > 0$	poleward of ±40°

Global-scale variations in (P - E) may account for the observed differences in salinity between the Atlantic and Pacific Oceans.

References

Lorenz, E.N. 1967 The Nature and Theory of the General Circulation of the Atmosphere. World Meteorological Organization, Geneva. pp.51-53.

Oort and Rasmusson 1971 Atmospheric Circulation Statistics. U.S.Gov't.Printing Office, NOAA. Prof.Pap.No.5, 323 pp. 19-22.

Peixôto, J.P. 1970 Water vapor balance of the atmosphere from five years of hemispheric data. Nordic Hydrology, 2: 120-138.

Peixóto, J.P. 1973 Atmospheric water vapor flux computations for hydrological purposes. World Meteorological Organization, Reports on WMO/IHD Projects No.20, Geneva, Switzerland, 83 pp.

Sellers, W.D. 1965 Physical Climatology. Univ.Chicago Press, Chicago, 272 pp.

Starr, V.P. 1948 An essay on the general circulation of the earth's atmosphere. J.Meteorol. 5: 39-48.

Starr, V.P. 1968 Physics of negative viscosity phenomena. McGraw Hill Book Co., New York City, N.Y., 256 pp.

Notes submitted by
Richard D. Romea

THE FLUID TRANSPORTS

Abraham H. Oort

5. ATMOSPHERIC ENERGY CYCLE AND BUDGETS

Due to the sparsity of data in the Southern Hemisphere, only Northern Hemisphere statistics will be considered.

5.1 Atmospheric energy amounts.

Let us first look at various energy variations over a year:

N. Hemisphere	Surface - 75 mb layer		
Winter	Summer		
1.0	0.5	x 10^{20} cal.	Kinetic Energy $(\frac{1}{2} v^2)$
29	50		Latent Heat (Lq)
340	352		Potential Energy (gz)
1003	1036		Internal Energy $(C_v T)$
1373	1439		Total

For vertically integrated quantities the potential and internal energies above are proportional, and may be combined into a total potential energy. However, as shown by Lorenz, only a small portion of this total potential energy is available for conversion into kinetic energy. This available potential energy (A.P.E.) is the difference between the total potential energy of the atmosphere at any time, and the lowest total potential energy which could be achieved by an adiabatic redistribution of its mass. This may be approximated by the variance of potential temperature on isobaric surfaces. For further discussion see Lorenz (1967).

5.2 Atmospheric energy cycle.

Let us consider presently the net flow of energy necessary to drive atmospheric motions through the cycle:

Generation ⟶ A.P.E. ⟶ Conversion ⟶ K.E. ⟶ Dissipation

Using five years of daily radiosonde data (1958-1963) at 600 stations in the Northern Hemisphere, available potential energy (P) and kinetic energy (K) were subdivided into mean and eddy contributions. These "eddy" contributions include both stationary east-west, and time variations.

In Fig.7 we note:

i) Quantities into or out of tops and bottoms of boxes are influx from Southern Hemisphere to Northern Hemisphere.

ii) Energy reservoirs in boxes are in 10^5 J/m^2 input, and transformation rates in watts/m^2.

iii) $\frac{\partial}{\partial t}$ (P_m, P_e, K_e, K_m) due to seasonal cycle are negligible for these two months of the year.

iv) Values in parentheses are not directly calculated.

v) Only large scale motion is explicitly described.

It is clear that for the Northern Hemisphere in January the dominant input of mean A.P.E. is not diabatic heating but influx from the Southern Hemisphere. The largest portion of the generation term seems due to latent heat release which varies the most with latitude. Frictional dissipation occurs dominantly in the eddy kinetic energy term, and gives a dissipation time of approximately three days.

The circulation is clearly less energetic in July, and exhibits a significantly smaller cross-equatorial flow of P_m. In both months we find a small conversion of K_m to P_m and a somewhat larger conversion of K_e to K_m (negative viscosity, see Starr, 1968). This last term is the only source of mean kinetic energy in the cycle. For further discussion see Oort & Peixóto (1974 a,b).

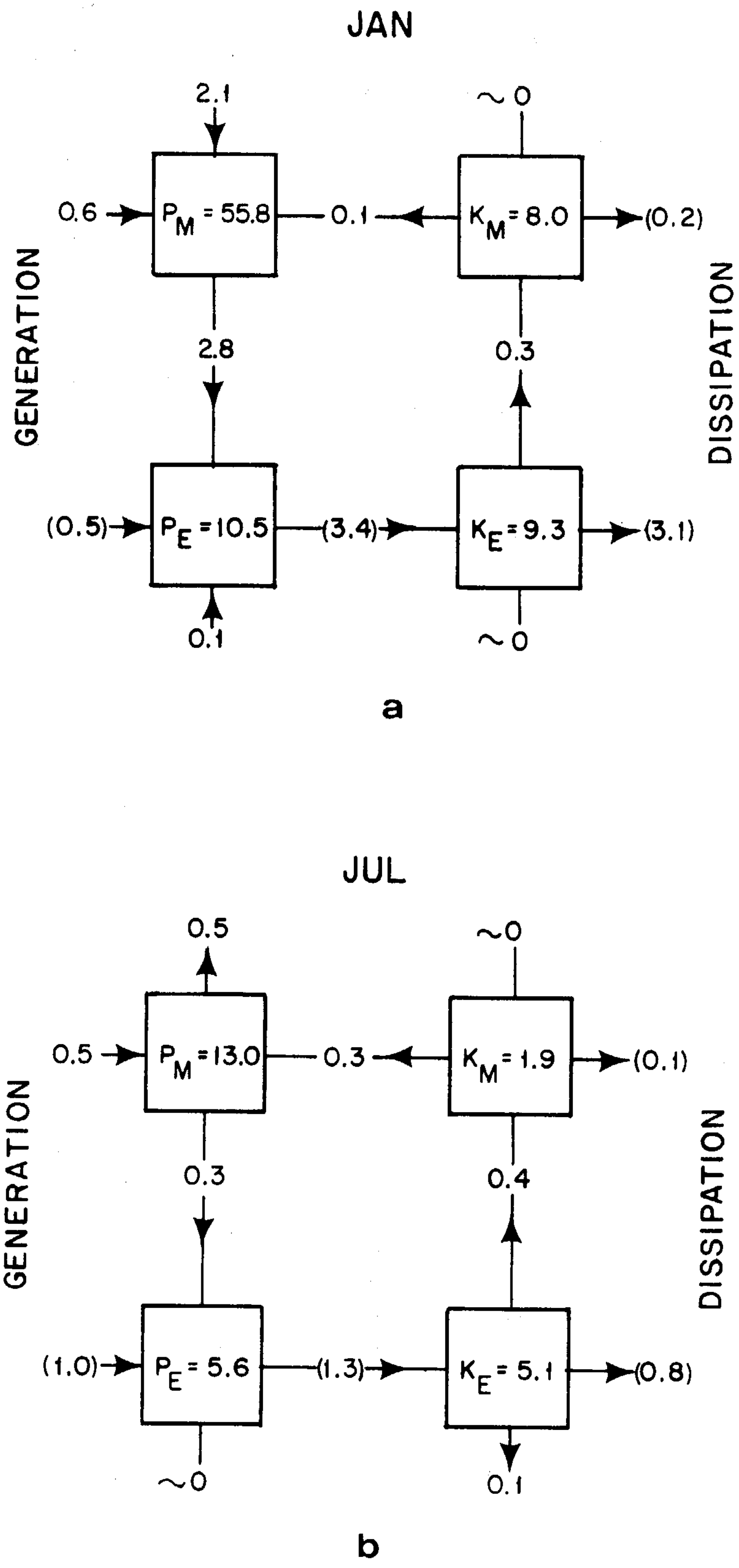
JAN
2.1
~0
0.6
P_M = 55.8
0.1
K_M = 8.0
(0.2)
GENERATION
2.8
0.3
DISSIPATION
(0.5)
P_E = 10.5
(3.4)
K_E = 9.3
(3.1)
0.1
~0
a
JUL
0.5
~0
0.5
P_M = 13.0
0.3
K_M = 1.9
(0.1)
GENERATION
0.3
0.4
DISSIPATION
(1.0)
P_E = 5.6
(1.3)
K_E = 5.1
(0.8)
~0
0.1
b

Fig. 7.

5.3 Annual variation of the ocean-atmosphere energy balance in latitude bands.

Let us consider a latitude band that extends in the vertical from the bottom of the ocean to the top of the atmosphere. If E denotes the total energy in the band:

(1) $\frac{\partial E}{\partial t}$ = (net rad.) Flux_{top} - div $(\text{Transport})_{\text{atm}}$ - div $(T)_{\text{ocean}}$

where geothermal heat flux, transport of icebergs, and horizontal radiative flux are neglected. The energy reservoirs considered are ocean, land, atmosphere, and snow and ice.

$$\frac{\partial E}{\partial t} = \frac{\partial}{\partial t}\left(S_o + S_L + S_A + S_I\right) \tag{2}$$

The atmospheric and oceanic energy fluxes are:

$$T_{ATM} = \int_0^{top} \rho\left(C_v T + gz + Lq + \frac{p}{\rho} + \frac{1}{2}V^2\right)\vec{V}\,dz \tag{3}$$

$$T_{ocean} = \int_{-275m}^{0} \rho c T \vec{V}\,dx \tag{4}$$

The data used are:

i) Flux at the top of the atmosphere: satellites (1964-1971)

ii) Atmosphere transport and storage: radiosonde (1958-1963)

iii) Ocean storage: all hydrographic and BT data as of 1973 available at National Oceanographic Data Center for the upper 275 m.

Error limits were estimated using data subsets. See Oort and Vonder Haar (1976) for further details.

Let us consider presently the different terms in Eq.2. The largest storage rates (see Figs. 9a and 9b) are found in the ocean (maximum of 100 watts/meter^2) centered at 40^{o}N in June and December and in the atmosphere (maximum of 20 watts/meter^2) north of 60^{o}N in May and the beginning of October. With these rates an estimate of $\frac{\partial E}{\partial t}$ can be made.

Utilizing Eq.(1), and calculating the net radiation input from satellite data (see Fig.8), and the atmospheric transport from the radiosonde data (see Fig.10a), residual estimate can be made of the northward flux of heat in the oceans (Fig.10b). One then finds a strong cross-equatorial transfer of heat in general from the summer to the winter hemisphere. Further, south of 25^{o}N the computed ocean heat transport is several times larger than the atmospheric transport. North of 40^{o}N, the reverse is true. For comparison, these estimates of ocean heat transport, at 20^{o}N, are twice as large as Budyko's estimate, and four times as large as Kirk Bryan's recent numerical ocean model estimates.

References

Lorenz, E.N. 1967 The nature and theory of the general circulation of the atmosphere. World Meteorological Organization, Publication 218: 115.

Oort, A.H. and J.P.Peixoto 1974 The annual cycle of the energetics of the atmosphere on a planetary scale. J.Geophys.Res. 79.

Oort, A.H. and T.H.Vonder Haar 1976 On the observed annual cycle in the ocean-atmosphere heat balance over the Northern Hemisphere. J.Phys.Ocean 6(6) (in press).

Peixoto, J.P. and A.H.Oort 1974 The annual distribution of atmospheric energy on a planetary scale. J.Geophys.Res. 79.

Vonder Haar, T.H. and A.H.Oort 1973 New estimate of annual poleward energy transport by Northern Hemisphere oceans. J.Phys.Ocean. 3: 169-172.

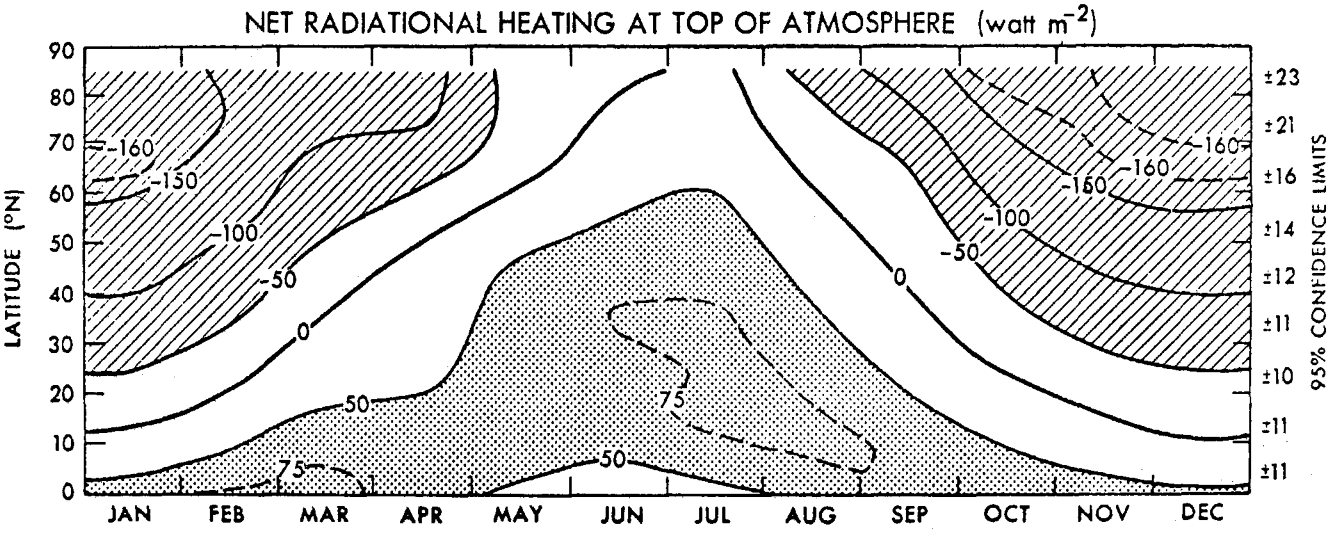

Fig.8. Net incoming radiation flux at the top of the atmosphere (F_{TA}) based on satellite data as a function of latitude and month of the year. Annual mean 95% confidence limits are shown on the right-hand side of the diagram (Oort and Vonder Haar, 1976).

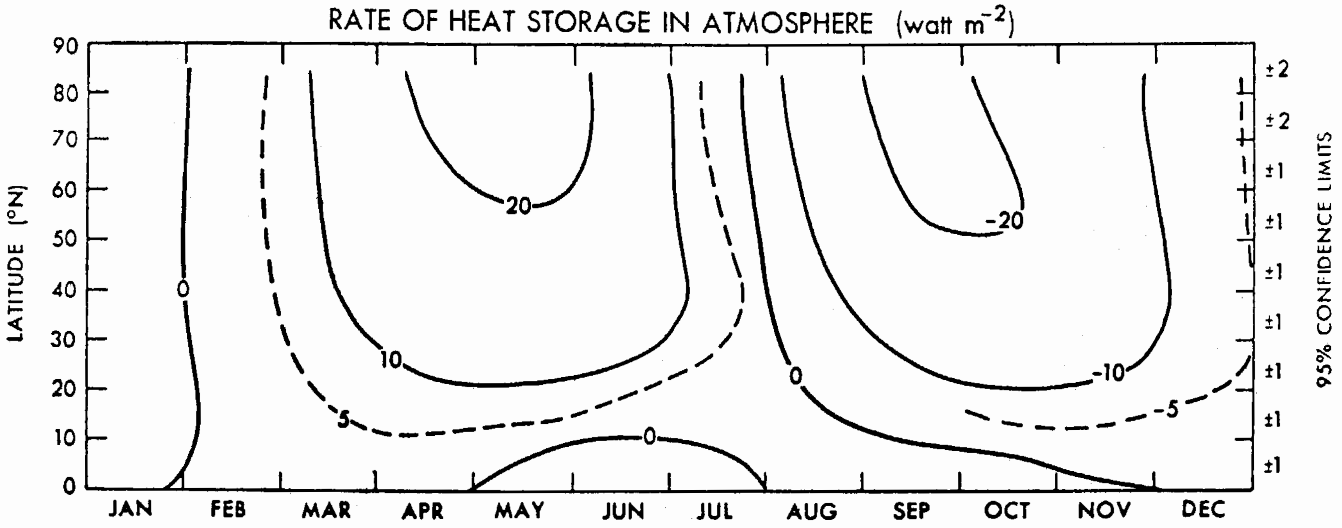

Fig.9a. Rate of heat storage in the atmosphere (S_A) based on radiosonde data as a function of latitude and month of the year (Oort and Vonder Haar, 1976).

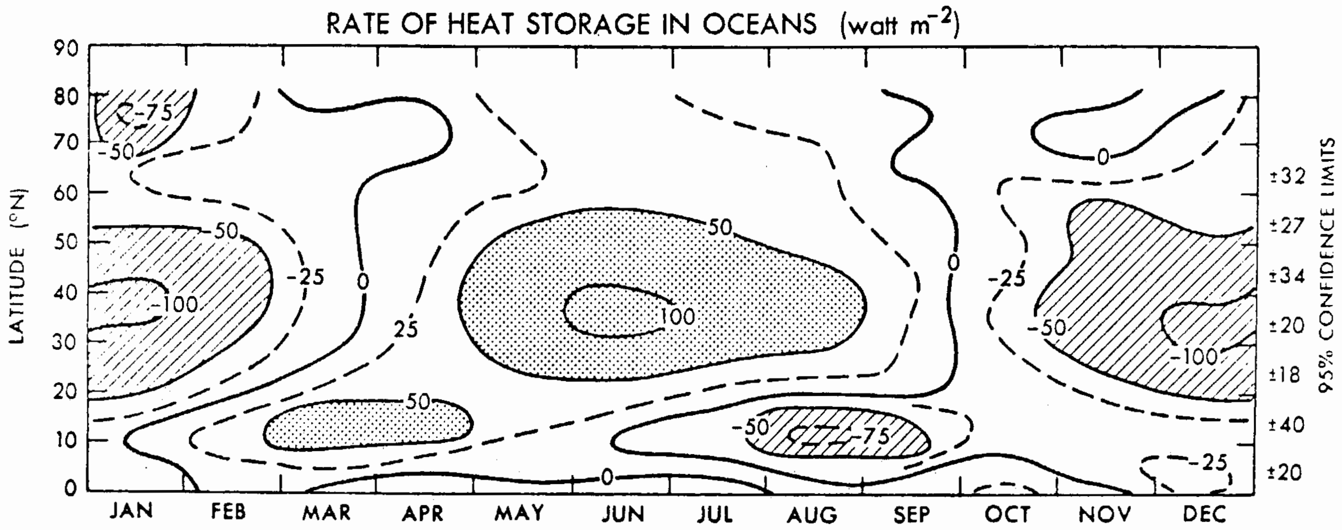

Fig.9b. Rate of heat storage in the oceans (S_O) based on hydrographic stations, MBT and XBT data as a function of latitude and month of the year. To obtain typical oceanic values divide by the percentage of the horizontal area covered by oceans (factor - 0.61 for the Northern Hemisphere as a whole).

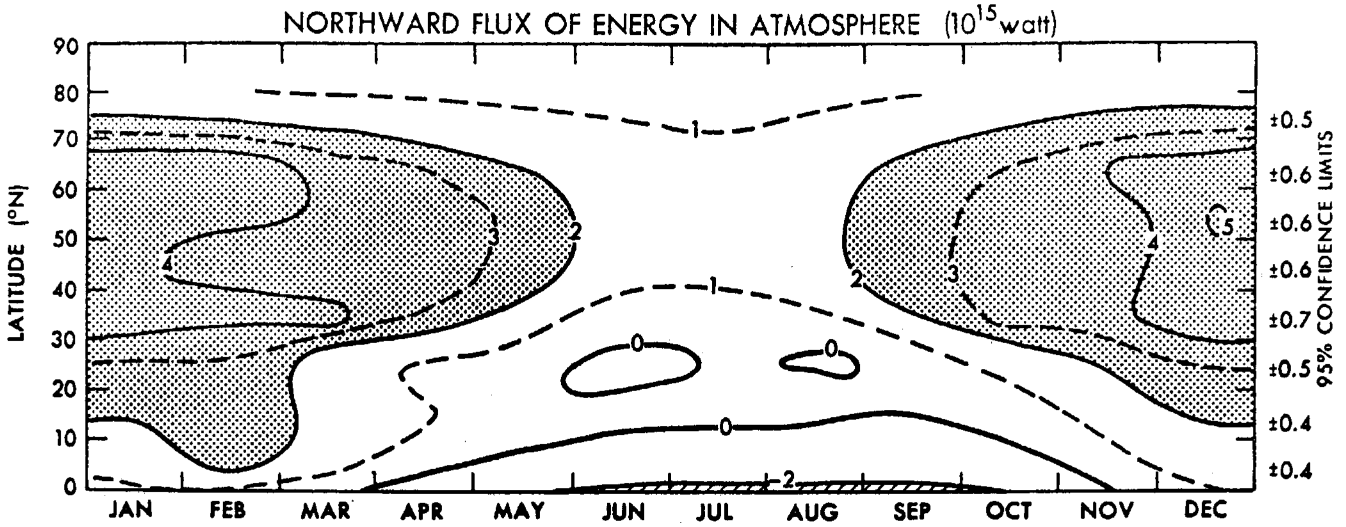

Fig.10a. Northward transport of energy due to atmospheric motions (T_A) based on radiosonde data. (Oort and Vonder Haar, 1976).

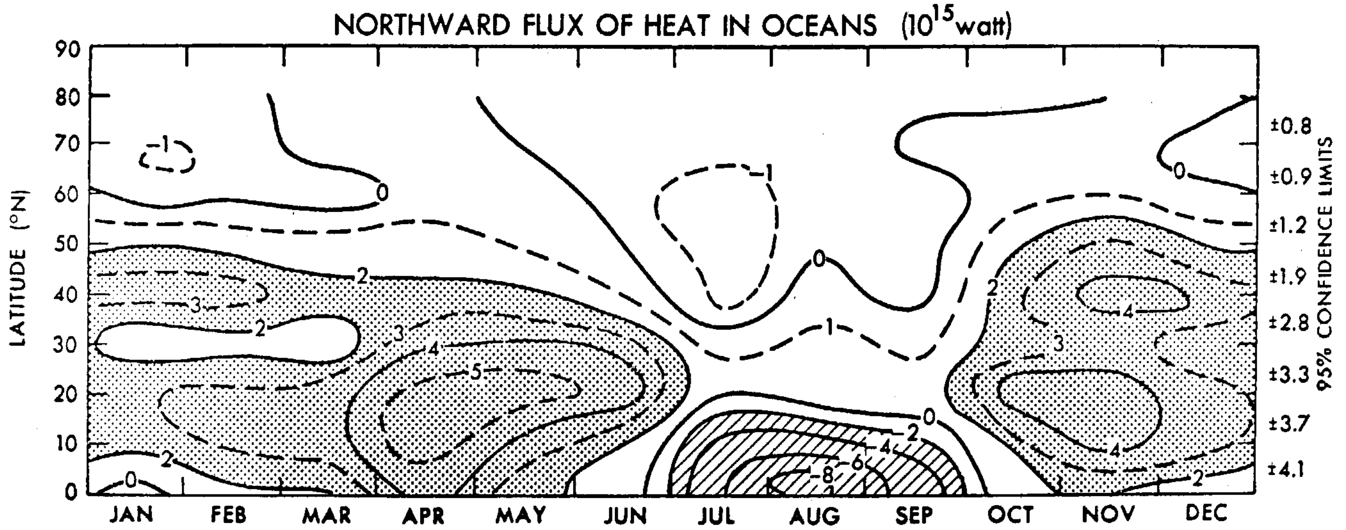

Fig.10b. Northward transport of heat due to oceanic motions (T_0) computed as a residual term in the earth's heat balance.

Oort, A.H. and J.P.Peixóto 1974 The annual cycle of the energetics of the atmosphere on a planetary scale. J.Geophys.Res. 79.

Oort, A.H. and T.H.Vonder Haar 1976 On the observed annual cycle in the ocean-atmosphere heat balance over the Northern Hemisphere. J.Phys.Ocean. 6(6) (in press).

Peixóto, J.P. and A.H.Oort 1974 The annual distribution of atmospheric energy on a planetary scale. J.Geophys.Res. 79.

Vonder Haar, T.H. and A.H.Oort 1973 New estimate of annual poleward energy transport by Northern Hemisphere oceans. J.Phys.Ocean. 3: 169-172.

Notes submitted by
Bruce A. Wielicki

PALEOCLIMATIC DATA

John Imbrie

1. Transfer functions

We derive empirical regression equations which estimate compositions from the percentage of fossil species in sediments taken from the sea bed, the surface temperature at the time when the species was alive. This is possible since the species when they are alive are found in the upper 60 m of the ocean. When they die they sink rapidly to the bottom and are moved only a very little extent by ocean currents, etc. (Even the Gulf Stream displaces the species only slightly.)

Each species has its own optimum value of temperature, salinity and seasonal change in temperature in which it thrives (Fig.1) when other ecological factors are held constant.

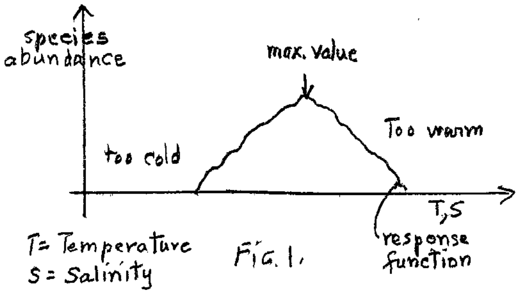

FIG. 1.

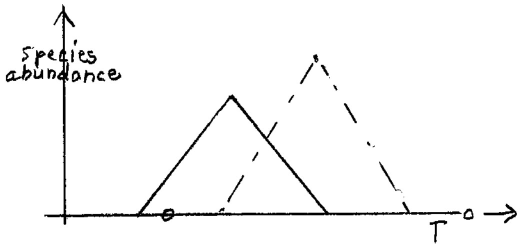

FIG. 2

Knowing the abundance of two or more species is, therefore, normally sufficient to determine the temperature (Fig.2) if other factors were known. If three species are responding to two controlling parameters (Fig.3), then equations specifying either parameter as a function of species abundance can be written. The CLIMAP transfer-function procedure generalizes this to n-dimensions, and uses typically six statistically-independent species groups to estimate summer surface temperature, winter surface temperature, and salinity. The response function of the species can be measured from recent (10^3 yrs) sediments, if we assume no change in the function over the last 500 K yrs., i.e. no evolution of foraminifera. These

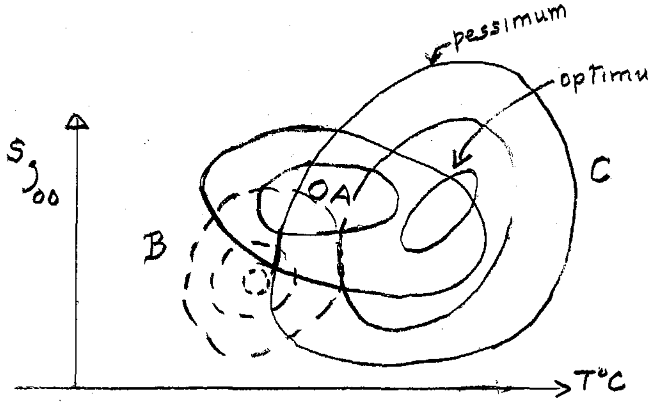

Fig.3 Numbers refer to abundance of species.

measurements reveal that temperature and salinity are somewhat separated. Moreover, since the animals bloom at different seasons of the year depending on species, it is possible to separate between T_{summer} and T_{winter}.

The laboratory precision in the temperature estimate is ±0.3°C. The standard error of the accuracy is ±1.3%.

The polar assemblage (now north of Iceland) occupied the whole region down to the latitude of Spain 18,000 B.P. (years before present), whereas the tropical assemblage changed very little. Thus the temperate assemblages had a narrower range of latitude 18,000 B.P. than they have today.

2. The geological reconstruction

In order to provide input for general circulation models of the atmosphere 18,000 B.P. such as the GFDL model (1) and Rand (2) three boundary conditions are required. These are, the extent and elevation of permanent ice, the global pattern of sea surface temperature and the continental geography. Furthermore, some models require the land albedo to be specified.

The procedure described in (1) provides the sea surface temperature. Age dating of cover is done by ^{14}C. The results for 18,000 B.P. are published in Science (3). The main features are, (1) the extension of sea ice in southern hemisphere around Antartica, (2) the eastern edges of oceans was much colder than today, possibly due to increased upwelling especially on the western coast of Africa and (3) the Gulf Stream in the North Atlantic shifted its position and swept almost directly eastward across the Atlantic, which left the latitudes 40°-60°N substantially colder at 18,000 B.P. (about 10°C).

Defining $\Delta T = T_{August}$ (18,000 B.P.) - T_{August} (today), a table may be constructed for the oceans:

	ΔT °C	
Ocean	Northern Hemisphere	Southern Hemisphere
Atlantic	-3.8	-1.2
Pacific	-2.3	-2.6
Indian	-0.8	-1.3
Average	-2.6	-2.0
Global Average	-2.3	

Table 1.

Results of numerical models reveal that the average air temperature change over land (ΔT) is -6.6°C, which agrees with records from pollen in lake sediments.

Thus there appears to be a three-to-one amplification i.e. $\Delta T_{land} = 3 \Delta T_{ocean}$. However, the August rainfall appears to be less by 15% at 18,000 B.P., according to GFDL model.

3. Time series analysis of a single core

The climate changes are related to the changes in Earth's orbit. These are the eccentricity which changes from .01 to .06 in approximately 100,000 yrs., the obliquity with period of 41,000 yrs. and precession, period 26,000 yrs, with a climate effect, however, of 22,000 yrs., because of precession of perihelion of orbit. Net effect due to precession, P, is

$$P \equiv \Delta(e \sin \pi)$$

where P means change in earth-sun distance in June with respect to 1950 value of half-major axis of orbit, e the eccentricity and π longitude of perihelion of orbit with respect to the moving vernal point. Thus the main effect of the eccentricity is to modulate the amplitude of precession (Fig.4). The system is assumed to be linear , i.e. the frequencies of the forcing should show up in the power spectrum and the phase shift of the response relative to the forcing should be constant in time for each forcing frequency. The power spectrum of the astronomical forcing is sketched in Fig.5. The eccentricity produces side lobes on the precession effect but it has no peak of its own. Thus if the earth's response is linear, then we expect no peak at 100,000 yrs. Now, take cores 468,000 yrs long and compute the power spectrum. The cores are analyzed for (1) δ018, (2) $T_{surface}$ (from transfer function as described in section (1) and (3) %C. davisiana, a radiolarian species (whose abundance is related to the surface salinity of Antarctic water). The analysis produces the following peaks (Table 2):

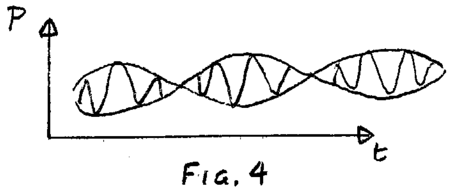

Fig. 4

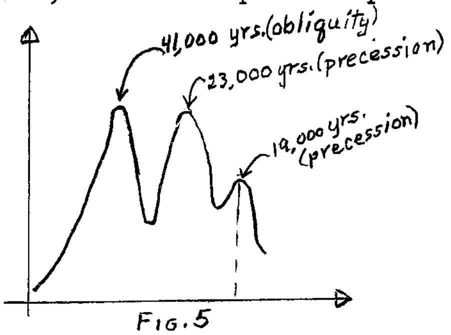

Fig. 5

Analysis of	A (10^3 yrs.)	B (10^3 yrs.)	C (10^3 yrs.)	
$T_{surface}$	94	42	24	19.5
018	106	43	24	19.5
% C.d	122	42	24	19.5
Predicted peaks from Astronomical theory	105	41.1	23.1	18.8

Table 2.

Three out of five of the peaks in B and C are significant at 5% level compared with the predicted peaks. The 41,000 yrs. component lags obliquely by 8,000 yrs. whereas the 23,000 yrs. lag is only 2 or 3 · 10^3 yrs. These values are constant to 350,000 years.

Forty thousnad years and 23,000 years are 25% and 10%, respectively, of the variance. The 100,000-year effect is 50% of variance. This peak may be due to a nonlinear response of earth to eccentricity. Wertmann (1964) has T_{growth} of ice sheets larger than τ_{melting} of ice sheets.

References

Gates, W.L. 1976 Modeling the Ice-Age Climate. Science 191: 1138-1144.

Holloway, J.L.Jr. and S. Manabe 1971 Mon.Weather Rev. 99: 335.

CLIMAP project members 1976 Science 191: 1131-1132.

Notes submitted by
Lars P. Røed

MODELING ICE CAPS

Gene E. Birchfield

An essential aspect of the study of climate is the dynamics of ice caps. On the surface of the earth, the two major ice sheets are the Antarctic ice cap, and the Laurentian ice sheet, which, 18,000 years ago, extended southward well onto the North American continent. With the prospect of including these ice caps more realistically into climate models, their morphology and dynamics should be studied more carefully.

At present Antarctic ice cap is about 4 Km. high, consisting of a massive central sheet, which is thickest on the eastern side, and a secondary western sheet. The mean annual temperature is -57°C at the center of the ice cap, which is significant because the tropopause is on the ground. The ice accumulation is 5 - 60 cm/year, with a low precipitation rate (10 - 15 cm/year; 1/3 that of the north pole). There is no ablation zone, and the loss of mass is presumably due entirely to flow out onto the ice shelves. The total volume of ice is estimated to be 2.8×10^7 Km^3. The rate of loss of mass around the edge of the ice cap gives a decay rate ($\Delta V/\Delta t$) of 2.34×10^3 Km^3/year, indicating a lifetime for the ice of 10^4 years.

The figures are similar for the Laurentian ice cap at 18,000 years before the present. The height is estimated to have been 3 Km in the center of North America, and 3.5 Km over Greenland. The maximum ice volume is estimated as: 2.6×10^7 Km^3 at 18 KBP (thousand years before the present), 1.75×10^7 Km^3 at 11 KBP, and 0.6×10^7 Km^3 at 8.5 KBP, indicating a rate of decay of 3×10^3 Km^3/yr., similar to the present Antarctic ice cap.

Dynamics

For the sluggish flow of a glacier, the governing equations are

$$0 = -\vec{\nabla} p + \vec{\nabla} \cdot \underset{\sim}{\Pi} - g\hat{k},$$

where $\underset{\sim}{\Pi}$ is the stress tensor, P is the pressure at mid-level, and the inertial and coriolis terms have been neglected. The balance is between the gravity, pressure, and stress forces. Assuming hydrostatic equilibrium, to a good approximation the shear stress acting at the bottom of the ice sheet is

$$\tau = -\frac{\rho g h}{2}\left(\frac{\partial h}{\partial x}\right)$$

A stress rate-of-strain law for a perfect plastic is assumed. No deformation will occur until a yield stress τ_0 is reached, after which there is an infinite amount of displacement. If we assume $\tau = \tau_0$ at the bottom, a one-dimensional model can be integrated to give the quadratic profile

$$h(x) = \sqrt{\frac{2\tau_0}{\rho g}(L-x)}\ .$$

Weertman's (1964) model uses the profile and incorporates both accumulation and ablation (Fig.1.).

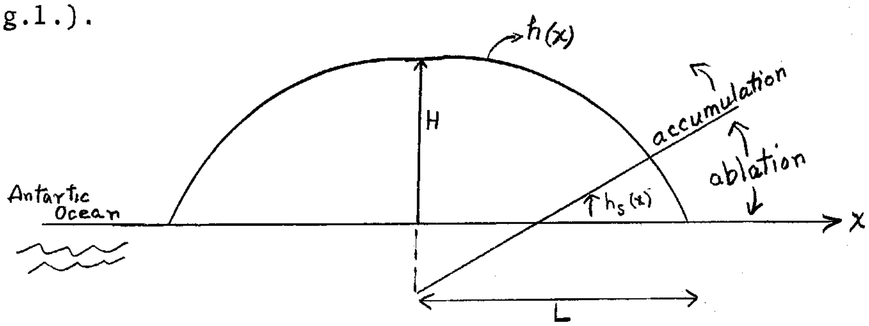

Fig. 1.

$h_s(x)$ is the snow line, which separates the two regions. The northern edge of the ice cap is assumed fixed by the Antarctic Ocean. L, the half width of the ice cap, varies in response to changes in $h_s(x)$. The model assumes an ablation rate of 1 m/year in the ablation zone.

When applied to the Antarctic ice cap, the results are very sensitive to the value of (a/a'), where a is the average accumulation rate in the region of accumulation, and a' is the average ablation rate in the zone of ablation. Using an empirically derived value for a/a' of 1/3, the model indicates that the growth of the ice cap is limited only by the size of the continent.

There is a phase lag of 10^4 years between fluctuations in the snow line and the response of the ice sheet. If the model is forced with northern hemisphere astronomical forcing, the effect is very small. The time constant for the ice cap is greater than 100,000 years, much longer than the two lowest astronomical forcing modes.

If a similar analysis is done on the Laurential ice sheet, the time scale is found to be 10 - 40 x 10^3 years, much closer to the time scale of the astronomical forcing. The ice cap will oscillate about a mean position, implying periodic ice ages, with periods of very little ice coverage.

Reference

Weertman 1964 J.Glaciology pp.145-158.

Notes submitted by
Richard D. Romea

THE EARTH'S RADIATION BALANCE

Thomas Vonder Haar

The radiative forcing of the atmosphere, which is amenable to being measured by satellites, is clearly an important climatic parameter.

Studies of the earth-atmosphere radiation budget by satellites span a large range of time and space scales, from local events on a scale of days to global phenomena with a period of years. Radiation begins to dominate the other diabatic heating processes (e.g., latent heat) as a space-time scale increases.

There are two basic approaches to the instrumentation for satellite observations: I) use of a broad detector 'seeing' horizon to horizon, and II) use of a telescope which rapidly scans a narrow field of view.

For Type I, the power at the dectector, P_D is given by $P_D = A_D \bar{N}_{\oplus} \Omega_{\oplus}$ where A_D is the detector area, $N_{\oplus}$ is the average radiance in Wm^{-2}steradian^{-1} and $\Omega_{\oplus}$ is the intercepted solid angle of the earth. $N_{\oplus}$ is the radiance leaving the 'top of the atmosphere', which for the wave lengths under consideration (solar $\lambda = 0.2\text{-}3.5\mu$ m, infrared $\lambda > 3.5\mu$ m) is about 30 km. The detector used is a thermister bolometer, whose response is given by

$$P_D = \sigma T_D^4 + K_1 (T_D - T_m) + K_2 \frac{\partial T_D}{\partial t}$$

where T_D is the detector temperature, σ is the Stéfan-Boltzman constant, T_m is the temperature of the detector mount, and K_1 and K_2 are correction constants for thermal conductivity to the mount and response lag, respectively. The typical intercept area is 10° to 20° GCA (Great Circle Arc). Differentiation between 'solar' and 'infrared' radiations is achieved by use of matched black and white detectors.

For Type II arrangement, $N_{refl} = \int \rho(\theta, \zeta, \psi) N_i \cos\zeta \, \partial\Omega$ where N_{refl} is the energy reflected from the earth in watt Wm^{-2}steradian^{-1}; N_i is the incident solar radiation at zenith angle ζ ; θ and ψ are the zenith and azimuth angles respectively of the satellite; and ρ , the reflectivity of the surface, is a complicated function of the three angles. The intercept solid angle is usually sufficiently small so that $N_{refl}(\theta, \zeta, \psi) \approx \rho(\theta, \zeta, \psi) N_i \cos\zeta \, \Delta\Omega$.

The energy emitted by the earth is infrared and is given by

$$N_{IR} = B(t_0) \cdot \tau_0 + \int B(T) \frac{\partial \tau}{\partial z} dz$$

where N_{IR} is the energy leaving the 'top' of the atmosphere. The first term on the right accounts for surface emission (B is the Planck function of T_0 , the surface temperature, and τ_0 is a surface transmission term). The second term on the right accounts for energy processes occurring at various heights z .

The dataset of radiation observations begins in the early 1960's with the ESSA, TIROS and NIMBUS satellites. The early satellites had Type I (flat plate) detectors, stabilization difficulties, and orbits that prevented contiguous sampling over an entire hemisphere. Later ones have had telescopic detectors with 100 km fields of view (Type II), improved Type I detectors such as thermopiles and have overcome the aforementioned difficulties. The observational record as a whole, however, is spotty; the data are more coherent when seasonally averaged.

Prior to satellite observations, it was thought that the net reflectivity of the earth (planetary albedo) was about 35%. Recent observations indicate a lower value ($\sim$30%), the discrepancy presumably due to the tropics being "darker" than previously assumed.

The Type I detectors make albedo measurements in the 'ratio' sense an important advantage; they look at the sun, then the earth, and compute the ratio. (The detectors can resolve the ± 3% change in solar radiation due to the eccentricity of the earth's orbit, indicating stability to this level, although the absolute accuracy may be worse). The most recent data from NIMBUS-6 using a specially calibrated instrument (Hickey and Smith, unpublished) give a solar constant of 1390 ± Wm^{-2}, where ± 1 indicates the variation over several months, not the absolute accuracy. (This agrees with early estimates (1930's), but disagrees with current measurements.)*

The global radiation budget may be written

$$R_{net} = I(1-\alpha) - W_{IR}$$

where R_{net} is the net radiation, I is the radiation incident, and W_{IR} is the infrared exitance of the earth.

The distribution of the planetary albedo, α , is predominently zonal, although some longitudinal variations are apparent in the tropics, and the influence of the continents is resolvable. It ranges from $<$ 20% in the tropics to $>$ 60% at the poles. The annual pattern of absorbed solar radiation, $I(1 - \alpha)$, peaks in the tropics and drops zonally to the poles. There is an apparent reciprocity relation: features that absorb less solar radiation emit less infrared, except, for instance, deserts which are highly radiative in the infrared but very reflective in the visible. Departures from reciprocity (as occur with cirrus or stratus clouds) are important for climate study. The net radiation over the globe averages to zero within the limits of observational errors ($\sim$3%).

The seasonal net-radiation data reveal several interesting features. 1) There is a reversal of the zonal gradient in net radiation in the Antarctic during winter (net radiation has a minimum at $\sim$ 60°S and begins increasing towards the south pole). 2) The southern hemisphere shows a generally greater excursion of net-radiation between seasons. 3) Winters, apart from the reversal mentioned above, are fairly similar between hemispheres, while summers are dissimilar.

Observational analyses of the coupling between atmospheric variables and the radiation budget are to date inconclusive. It is observed, however, that ΔT the equator-to-pole temperature gradient, is well-correlated with the equator-to-pole gradient of the net radiation, lagging it by about a month. Interannual variations in net radiation (for a given time of year) are not inconsequential, and may be due to variability in cloudiness.

References

Raschke, Vonder Haar, Posternak, Bandeen. 1973 The Radiation Balance of the earth-atmosphere system during 1969-1970 from NIMBUS 3 Radiation Measurements. NASA TN D-7249 or JAS 30(3).

---

* A recent (7/76) rocket flight carrying a twin to the satellite instrument, together with several absolute cavity radiometers has shown that the absolute value of the "solar constant" is still most probably $\sim$ 1365 $w\cdot m^{-2}$.

Ellis, Vonder Haar 1976 Zonal average earth radiation budget measurements from satellites for climate studies. Atmos.Sci.Paper No.240 - Dept.Atmos.Sci., Colorado State University.

Ellis, Vonder Haar 1976 The annual cycle in planetary radiation exchange with space - COSPAR Paper No. C.46.4.

Vonder Haar, Suomi 1971 Measurements of the earth's radiation budget from satellites during a five-year period. Part I. JAS 28(3).

Oort, Vonder Haar On the observed annual cycle in the ocean-atmosphere heat balance over the Northern Hemisphere (to be published in JPO).

Vonder Haar 1972 Natural variation of the radiation budget of the earth-atmosphere system as measured from satellites. Conf.on Atmos.Radiation, Aug.7-9, 1972, Fort Collins, Colorado AMS.

Vonder Haar 1973 New estimate of annual poleward energy transport by Northern Hemisphere oceans. JPO 3(2).

Notes submitted by
Steven M. Ashe

THE EARTH'S RADIATION BALANCE (#2)

Thomas H. Vonder Haar

This lecture describes variations of the earth's radiation budget, both in space and time, as measured by satellites.

Recapping the last lecture, (Vonder Haar Lecture #1), satellite data has shown the earth's mean albedo is approximately 30% lower than previous ground-based estimates of 35%. The difference is due to more sunlight being absorbed into the tropical oceans. Also, recall that on an annual basis, each hemisphere is in net radiative equilibrium individually, in spite of their large difference in land-sea ratio. This implies there is no net annual heat transport across the equator.

Fluctuations in time and space

The variability of albedo and I.R. flux are important for climatological studies; e.g. a variation in a typically low variable region may be more significant than a variation in typically highly variable region. Although cloudiness seems to be the main cause of variations in albedo and I.R. Flux, the satellite data base is relatively short and sparse on cloud data.

Global maps of the deviation from the zonal mean, (Vonder Haar and Ellis (1974)) and of the relative dispersion of a seasonal mean quantity from year to year, (Vonder Haar (1972)) have been made for albedo and I.R. flux from satellite data. Generally, the highest seasonal relative dispersions occur over land (e.g. ± .02 ly/min for the I.R. flux, approximately 20% of the mean.

A cloud-free albedo chart of the earth can be made from minimum albedo values at each place over a period of time. Away from the icy poles, this mainly shows the land-sea albedo difference. The zonally averaged picture is:

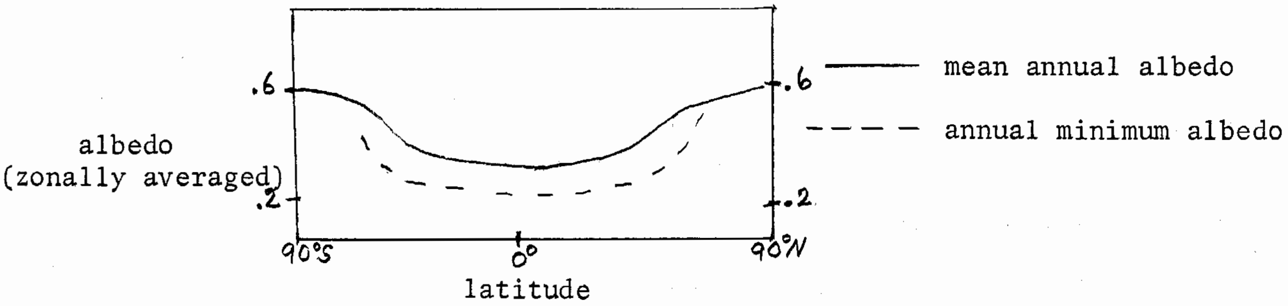

Comparison with the average albedo shows that the relative contributions to the total albedo of .30 are approximately:

clouds	45-50%
oceans	15%
clear atmosphere	15%
land	10%
snow and ice	10-15%

Seasonal Trends

The earth is not in radiative equilibrium over each month, only on an annual average. For the earth as a whole, there is a wave of net radiation, (Ellis and Vonder Haar (1976)).

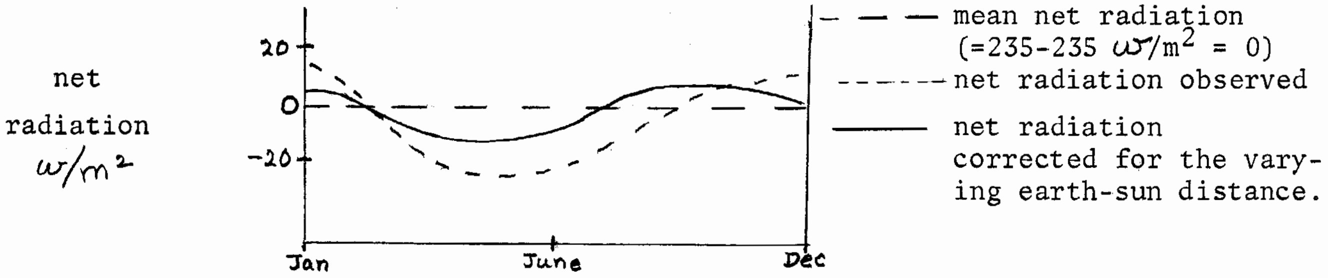

Approximately half of this wave can be explained by the eccentricity of the earth's orbit. However, there is still a residual wave, due to the different radiative properties of northern hemispheric continents and southern hemispheric oceans. Such correlations and their long term variations could be important for climate studies.

Climate Studies

Glenn White, using satellite data, has looked for correlations between zonally averaged surface temperature, T, and albedo and I.R. flux, to test the relations used in simple climate models. He took 12 monthly mean values of these three quantities for each 10^o latitude strip, and fitted (by least squares) the albedo and I.R. flux as a function of T by straight lines A + BT (at each strip, so that the A's and B's vary with latitude). Away from the tropics, above 30^o latitude, the fit is good and $\frac{d}{dT}$ albedo < 0, $\frac{d}{dT}$ I.R. > 0), probably due to ice and snow cover. In the tropics, the fit is not as good; however, the weak correlations have the opposite sign. Presumably the main effect here is due to cloudiness.

Oort and Vonder Haar (1976) made latitude vs. month charts of the zonal mean net radiation balance for the northern hemisphere over one year, from satellite data. Combining this with the same type of charts for ocean temperature and atmospheric heat transport, they found that the oceans must be transporting large amounts of heat northwards in the winter season (maximum 5 x 10^{15} watts, approximately double the previous estimate of Sellers (1965)). Two strong northward pulses were noted in November and April. The overall findings are consistent with the satellite measurements mentioned above, of more sunlight being absorbed into the tropical oceans than had previously been estimated.

References

Ellis, J.S. and T.H.Vonder Haar (1976) The annual cycle in planetary radiation exchange with space. COSPAR paper No.C. 4b.4.

Oort, A.H. and T.H.Vonder Haar (1976) On the observed annual cycle in the ocean-atmosphere heat balance over the northern hemisphere. Accepted for publication in J.Phys.Oceanography.

Sellers, W.D. (1965) Physical Climatology. U.Chicago Press, 272 pp.

Vonder Haar, T.H. and J.S.Ellis (1974) Atlas of radiation budget measurements from satellites (1962-1970). Atmospheric Science, paper No.231, Colorado State University.

Vonder Haar, T.H. (1972) Natural variation of the radiation budget of the earth-atmosphere system as measured from satellites. Preprint volume of the Conference on Atmospheric Radiation, Aug.7-9, 1972, Fort Collins, Colorado, pp.211-219. Published by AMS, Boston, Mass.

Notes submitted by
David Pollard

ANALYTICAL BEHAVIOR OF CLIMATE MODELS

Gerald North

Types of climate models, increasing in complexity:

a) global average

b) zonal and annual averages, with latitude dependence, as done by Budyko (1969) and Sellers (1969)

c) intermediate

d) global circulation models.

The type (b) models investigate how the climate changes as the solar constant Q varies. Recent models have been produced by North (1975 (a), (b)) and Held and Suarez (1974).

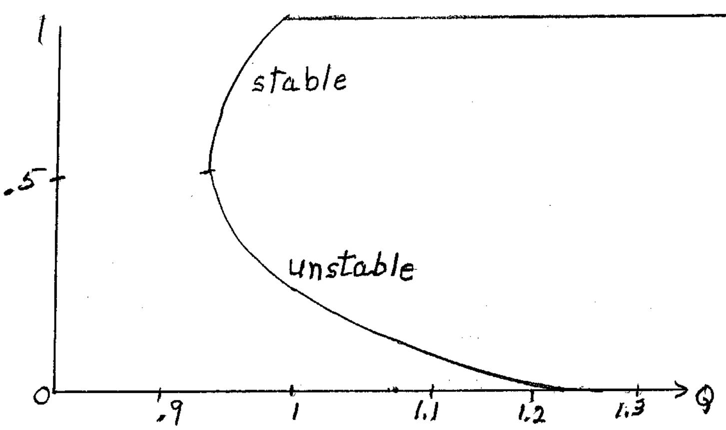

x_s = sine of latitude of ice/no-ice division.

At present, $x_s = .95$

The models are based on energy balance - for each zonal strip, transport of energy out + outgoing infrared radiation flux = absorbed solar heating rate. In a simple model, each of these components is parameterized in terms of the surface temperature $T(x)$. (x = sine of latitude).

Outgoing radiation $I = A + BT$, where A and B are constants evaluated from satellite data. (The linear relation gives very good correlations between I and T, tested by Cess and White and Vonder Haar.).

Absorbed solar heating rate = $QS(x)\;a(x, x_s)$

$S(x)$ = distribution of heat over the earth

$\approx 1 + S_2 P_2(x)$, P_2 is second Legendre polynomial.

(Note - these models have symmetric northern and southern hemispheres, so only symmetric functions of x appear); Q = solar constant/4;

$a(x, x_s)$ = fraction of heat absorbed = 1 - albedo

$$= \begin{cases} .4, & x > x_s \\ .7, & x < x_s \end{cases}$$

Divergence of heat from a strip is represented by a diffusion term, $-D\nabla^2 T$. This is equivalent to random transport by atmospheric motions which fluctuate rapidly compared to the climate response time scale. Resulting equation is

$$-D\frac{d}{dx}\left[(1-x^2)\frac{dT}{dx}\right] + A + BT = QSa$$

with boundary conditions $\nabla T = 0$ at $x = 0$ and 1 and $T(x_s)$ set at -10°C.

Solution by either solving above and below ice-line and matching, or by expansions using Legendre polynomials, (which are eigenfunctions of the diffusion operator:

$$\frac{d}{dx}\left[(1-x^2)\frac{dP_n}{dx}\right] = -n(n+1)P_n(x)$$

(for latitude dependent diffusion coefficient, appropriate eigenfunctions should be used).

$I(x) = A + BT(x)$ is used as the independent variable.

Put $I(x)=\sum I_n P_n(x)$, then using orthogonality the balance equation leads to

$$Q(x_s) = I_s\left[\sum_n \frac{H_n(x_s)\, P_n(x_s)}{n(n+1)D+1}\right]^{-1}$$

where $I_s = I$ and

$$H_n(x_s) = (2n+1)\int_0^1 S(x)\, a(x, x_s)\, P_n(x)\, dx$$

The function $Q(x_s)$ is shown in the first figure. Climate descriptions in terms of the first two modes are considered. Using present-day values of x_s and Q, D is determined and hence $T(x)$ found. Good agreement with observed $T(x)$ is found.

The two-mode system leads to a simple expression for heat crossing a latitude circle

$$\mathcal{H} \propto T_2\, x(1-x^2) D \qquad (T = T_0 + T_2 P_2(x))$$

Again find good comparison with observations. A comparison of energy absorbed as given by observations, the total model input, and the model input as seen by the two-mode approximations shows that the two-mode curve gives the best fit -- because the ice-line discontinuity is smoothed out.

The budyko model uses an empirical transport term $\gamma(T-\bar{T})$, where $\bar{T}$ is mean temperature.

For the two-mode model,

$$-D\nabla^2 T = 6 D T_2 P_2(x) = 6 D (T(x) - T_0);$$

so the diffusion term is like Budyko's flux term. The models differ though in that Budyko's model retains the discontinuity in energy absorbed, whereas it is smoothed in a two-mode truncation.

The two-mode analysis can also handle some variations to the model (see North, 1975b for details):

(1) latitude-dependence diffusion, $D = D_0(x)$. This is formally equivalent to the constant D case;

(2) add a transport $v(x)\nabla T(x)$ with given $v(x)$. This can be absorbed in the diffusion term. (Any transport by a divergence-free field cannot be distinguished from diffusion in the two-mode model);

(3) D related to the T gradient. A quadratic equation for Q (given x_s) is found. One set of solutions is physically unrealistic, the other is very close to the solution with constant D;

(4) effects of inhomogeneous cloudiness

$$I = A(x) + BT(x)$$

Find that formula for outgoing radiation can be modified to fit the data more closely, but the modification has very little effect on the two-mode results.

(5) D is a function of x_s and x

e.g.

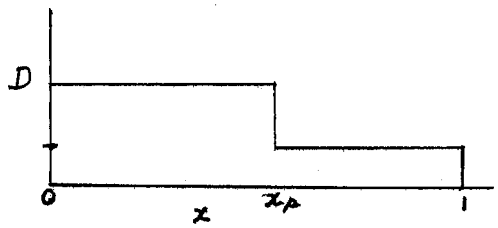

(transport suppressed in ice regions to simulate effect of ice cover on ocean transports).

Find that two-mode results are not affected much if the change in diffusion value is small.

If the ice-age climate is investigated by putting $x_s = .85$, (this corresponds to a decrease in Q of 1.3%), one finds

	observed	two-mode model
ΔT_0 (mean)	$\sim -6^{o}C$	- 5.8
ΔT (equator)	~ -3	- 3.8
ΔT (pole)	~ -20	- 9.3

(observations from Flint, 1971)

(note - the truncation error involved in the two-mode model is greatest at the poles).

Possible extensions of the model:

(a) add longitudinal variation

(b) allow for north-south asymmetry, and add seasonal variations (the Milankovich theory could be studied then). An explanation of why the two-mode works so well is that the global mean annual climate has scale of 10,000 km (so only two modes required for description) and corresponding 50-day time scale, whereas heat transport is associated with motions with 1000 km and three-day scales. The relatively short scale motions then have a diffusive effect on the large scales.

The stability of the model is analyzed by adding a term $C\frac{dI}{dt}$ to the energy budget and perturbing the steady solution. (C is a constant heat capacity.) It is found that the system is stable if $\frac{dQ}{dx_s} > 0$, and unstable if $\frac{dQ}{dx_s} < 0$ (see North 1976 for details). It is possible that this result is a general one, so it may be possible to prove it using some general "thermodynamic" property?

References

Budyko, M.I. 1969 The effect of solar radiation variations on the climate of the earth. Tellus 21.

Flint, R.F. 1971 Glacial and quaternary geology.

Held, I.M.Suarez 1976 Simple albedo feedback models of the icecaps. Tellus 36.

North, G.R. 1975(a) Analytical solution to a simple climate model with diffusive heat transport. J.Atmos.Sci. 32(7).

North, G.R. 1975(b) Theory of energy-balance climate models. J.Atmos.Sci.32(11).

North, G.R. 1976 A Stability Theorem for Energy-Balance Climate Models with Diffusive Heat Transport. (preprint).

Sellers, W.D. 1969 A climate model based on the energy balance of the earth-atmosphere system. J.Appl.Met. 8.

Notes submitted by
Michael K. Davey

ANALYTICAL BEHAVIOR OF CLIMATE MODELS (#2)

Gerald North

I. Waste Heat Green's Function

Consider the thermal response of a simple energy balance climate model to a localized heat source, $g\delta(x-x_1)$. One writes the original energy balance equation with the added term:

$$-D\nabla^2 I(x)+I(x)=QS(x)\,a(x,x_s)+g\delta(x-x_1),$$
$$I(x_s)=I_s$$

where all symbols were defined in the previous lecture. As usual we expand in modes $(I(x)=\sum I_n P_n(x))$ and get

$$L_n I_n = QH_n(x_s)+(2n+1)g\,P_n(x_1),$$
$$\sum I_n P_n(x_s)=I_s.$$
$$(L_n\equiv n(n+1)D+1)$$

Now consider I_n^0, x_0 to correspond to the solution when g = 0 so that departures can be represented as in the stability analysis:

$$I_n = I_n^0+\delta_n,$$
$$x_s = x_s+\varepsilon.$$

ε and the δ_n are related by:

$$\varepsilon\cong-\left(\sum P_m\delta_m\right)\left(\sum I_\ell^0 P_\ell'\right)^{-1}.$$

The linearized perturbation equations are:

$$L_n\delta_n = QH_n'(x_0)\varepsilon+(2n+1)g\,P_n(x_1)$$

Inserting the relation between ε and the δ_n we have

$$\delta_n+\left(\frac{QH_n'}{\sum_\ell I_\ell^0 P_\ell'}\right)\frac{1}{L_n}\sum_m P_m\delta_m=(2n+1)g\,\frac{P_n(x_1)}{L_n}$$

This last is a matrix operating on the vector δ_n to give the right-hand side. We may represent the matrix by

$$\sum_m\left(\mathbb{1}_{nm}+F_nP_m\right)\delta_m=(2n+1)g\,\frac{P_n(x_1)}{L_n}.$$

The problem is to invert the matrix. This is possible in the present case because of the way the n and m dependence factors. Expanding in a geometric series:

$$\left(\mathbb{1}+\underset{\sim}{F}\,\underset{\sim}{P}\right)^{-1}=\mathbb{1}-\underset{\sim}{F}\,\underset{\sim}{P}+\underset{\sim}{F}\,\underset{\sim}{P}\cdot\underset{\sim}{F}\,\underset{\sim}{P}+\underset{\sim}{F}\,\underset{\sim}{P}\cdot\underset{\sim}{F}\,\underset{\sim}{P}\cdot\underset{\sim}{F}\,\underset{\sim}{P}-\cdots$$
$$=\mathbb{1}-\underset{\sim}{F}\,\underset{\sim}{P}\,(1-P\cdot F+(P\cdot F)^2-\cdots$$
$$=\mathbb{1}-\frac{\underset{\sim}{F}\,\underset{\sim}{P}}{1-P\cdot F}$$

Note that the $P\cdot F$ is just a number:

$$P\cdot F=\sum_\ell\frac{P_\ell\,Q\,H_\ell'}{L_\ell\left(\sum_m I_m^0P_m'\right)}$$

The final result for δ_n is now given by

$$\delta_n = g(2n+1)P_n(x_1) - g\,\frac{F_n}{1+F\cdot P}\sum_{\ell}\frac{(2\ell+1)}{L_\ell}P_\ell(x_0)P_\ell(x_1)$$

The first term represents the "direct" or "fast" response of the climate while the second incorporates the ice feedback part. The denominator of the second term can be shown to be proportional to $\frac{dQ}{dx_0}$; in other words, the response diverges if the equilibrium solution is near a bifurcation point. The summation is a cusp-shaped function of x_1, for fixed x_0 , peaked at $x_0 = x_1$. Since we have linearized the system, we can find the response to any heating distribution simply by integrating the last equation over x_1 , weighted by the heat distribution.

Another way of approaching this problem is not to linearize but to deal directly with the nonlinear system. Consider a heating distribution: $gf(x) = g\sum f_n P_n$. Now one proceeds in exactly the same way as finding the $Q(x_s)$ curve of the last lecture, only this time keep Q fixed and ask for $g(x_s)$. The result is

$$g(x_s) = \frac{I_s\left(1 - \frac{Q_0}{Q(x_s)}\right)}{\sum_n \frac{f_n P_n(x_s)}{L_n}}$$

II. Seasonal Climate Model

a) Solar Radiation

The solar radiation reaching the top of the atmosphere per unit area per unit time averaged over a day is given in Seller's book:

$$S(x,t) = S_0\left(\frac{r_0}{r}\right)^2\left(x H \sin\delta(t) + \sqrt{1-x^2}\sin H\cos\delta(t)\right. \tag{1}$$

where H is the half-day length (24 hours = 2π) and is given by the root of

$$\cos H = \frac{-x}{\sqrt{1-x^2}}\tan\delta(t), \qquad H \geqslant 0. \tag{2}$$

For climate models using Legendre polynomials as a basis set, it is convenient to expand $S(x,t)$ into such a series as well:

$$S(x,t) = \sum_n P_n(x)\,S_n(t) \tag{3}$$

By defining a function $W \equiv H - \pi/2$, it is possible to show that n = 1 is the only odd term in the series (3). Virtually all of the seasonal information is carried by this antisymmetric term. This coefficient may be calculated analytically:

$$S_1(t) = S_0\left(\frac{r_0}{r}\right)^2\frac{\pi}{2}\sin\delta(t)$$

By elementary orbital mechanics one can also show that $\sin\delta(t) = \sin\delta_0\sin\lambda(t)$ where δ_0 is the earth's obliquity and $\lambda(t)$ is the longitude of the earth about the sun. For a circular orbit $\lambda(t) = 2\pi t$, with order ε corrections for an elliptical orbit. The reason for this excursion is to show that the earth's orbital variations may be easily incorporated in such a formalism.

b) Observed Seasonal Temperatures
(Coakley & North, unpublished).

One may take zonally-averaged temperature data and expand:

$$T_{obs}(x,t) = \sum_{\ell} A_{\ell 0} P_\ell(x) + \sum_{\ell,n} \left(A_{n\ell} \cos 2\pi nt + B_{\ell n} \sin 2\pi nt\right) P_\ell(x)$$

To compare with simple models we utilize data from only one hemisphere, by considering the southern hemisphere to be the same as the northern but lagged by six months. It turns out that very good fits are obtained with rather drastic truncations. For example, truncating the series at $\ell = 4$, $n = 2$ leads to an R.M.S. error of only .85°C.

Data:

ℓ	n	$A_{\ell n}$	$B_{\ell n}$
0	0	14.9	0
0	2	-.16	.19
1	1	-15.33	-2.10
2	0	-28.00	0
2	2	.799	.258
3	1	-4.03	-.05
4	0	-3.51	0
4	2	.95	-.56

From the above we see that virtually all of the seasonal information is carried by the $\ell = 1$, $n = 1$ mode. Calculation of this mode should be possible by a simple climate model.

c) Models

The seasonal models presented here are the simplest possible extension of the mean annual models discussed in the last lecture. As before we consider a large part of $I_n(t)$, $\hat{I}_n$ the annual mean, and a small departure $\delta_n(t)$ which represents seasonal effects.

Model 1.

$$C\delta_n + L_n\delta_n = q_n(t),$$

where

$$q_n(t) = \frac{(2n+1)}{2} \int_{-1}^{1} s(x,t) P_\ell(x)\, a(x,x_0)\, dx$$

(minus a mean anneal part)

C = a heat capacity per unit area to be adjusted as a phenomenological constant. Results: This model indeed filters all of the response into the δ_1 mode.

Small semiannual harmonics appear in δ_0, δ_2 which is encouraging. The problem is that δ_1 is too large by a factor of 10.

Model 2.

This model divides the hemisphere into decoupled land (40%) and ocean (60%) equations. The values of C_L and C_W are taken to be 30 days and about four years. This time the amplitude is reduced because of the low thermal response of the oveans but is still too large by a factor of four.

Model 3.

This model is a simple extension of Model 2 but allows heat to pass from land to water by a term

$$\gamma(T_L - T_W)$$

which couples the land and water equations together. One can now obtain the observed value of δ_1 by merely adjusting γ.

Another interesting effect which can be studied is the snow feedback. If $a(x, x_s)$ is allowed to vary by letting x_s follow some isotherm as in the mean annual models, the heating has an additional term

$$s_1(t)\,T_1(t),$$

which when averaged through the year gives a contribution to T_0, the global average temperature. In this case one finds that ΔT_0 due to this effect is about +2.5°C.

III. Stochastic Climate Equation

The simple climate models discussed here seem to imitate reality enough to ask why. In this section we examine a stochastic analogy which under the right conditions has as its ensemble average the diffusive climate model.

Consider the system:

$$C\frac{\partial G}{\partial t} + CV\cdot\nabla G + G = H(x,t),$$

where $G(x,t)$ is the outgoing radiation function; C is a heat capacity/area, $H(x,t)$ is a given nonrandom heating function; $\vec{V}(x,t)$ is a given random variable with zero mean and normally distributed; it is also divergence-free. Furthermore, assume that $\vec{V}(x,t)$ is homogeneous and isotropic. Thus in two dimensions

$$\langle V(x,t)\,V(x',t')\rangle = V^2\rho(x-x',t-t')\,\mathbb{1},$$

$$\langle V\rangle = 0$$

$$\langle V_1 V_2\rangle = \rho_{12}$$

$$\langle V_1 V_2 V_3\rangle = 0$$

$$\langle V_1 V_2 V_3 V_4\rangle = \langle V_1 V_2\rangle\langle V_3 V_4\rangle + \langle V_1 V_3\rangle\langle V_2 V_4\rangle + \langle V_1 V_4\rangle\langle V_2 V_3\rangle$$

This last a property of multivariate normal statistics.

Now Fourier Transform using periodic boundary conditions (dropping factors of 2π)

$$V(\underline{x},t) = \sum_{K,w} V_{K,w}\, e^{i(\underline{K}\cdot\underline{x}+wt)}$$

where

$$V_{Kw} = \int_{x,t} e^{-i(\underline{K}\cdot\underline{x}+wt)}\, V(\underline{x},t)$$

By analogy, define

$$\langle V_{pw} V_{qw'}\rangle = \delta_{p,-q}\,\delta_{w,-w_1} R_{q,w} = \int_{\substack{x\\t}}\int_{\substack{x'\\t'}} e^{-i(px+wt)-i(qx+w_1t)}\langle V(x,t)\,V(x_1,t_1)\rangle$$

The mass continuity equation $\nabla\cdot\underline{V}=0$ leads to $\underline{K}-\underline{V}_{Kw}=0$ and the identity

$$\underline{K}\cdot\underline{V}_{K-q,w} = q\cdot\underline{V}_{K-q,w}.$$

For the radiation equation

$$C\frac{\partial G}{\partial t} + CV\cdot\nabla G + G = H$$

we define, by analogy to turbulence, the "Radiation Reynolds Number" $R = \frac{CV\cdot\nabla G}{G} \sim 1$ in climatology. This is the ratio of advected to outgoing radiation. Using a rectangle with periodic boundary conditions in x and y, we Fourier transform:

$$i\omega c g_{Kw} + \sum_{q,w''} m_{\substack{Kq\\ ww''}} g_{qw''} + g_{Kw} = h_{Kw}$$

where

$$m_{\substack{Kq\\ ww''}} = iq\cdot V_{K-q,w-w''}C$$

In matrix form

$$iwCg + mg + g = h$$

or implicitly

$$g = \frac{1}{1+iwc}h - \frac{1}{1+iwc}mg$$

Iterate the implicit equation to generate an explicit series:

$$g = \frac{1}{1+iwc}h - \frac{1}{1+iwc}m\frac{1}{1+iwc}h + \frac{1}{1+iwc}m\frac{1}{1+iwc}m\frac{1}{1+iwc}h - \cdots$$

We can use a shorthand symbolic form

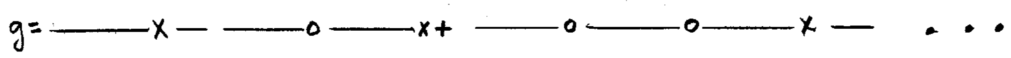

This is a power series in R which always diverges so can only be summed in a series of infinite subsets. We extend our graphological notation to denote ensemble averages; using normal statistics for the random V and g :

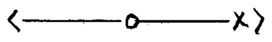

$$= \frac{1}{1+iwc}\langle m\rangle\frac{1}{1+iwc}h = 0$$

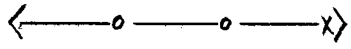

$$= \frac{1}{1+iwc}\langle m\frac{1}{1+iwc}m\rangle\frac{1}{1+iwc}h =$$

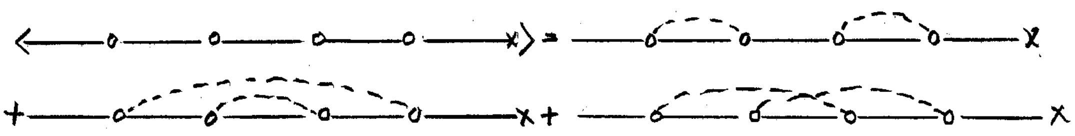

These graphs are called propagators. $\frac{1}{1+iw''c}$ is a bare propagator. Note that it is a nonrandom operator on the indices of m .

We demonstrate the evaluation of 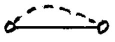 :

$$\langle m\frac{1}{1+iwc}m\rangle_{\substack{KP\\ ww''}} = -\sum_{q,\omega''} qP\langle V_{K-q,w-w''}\frac{1}{1+iwc}V_{q-p,w''-w'}\rangle c^2$$

After tedious manipulation this becomes

$$= -\delta_{K,P}\delta_{w,w'}V^2K^2C^2\sum_{\omega''}\int\frac{\rho(0,t)e^{i(\omega''-\omega)\tau}}{1+i\omega''c}d\tau$$

The ω'' summation can be performed by contour integration to give

$$\langle m\frac{1}{1+iwc}m\rangle_{\substack{KP\\ ww''}} = -\delta_{K,p}\delta_{w,w'}V^2cK^2\int_0^\infty d\tau\,\rho(0.\tau)e^{-\tau/c-i\omega\tau}$$

If $\rho(o,\tau)$ falls off rapidly compared to c and $1/\omega$, the integral is just the autocorrelation time of the velocity field, τ_v. In general,

$$\langle \mathfrak{M} \frac{}{1+i\omega c} \mathfrak{M} \rangle_{\substack{kp\\ ww'}} = -\delta_{k,p}\,\delta_{w,w'}\,K^2 D_0(w).$$

Examination of higher graphs such as the sequence (linked bubbles)

$$\Sigma_B =$$

shows that each term factors into products of individual bubbles

$$\Sigma_B = -\frac{\delta_{k,p}\delta_{ww'}}{1+i w c}\left[1 - K^2 D_0 + \frac{(K^2 D_0)^2}{1+i w c} - \ldots\right] = \frac{\delta_{k,p}\delta_{ww'}}{1+i w c + K^2 D_0(w)},$$ (geometric series).

We have resumed an infinite sequence of the graphs (leaving out many of the more complicated ones) to get a closed form for $\langle g_{kw}\rangle$.

Now consider the diffusion equation:

$$C\frac{\partial\langle G\rangle}{\partial t} - D\nabla^2\langle G\rangle + \langle G\rangle = H.$$

Fourier transforming we find

$$\langle G\rangle_{kw} = \left(\frac{1}{1+i w c + K^2 D}\right)_{\substack{kw\\ k'w'}} H_{k'w'}$$

In other words, the summation of the bubble subset is equivalent to the diffusion approximation, provided the autocorrelation time of the velocity field is short compared to the response time of the system (C) and the driving period (ω^{-1}). In fact, under these circumstances D is given by the classical form $D \sim C V^2 \tau_v$. This last result is not quite correct since some higher graphs also have pieces which go as k^2 so that

$$D \sim C V^2 \tau \text{ + higher corrections.}$$

These latter are called renormalization corrections. They are small for small "radiation Reynolds number", but could be large otherwise. In any case the diffusion coefficient is determined phenomenologically in a climate model and need not be calculated from first principles.

Finally, we can ask about summing larger subsets of graphs. Kraichnan has provided a prescription called the direct interaction approximation to a nonlinear integral equation for $\langle g\rangle$. For low "radiation Reynolds numbers" as seem to be the case in climate, this may not be necessary.

References

Kraichnan, Robert H. 1970 Turbulent Diffusion in Baker and Gammel, The Padé Approximation in Theoretical Physics, New York Academic Press. p.129.

Sellers, William D. 1965 Physical Climatology. Chicago. The University of Chicago Press. p.232.

Notes submitted by
Lawrence C. Kells.

WATER MASS ANALYSIS AND THE DEEP OCEAN CIRCULATION

Claes Rooth

I. General Background

The main effect of the ocean on the atmosphere is due to the sea surface temperature because the salinity variations are too small to significantly affect the water vapor pressure, and the roughness of the sea surface is also relatively unimportant. The sea surface temperature affects the atmosphere primarily by controlling the evaporation rate (the water vapor pressure doubles for every $10^{o}C$ rise), and also by a smaller sensible heat transfer.

Most of the ocean does not move very far in one year. A simple analysis shows that the return flow of the Gulf Stream takes approximately three and one-half years, even though the flow in the Gulf Stream itself may move 30^{o} of latitude in 30 days. Because of this slow movement, the seasonal atmospheric variations affect the ocean surface mainly in a local way and so the advection processes are less important on the seasonal time scale. The relative slowness of interior advection allows the development of regional responses to atmospheric circulation, e.g. the formation of 18^{o} water in the Sargasso Sea.

Cold dry air comes off the North American continent in the winter and cools the surface of the Sargasso Sea. The initial thermal response is followed by a large scale adjustment which can be understood in terms of potential vorticity modifications.

Consider the potential vorticity defined by $f/\frac{dz}{d\rho}$ where ρ can be regarded as the potential density and so $dz/d\rho$ defines an effective scale height. Because of the intense cooling $\frac{dz}{d\rho}$ is increased and so the potential vorticity is decreased.

Due to β-effects, this low potential vorticity water tends to spread southward, developing a baroclinic circulation perturbation which is superimposed on the subtropical Sverdrup drift. Tracer observations indicate a recirculation time scale significantly less than the roughly three-year time of the mean gyre. The volume of this low potential vorticity water is large enough to smooth out interannual heat flux variations. Its mean temperature has been quite stable near $18^{o}C$ during the era of modern oceanographic observations, but in recent years a possibly significant warming tendency has been observed. The associated infliction of the vertical temperature profiles is so striking that a special name, Eighteen Degree Water (EDW) has been coined.

The EDW is found in winter time at the surface in the northwestern point of the subtropical gyre. As it moves southward it encounters a smaller f. In order to conserve potential vorticity the thickness of the layer decreases, forming a southward-pointing wedge of minimum stability which is recognizable all over the Western Atlantic Basin, as far down as the Caribbean Islands.

Conventional wisdom says that deep water is formed by sinking in a few small areas of the ocean and this is balanced by a small upwelling over the vast area of the rest of the ocean. The heat put into the surface thermocline tends to stabilize it and so the upwelling of cold water would have to be balanced by the downward diffusion of heat.

$$\text{i.e. } \omega \frac{dT}{dz} = \frac{\partial}{\partial z}\left(K\frac{\partial T}{\partial z}\right)$$

Neither the upwelling velocity ω nor the diffusion constant K can be measured directly. The circulation time of the deep ocean is about 1,000 years and using this and the average depth of the ocean gives an estimate for $\omega = \frac{3000\,m}{1000\,yrs} = 10^{-3}\,cm/sec$. For a value of $K = 1\,cm^2/sec$, a density scale height of 1000 m $\left(= \frac{K}{\omega}\right)$ is obtained, and this agrees roughly with the thermocline depth. More recent measurements of k however, suggest that it is at most about 0.2 cm^2/sec and as a new mechanism is required to explain the upwelling of cold deep water.

It is proposed, in these lectures, that it is more reasonable to assume that water masses in the oceans move mainly along lines of constant potential density, and hence that water mass modification occurs mainly in upper and side-wall boundary layers.

Profiles of potential temperature in the ocean have a minimum depth at the equator and the lines of constant potential temperature surface near the poles. Salinity profiles show tongues of less saline water projecting from the surface near the poles to mid-depth equatorial regions, and these tongues are normally assumed to indicate the water mass motions. (see Reid and Lynn, Deep Sea Research, 1971, 18: 1063).

To support further arguments, it is necessary to briefly discuss the equation of state of sea water.

The density of sea water is a function of three variables, temperature, salinity and pressure. σ is defined by $\sigma = 10^3(\rho - 1)$ where ρ is density. Two definitions of σ are widely used. σ_T is the value of σ which the water would have if it were brought to the surface pressure with its *in situ* temperature and salinity. σ_θ is the value of σ which the water would have if it were brought to the surface adiabatically. Neutral surfaces along which fluid particles have the same density are harder to define because of the dependence of density on pressure. This is very complicated because of a substantial influence of salinity on the compressibility. Another complexity which is significant for many theories of climate feedback,the existence of a density *extremum* (at +4°C for fresh water and about -4°C for sea water). The thermal expansion coefficient of sea water at the freezing point is positive, but extremely small, so that the density variations in high latitude oceans are dominated by small salinity fluctuations, whereas in tropical regions temperature effects overwhelm the variations in salinity.

Notes submitted by
Trevor J. McDougall

II. INFORMATION FROM SOME CHEMICAL TRACERS.

Claes Rooth

The oxygen which is put into surface waters, and which is consumed by respiration and decay in deep water, has long been used as a tracer in oceanography. A typical picture from the western Atlantic Ocean is shown in Fig.1. The simple motion of a broad spreading tongue associated with a meridional over-timing, ignores boundary currents like the Gulf Stream, which may diverge to the interior and which may also cause intense mixing near continental boundaries. Quantitative interpretation of the distributions of dissolved oxygen is severely hampered by the fact that the consumption rate is an unknown function of biological parameters. Radioactive tracers are much more powerful diagnostic tools, since their decay rates are precisely known. We will here consider some implications of observed distributions of three such substancies, i.e. Radon (^{222}Rn), Tritium (^{3}H) and radio carbon (^{14}C), with half lives of approximately four days, 12 years, and 5000 years, respectively.

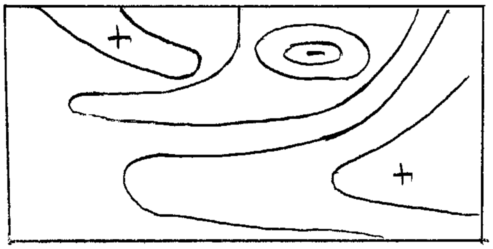

Fig. 1.

The deep ocean circulation, which is (believed to be) on the scale of 10^3 years, needs tracers with lifetime on the scale of 100's of years. ^{14}C is useful only on the large scale mean circulation (time resolution ~ 50 years) and is complicated now by a mixture of transients superimposed on the natural background. Tritium (^3H) is promising for many basin scale phenomena, especially since the bomb tests of the 1960's provided an amplification of the tritium content to an amount 300-400 times the natural background in the entire hydrosphere. Furthermore, since tritium is found in $^3H^1H^{16}O$ it stays with the water mass itself. (The concentration, expressed as the ratio between ^3H and ^1H ($^3H/^1H$), currently ranges from 1 - 10 x 10^{-18} in oceanic surface waters. The effective detection limit is about 10^{-19}. A concentration of 10^{-18} is one tritium unit (T.U.) i.e. 10^{-18} $^3H/^1H$ = 1 T.U.).

^{14}C and tritium are both formed in the atmosphere by H-bombs. As mentioned above, the natural background for tritium is negligible, while ^{14}C has a large cosmic ray related natural abundance. Radiocarbon has also been diluted by burning of fossil fuels, so that the net forcing function is extremely complicated. Tritium rains out at latitudes of the bomb tests, i.e. in the northern hemisphere, whereas ^{14}C occurs in carbon dioxide and is only slightly soluble in water, and therefore takes several years to get into the seasonal thermocline. Hence bomb ^{14}C reached the oceans more uniformly in both northern and southern hemispheres.

Earlier measurements and studies of tritium (Suess, Munnich and Roether) in the mid-1960's indicated that to the first order it is correlated with high surface temperatures, i.e. higher values in surface water, whereas deep water has low tritium and low temperatures. (Fig.2). Recently, however, tritium is beginning to appear in deep water, which may be associated with the various zones of winter convection and water mass formation.

Measurements in the Sargasso Sea (cf. Lecture I) show that from Bermuda to Puerto Rico, the tritium concentration, which is irregularly distributed with depth, is systematically related to the potential temperature. From the surface

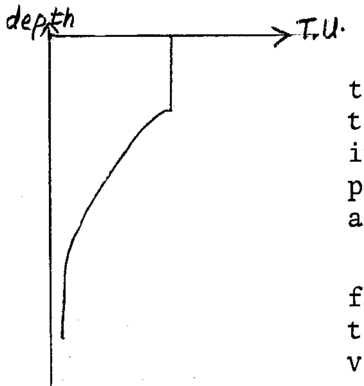

FIG. 2

to the 12°C isotherm, tritium and dissolved O_2 are both functions of potential density only. Below this isotherm tritium increases to the north (Fig.3) whereas oxygen is a function of potential density down to the bottom. (This is seven years after bombs.)

Assume that mixing takes place, along ρ = coast surfaces (e.g. near baroclinic regions). If this mixing is due to large scale eddies any attempt to measure mixing along vertical or horizontal surfaces will give

$$\frac{K_V}{K_H} = s^2 \quad ; \quad s = \left(\frac{\partial z}{\partial x}\right)_\rho$$

Here K_v and K_H are vertical and horizontal coefficients, respectively, whereas s is the slope of density surfaces (Fig.5). Typically one finds $K_V \sim 1$ cm^2/sec, $K_H \sim 10^7$ cm^2/sec and $s = .3 \times 10^{-3}$, which indicates that mixing does take place along density surfaces.

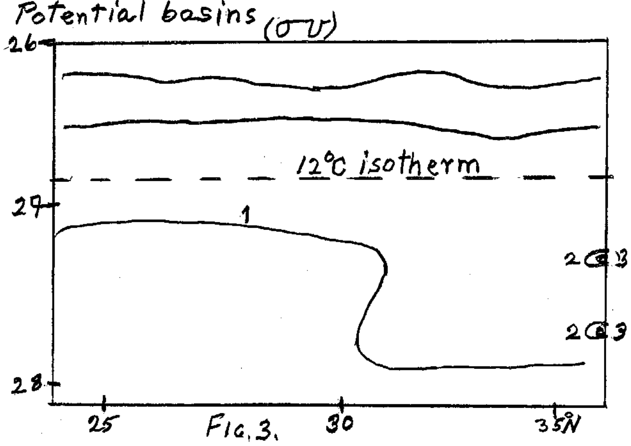

Fig. 3.

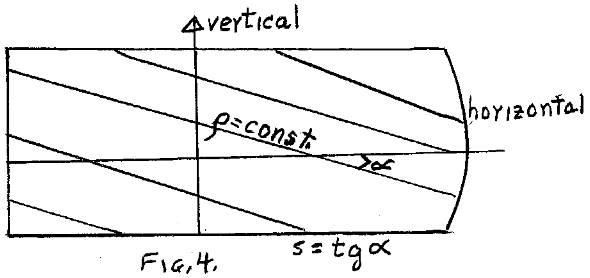

Fig. 4.

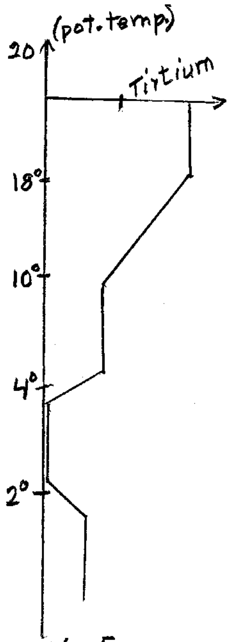

Fig. 5

If this is true this may be used to explain the feature of Fig.4. On the boundary of the gyre the surfaces of constant potential density do not coincide, therefore there will be mixing <u>across</u> surfaces of constant potential density due to <u>mixing along</u> ρ = constant surfaces. The lateral mixing (i.e. along ρ = constant) may also be used to explain the observed tritium below 10° (Fig.5). To account for the observed mixing of tritium down to this great depth in this short time (five years) a vertical eddy diffusion with $K_V < 1$ cm^2/s is too small. Thus lateral mixing by mesoscale eddies (300 km) (i.e. along ρ = constant surfaces) is needed to explain the observed tritium.

The abyssal radiocarbon distributions have been modeled by Veronis and Kuo, and recently by Fiadeiro, and found to be reasonably rationalized by assuming β-controlled current kinematics and vertical and horizontal diffusivities of approximately one and 10^7cm^{2}sec. Since 10^7cm^2 gives a lateral diffusion time scale in a typical ocean basin (D/T ~ 2000 km) of approximately 100 years, the possibility remains that the "vertical" mixing is everywhere limited to such wall layers and surface fronts.

Enhanced vertical mixing in side wall boundary layers has been indicated by Biscaye and Ettreim on the basis of radon profiles. They claim local values of X_V of several hundred c.g.s. units, which would provide an average χ_v of one unit if applied to an edge strip amounting to a few tenths of one percent of the ocean surface. Their interpretation of the radon profiles must be accepted with caution, however, since the observed tracer distributions could also be due to lateral diffusion from side slopes.

In summary, there remains a considerable uncertainty regarding the extent to which interior vertical mixing influences abyssal waters. The upper main thermocline is to first order lateral advective, however, and it appears safe to assume, in the construction of climatic feedback models, that the subtropical and equatorial surface waters are effectively isolated from the abyssal circulation.

Notes submitted by
Lars P. Røed

WATER MASS ANALYSIS AND THE DEEP OCEAN CIRCULATION (III)

Claes Rooth

First we shall consider some more evidence for the conclusion made last time, that most of the oceanic mixing takes place on constant density surfaces.

Let c be the distribution of a scalar quantity (in this case, the concentration of a tracer, such as oxygen or tritium), φ be the diffusive flux of the scalar across a constant density surface, and q be the diffusive flux of buoyancy across the constant density surface. We can write, employing density as the vertical coordinate:

$$q = \langle \omega' \rho' \rangle$$
$$\varphi = \langle \omega' c' \rangle$$

where $\omega = \frac{d\rho}{dt}$ represents deviations from the mean value, and $\langle\ \rangle$ represents the time-averaged value.

We can write the equation for tracer mixing in density coordinates, using the Boussinesq approximation:

$$c_t + (u c_x + v c_y)_{\dot{Q}} + \dot{\rho}\,\frac{\partial c}{\partial \rho} + \lambda c = + \frac{\partial \rho}{\partial z}\,\frac{\partial \varphi}{\partial \rho} + D\left(\nabla_\rho^2 c + \nabla c \cdot \nabla \ln\left(\frac{\partial z}{\partial \rho}\right)\right),$$

where the subscript ρ indicates a quantity or operation on constant density surfaces, λc is a term representing *in situ* decay, J represents interior sources and D is the coefficient of lateral diffusion

$$\dot{Q} = \frac{\partial q}{\partial z} = \frac{\partial \rho}{\partial z}\,\frac{\partial q}{\partial \rho}.$$

Assuming mixing similarity, we can write: $$\frac{\varphi}{\frac{\partial c}{\partial z}} = \frac{q}{\frac{\partial \rho}{\partial z}}$$

or: $$\varphi = q\,\frac{\partial c}{\partial Q}.$$

We can therefore write:

$$\frac{\partial \rho}{\partial z}\frac{\partial \psi}{\partial \rho} = \dot{\rho}\frac{\partial c}{\partial \rho} + \frac{\partial \rho}{\partial z} q \frac{\partial^2 c}{\partial \rho^2}$$

The equation for tracer mixing can then be written:

$$c_t + (\vec{V} - D\nabla/n \frac{\partial z}{\partial \rho}) \cdot \nabla_q c + \lambda C = g + D\nabla_\rho^2 c + \frac{\partial \rho}{\partial z} q \frac{\partial^2 c}{\partial Q^2}$$

If we now regard the ratio of the diffusive flux of buoyancy to its mean gradient in the z-direction as a constant K, we can rewrite the last term on the right-hand side as:

$$K\left(\frac{\partial \rho}{\partial z}\right)^2 \frac{\partial^2 c}{\partial \rho^c}$$

Since $\lambda \gtrsim 0$, any regime where vertical transport processes dominate will show $\frac{\partial^2 c}{\partial \rho^2} \geqslant 0 \; (L_t - J << \lambda c)$. Therefore any negative curvature in a plot of c against density must be due to horizontal advection, or to interior source terms.

We now consider tritium and oxygen distributions in the Pacific. Observations show concentrations of the tracers plotted against σ_θ (the density that sea water would have at the ocean surface) from four stations over 10° of latitude and 30° of longitude. We find that for each tracer the station's values form a single curve, and that the curves for oxygen and tritium are essentially parallel above the oxygen minimum, with virtually no tritium below the oxygen minimum. The oxygen and tritium concentration distributions between σ_ϑ 26 and 27 - corresponding to the upper main thermocline - show clear indications of dominance by horizontal transports, based on the curvature criterion. The sharp limitation of the tritium distribution contrasts with the Atlantic, where substantial tritium is found below the oxygen minimum level. This is particularly interesting since the surface concentration of tritium is higher in the Pacific than in the Atlantic. The difference can be explained by the lack in the North Pacific of a strong convective zone at high latitudes, and at high mean density, while the North Atlantic has such a zone. This contrast supports the idea that mixing between deep waters and the surface occurs mainly along constant density surfaces between the interior points and the winter-time convection zones. Further confirmation of this motion can be found in the abyssal radiocarbon distributions in the Pacific.

It follows that oceanic cooling in polar regions would not affect surface conditions in the tropical and subtropical regions, since the poles would communicate principally with each other by transport in the deep water.

The subtropical and tropical waters above the 10°C surface interact with the surface layers in the convective regimes, mainly located poleward of 30° latitude, and in the equatorial upwelling regimes.

There is a substantial amount of indirect evidence and modeling results which indicates that upwelling of cold water is an important element of the tropical surface regime. If the polar bottom waters are not the source for the upwelling water, we must look to midlatitude sources, and hence to the dynamics of the subtropical gyres. The studies by Vonder Haar and Oort of the partition of global heat flux between atmosphere and ocean (cf. lecture by Oort) independently confirm the importance of oceanic heat transport in the 10°-20° latitude band.

The key to understanding this region lies in determination of the depth distribution of the geostrophic part of the Sverdrup transport. Pedlosky (1968) discussed the partition of the latter between Ekman drift and geostrophic motion. The Ekman drift is maximal near the latitudes of maximum wind stress, where the Sverdrup transport vanishes. With $\tau_x f^{-1}$ about 10^4g/cm sec, a 10°C difference in temperature between the Ekman drift and the mean geostrophic drift would carry 10^5 cal/cm sec. Distributed over 2° of latitude, the associated upwelling cooling of the surface amounts to 400 Ly/day, or about half of the daily insolation.

A pronounced feedback on atmospheric dynamics by such upwelling cooling was demonstrated in a model of the Intertropical Convergence Zone by Pike (1971). He showed that the upwelling induced by the wind patterns along a zonal ITCZ was sufficient to cause the zone to be displaced from the equator, even with symmetric insolation. To produce realistic sea surface temperatures, he had to choose an effective source temperature of the upwelling water of 15°C. This is quite consistent with the tracer indications that the directly wind-driven Sverdrup regime is limited to temperatures above 10°C.

Pike's model involves another element which is important to the understanding of long time scale air-sea interaction. This is the notion that the surface cooling by upwelling, is insensitive to the mechanics of the turbulent mixing processes. When sustained upwelling occurs, it becomes necessary for the large scale circulation to supply the upwelling water by geostrophic currents. The effective source temperature for the upwelling water is therefore controlled by a global adjustment process, and ultimately by the influence of the convective zones on the potential vorticity distribution with respect to the density field. To understand the long time scale heat budget of the tropical upwelling, we must therefore study the convection regimes in the poleward half of the subtropical gyres. The mixing mechanics in the upwelling zones is only significant for the transient response problem on seasonal and shorter time scales.

Let us now consider how one might go about constructing a model for a subtropical gyre as an element in a climate model of intermediate complexity between the General Circulation Models (GCM) and the Sellers type (c.f. lecture by North).

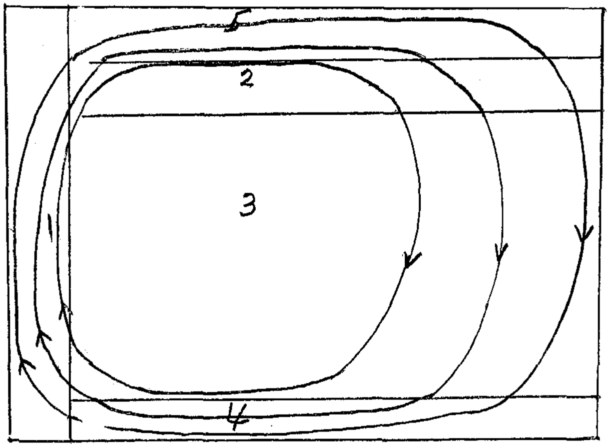

Fig. 1.

An idealized Gulf Stream gyre combines at least four, perhaps five distinct dynamic regimes - each with a characteristic dominant element in its mechanics (Fig.1) five regimes, as shown in Fig.1.

Region 1 is the fast western boundary current carrying sensible heat northward, while Region 2 is the region of intensive heat exchange where convective mixing occurs in winter. In Region 2 there is substantial vertical mixing of water. Region 3 is the region of quasigeostrophic transport along constant density surfaces. There the heating regime is limited to the surface water. Vertical mixing here can be neglected on the time scale of the gyre's circulation. Region 4 is a narrow zone of upwelling, the heat source for the gyre. Region 5 is the path of the Gulf Stream after it separates from the western boundary. Here lateral eddy dynamics dominate and the surface water cools as it crosses the Atlantic. Regions 1 and 2 are characterized by a balance between a lateral advection and surface cooling with

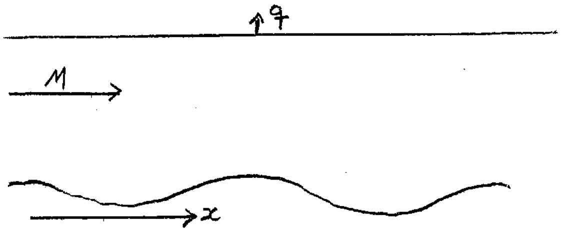

FIG.2

convective adjustment. Such a regime is amenable to a partial analysis of the surface temperature distribution, if the approximation is accepted that no significant mixing occurs below the convection adjustment depth (no corrective entrainment).

Consider a channel of fixed cross section and variable depth as in Fig.2. A mass of water M (mass/unit time) moves through the channel, having been heated at some point upstream. The heat q released at the surface of the fluid by the water mass can be written:

$$q(x) = \frac{\partial}{\partial x}(MT)$$

where T is the water temperature and x is the distance along the channel. Since, in a steady-state situation, the discharge M is the same for any cross section of the channel, we can write:

$$q(x) = M\frac{\partial T}{\partial \lambda}$$

We can similarly consider a source of heat in an ocean having, as in Fig.3, instead of assuming a source of uniform temperature, we now define a mass transport function relative to temperature, M(T).

$$M(T) \equiv \int_{T}^{T_{max}} m(T)\,dT$$

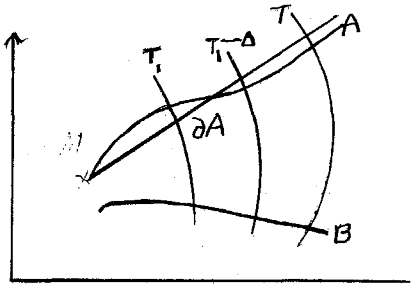

FIG. 3

where T_{max} is the surface temperature in the source region, and M(T) is the mass flux per unit temperature interval across the vertical surface through the isotherm $T = T_{max}$.

If we now assume that interior mixing below the convective adjustment depth associated with surface cooling is negligible, then it is easily seen that the heat loss to the atmosphere between the surface isotherms T_1 and $T_1 - \delta T$ is

$$\delta H = M(T_1)\,\delta T$$

Thus, if the heat loss per unit area is Q(T) - dependent on the temperature - then the area δA between these isotherms is given by

$$Q\,\delta A = \delta H = M(T_1)\,\delta T$$

$$\text{or}\quad \frac{\delta A}{\delta T} = \frac{M(T)}{Q(T)}$$

This expression should be seasonally applicable in Region 1, and applicable to the winter temperature distribution in Region 2, provided allowance is made for local seasonal heat storage effects, i.e. Q has to be the mean annual heat loss as a function of the minimum winter temperature.

The equatorward gyre section is the simplest regime, with seasonal surface heat storage, and almost certainly a main thermocline flow which conserves potential vorticity. Since the geostrophic component of the Sverdrup transport increases along the flow, surface water must be entrained from the seasonal thermocline regime into the geostrophic gyre circulation. This is clearly evident in the North Atlantic in the formation of a sharp salinity maximum at about 100 m depth, which is traceable into the Caribbean, and the Gulf of Mexico. The persistence of this thin ($\sim$50 m) salinity anomaly for an advection time of a year or so bears evidence to the weakness of the vertical mixing even in the near-surface layers.

The outstanding dynamic problem in understanding the gyre dynamics appears from this point of view to be the response to surface cooling in the poleward branch, modified by the dynamic effects of Gulf Stream eddy processes, and the surface water entrainment in Region 3, which must be largely responsible for the determination of the transport function M(T).

Turning finally to the cold water circulation, acceptance of the subtropical gyre as essentially isolated from underlying waters, implies that the polar regions communicate with each other through the abyssal and high latitude surface dynamics.

Tracer evidence, as well as estimates of current rates of deep water formation suggest a time scale of order 10^3 years for this process. The mean vertical mixing rate in the abyssal regions is pretty well pegged at an equivalent vertical eddy diffusivity of about 1 cm L/sec, but many indications exist that this mixing is not horizontally uniform in the mean, but varies by several orders of magnitude. From the point of view of climate dynamics, it is important to realize that substantial climate fluctuations occur on the time scale of the abyssal circulation. The abyssal property distributions are therefore not likely to be in equilibrium with the short term climatic state.

Even more confounding is the fact that ice sheet volumes have fluctuated enough to provide a mean salinity fluctuation of close to 1 $^{o}/oo$ (1/40 of 35 $^{o}/oo$). If such a fluctuation occurs over 10^4 years, such as in the major ice age decay phases, a salinity adjustment lag of about 0.1 $^{o}/oo$ in the deep waters would be expected, if the present turnover rate were still valid. Some melt water supply at the surface is likely to stabilize the ocean system, leading to an ever greater adjustment lag. No credible theories exist at present for how the high latitude heat transports would be modified by this effect but a reasonable hypothesis appears to be that the formation of intermediate water of low salinity and low temperature would be enhanced at the expense of deep water formation. The implied cooling of the main thermocline would lead to a transient heat transfer from ocean to atmosphere which might act as a positive feedback on the glacier melting process. Careful study of this problem appears to be warranted.

In summary, recent developments in tracer chemistry have provided a set of tools for the study of long time scale transport processes. Available data force a revaluation of current thinking about thermal circulation in the oceans. Together with the fact that stationary ocean response is expected only on time scales of several thousand years one must conclude that any ocean dynamics relevant to the climate problem is not available at present, but also that some promising directions of inquiry can be identified.

References

Callahan, J.E. 1972 The structure and circulation of deep water in the Antarctic. Deep-Sea Research 19: 563-575.

Ellett, D.J. and J.H.A.Martin 1973 The physical and chemical oceanography of the Rockall Channel. Deep-Sea Research 20: 585-625.

Gill, A.E. and P.P.Niiler 1973 The theory of the seasonal variability in the ocean. Deep-Sea Research 20: 141-177.

Lazier, J.R.N. 1973 The renewal of Labrador Sea Water. Deep-Sea Research 20: 341-353.

Lee, A. and D.Ellett 1965 On the contribution of overflow water from the Norwegian Sea to the hydrographic structure of the North Atlantic Ocean. Deep-Sea Research 12: 129-142.

Lynn, R.J. and J.L.Reid 1968 Characteristics and circulation of deep and abyssal waters. Deep-Sea Research, 15: 577-598.

Montgomery, R.B. 1938 Circulation in upper layers of southern North Atlantic deduced with use of isentropic analysis. Papers in Phys.Oceanog. and Meteorology 6(2) M.I.T. and W.H.O.I. 56 pp.

----------------and W.S.Wooster 1954 Thermosteric anomaly and the analysis of seria oceanographic data. Deep-Sea Research 2: 63-70.

Pedlosky, J. 1968 An overlooked aspect of the wind-driven oceanic circulation. J.Fluid Mech., 32: 809-821.

Pike, Arthur C. 1971 Intertropical Convergence Zone studied with an interacting atmosphere and ocean model. Mon.Wea.Rev. 99: 469-477.

Pingree, R.D. 1972 Mixing in the deep stratified ocean. Deep-Sea Research 19: 549-561.

Reid, J.L. and R.J.Lyon 1971 On the influence of the Norwegian-Greenland and Weddell Seas upon the bottom waters of the Indian and Pacific Oceans. Deep-Sea Research 18: 1063-1088.

Weyl, P.K. 1968 The role of the oceans in climatic change: a theory of the ice ages. Meteor.Monog. 8(30) American Meteor.Soc.,Boston, Mass.: 37-62.

Notes submitted by
Glenn H. White
and
Toshio Yamagata.

GENERAL CIRCULATION MODELS AND CLIMATE

Richard C. J. Somerville

I. History and Perspective

During World War I, L.F.Richardson formulated finite-difference analogs to the equations of motion of the atmosphere. His attempt (by hand calculation) to predict six-hour surface pressure change, at a point in northern Europe, failed, due to both poor initial data and an unstable finite-difference scheme. The first successful numerical weather prediction was achieved shortly after World War II, utilizing the quasigeostrophic approximation to the equations of motion. Phillips, in 1956, published the first numerical general circulation model (GCM), using a similar system of equations. With the vast increase since then in computer speed and storage, modern GCM's now have returned to the "primitive" equations to model atmospheric dynamics. These latest and largest of the numerical models will be considered here. GCM modeling is most active in the United States, with research groups at GFDL, UCLA, NCAR, RAND, and GISS. We may write the equations as:

$$\frac{d\vec{V}}{dt} + f\hat{K}\times\vec{V} + \nabla_\sigma\phi + \sigma\alpha\nabla\pi = \vec{F}$$

$$\frac{\partial\pi}{\partial t} + \nabla_\sigma\cdot(\pi\vec{V}) + \frac{\partial}{\partial\sigma}(\pi\dot{\sigma}) = 0$$

$$p\alpha = RT$$

$$\frac{d\theta}{dt} = \frac{1}{c_p}\,\frac{\theta}{T}Q$$

$$\frac{1}{\pi}\frac{\partial\phi}{\partial\sigma} = -\alpha$$

$$\frac{dq}{dt} = -C+E$$

where: $\vec{V}\sim$ horizontal velocity, $\nabla_\sigma\sim$ 2-dimensional gradient operator, $\sigma\sim$ vertical pressure coordinate normalized to ground elevation, $p\sim$ atmospheric pressure, $\pi = (P_{\text{top}} - P_{\text{bottom}}$, $\vec{F}\sim$ horizontal friction force, $Q\sim$ heating rate per unit mass, $\phi\sim$ geopotential, $q\sim$ water vapor mixing ratio, $C\sim$ rate of condensation, $E\sim$ rate of evaporation, and the remaining notation is conventional.

If these equations are finite differenced in space, a typical number of degrees of freedom in a global domain is:

$$\underbrace{10^2}_{\substack{\text{grid pts.}\\ \text{in E-W}\\ \text{direction}}} \;\bullet\; \underbrace{10^2}_{\substack{\text{N-S}\\ \text{grid pts.}}} \;\bullet\; \underbrace{10}_{\substack{\text{vertical}\\ \text{layers}}} \;\bullet\; \underset{\substack{\text{dependent}\\ \text{variables at}\\ \text{each point}}}{(6+\ldots)} \;\sim\; 10^6$$

The above system may be integrated in finite time intervals of approximately five minutes. This limit is set by computational stability criteria, and will decrease with decreasing horizontal grid spacing. Most models utilize second-order explicit finite-difference schemes. The source/sink terms ($\vec{F}$, Q, C, and E), are parameterized in terms of the model variables, and specified boundary conditions include incoming solar radiation, ground topography, and usually sea surface temperature. (See Fig.1).

There are basically two classes of utilization of a GCM:

1) NUMERICAL WEATHER PREDICTION . . . Observed weather provides initial conditions for the GCM, which is integrated to predict future weather. Forecast skill is most useful in the one-to-three day range, although slight skill is noticeable out to about 10 days. Currently operational forecasts use guidance from numerical models, as this procedure has proved significantly more skillful than purely subjective forecasts.

2) QUASI-EQUILIBRIUM STATISTICS, OR "CLIMATE" . . . The model atmosphere is spun-up from an irrelevant initial state, and run until its time-average statistics can be determined. It should be noted that GCM offers a complete and consistent global data set, even if not always a completely realistic one. Spin-up times are on the order of 30 days of simulated time, whereupon the model is usually run for another month or more. A GCM may use ~1 hour of large computer time (CDC 7600) per simulated day. Runs much longer than a few simulated months are extremely costly.

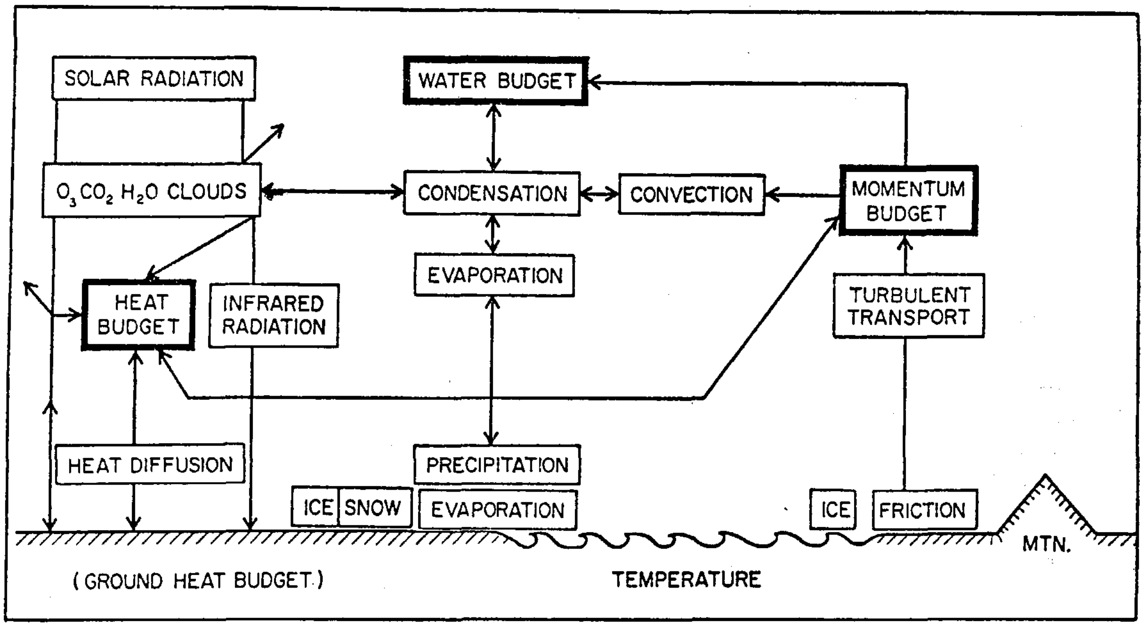

Fig.1. Schematic diagram of interactions of physical processes in a typical atmospheric model.

II Typical Monthly Mean Fields from GCM's

The various GCM's tend to give similar results.

1) Zonally averaged velocity fields. The principal features of the zonal wind compare fairly well in both magnitude and position with observations. Meridional and vertical velocity fields are harder to observe and therefore to compare, but basic agreement of the meriodinal cells is evident.

2) The model energy cycles proceed in the same sense as that observed. However, the models tend to exhibit mean available potential and kinetic energies which are significantly larger than observed, and eddy energies which are too small.

3) The spatial kinetic energy spectrum, while exhibiting consistently less eddy kinetic energy than observed, is qualitatively faithful to the real atmosphere.

4) Meridional transports of momentum and sensible heat reflect the above-mentioned tendency of the GCM's to underestimate eddy transport and over-estimate mean transport.

5) The zonal mean diabatic heating rates are qualitatively reasonable, although their effects are limited both by fixing sea surface temperatures, and by constraining lapse rates.

6) Zonal mean precipitation values in GCM's are within the error limits of the observations.

7) Zonal mean temperature profiles are reproduced well, except near the poles.

8) Geographical distributions of meteorological fields tend to show the broad-scale features of observed climate, but are locally erroneous in many details.

III Sensitivity, and the Predictability Problem

In the 1960's Lorenz and others examined the detailed predictability of weather, and its dependence on errors in initial conditions (assuming the model is perfect). Three approaches were used:

a) slightly perturb initial conditions in a GCM and observe the divergence of the solutions;

b) find two similar atmospheric states in the data base and study their observed subsequent evolutions;

c) utilize turbulence theory. All three methods gave an initial small error doubling time of about two to three days and a limit to useful predictability of a few weeks.

No such theory exists for the prediction of climate statistics, however, and only the seasonal cycle is known by experience to be predictable in some statistical sense. A critical question is whether or not the climate is a function only of external conditions. GCM climates appear to be a unique function of boundary conditions and forcing.

A basic concern, however, in interpreting GCM results is the sensitivity of the models to their parameterizations. We do not know, in many cases, how much of the present climate is parameterized into the models, and how much of their sensitivity to varying parameterizations is physically realistic.

These questions of the predictability of climate and its sensitivity to "external" and "internal" forcing are currently being actively investigated using GCM's as well as other classes of climate models. Despite the expense and the many imperfections of current GCM's, it is likely that many questions of climate theory will ultimately be answered, quantitatively and credibly, only with the aid of these complex and comprehensive models.

References

The following recent surveys are useful guides to the large literature of general circulation models.

Global Atmospheric Research Program, 1974: Modelling for the First GARP Global Experiment. GARP Publications Series No.14, Geneva, World Meteorological Organization, 261 pp.

Global Atmospheric Research Program, 1975: The physical basis of climate and climate modelling. GARP Publications Series No.16, Geneva, World Meteorological Organization, 265 pp.

National Academy of Sciences, 1975: Understanding Climatic Change. Washington, D.C., 239 pp.

Schneider, S.H., and R.E.Dickinson 1974 Climate modeling. _Rev.Geophys.Space Phys._, _12_: 447-493.

Smagorinsky, J., 1974 Global atmospheric modeling and the numerical simulation of climate, in _Weather and Climate Modification_, W.N.Hess, Ed., Wiley:633-686.

Notes submitted by
Bruce A. Wielicki

ABSTRACTS OF SEMINARS

ENERGY EXCHANGE OVER THE NORTH AND SOUTH ATLANTIC OCEANS

Andrew F. Bunker

Charts of calculated energy exchange across the surface of the North and South Atlantic Oceans have been constructed. Wind and temperature observations obtained from about nine million ship weather reports were entered individually into the bulk aerodynamic equations with exchange coefficients that varied with wind speed and stability. The individual fluxes were averaged to obtain monthly and annual means of latent and sensible heat and momentum. Net radial fluxes were calculated using Budyko's (1963) formulas. Monthly and annual averages for 32 years have been formed for 740 subdivisions of the ocean. Averages for each month from 1941 through 1972 were computed for 114 10° squares to study the variations and anomalies of the fluxes, meteorological variables and sea temperature. Charts giving annual averages of the net heat gain by the ocean, evaporation, sensible and radiational heat exchange, wind stress components, and meteorological variables were presented. A chart was constructed showing anomalies of the net heat gain by the oceans for January 1965. One band of negative anomaly extended from the Norwegian Sea across the equator to 35°S.

Numerous graphs of the annual cycles of energy exchange and meteorological variables were presented for particularly interesting areas of the North and South Atlantic Oceans. The net annual heat loss by the fast-moving warm core of the Gulf Stream is greater than in any area of the ocean. This heat loss is the result of rapid advection of warm water from the subtropical source region into an area swept by cold dry continental air masses much of the year. North of the Arctic Circle a major heat-loss area cuts across parts of the Norwegian and Barents Seas. It is in this area that the North Atlantic Deep Water is formed by the cooling and sinking of surface water advected from the south. One cause of the cooling is the negative radiation exchange during five fall and winter months. The Labrador Current advects cold water southeastward past Newfoundland. After it crosses the 51st parallel it gains heat through both radiation and condensation of water vapor upon the water's surface. In the tropics the water gains much energy through solar radiation. In the trade wind region of the North Atlantic evaporation is large and only a moderate amount of heat is retained by the ocean. Just south of the equator cold water upwells which limits the evaporation and over 100 W m^{-2} is retained by the water. Similarly, large amounts of heat are gained by the cold waters upwelling along the west coast of Africa from Gibraltar to South Africa. Because of the cold water drifting northward across 50°S there is a band of heat gain by the water.

RECYCLING ROTATING FLOW OVER VARYING BOTTOM TOPOGRAPHY

Michael K. Davey

The Antarctic Circumpolar Current flows westward in an annular configuration.It is a deep current, and consequently its course is influenced by the bottom topography. Previous theoretical work on flow over bottom topography relies on either prescribed upstream conditions (e.g. Boyer (1971), Huppert and Stern (1974) or on $O(1)$ β-effect and $O(1)$ topography variation (e.g. Kamenkovich (1962), Johnson and Hill (1975)). For a circumpolar flow, the latter theories require corresponding f/H contours (f = Coriolis parameter, H = fluid depth). The aim of the theory presented here is to investigate a situation for which neither upstream conditions nor f/H contours can be used.

Steady homogeneous flow in a rotating annulus, driven by a prescribed surface velocity (e.g. a differentially rotating rigid lid as is common for laboratory experiments), is considered. The Ekman number E and the Rossby number ε are both much less than unity, and the ratio h = topography height/fluid depth is restricted to $O(\max(\varepsilon, E^{\frac{1}{2}}))$. The ratio $\varepsilon/E^{\frac{1}{2}}$ is a measure of the distance a vertical column of fluid travels in the time required for Ekman suction effects to be significant. Varying the size of $\varepsilon/E^{\frac{1}{2}}$ gives different parameter regimes to study, ranging from the linear viscous case ($\varepsilon << E^{\frac{1}{2}}$) to the case of conservation of potential vorticity to zeroth order ($\varepsilon >> E^{\frac{1}{2}}$). The case $\varepsilon >> E^{\frac{1}{2}}$ will be discussed in detail.

To zeroth order in ε ,

$$\nabla^2\psi + \frac{h}{\varepsilon} = F(\psi)$$

where ψ is the streamfunction for the geostrophic flow. To find ψ , both where $F(\psi)$ and the total azithmuthal transport $Q = \psi(r_2) - \psi(r_1)$ are needed. (r_1 and r_2 are the inner and outer radii of the annulus). The recycling nature of the flow means that the large length scale $\varepsilon/E^{\frac{1}{2}}$ is available, and higher order viscous effects determine F and Q. A circulation condition (applicable to all the parameter regimes) was found -

$$\Gamma(\psi) = \tfrac{1}{2}\Gamma_T(\psi)$$

($\Gamma_T(\psi)$ is the circulation around ψ = constant, using prescribed top surface velocities). An implicit expression for $F(\psi)$ results, which involves a reference level for the height of the topography as seen by a fluid column following streamline ψ . Solutions were obtained by iteration for the special case of constant surface vorticity and h varying azimuthally only. Symmetric topography gave flow patterns with corresponding symmetry. If the topography diverts the flow significantly, then Q is greatly reduced, and the streamline pattern may differ qualitatively from those obtained by assuming constant .

References

Boyer, D.L. G.F.D. 2, 1971.

Huppert, H.E., M.E.Stern J.F.M. 62, 1974.

Johnson, J.A., R.B.Hill Deep-Sea Res. 22, 1975.

Kamenkovich, V.M. Akad.Nauk. SSR, Inst.Okean,Trudy 56, 1962.

UPWELLING NEAR AN ICE EDGE

Tor Gammelsrød and Lars P. Røed

In models of the atmosphere and oceans the ice coverage sometimes plays an important part. The simplest climate models invoke the changes in the earth's albedo due to the ice coverage, while the more detailed models also take the insulating effect of the ice into account.

The model we present here investigates another effect of the ice, namely the possibility of a wind-driven, open-ocean upwelling near an ice edge. The ice is modeled as a thin surface sheet which partially covers the ocean. It is free to move in the vertical, but has no horizontal motion, which entails that in the ice-covered region the wind stress has no influence. The study is confined to a linear constant density model with no horizontal friction. Both time-dependent and steady-state cases are considered.

These assumptions entail that in the steady state of a two-dimensional model circulation beneath the ice is impossible. Thus the ice acts almost as a coast. In the time-dependent case the time scale of the friction, assumed to be proportional to the geostrophic velocity, is found to be of order 10 days. It is argued that this is also the time scale for the onset of the upwelling.

We conclude that it is possible that up- or down-welling phenomena occurs in the vicinity of an ice edge. This may be important in processes such as bottom water formation and freezing (melting) of the ice. Therefore the problem deserves further investigation with more sophisticated models including stratification, as well as lateral diffusion of momentum and vertical mixing of density.

MARTIAN CLIMATOLOGY

Peter J. Gierasch

If Mars has permanent CO_2 polar caps, atmospheric heat transport may cause the atmospheric pressure to be extremely sensitive to variations of solar heating at the poles. This could happen because atmospheric heating depends on density, which depends strongly on the polar temperature through the vapor pressure relation. A simple climatological model for polar heat balances is used to study the question, and it is found that a climate instability may be possible. Complete evaporation of the polar caps may be triggered if the absorbed solar energy at the poles increases by about 20%.

Reference

Gierasch, P.J. and O.B.Toon 1973 Atmospheric pressure variation and the climate of Mars. J.A.S. 30: 1502-1508.

STABILITY OF THE JOVIAN GENERAL CIRCULATION

Peter J. Gierasch

Ingersoll and Cuzzi (1969) pointed out that the prograde and retrograde jets associated with belts and zones on Jupiter must be thermal winds due to horizontal temperature gradients beneath the visible clouds. The stability of such gradients is puzzling. It is easy to show that if baroclinic instability occurs then the resulting mixing should effectively destroy the temperature contrasts. In this lecture, a progress report is made on investigation of baroclinic instability in an atmosphere which overlies a deep motionless layer. Eady's model, with uniform potential vorticity in the basic state, is to investigate the influence of the deep layer on growth rates. Both geostrophic and nongeostrophic models are treated. The results show that growth of instabilities is suppressed if the underlying layer is weakly stratified. In the limit of no stratification and infinite depth, instabilities exist only if the Richardson number in the upper layer is less than unity.

Reference

Ingersoll, A.P. and J.N.Cuzzi 1969 Dynamics of Jupiter's cloud bands. J.A.S. 26: 981-985.

VARIATIONS IN THE EARTH'S ORBIT: PACEMAKER OF THE ICE AGES

John Imbrie

(i) Three indices of global climate have been monitored over the past 450,000 years in Southern Hemisphere ocean floor sediments.

(ii) Over the 10^{-4} to 10^{-5} cycles per year frequency range, climatic variance of these records is concentrated in three discrete spectral peaks at 23,000-year, 42,000-year, and approximately 100,000-year periods. These peaks correspond to the dominant periods of the Earth's solar orbit, and contain respectively about 10 percent, 25 percent and 50 percent of the climatic variance.

(iii) The 42,000-year climatic component has the same period as variations in the obliquity of the Earth's axis and retains a constant phase relationship with it.

(iv) The 23,000-year portion of the variance displays the same periods of frequencies (about 23,000 and 19,000 years) as the quasiperiodic precession index.

(v) The dominant, 100,000-year climatic component has an average period close to, and is in phase with, orbital eccentricity. Unlike the correlations between climate and the higher-frequency orbital variations (which can be explained on the assumption that the climate system responds linearly to orbital forcing), an explanation of the correlation between climate and eccentricity probably requires an assumption of nonlinearity.

DYNAMICS OF JUPITER'S ATMOSPHERE

Andrew P. Ingersoll

The presence of an internal heat source, the lack of a solid surface and the great size of Jupiter account for many of the differences between Jovian and terrestrial weather patterns. On both planets, absorption of sunlight at the equator leads to poleward heat flow, but on Jupiter this flow takes place in the interior, and is essentially a poleward redistribution of internal heat. Atmospheric motions are mainly in the east-west direction, and seem to transport very little energy across latitude circles. Theories of convection which postulate a near-adiabatic interior can explain this poleward redistribution of internal heat. Specific details are worked out for mixing-length theory. Jupiter's banded cloud patterns are thought to be driven by moist convection, in a process similar to that which drives the earth's tropical Hadley circulation. Frictionally-driven convergence at the base of the clouds gives rise to heating within the clouds, which powers a self-excited disturbance consisting of zonally-symmetric cloud bands. The extreme stability of these Jovian patterns may be controlled by the deep convecting portion of the atmosphere below the clouds.

THE GLOBAL ENERGETICS OF ICE-AGE OSCILLATIONS: INFERENCES BASED ON A STATISTICAL-DYNAMICAL MODEL OF CLIMATE

Barry Saltzman

Conservation equations for water in all forms and thermodynamic energy are developed for the complete atmosphere-hydrosphere-lithosphere-cryosphere system, allowing the possibility for temporal variations of all significant components of the system that may be involved in long term climate changes. Using these equations we find an integral constraint on the fluctuations of the mean, mass-averaged ocean temperature that accompany glacial fluctuations. Some possible inferences are discussed based on speculations concerning the variations of the net radiative flux at the top of the atmosphere.

If we assume that "radiative equilibrium" always prevails we are led to conclude that the mean ocean temperature must reach its maximum value at very nearly the same time that the ice volume reaches a maximum, mainly due to the release of latent heat of fusion during the ice formation. However, if we assume that the atmospheric climate tends to achieve a quasistatic equilibrium with the lower boundary ice coverage and ocean surface temperature, at least when the ice volume is near its maximum or minimum, it follows that there can be a net radiative flux at the top of the atmosphere equal in both magnitude and direction to the net flux of heat across the ocean surface. In fact, from the results of a statistical-dynamical model of climate based on prescribing this atmospheric equilibrium (Saltzman and Vernekar, 1971, 1975) we find that there should be a net downward flux of radiation (and, hence, of heat into the oceans) during a glacial maximum and a net upward flux during present, quasi-interglacial, conditions. If this finding is valid it follows that the mean ocean temperature should increase during the period of maximum ice formation and ice extent and reach its maximum after the maximum ice volume is achieved, a result that is in substantial accord with the ice-age scenario recently proposed by Newell (1974).

Since it is generally agreed that the surface water temperatures were in fact colder during the ice age than at present (CLIMAP, 1976), we infer that these mass-averaged ocean temperature changes must reflect conditions of the deeper water masses with attendant changes in the strength and form of the main thermocline. A mechanistic, dynamical, theory that can account for the implied oscillation between ocean temperature and ice formation remains to be developed.

INTERACTION OF A UNIFORM WIND STRESS WITH INERTIA-GRAVITY WAVES

Melvin E. Stern

An inertia-gravity wave which propagates upwind and upwards in the thermocline has a reflection coefficient r which is greater than unity ("over-reflection") as a result of the wave current interaction in the mixed layer which overlies the thermocline. The second order amplitude effect of the wave is to produce a mixed layer transport having the same direction as the wind stress $\underline{\tau}$, whereas the undisturbed (Ekman) transport is perpendicular to $\underline{\tau}$. The amplification factor $|r|-1$ is proportional to $|\underline{\tau}|$, and increases as the frequency of the incident wave approaches the coriolis parameter f . A preferred lateral scale is also given, and it is suggested that the spectral peak near f in the ocean is maintained by successive amplification of wave packets entering the mixed layer. We also show that the turbulent Ekman flow at the upper boundary of a two-layer density model, such as can be realized in the laboratory, should become unstable with respect to long (hydrostatic) interfacial waves.

WORLD OCEAN CIRCULATION

George Veronis

Models of world ocean circulation for a two-layer ocean driven by wind stresses, by thermal forcing and by a combination of the two has been developed. The wind-driven model focuses on the dynamical balances responsible for the separation of western boundary currents (Gulf Stream, Kuroshio, etc.) from the coast at temperate latitudes and on the role played by poleward eastern boundary currents (Norwegian, Alaskan, etc.) on the separation mechanism. For these analyses the transports and thermocline depths are calculated once the thermocline depth is given near the eastern boundary. For the second model the thermal driving is parameterized by an upwelling whereby lower-layer water is transformed to upper-layer water. Various possibilities are explored. The behavior of the system for different prescribed sinks of upper-layer water in the polar region is outlined. The third model involves a relatively complex analysis for the interior dynamics even though the basic balance is quasi-geostrophic. Transports are again derived and the distribution of the upper- and lower-layer water can be calculated. The significant results of the analysis are based on specifying the separation latitudes (since the mechanism for separation is understood from the analysis of the wind-driven part). The magnitude of the upwelling velocity, deduced to be 1.5×10^{-5} cm $\sec^{-1}$, agrees with the value derived from totally different physical considerations. The distribution of the sinking regions in the polar regions are also deduced and they yield effective heat sinks which are the same magnitudes as those estimated from observations and empirical formulae.

THERMAL OSCILLATIONS IN A FLUID HEATED FROM BELOW AND COOLED TO FREEZING FROM ABOVE

Pierre Welander

A theoretical discussion is given of the thermal transients and self-sustained oscillations in a fluid, heated at a constant rate below the surface, and cooled from the top strongly enough to allow freezing. Assuming that the fluid is well-mixed and that the thickness of the ice is small compared to the fluid depth, it is shown that the system can have none, one, or two steady states. The ice-covered steady state is stable for small perturbations, however, the ice-free steady state may be unstable, adding a thin ice sheet. Transient developments may include both ice-covered and ice-free states. In the case where no steady state exists the system exhibits periodic self-sustained oscillations. An application to the Arctic Ocean is being considered.

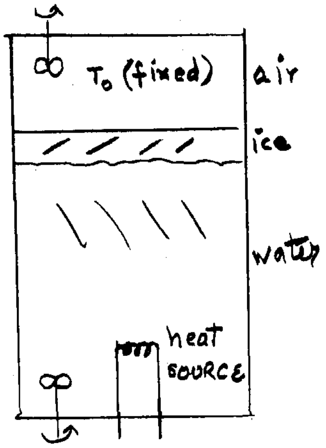

Fig.1 Experimental apparatus.

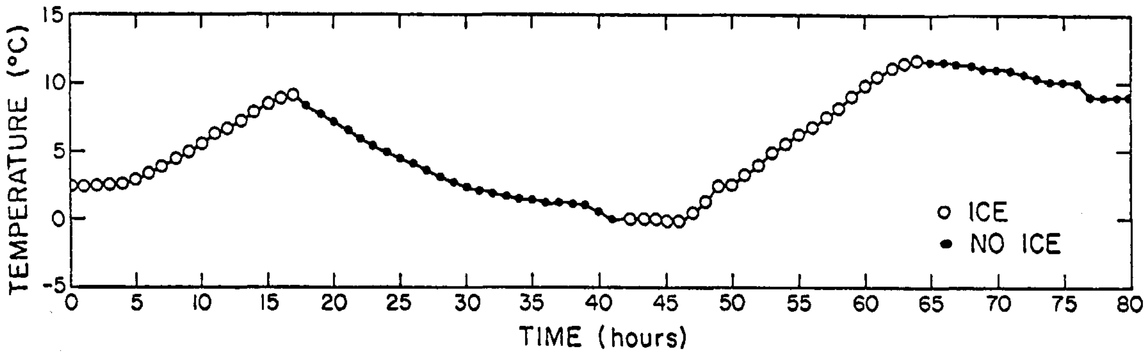

Fig.2 Temperature measured in the middle of the water tank.

CIRCULATION INDUCED BY EDDIES AND WAVES

Peter B. Rhines

A review of Taylor's formulation of turbulent diffusion (single particle statistics) was followed by a description of the Lagrangian ensemble-mean flow, and dispersion about the mean, in geostrophic turbulence. An expression for the difference between Lagrangian and Eulerian (time-) mean flow was suggested, for turbulence or waves, to be $\bar{u}_i = \partial K^{ij}/\partial x_j$, where K^{ij} is Taylor's expression for the diffusivity, $K^{ij} = \int_0^t u_j(t\,x_0)\,u_i(t+\tau\,x_0)\,d\tau$.

The inescapable result of Kelvin's theorem is that eddy- or wave-motion induces mean Eulerian circulation. In various cases of interest the 'mean' refers to zonal-, time- or ensemble averaging. For zonal averaging an inviscid flow (with slowly varying spatial statistics) yields an exact expression for the change in the Eulerian circulation since t = 0: $[\bar{u}_e] = -\frac{1}{2}\beta\,\overline{\eta^2}$, where η is the y-displacement of fluid particles since t = 0 and β is the gradient of mean potential vorticity. This westward flow holds for latitudes free of forcing. If, in Whitehead's (Tellus 27, 1975) laboratory experiment, the motion is driven by a plunger, jet-like eastward flow will occur at forced latitudes to conserve total angular momentum. This problem has interesting structure: when bottom friction (coefficient D) is added, $\bar{u}_e$ becomes exactly twice the inviscid value, for motion with long coherence-memory and bounded displacements. For short memory (relative to the spin-up time), $\bar{u}_e$ equals the inviscid value. But if the flow is turbulent rather than wavelike (in the sense that η^2 increases without bound), $\bar{u}_\ell = -\beta K_{yy}/D$ instead. The Lagrangian mean flow here is close to $\bar{u}_\ell$, if the waves or turbulence are slowly varying in space (relative to the eddy size). But, it is amusing that the Kelvin circulation $\oint \underline{u}\cdot d\underline{s}$ about a marked fluid contour initially lying on a latitude circle, is opposite (eastward), of equal magnitude to $\bar{u}_\ell$. A local (in space) formulation shows how turbulence drives Sverdrup flow, with an effective wind-stress curl of $\partial/\partial x_i\,(K_{ik}\,\partial Q/\partial x_k)$ where Q is the mean potential vorticity.

The relationship to earlier work of Taylor, Dickinson, Welander, Green and Stern was described. Numerical experiments showed the growth of zonal jet-like flows dur to forcing or to energy release by baroclinic instability. Gareth Williams has recently invoked similar models to explain Jupiter's bands.

ON TRAJECTORIES OF ROSSBY WAVE-PACKETS RELEASED IN A LATERAL SHEAR FLOW

Toshio Yamagata

In geophysical fluid systems, it is of interest to understand the behavior of Rossby waves in a lateral shear flow. Several works in meteorology studied the influences of the lateral wind shear on large-scale wave propagation into the Tropics (Mak, 1969; Charney, 1969). The basic physical mechanisms that underlie these works are Rossby wave reflexion and absorption by the zonal shear flow. Bennett and Young (1971) and Dickinson (1970) discussed the development of a Rossby wave critical "level" after the switch-on of a steady forcing in this context. In the oceans, it is well-known that Rossby waves generated by the large-scale wind systems play a dominant role in establishing the global ocean circulation. When we discuss the variabilities of the ocean circulation, it will be necessary to study the interaction between Rossby waves and currents. Here, with a ray-tracing method, I consider the problem of reflexion and critical "level" absorption of barotropic non-divergent Rossby waves in a barotropic ocean of constant depth, where the mean current flows in the east-west direction or in the north-south direction, with a ray tracing method.

References

Bennett, J.R. and J.A.Young 1971 Mon.Wea.Rev. 99: 202-214.

Charney, J.G. 1969 J.Atmos.Sci. 26: 182-185.

Dickinson, R.E. 1970 J.Atmos.Sci. 27: 627-633.

Mak, M.E. 1969 J.Atmos.Sci. 26: 41-64.

Yamagata, T. 1976 J.Oceanogr.Soc. Japan 32: 164-170.

THE PLANETARY AND BENTHIC BOUNDARY LAYER SYMPOSIUM

Abstracts of Seminars

THE BOTTOM BOUNDARY LAYER OF THE DEEP OCEAN

Laurence Armi and Robert C. Millard, Jr.

Some aspects of the bottom boundary layer of the deep ocean are exhibited in profiles of salinity and temperature made with a Woods Hole Oceanographic Institution/Brown CTD microprofiler. Profiles from the center of the Hattaras Abyssal Plain have a signature that is characteristic of mixing up a uniformly stratified region. Over rough or sloping topography, to the East and West of the abyssal plain, the profiles have more complicated structure. All profiles show a well-mixed layer above the bottom; the penetration height of the layer varies from about 10 m to 100 m and is correlated with the one-day mean velocity, inferred from current meters located above the bottom boundary layer. Over the Hatteras Abyssal Plain the mixed layer extends above the bottom about six times the turbulent Ekman layer height. Over rough and sloping topography the penetration height is between the Ekman layer height and the height observed on the flat abyssal plain.

A model of entrainment and mixing for a flat bottom boundary layer is outlined. This model is incomplete because we find too little known of the structure of turbulence above an Ekman layer. An alternate model is suggested by the estimate, from the correlation of penetration height with velocity, of the internal Froude number of the mixed layer, $F \approx 1.7$. This value indicates that the large penetration height may be due to the instability of the well-mixed layer to the formation of roll waves.

RADON AND RADIUM AS GEOCHEMICAL TRACERS OF ABYSSAL MIXING PROCESSES

Pierre E. Biscaye and Jorge L. Sarmiento

The noble gas radon-222 is a chemically inert naturally occurring radioisotope with a four day half life. It is suitable for the study of mixing in the bottom few hundred meters of the water column. Its ultimate radioactive grandparents, uranium-238, -234 are very long lived, soluble and therefore well-mixed in the world oceans. Its less-distant grandparent, thorium-230, is rapidly removed from sea water and decays in the sediments to radium-226, the immediate parent of radon-222. Because thorium-230 and radium-226 are more abundant in the sediments than in the overlying sea water, there is a strong concentration gradient of radon-222 across the sediment-water interface. It is the diffusion of this "excess" radon from the sediment and its distribution in the overlying water column which provides the tracer for mixing near the ocean floor. In the two-three weeks that it takes this radon to decay away to undetectable quantities, it generally is mixed up to heights of 50 to 350 meters above the sediment-water interface although heights of up to 1000 meters are occasionally observed in high energy environments such as deep ocean passages. A similar concentration gradient for radium-228, an isotope in another naturally-occurring radioactive decay series, permits its use as another tracer of benthic mixing processes. Its half life of six years, however, permits its diffusion up to heights over 1.5 km above the sediments and it thus records mixing processes of much longer time scales.

Measurements of excess radon in the waters of the continental shelf and the upper continental slope in the New York Bight indicate, at this point qualitatively, several problems in, as well as potential uses of, the excess radon method. First is the spatially heterogeneous source function of excess radon from the sediments; the potential excess radon productivity of sediments in the New York Bight varies by over an order of magnitude over distances of tens of kilometers. This poses problems in the assumption of no horizontal concentration gradients in one-dimensional vertical mixing models, but opens the possibility of measuring horizontal transports from radon emanating from local point or line sources. This horizontal heterogeneity is not likely to be as marked in the deep sea where most work on radon has been done (see below). An additional feature that has persisted in New York Bight observations over almost two years is the presence of a zone of zero-to-low excess radon immediately above the sediments over a water depth range of from about 500 to 2000 m on the upper continental slope. The zone is coincident with a minimum in suspended particle concentrations and the two distributions suggest active mixing along isopycnal surfaces between interior ocean water and water in contact with the upper continental slope.

A time series study of excess radon, suspended particulates, current velocity and STD measurements was made in two adjacent but dynamically different bottom mixing regimes in the North American Basin. In most cases on the Blake Bahama Outer Ridge under the Western Boundary Undercurrent, a relatively thick (300-400 m) bottom mixed layer was characterized by a well-mixed temperature profile, high concentrations of suspended particles and statistically homogeneous concentrations of excess radon. The time-averaged vertical eddy diffusivities calculated from a one-dimensional exponential model at two sites ranged from ~ 300 to ~ 700 cm^2/sec. By contrast, most casts at a single location on the Hatteras Abyssal Plain revealed a thinner ($\sim$50-80 m) bottom mixed layer characterized by a well-mixed temperature profile, lower but less variable concentrations of suspended particles, and a more regular decrease of excess radon concentrations above the bottom. A time averaged model vertical eddy diffusivity was 12 cm^2/sec. Thus, for the two regimes the indications of vertical mixing given by excess radon distributions accorded well with indications of dynamic interaction of the water with the sediments.

The excess radon data from the GEOSECS Atlantic and Pacific cruises provide the first opportunity to study the behavior of this tracer over a wide range of bottom mixing regimes in the context of high quality measurements of temperature, salinity and other water-mass characteristics. Profiles with bottom mixed layers were observed at over two-thirds of the stations where sufficient data was obtained to study them. They range in thickness from 15 to 160 meters with a higher average thickness in the Pacific. Excess radon, potential temperature and salinity are well mixed within the layers. They are capped by a "thermocline" layer characterized by a greatly reduced mixing rate that usually prevents measurable penetration of excess radon. About 45% of the profiles appear to show cooling of the boundary layer which suggests that in many cases these layers are advective features that move independently of the overlying water mass. The remaining layers could have been formed by mixing up a uniformly stratified region of the water column.

At 14 widely-scattered locations we were able to calculate model vertical eddy diffusivities from radon-222 profiles. These diffusivities and those obtained from the longer-lived radium-228 (half life six years) show an inverse relationship to buoyancy gradients calculated from the STO data. This means that the buoyancy flux and, thus, the turbulent energy dissipation into buoyancy are relatively constant with depth and from one location to another. The buoyancy flux has a mean of 4×10^{-6} cm^2/sec^3. Heat fluxes calculated with the diffusivities average 33 μcal/cm^2/sec in the Atlantic and 9 μcal/cm^2/sec in the Pacific.

THE DYNAMICS OF SHEARED THERMOCLINES

Giles M. Corcos

It is shown that the dynamics of a fully turbulent free shear layer in stratified or homogeneous fluid exhibits a surprising degree of coherence and two-dimensionality. The presence of smaller scale three-dimensional and random motion does not seem to influence the evolution of these coherent structures. A detailed discussion of the two-dimensional dynamics of these motions divides the evolution into a preliminary period during which the instability develops on a single length scale and a second period during which the layer grows by the systematic increase of the length as well as the amplitude of the typical waves. The instability is interpreted as a systematic increase in the concentration of vorticity into ever larger and ever more distant centers. For stratified flows the process is arrested by the competing baroclinic generation of vorticity in other regions. Models of the process predict the maximum scale and amplitude of the larger waves which can develop in a given thermocline. From this prediction the final thickness of the layer is deduced. It agrees with experimental observations. The study of fully-deterministic nonlinear unstability sheds some light on the phenomenon of turbulent entrainment and explains why it is insensitive to the value of the Reynolds number. While entrainment is not a result of large scale dynamics, mixing is not, and most likely requires three-dimensional motion.

Some new evidence is presented about the origin of three-dimensionality.

TURBULENT INTERFACE LAYERS

Gabriel T. Csanady

Turbulent flow on either side of a density interface is similar to wall-layer flow, and exhibits, in particular, a logarithmic or "buffer" layer. The two parameters defining the logarithmic velocity profile, Karman's constant and roughness length, could theoretically be different. Experimental evidence on air-water and salt-freshwater interfaces shows Karman's constant to be the same as over a solid plate. However, the roughness length varies in a complex way with flow parameters. The factors which determine roughness length are not well explored, although there are indications that this parameter depends on the energy balance of a viscous or wavy sublayer very close to the interface. There is also a possibility that surface tension variations influence the roughness of the air-side of the air-water interface by extracting energy from the sublayer. In a certain range of parameter space the roughness length r of a salt-freshwater interface depends only on a characteristic relation velocity u, viscosity ν and effective gravity $g\varepsilon$. Similarity of interfacial momentum transfer implies a constant ratio of viscous to gravity forces, which results in the formula for the roughness length:

$$r = \text{const.}\sqrt{\frac{u\nu}{g\varepsilon}}.$$

At the interface a maximum of the velocity gradient occurs, which is often substantially (by a factor of 2 - 8) less than stress divided by molecular viscosity, implying an effective viscosity several times the molecular value. This is not "eddy" viscosity, however, because turbulent eddies at the interface are suppressed by stability.

NEAR-BOTTOM CURRENTS AND THE GENESIS OF SEA-FLOOR WAVES AND FURROWS

Roger D. Flood

Deep-ocean currents play an important role in the erosion, transportation and deposition of the fine-grained, cohesive sediments found in the deep sea. These deep currents are closely related to the formation of dense water types in the polar regions. Deep currents have been important since drifting continents opened the ocean basins to the polar waters about 40 million years ago. The currents transport and deposit sediment derived from nearby sources to form a series of large sediment drifts, each is usually several hundred meters thick and extends over an area of more than $10^4 km^2$. As the drifts have been built up, several types of bed forms have been developed by the currents on the surface of the sediment drifts. These bed forms are suggestive of the structure of the water flow. Two bed forms have been studied in some detail on the Blake-Bahama Outer Ridge, a fine-grained sediment drift complex off the Eastern United States (water depth 3000-5000 m). Furrows (almost rectilinear grooves 1's-10's m deep, 1's-100's m wide, spaced 10's-100's m apart and oriented with the long axis parallel to the mean current flow) are related to secondary circulations developed within the well-mixed benthic boundary layer. Large mud waves (2 km wavelength, 50 m amplitude, 45° to the mean current flow) may result from the interaction of the sediment surface and the lower part of the water column. These bed forms appear to be widespread in the deep sea where deep currents are important.

TIME-DEPENDENT DEVELOPMENT OF FLOW OVER BOTTOM TOPOGRAPHY

Herbert E. Huppert

The interaction between temporarily varying currents and variable bottom topography was investigated by the numerical, analytical and experimental examination of the following simple model. The flow of an inviscid, stratified fluid is initiated from relative rest in a uniformly rotating system containing an isolated topographic feature. The evolution of the flow distributes vorticity and temperature in such a way that relatively cold (heavy) fluid with anticyclonic vorticity exists over the topographic feature, while fluid originating from above the topographic feature sinks, thereby inducing a warm (light) anomaly with cyclonic vorticity. For sufficiently strong oncoming flows, the shed fluid continually drifts downstream in the form of a relatively warm eddy. If the oncoming flow is relatively weak, the interaction between the anticyclonic and cyclonic vorticity distribution traps the warm eddy and it remains in the vicinity of the topographic feature.

The above mechanism may explain: some recent observations of an eddy in the vicinity of the Atlantis II Seamount; some observations of a warm patch near Brontosaurus Bump seen in the second leg of the 1975 IOS Topographic Experiment; and the occurrence of cyclogenesis downstream of the large mountain chains of the Earth.

The talk combined aspects of work carried out with the help of K. Bryan, A. McEwaneg, R. Hendry and the many scientists who contributed to the IOS Topographic Experiment.

KOLMOGOROV IN THE BOUNDARY LAYER

Willem V.R. Malkus

It has often been noted (e.g. Kraichnan 1974) that Kolmogorov's 1941 theory for the energy level in the interial sub-range has achieved "an embarassment of success". For example, it appears to apply quite well to the steady state turbulent boundary layer. Another excessively successful result comes from requirement that the mean velocity in a shearing flow vary logarithmically in an overlap region of the "law of the wall" and the "velocity-defect law" of the interior flow. An extensive logarithmic region is observed, yet there is no logical or dynamic reason for any overlap of the two "laws". It is proposed here that both these results can be explained as properties of the explosive subcritical instabilities whose growth in scale and whose momentum-transfer properties recently have attracted much experimental and theoretical attention (e.g. Landahl (1972)). Here the view is offered that the expanding roll-hairpin instability is the flow element which produces the 5/3 range in the energy spectrum, and that this is due to the average unilateral spectral flow of energy even in ranges where the overall flux approaches zero. In this view the universal Kolmogorov constant is the square of the transition range Reynolds number and, in the shear flow case, proportional to the boundary Reynolds number. When, in addition, it is required that the flow resulting from these explosive instabilities be both stable in the mean and represented by a "smooth" spatial spectrum, one finds a complete velocity-defect law. This result requires both an extensive logarithmic region and (for Poiseuille flow) a parabolic interior independent of a wall law. Addition of a smooth wall condition on the above requires that the von-Kármán constant be proportional to the amplitude of the explosive boundary instabilities, and in turn to the boundary Reynolds number.

TESTS OF NUMERICAL MODELS OF THE SEASONAL THERMOCLINE

Pearn P. Niiler

Over large areas of the oceans, heat is stored in summer locally in the surface layers and removed again in winter. The vertical temperature distribution and the sea-surface temperature are dependent upon how this thermal energy is distributed vertically by turbulent exchange processes. Conservation equations for local storage of momentum, heat and turbulent energy are used to construct a model of the vertical exchange processes in the water column. Active turbulence fills the mixed layer and a weakly diffusive column exists below the mixed layer. The source for the turbulence is from energy sources in the atmosphere on the ocean surface and within the mixed layer turbulent energy is created by a shear of the mean flow. A fractional amount of each energy flux from each source is made available for entrainment of dense fluid into the mixed layer. The parameters of this factional exchange are selected both from best least square fits to the evolving density profile in entrainment experiments in the laboratory and ocean observatories of intense, rapid deepening events under strong mid-ocean storms. The parameters which govern the seasonal (or long-term behavior) of the seasonal thermocline are selected by best fit to data at ocean station Papa. With identical coefficients the seasonal thermocline near Ocean Station November (subarctic Pacific). The best fit to the profile is with variance of $(0.27^{\circ}\mathrm{C})^2$ within 8°C seasonal temperature cycle (subtropical Pacific), is predicted to within a variance of $(0.31^{\circ}\mathrm{C})^2$, within a seasonal surface amplitude of 3.5°C. The most glaring weakness of the model is that the seasonal ocean surface temperature cycle is most sensitive to the nature of turbulent diffusion below the mixed layer and dissipation of energy during deep convection in winter. There are mechanisms about which there is a dearth of observation in the oceans, and which must be understood before a study of longer time scale (climatic) response of the upper layer can be carried out.

ONE-POINT AND TWO-POINT STATISTICS IN THE ATMOSPHERIC SURFACE LAYER

Hans A. Panofsky

Effects of mechanical turbulence and heat convection have been successfully combined in the atmospheric surface layer by Monin-Obukhov scaling. In this hypothesis there are universal relationahips among quantities scaled by length

$$\frac{u_*^3 C_p \rho T}{k g H v}$$

and velocity u_*, the surface friction velocity. This scheme satisfactorily accounts for statistics of vertical velocity fluctuations and other statistics involving vertical velocities, including variances, spectra and cospectra.

The theory does not hold for statistics of horizontal fluctuations; for these, the thickness of the boundary layer z_i seems to be important, as it affects eddy size. Thus, over flat sites, the standard deviations of horizontal velocity components obey relations of the form

$$\frac{\sigma_u}{u_*} = \varphi\left(\frac{z_i}{L}\right)$$

independent of height z, which affects vertical, but not horizontal eddy size. ψ appears to be universal, at least over flat terrain.

Models for two-point statistics are made most easily for coherence and phase delay. For coherence, Davenport's hypothesis supplies an empirical fit

$$Coh(n, \Delta x_i) = e^{-a n \Delta x_i / V}$$

where n is frequency and V the mean speed in the layer Δx_i. Δx_i is a separation in the horizontal or vertical, a is the decay parameter which is generally small in unstable air and over smooth terrain (e.g., water) and increases with angle between anemometer line and wind. "a" also increases with separation in stable air. Simple theories exist to account for all these effects.

Horizontal phase delay is well described by Taylor's hypothesis for small $\frac{\partial u}{\partial z}/n$; for small n, eddies travel faster than the wind.

There is also a small phase delay in the vertical depending on the vertical wind shear.

TRANSPORT PROCESSES IN SLOPING SIDE WALL BOUNDARY LAYERS

Claes Rooth

The most profound influences of bottom and side wall boundary layers on stratified fluid motion occur when these layers (B.L.) act as sources or sinks for fluid, relative to the interior domain.

It is easily shown that a constant diffusivity ($\mathcal{K}$) for heat (density) leads to boundary layer flows along sloping insulating walls. The fluid volume transport induced is $\mathcal{K} s^{-1}$ parallel to the wall, where side wall suction will thus occur wherever the walls are curved. (s is the side wall slope.)

The main concern in this lecture is with the case where interior diffusion of heat is negligible, while heating or turbulent mixing occurs in the boundary layers.

An especially simple class of phenomena where this happens is found in the response of enclosed basins to geothermal heating. The critical parameter of the problem is the amount of peripheral heat input, $\frac{\partial Q}{\partial z}$, per unit height increment, divided by the horizontal area, enclosed by the corresponding depth contour $(A(z))$. Boundary layer suction due to the inclined flow leads to convergent or divergent interior vertical velocity which depends only on the B.L. forcing, and *not* on the interior stratification. Asymptotically, neutrally stratified layers alternating with stably stratified ones will develop, according to the sign of $\frac{\partial}{\partial z} A^{-1} \frac{\partial Q}{\partial z}$.

If turbulent mixing of heat is limited to the B.L., a similar situation occurs, only now there is no volume transport along a flat side wall - only a heat flux determined by an appropriate Richardson or Monin-Obukhov scaling. We have now a situation where gradients in slope normalized turbulent intensity lead to a secondary B.L. of the same type as in the geothermal heating case. The main difference is that cooling as well as heating occurs in this secondary B.L. The induced vertical velocities of the interior domain are controlled entirely by the B.L. heat flux in such a sense that vertical advection redistributes the latter over an appropriate adjustment area.

BOUNDARY LAYER AND LARGE SCALE DYNAMICS

Edward S. Sarachik

We can get some idea of the interchanges across the air-sea interface by looking at the net heat budgets of the earth-atmosphere system, the atmosphere separately, and the ocean separately. The oceanic heat flux (temporally and zonally averaged) is poleward and peaks in the subtropics, indicating net heating at the interface (by radiation, latent and sensible heating) equatorwards of the peak, and net cooling polewards of the peak, the net flux not exceeding 100 langley/day. Using these surface fluxes, the Monin-Obukhov lengths are calculated for ocean and atmosphere leading to the conclusion that the tropical ocean boundary layer is convectively driven, with moisture playing the dominant role.

It is pointed out that cumulus convection is a type of convection not generally encountered in other branches of Geophysical Fluid Dynamics, "σ convection", in which the upward motion covers a fractional area σ small compared to unity, allows a downward vertical velocity (almost everywhere) even when the large scale vertical velocity is upward. This permits a new mode of equilibration of boundary layer growth which is actually realized in the tropical atmosphere.

The role of water vapor in convectively driving the tropical atmosphere is described. A model tropical atmosphere is described which is layered according to the three possible roles of water vapor:

1. The subcloud layer is driven by buoyancy produced by the light weight of water vapor and is held down by subsidence compensating deep and shallow clouds.

2. The shallow cloud layer is driven by the buoyancy produced by condensation in the shallow clouds and is held down by the subsidence compensating the deep clouds.

3. The deep (cumulonimbus) cloud layer which extends to the tropopause in which the net heating produced by the cumulonimbus is balanced by the radiative cooling. The temperature and moisture structure of such an atmosphere is completely determined once the evaporation is specified, and closely resembles the actual tropical atmosphere.

ON THE IMPORTANCE OF DENSITY STRATIFICATION TO THE BOTTOM BOUNDARY LAYER ON THE WEST FLORIDA CONTINENTAL SHELF

George Weatherly

Observations in the bottom boundary layer (BBL) of the West Florida Continental Shelf obtained over a five-day period in July, 1975, at 100 m depth at latitude 26°N reveal considerable veering in the current direction ($\sim 50^{\circ}$ counterclockwise looking down) near the bottom ($z \lesssim$ 5-10 m) as the bottom is approached and localized heating or cooling in the BBL depending on the direction and speed of the current. It is argued that the observed direction veerings are consistent in sense, magnitude, and region of occurrence (very near the bottom) with the Ekman veering occurring in a stably stratified planetary boundary layer. Data is presented to show that the water column is stably stratified with the greatest stratification occurring in the BBL. The localized heating or cooling observed in the BBL is argued to be due to either downwelling or upwelling induced by Ekman transport down or up-slope in the BBL. Because of a change in bottom slope at the site of the experiment, it is also argued that the cooling rate in the BBL associated with a northward current should be about 10 times larger than the heating rate associated with a southward current of the same strength. Agreement with observations is good.

AN ACOUSTIC SENSOR OF VELOCITY FOR BENTHIC BOUNDARY LAYER STUDIES

Albert J. Williams, 3rd and John S. Tochko

The techniques of flow measurement which have been successful in laboratory studies of boundary layer turbulence are difficult to use in the ocean; and the current meters generally used in the ocean are not suited to measuring bottom boundary layer flow. A suitable sensor for bottom turbulence measurements should measure vector components, respond linearly to these components, maintain an accurate zero point, disturb the flow negligibly or in a well-predicted way, and sense a small enough volume to represent the important scales of the flow. We have constructed an acoustic travel time sensor in a configuration that will allow vector components of the flow to be measured with sufficient accuracy to compute Reynolds stress at a point 50 cm above the bottom. This sensor responds linearly to horizontal and vertical flows in flume tests. When the flow is neither horizontal nor vertical, the wake from one acoustic transducer may interfere with the measurement along one sensing path but there is sufficient redundancy in the determination to reject this path and still resolve the vector velocity. An instrument using four of these sensors is being designed to measure Reynolds stress in the lower six meters of the ocean.

THE BENTHIC BOUNDARY LAYER AND ITS INTERACTION WITH THE BOTTOM SEDIMENT

Mark Wimbush

A decade ago, interest in the abyssal-benthic boundary layer was generated by reported measurements of surprisingly thick, strongly unstable thermal gradients over the deep-sea floor. Much recent interest is focused on measurements of surprisingly thick bottom mixed layers!

Temperature and salinity measurements in the lowest three meters of the deep ocean off Southern California gave results consistent with theoretical expectations. 'Typical' magnitudes of various scales were compared with sublittoral and atmospheric boundary layer values:

	Deep sea	Continental shelf	Atmosphere
Friction velocity u_*	1 mm/s	1 cm/s	1 m/s
Ekman layer thickness $\chi \frac{u_*}{f}$	10 m	(100 m)	1000 m
Logarithmic layer thickness	1 m	10 m	100 m
Viscous sub-layer thickness $\frac{10\nu}{u_*}$	1 cm	(1 mm)	(1 cm)
Buoyancy scale $L_{M-O} = \frac{-c_p \rho u_*^3}{\chi g \alpha H}$	(-100 m*)	($\lvert L_{M-O} \rvert > 1000$ m)	$\lvert L_{M-O} \rvert > 10$ m
Diffusion scale $\left(\frac{\nu^3}{\epsilon}\right)^{1/4}$ in upper log layer	1 cm	1 mm	1 mm

(values in parentheses are probably meaningless because other scales dominate)

χ = Von Kármán's constant.

Action of the flow on the sediment may result in: I) bed-load transport, II) suspended load transport, III) formation of sediment ripples. These, in turn, react on the flow resulting in: i) $u(0) > 0$ (so z_0 is greatly increased, and energy is extracted from the flow by grain-grain rubbing), ii) energy extracted from flow to maintain suspension, iii) friction drag increased and form drag introduced (so z_0 is again increased). These interactions do not occur, unless critical shear stresses are exceeded. To study these interactions a series of experiments is being conducted, combining water velocity and temperature recordings with time-lapse stereophytography of the sea bed.

---

[*] assuming H is the upward geothermal heat flux; however H may depend more on the past thermal history of the water.

TURBULENCE CONSTITUTIVE EQUATION AND BOUNDARY-LAYER MODELING

John C. Wyngaard

Approximate forms of the balance equations for Reynolds stress, heat flux, and other second moments are useful both for numerical models as well as aids in interpreting surface-layer data. As an example of the latter, we show that measurements of the scintillations of a laser beam over a horizontal path in the surface layer can be used to infer the vertical heat flux. The link between the scintillations and the heat flux is the behavior of the budgets of turbulence energy and temperature variance, both now very well-understood in the surface layer.

While these balance equations, or budgets, are less well-understood over the boundary layer as a whole, there are simple engineering closure models of the budgets which can be used to study the properties of idealized cases. In this way the broad features of a neutral Ekman layer with and without a capping inversion, a convective layer, and a stably stratified layer have been predicted to be quite distinct. The neutral Ekman layer adopts as height scale u_*/f, while the inversion-capped case is forced to scale with z_i, the inversion base height. Thus $u_*/f z_i$ is a key parameter in the latter, and it is shown that as it gets large the flow adopts a two-layer structure: channel flow below, and a shift (through as much as 90° in direction) to geostrophic flow above.

The convective layer also has z_i as the vertical height scale while the stably stratified layer is predicted to scale with the half power of the product of u_*/f and L (the Monin-Obukhov length).

Real atmospheric (and benthic) boundary layers inevitably are horizontally inhomogeneous. The simplest such case - flow over a *locally* inhomogeneous surface - is discussed. It is shown that if the mean state in the Reynolds decomposition is defined through an *area* average, then the resulting mean momentum equations look just like those for the idealized, horizontally homogeneous case. In the latter case, however, the mean is defined through an *ensemble* average, and thus the Reynolds stress in this case different. There is a contribution due to the local inhomogeneity, and it is suggested that this can be understood through solution of the model equations in the usual (ensemble average) framework.

It is shown that if the locally-inhomogeneous problem is approached via a perturbation expansion, the linearized disturbance equation is much more general, but no more difficult to solve numerically, than the Orr-Sommerfeld equation. The new terms, due to the use of a constitutive equation rather than an eddy viscosity, are interpreted as representing the effect of the disturbance on the effective viscosity.

FELLOWSHIP LECTURES

ON DYNAMIC FEEDBACK EFFECTS IN AXIALLY ASYMMETRIC ATMOSPHERIC MODELS

Steven M. Ashe

I. INTRODUCTION

This research concerns the theory of the time-average motions of the atmosphere in midlatitudes at heights beneath the tropopause. Although the basic structure of the earth's atmosphere is zonal, the presence of continents and oceans introduces asymmetries which not only have a probound effect on the zonal circulation, but have many features interesting in their own right.

As an illustration of the phenomena that make up the time-average asymmetric circulation, consider the instantaneous field of pressure at some middle-troposphere height. Such a distribution is illustrated diagramatically in Fig.1. The pressure field is basically zonal, with wave numbers five ∼ six having the maximum amplitude. When a sequence of these highly transient snapshot views is averaged over several synoptic periods (e.g. a month), the high-frequency components are filtered out, and a pattern of small amplitude wavelike structure of low zonal wave number persists.

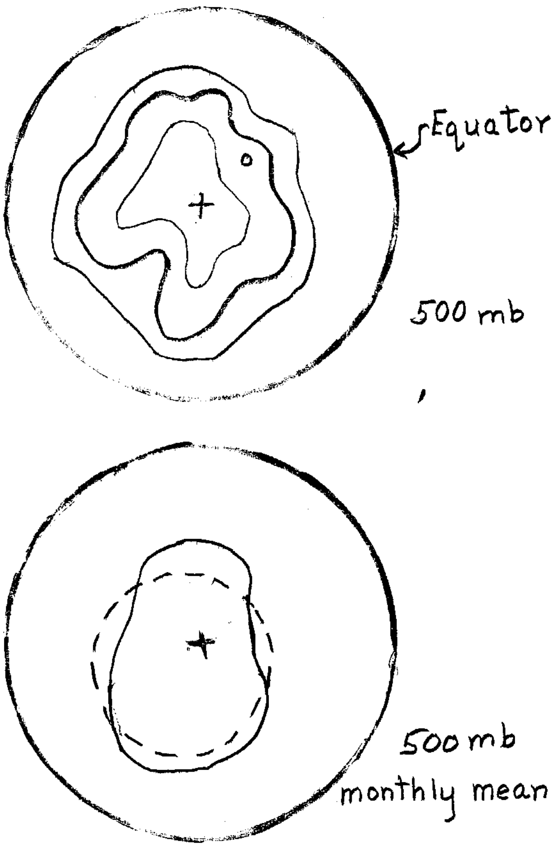

Fig. 1.

This persistent pattern is very strongly a function of season (due in part to the seasonal change in the thermodynamic properties of land and ocean) and is sometimes called the "global monsoon". The pattern from year to year, however, is noticeably uniform.

Since this asymmetric distribution in the pressure field (and likewise temperature, wind, etc.) looks like a small perturbation on a large zonal flow, the dynamics are amenable to linearized analysis, and consequently this was one of the first problems tackled with the advent of quasigeostrophic theory.

As a meteorological problem, the theory of the asymmetric motions has not been as simple as the above comment would indicate. It is, in fact, one where there are a multitude of physical effects all contributing to the total picture, with most dependent not only on each other, but on the asymmetric variables themselves.

Schematically, $\frac{d}{dt}(p, T, v, \dots) = f(q)$

where p, T, and v are the asymmetric pressure, temperature and velocity fields, and q represents the asymmetric component of diabatic heating which includes all those processes filtered out or averaged over (i.e. whose physics do not appear explicitly in the equations of motion). The problem is complicated by the fact that q is not independent of p,T,v ..., but entails certain processes which are very dependent on them. Some of these will now be investigated.

The equations of motion, when time-averaged and scaled using the zonal flow, indicate three formal mechanisms associated with the asymmetric perturbations:

1) asymmetries in the stochastic properties of the instantaneous fields (convergencies of spatial and temporal Reynold's Stresses),
2) the zonal distribution of heat sources and sinks within the atmosphere and at its bottom boundary, and
3) the interaction between the flow field and orography.

The above are the formal manifestations of a number of physical mechanisms, among which one might isolate the following:

1) deflection of the flow (predominantly the zonal wind) by orography introducing a vertical velocity at the surface, and the finite-amplitude effects of topography blocking the flow, (and depending on the static stability) forcing it around mountains;
2) latent heat release, which includes that associated with rising motion due to topography, that associated with free turbulent convection, and that associated with stratoform clouds in storm systems;
3) sensible heat flux, mainly in the form of convection over continents in summer and rectification by western oceanic boundary currents of synoptic-frequency temperature oscillations in winter;
4) radiational asymmetries, which are probably small.

The above processes are easily seen to depend on the motion and temperature fields themselves, and so their physics must somehow be included in order to close the problem.

The classical theoretical approach involves writing some appropriate system of equations for the asymmetric motion fields, and to then prescribe the basic zonal state, the diabatic heating fields and the eddy convergences, using observations (often indirect) of these quantities in order to see what flow field results. Even this problem is far from complete. The entire interactive problem (with limits on the oceanic role) has been simulated by GCM's, but any elucidation of the relative importance of these processes has not been forthcoming. Attempts to incorporate the physica of these processes dynamically into analytical models started with Doos (1962) and has proceded slowly since (see Saltzman 1968 for a review of these). Few substantial improvements over Doos' primitive parameterization of diabatic heating have appeared, although interest is increasing (see for example Saltzman and Ashe 1976b).

II. EQUATIONS OF MOTION

I shall be using nondimensionalized quasigeostrophic equations of a beta-plane. All variables are expanded in powers of the Rossby number in the following manner: There are proscribed 0(1) variations of the pressure and density in the vertical, together with an $0(R_0)$ variation of the temperature with height (and hence of p and ρ with height), that constitute a prescribed standard atmosphere. The horizontal, temporal and vertical variabilities of the motion fields, etc. are at $0(R_0^2)$. In detail:

$$x' = Lx \qquad y' = Ly \qquad z' = Dz \qquad u' = Uu(x,y,z,t) \qquad v' = V(x,y,z,t)$$

$$w' = \frac{DU}{L} R_o w(x,y,z,t) \qquad \eta' = h\eta$$

$$\rho' = \rho^* [\rho_s(z) + R_o \epsilon(x,y,z,t)]$$

$$p' = 2\delta p^* [p_s(z) + \epsilon R_o p(x,y,z,t)] \qquad T' = T^*[1 - R_o \Gamma z + \epsilon R_o T(x,y,z,t)]$$

$$f' = f_o [1 + R_o \beta y]$$

where a prime denotes a dimensional quantity; ρ^*, p^* and T^* are dimensional <u>surface</u> values of the standard atmosphere density, pressure and temperature; L is the length scale, D the tropopause height and U a characteristic velocity; the subscript 's' denotes a standard atmosphere variable; η' is the dimensional topographic height and h a characteristic scale height for it; and $\beta = \frac{L \cot \phi_o}{a R_o}$ where a is the radius of the earth, and ϕ_o a typical mid-latitude. $R_o = \frac{U}{f_o L}$ Rossby No., $\epsilon = 4 \left(\frac{L}{\delta r^*}\right)^2$ Froude No., $f_o = 2\Omega \sin \phi_o$ where Ω is the angular frequency of rotation of the earth, $r^* = \frac{gH}{f_o}$ the Rossby radius, $\delta = \frac{D}{2H}$ where $H = \frac{g}{RT^*}$ is the scale height of the standard atmosphere. Further, letting $q' = R_o \epsilon \frac{U}{L} c_p T q$, and noting that $\frac{D}{L} = O(R_o)^2$, $\epsilon = O(R_o)$, $2\delta = O(1)$, $\frac{R}{c_p} = O(R_o)$, $\Gamma = O(1)$ and $\frac{L}{a} = O(R_o)$, after substitution in the 'primitive' equations of motion and expanding u, v, w, T, ρ, p, q and η in the usual way, one obtains:

$$\nabla^2 \psi_t - \psi_y \nabla^2 \psi_x + \psi_x \nabla^2 \psi_y + \beta \psi_x = \frac{(\rho_s w)_z}{\rho_s}$$

$$-\psi_y T_x + \psi_x T_y + \sigma w = q$$

$$T = \psi_z + \Gamma^2 z^2 (1 - \tfrac{1}{2} \delta z)$$

$$w = \Delta(\psi_x \eta_y - \psi_y \eta_x) + \mathcal{F} \nabla^2 \psi \quad at \ z = 0$$

where all variables u, v, w, and T are the leading terms in the Rossby No. expansions, and

$$\sigma = \frac{2\delta \frac{R}{c_p} - \Gamma R_o}{\epsilon} \quad \text{is the static stability,}$$

$$\mathcal{F} = \frac{E}{2\delta R_o} \quad \text{where } E = \frac{F'}{f_o}$$

$$\Delta = \frac{h}{D R_o}$$

Note that only the O(1) component of ρ_s enters here; the O(R_0) components exactly cancelled in formation of the vorticity equation.

Typical values (the ones to be used later) are:

$$D=10^4 m,\ L=10^6 m,\ U=10 m/sec,\ F'=4\times 10^{-6} sec^{-1},\ \Gamma'=6.5\times 10^{-3} K/m,$$
$$\rho^*=1.23 Kg/m^3 \text{ and } T^*=288K \text{ implying}$$
$$R_0=9\times 10^{-2},\ \beta=2.0,\ \delta=0.6,\ \sigma=1.1,\ \epsilon=1.3\times 10^{-1},\ \mathcal{F}=0.37,\ r^*=2.6\times 10^6 m.$$

It can be argued that the asymmetric time-average flow induced by topography is probably comparable to that due to heating. The ratio Δ of the topographic scale height to the depth of the fluid must be less than unity for the flow to be geostrophic at the surface. But it must be greater than O(R_0) for its induced asymmetries to be resolved by the above quasigeostrophic equations. Hence the equations are formally linearized about the zonal state by setting all variables ξ,

$$\xi=\langle\xi\rangle+\Delta\xi^*$$

where $\langle\xi\rangle$ denotes the zonal average value (to be prescribed where necessary) and ξ^* the quasigeostrophic component of the departure from this average. The following equations in the zonal departures (asymmetric variables) results, with asterisks ignored:

$$\left(\frac{\partial}{\partial t}+U\frac{\partial}{\partial x}\right)\nabla^2\psi+\beta\frac{\partial\psi}{\partial x}=\left(\frac{\partial}{\partial z}-2\delta\right)w \quad \dots (1)$$

$$\left(\frac{\partial}{\partial t}+U\frac{\partial}{\partial x}\right)\frac{\partial\psi}{\partial z}+\sigma w=q \quad \dots (2)$$

$$T=\frac{\partial\psi}{\partial z} \quad \dots (3)$$

$$w=U\frac{\partial n}{\partial x}+\mathcal{F}\nabla^2\psi \text{ at } z=0 \quad \dots (4)$$

where $U\equiv\langle u\rangle$.

III MODELING

The following simplifying assumptions are now made: 1) there is a rigid lid at the tropopause (z = 1); 2) the zonal perturbations and zonal wind are uniform in y; 3) there is a bottom Ekman layer that introduces a surface vertical velocity proportional to the vorticity at the surface. (Simplifications 1) and 2) cannot of course be justified for studies aimed at reproducing observed patterns. In fact, they are fairly easily removed. However, they introduce no new physics into the solutions obtained here).

In choosing U, a vertical profile was wanted that rendered the equations into tractable form and introduced no possible instabilities. The choice was to take the following expression involving the potential vorticity of the zonal state $\frac{1}{U}\left[\beta-\sigma\frac{\partial}{\partial z}\left(\frac{\frac{\partial}{\partial z}(\rho_s U)}{\rho_s}\right)\right]$ to be a uniform positive constant. This constraint, can give a quite reasonable-looking profile. However, for two-level models, which also shall be considered, imply a U with constant shear in the vertical. Hence for this summer's modeling U = constant was chosen, which is compatible with both continuous and two-level models. Taking the basic state to be barotropic introduces certain constraints on the zonal perturbations that can develop (there can be no lateral

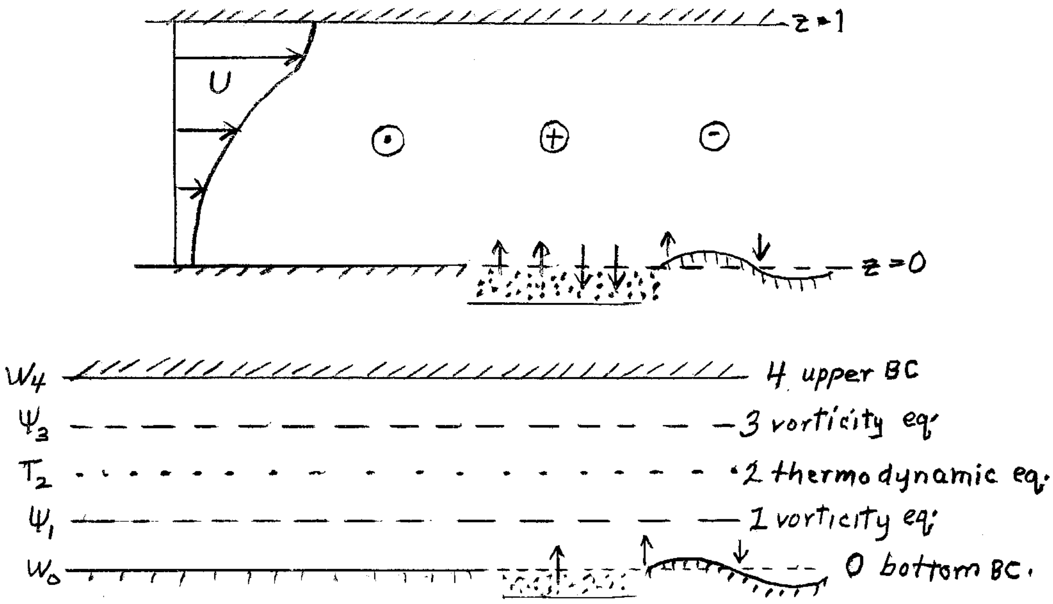

FIG. 2

advection of heat, in particular), but the zonal perturbations are still baroclinic, and the analysis is facilitated.

The continuous model is illustrated schematically in Fig.2. The two-level modeling is of the Phillips' type: there are two vertical modes allowed in the pressure (streamfunction) perturbation, and hence, by the thermal wind equation, there can be one in the temperature. That is, streamfunction is determined at two points in the vertical, and the temperature at one. The rigid lid condition is applied at level 4 (see Fig.2), the lower boundary condition (Ekman layer and orographic w) at level 0, the vorticity equation at levels 1 and 3 and the thermodynamic equation at level 2.

IV ZONAL TRANSFORM

The equations (1) - (4) are now put into spectral form (all variables are assumed to be periodic over a nondimensional length $\mathcal{L}$).

Let $$\Psi_n(z) \equiv \frac{1}{\mathcal{L}} \int_{-\mathcal{L}/2}^{\mathcal{L}/2} \psi(x,y,z,t)\, e^{i\bar{n}(x-ct)}\, dx \qquad \ldots \quad (5)$$

where $\bar{n} = \frac{2\pi n}{\mathcal{L}}$, $n \neq 0$

and likewise for T_n, W_n, Q_n . Herein $\mathcal{L}$ will correspond to the 45° latitude circle, i.e. $\mathcal{L} = \frac{2\pi a \cos 45^\circ}{L}$, so that $\bar{n} \approx \frac{n}{4}$. The steady-state solution for a particular n can be written as $\psi(x,z) = 2|\Psi_n(z)| \cos \bar{n}(x - \phi(z))$ where

$$\phi(z) = \frac{1}{\bar{n}} \arctan \left\{ \frac{-\mathrm{Im}\{\Psi_n(z)\}}{\mathrm{Re}\{\Psi_n(z)\}} \right\} .$$

The general solution is a sum over n .

The spectral equations are: $i\bar{n}[\beta - \bar{n}^2(U-c)]\Psi_n(z) = W_n'(z) - 2\delta W_n(z)$ (6)

$$i\bar{n}[U-c]\Psi_n'(z) + \sigma W_n(z) = Q_n(z) \qquad (7)$$

where a prime denotes $\frac{\partial}{\partial z}$. Q_n remains to be prescribed or expressed in terms of Ψ_n and W_n. The 'extra' term $-2\delta W_n$ expresses the fact that there can be a vertical convergence of mass by a uniform vertical velocity through the stratified atmosphere (recall that δ is a measure of the stratification).

The upper boundary condition takes the form

$$i\bar{n}(U-c)\Psi_n'(1) = Q_n(1); \qquad \ldots(8)$$

the lower boundary condition becomes

$$i\bar{n}(U-c)\Psi_n'(0) - \bar{n}^2\sigma\mathcal{F}\Psi_n(0) = -\sigma i\bar{n}\,U\mathcal{H}_n + Q_n(0) \qquad \ldots(9)$$

where $\mathcal{H}_n$ is the transform of the dimensionless topographic height $\eta(x)$.

V. SIMPLE ANALYTIC EXPRESSIONS FOR Q_n.

Realistic parameterizations of the physical processes embodied in q are by nature complex (see section I). The purpose of this study is to investigate the properties that such parameterizations may introduce into the solutions for our model atmosphere. In the attempt to gain some insight into this problem, only the most simple forms that these parameterizations might take will be considered. They are of the general form

$$q = f(\xi) \quad \text{or} \quad q = f(\xi(L_0))\,P(z)$$

where ξ is a dependent variable (ψ, T or w) and $P(z)$ gives a profile for the vertical distribution of q in the case where the variable ξ is evaluated at some height L_0. Three particular forms will be investigated:

1) heating proportional to the vertical velocity at some height L_0:

$$Q_n(z) = K W_n(L_0)\,P(z)$$

2) Newtonian 'convection' at the surface due to some subsurface 'ground' temperature, $T^{(g)}$:

$$Q_n(z) = -K(T_n(0) - T_n^{(g)})\,P(z).$$

3) Newtonian cooling to an equilibrium temperature, $T^{(e)}$:

$$Q_n(z) = -K(T_n(z) - T_n^{(e)}(z)).$$

Steady-state forced solutions can (and will) be readily derived with the aforementioned parameterizations. The question of the stability of such solutions to infinitesimal perturbations arises, i.e. if $\Psi(z,t) = e^{-i\bar{n}c}\,\Psi(z)$ where Ψ is the zonal Forier transform of ψ, will the imaginary part of c be negative, that is, will the perturbation damp out? All of the problems herein considered are of a general form $\frac{\partial\zeta}{\partial t} + \mathcal{L}(\zeta) = f(x,z)$ where ζ is ψ or $\frac{\partial\psi}{\partial z}$, $\mathcal{L}$ is a linear differential operator involving $\frac{\partial}{\partial x}$ and $\frac{\partial}{\partial z}$, and f is a forcing function (e.g. $\mathcal{H}_n, T_n^{(e)}, T_n^{(g)}$). Let $\bar{\zeta}$ be a steady state solution so that $\mathcal{L}(\bar{\zeta}) = \bar{f}$, and let $\zeta'(t)$ be infinitesimal perturbation $(\zeta = \bar{\zeta} + \zeta')$. Then $\frac{\partial\zeta'}{\partial t} + \mathcal{L}(\bar{\zeta}) + \mathcal{L}(\zeta') = \bar{f}$ since $\frac{\partial\bar{\zeta}}{\partial t} \equiv 0$ and $f' \equiv 0$. Subtracting the steady state equation gives $\frac{\partial\zeta'}{\partial t} + \mathcal{L}(\zeta') = 0$ which is the general form of the stability problem; formation of the analogous equation for particular cases will be obvious.

VI. SOME GENERAL PROPERTIES.

The equations (1) - (4) can be written in 'transport' form by defining

$$\hat{V} = \rho_s \Psi_x$$
$$\hat{T} = \rho_s \Psi_z$$
$$\hat{W} = \rho_s W$$
$$\hat{q} = \rho_s q$$

so that

$$\left.\begin{aligned} &\hat{V}_{xt} + U\hat{V}_{xx} + \beta\hat{V} = \hat{W}_z \\ &\hat{T}_t + U\hat{T}_x + \sigma\hat{W} = \hat{q} \\ &\hat{T}_x = \hat{V}_z + 2\delta\hat{V} \end{aligned}\right\} \quad . \quad (10)$$

Vertically integrating, so that $\mathcal{V} \equiv \int_0^1 \rho_s v\, dz = \int_0^1 \hat{V} dz$ represents the total meridional mass flux through a column, two well-known results are recovered: if $\hat{W}(0) = \hat{W}(1) = 0$, then $\mathcal{V}$ is a barotropic Rossby wave in x, with phase speed $c = U - \frac{\beta}{\bar{n}^2}$, which independent of any and all heating $\hat{q}$ within the atmosphere. Since these represent solutions for $\mathcal{V}$ which are not unstable, any instabilities introduced through feedbacks in $\hat{q}$ must grow antisymmetrically with height (so that the mass-weighted vertical average is stable). Second, for steady forcing by topography with $q = 0$, the above equations show that the response will be in phase with the orography in the frictionless case (since the eigenvalues of the operator $\frac{\partial^2}{\partial x^2}$ are $\bar{n}^2$ and are all real), likewise, even in the presence of surface friction, there will be no phase shift with height.

A general stability theorem is readily obtained. Taking Eq.(6), multiplying by ρ_s, taking the real part, multiplying by the complex conjugate of $\Psi_n (\Psi_n^*)$ and integrating in the vertical (by parts where necessary), gives

$$-i\bar{n}^3 c_i \int \rho_s |\Psi_n|^2 dz = -\mathbb{R}e(\rho_s W_n \Psi_n^*)\Big|_{z=0} - \mathbb{R}e\left\{\int W_n \rho_s \frac{d}{dz}\bar{\Psi}_n^{*} dz\right\}$$

Defining the growth rate λ by $\lambda = \bar{n}c_i$ where c_i is the imaginary component of the phase speed, and noting that $\int \rho_s |\bar{n}\Psi_n|^2 dz$ is proportional to the total zonal perturbation kinetic energy in a column (in wave number space), the above becomes

$$\lambda \hat{K}_n = \mathbb{R}e\left\{(\rho_s W_n \Psi^*)\Big|_{z=0}\right\} + \mathbb{R}e\left\{\int W_n \rho_s \frac{d}{dz}\Psi_n^* dz\right\} \quad . \quad . \quad (11)$$

A similar procedure applied to (7) gives

$$\sigma^{-1}\bar{n}c_i \int \rho_s \left|\frac{d\Psi_n}{dz}\right|^2 dz = -\mathbb{R}e\left\{\int \rho_s W_n \frac{d}{dz}\Psi_n^* dz\right\} + \mathbb{R}e\left\{\int \rho_s Q_n \frac{d}{dz}\Psi_n^* \sigma^{-1} dz\right\}.$$

Noting that $\frac{d}{dz}\Psi_n$ is the zonal perturbation temperature, $\sigma^{-1}\int \rho_s \left|\frac{d}{dz}\Psi_n\right|^2 dz$ defines the available potential energy in a 'column' of wavenumber space, $\hat{A}_n$. So

$$\lambda \hat{A}_n = \mathbb{R}e\left\{\int \rho_s W_n \frac{d}{dz}\Psi_n^* dz\right\} + \mathbb{R}e\left\{\sigma^{-1}\int \rho_s Q_n \frac{d}{dz}\Psi_n^* dz\right\} \quad . \quad . \quad . \quad (12)$$

Combining (11) and (12) gives

$$\lambda(\hat{A}_n + \hat{K}_n) = \mathbb{R}e\left\{(\rho_s W_n \Psi_n^*)\Big|_{z=0}\right\} + \mathbb{R}e\left\{\sigma^{-1}\int \rho_s Q_n \frac{d}{dz}\bar{\Psi}_n^{*} dz\right\} \quad . \quad . \quad . \quad (13)$$

The lower boundary condition $\mathcal{W}_n\big|_{z=0} = -\bar{n}^2\mathcal{F}\,\Psi_n\big|_{z=0} + i\bar{n}\,U\,\mathcal{H}_n$ implies

$$\lambda(\hat{A}_n+\hat{K}_n) = -\bar{n}^2\mathcal{F}(\rho_s|\Psi_n|^2)\big|_{z=0} + \bar{n}U(\rho_s\mathbb{R}e\{i\Psi_n^*\mathcal{H}_n\})\big|_{z=0} + \sigma^{-1}\mathbb{R}e\{\textstyle\int\rho_s Q_n\frac{d}{dz}\Psi_n^* dz\} \tag{14}$$

For unforced response of the system

$$\lambda = \frac{-\bar{n}^2\mathcal{F}(\rho_s|\Psi_n|^2)\big|_{z=0}}{\hat{A}_n+\hat{K}_n} < 0 \text{ i.e. the system is unconditionally stable.}$$

If , however, Q_n is a function of the variables Ψ_n, T_n or $\mathcal{W}_n$ (as will be considered) the solutions must be investigated individually.

Analogous equations hold for the two-level model, except that now

$$\hat{K}_n = \rho_1|\bar{n}\Psi_1|^2 + \rho_3|\bar{n}\Psi_3|^2 \quad \text{and} \quad \hat{A}_n = \sigma^{-1}\rho_2|\Psi_3-\Psi_1|^2.$$

Application of the lower boundary condition has almost always been of the form $\mathcal{W}_0 = -\bar{n}^2\mathcal{F}\Psi_0 + i\bar{n}U\mathcal{H}_n$ where Ψ_0 is extrapolated using Ψ_1 and Ψ_3, i.e. let $\Psi_0 = a\Psi_1 + (1-a)\Psi_3$. Straight linear extrapolation gives a = 1.5, although one occasionally finds other values used. The unforced response is however not unconditionally stable as above. In fact

$$\lambda = \frac{-\bar{n}^2\mathcal{F}a\rho_1|\Psi_1|^2 - \bar{n}^2\mathcal{F}(1-a)\rho_1\mathbb{R}e\{\Psi_3\Psi_1^*\}}{\hat{A} + R.} .$$

If a = 1, one obtains the condition corresponding to that above. For other values, as are almost invariably used, the possibility of spurious instabilities arises, depending on the phase between Ψ_1 and Ψ_3 and on their relative amplitudes. This problem will be investigated as it arises subsequently.

VII. HEATING PROPORTIONAL TO THE VERTICAL VELOCITY AT SOME HEIGHT.

There are situations in which it is plausible to consider a component of the diabatic heating to be dependent on large scale vertical uplift or subsidence.

Introduction of a diabatic heating proportional to the vertical velocity everywhere corresponds to a modification of the gross static stability of the atmosphere, as can be seen from the thermodynamic Eq.(2), $\frac{\partial T}{\partial t} + U\frac{\partial T}{\partial x} + \sigma w = q$, letting $q = Kw$.

A more interesting situation arises if it is presumed that the heating is proportional to the vertical velocity of some height L, (which might correspond to a gross 'lifting condensation level'). In particular, let $q = K\,P(z)\,w(L)$, and take $P(z) = 1$, so that the heating is distributed uniformly in the vertical. Substitution in the spectral equations (6)-(7) and elimination of Ψ_n gives

$$\frac{d^2}{dz^2}\mathcal{W}_n - 2\delta\frac{d}{dz}\mathcal{W}_n + \left(\frac{\beta}{U-c} - \bar{n}^2\right)\left(\sigma\mathcal{W}_n - K\,\mathcal{W}_n(L)\right) = 0 \tag{15}$$

Letting $\omega = \sigma\mathcal{W}_n - K\mathcal{W}_n(L)$ gives a homogeneous equation in ω

$$\frac{d^2}{dz^2}\omega - 2\delta\frac{d}{dz}\omega + \left(\frac{\beta}{U-c} - \bar{n}^2\right)\omega = 0 \tag{16}$$

With a flat, frictionless lower boundary, $\mathcal{W}_n(0) = 0$. In terms of ω the boundary conditions become $\omega(0) = -K\mathcal{W}_n(L)$, $\omega(1) = -K\mathcal{W}_n(L)$. But using the definition of ω , $\omega(L) = (\sigma-K)\mathcal{W}(L)$ so that the boundary conditions can be written

$$\omega(0)=\frac{K}{K-\sigma}\,\omega(L) \qquad \omega(1)=\frac{K}{K-\sigma}\,\omega(L) \tag{17}$$

Solutions to the DE for ω are

$$\left.\begin{aligned} \omega &= e^{\delta z}(c_1\cosh\alpha z + c_2\sinh\alpha z) \\ \text{where}\quad \alpha^2 &\equiv \delta^2+\bar{n}^2-\frac{\beta}{U-c} \end{aligned}\right\} \tag{18}$$

Note that c is complex, hence so is α^2, and ω involves both circular and hyperbolic trig functions. From the above one writes expressions for $\omega(0)$, $\omega(L)$, and $\omega(1)$, which when substituted into the boundary conditions give two homogeneous equations in c_1 and c_2. For non-trivial solutions the determinant must vanish, which yields:

$$-e^{\delta}\sinh\alpha+\frac{K}{K-\sigma}e^{\delta L}\sinh\alpha L+\frac{K}{K-\sigma}e^{\delta(L+1)}\sinh\alpha(1-L)=0 \tag{19}$$

This transcendental equation determines α, from which the real and imaginary parts of c are obtained:

$$c_r = U-\frac{\beta(\bar{n}^2+\delta^2+\alpha_i^2-\alpha_r^2)}{(\bar{n}^2+\delta^2+\alpha_i^2-\alpha_r^2)^2+4\alpha_r^2\alpha_i^2}$$

$$c_i = \frac{-2\beta\alpha_r\alpha_i}{(\bar{n}^2+\delta^2+\alpha_i^2-\alpha_r^2)^2+4\alpha_r^2\alpha_i^2}$$

For a growing or decaying mode, α_r and α_i must both be nonzero. Conversely, any mode with either $\alpha_i=0$ or $\alpha_r=0$ is an oscillatory solution.

Consider the case L = ½. The above transcendental equation in α (Eq.19) simplifies to

$$\sinh\frac{\alpha}{2}\left[\frac{K}{K-\sigma}e^{\delta}-2e^{\delta/2}\cosh\frac{\alpha}{2}\right]=0 \tag{20}$$

There are two classes of solution:

1) $\sinh\frac{\alpha}{2}=0$ which has solutions $\alpha_r=0, \alpha_i=2j\pi$ where j is any integer. If j = 0 then $\alpha=0$ and the general solution for $\omega(z)$ used previously is no longer valid. Now $\omega=e^{\delta z}(c_1+c_2 z)$. It can be shown that this corresponds to an oscillatory mode if $\frac{K}{K-\sigma}=-(\sinh\frac{\delta}{2})^{-1}$; for other values of K, σ and δ, $\alpha=0$ does not correspond to a mode of the system. When $j\neq 0$, there are simple oscillatory solutions $c_r=U-\frac{\beta}{\bar{n}^2+\delta^2+4j^2\pi^2}$.

2) $-2e^{\delta/2}\cosh\frac{\alpha}{2}+\frac{K}{K-\sigma}(1+e^{\delta/2})=0$ which can be expressed as the coupled real equations

$$\begin{cases}\cosh\frac{\alpha_r}{2}\cos\frac{\alpha_i}{2}=K\cosh\frac{\delta}{2}\\ \sinh\frac{\alpha_r}{2}\sin\frac{\alpha_i}{2}=0.\end{cases}$$

One set of solution is

$$\left.\begin{aligned}\alpha_i &= 2j\pi \quad j=\text{even}\\ \alpha_r &= 2\operatorname{arccosh}\left(\frac{K}{K-\sigma}\cosh\frac{\delta}{2}\right)\end{aligned}\right\}\ \frac{K}{K-\sigma}>0$$

and

$$\left.\begin{array}{l}\alpha_i = 2j\pi \qquad j = \text{odd} \\ \alpha_r = 2\,\text{arccosh}\left(-\frac{K}{K-\sigma}\cosh\frac{\delta}{2}\right)\end{array}\right\}\ \frac{K}{K-\sigma} < 0 \qquad ;$$

While another set is

$$\left.\begin{array}{l}\alpha_r = 0 \\ \alpha_i = 2\,\text{arccos}\left(\frac{K}{K-\sigma}\cosh\frac{\delta}{2}\right)\end{array}\right\}$$

Hence if $\left|\frac{K}{K-\sigma}\right|\cosh\frac{\delta}{2} < 1$, only the 'arccos' solution exists, $\alpha_r = 0$, and all solutions are strictly oscillatory. If, however, $\left|\frac{K}{K-\sigma}\right|\cosh\frac{\delta}{2} > 1$, only the 'arccosh' solutions exist, and there will be one growing and one decaying mode for each j. For $K > 0$, $\left|\frac{K}{K-\sigma}\right|\cosh\frac{\delta}{2} > 1$, so all solutions (for all wavenumbers) are unstable.

The intuitively analogous model in the two-level case is that where $Q_2 = KW_2$, since W_2 is defined as W at $z = \frac{1}{2}$. This however corresponds only to a modification of the static stability, so there are only stable modes, the opposite result from the above. This suggests caution be used in making analogies corresponding to particular heights: Q_2 and W_c behave more like first modes in the vertical structure, rather than like Q and W at $z = \frac{1}{2}$.

VIII. HEAT TRANSFER AT THE LOWER BOUNDARY

Observations indicate that the largest component of the asymmetric diabatic heating in midlatitudes is the combination of sensible plus latent heat flux through the boundary layer. Several studies have used the simplest possible parameterization of the convergence of this flux, namely $q = -K[T(0) - T_g]\,P(z)$ where T(0) is the air temperature at z = 0 and T_g is the temperature of the ground or sea below; P(z) is the vertical profile of the heat flux convergence, and K is a 'Newtonian convection' coefficient.

Realistically, K is strongly dependent on the nature of the underlying surface and should be a function of the horizontal coordinates, and it should also depend on some stability criterion such as the surface static stability, a boundary-layer Richardson Number, or more simply on $(T(0) - T_g)$ itself.

For the present, however, K will be taken to be a positive constant, and $P(z) = 1$. It is also presumed that T_g can be taken as externally prescribed.

Denote the transform of T_g as $\mathcal{T}_g$ (as in section IV) so that

$$Q_n = -K\left[\frac{d}{dz}\Psi_n(0) - \mathcal{T}_g\right]. \tag{21}$$

In the absence of topography or friction, the lower boundary condition becomes $i\bar{n}(U-c)\mathcal{T}_n(0) = -K\mathcal{T}_n(0)$ for the stability problem. Taking real and imaginary parts of c, $\bar{n}c_i = -K$, so that all modes are stable $(K > 0)$.

For the more general case, procede as follows: Elimination of W_n from (6)-(7), and substitution of the expression for Q_n gives a potential vorticity equation

$$\frac{d^2}{dz^2}\Psi_n - 2\delta\frac{d}{dz}\Psi_n + \sigma\left[\frac{\beta}{U-c} - \bar{n}^2\right]\Psi_n = \frac{-2\delta K}{i\bar{n}(U-c)}\left[\frac{d\Psi_n}{dz}(0)\right] \tag{22}$$

whose solutions are

where

$$\left.\begin{aligned} \Psi_n(z) &= e^{\delta z}(c_1 e^{\alpha z} + c_2 e^{-\alpha z}) + \frac{2\delta K}{\bar{n}(U-c)}\left[\frac{d\Psi_n}{dz}(0)\right] \\ \alpha^2 &\equiv \delta^2 + \sigma\left(\bar{n}^2 - \frac{\beta}{U-c}\right). \end{aligned}\right\} \tag{23}$$

Application of the boundary conditions $i\bar{n}(U-c)\left[\frac{d\Psi_n}{dz}(1)\right] = -K\left[\frac{d\Psi_n}{dz}(0)\right]$ and $\left[K - i\bar{n}(U-c)\right]\left[\frac{d\Psi_n}{dz}(0)\right] + n^2\sigma\mathfrak{F}\Psi_n(0) = 0$, give after some manipulations the requirement that

$$\begin{aligned} &-i\bar{n}(\alpha^2-\delta^2)(U-c)\left[K+i\bar{n}(U-c)\right]e^{\delta}\sinh\alpha + i\bar{n}\sigma\mathfrak{F}\left\{\sigma\bar{n}^2(U-c)\left[\beta-\bar{n}^2(U-c)\right]e^{\delta} + \right. \\ &\left.(2\alpha\cosh\alpha + 2\delta\sinh\alpha) - 2\alpha\sigma i\bar{n}K\left[\bar{n}^2(U-c)-\beta\right] - 2i\bar{n}\delta K(\delta^2-\alpha^2)(U-c)e^{\delta}\sinh\alpha\right\} = 0 \end{aligned} \tag{24}$$

for non-trivial solution. This is a complex, irrational transcendental equation in c (recall $\alpha = f(c)$). For the frictionless case, one gets the oscillatory solutions implied by $\sinh\alpha = 0$ (internal Rossby modes) and that implied by $\alpha^2 = \delta^2$ (on external Rossby mode), as well as the result $c = U - i\frac{K}{\bar{n}}$ which gives the decaying (stable) solution $\bar{n}c_i = -K$. For $\mathfrak{F} \neq 0$, attempts were made to obtain solutions numerically, but I was unable to (within the time and expense constraints of the summer program).

Some information concerning the forced response with T_g prescribed can be obtained directly from the lower boundary condition in the frictionless case. Substitution of $Q_n = -K[T_n(0) - T_g]\,P(z)$ into the boundary condition (9) gives

$$u\frac{d}{dx}T_n(0) + KP(0)T_n(0) = KP(0)T_g$$

which, presuming T_g is real (phase shift of 0 relative to the origin), gives

$$|T_n(0)| = \frac{T_g}{\sqrt{1 + \left(\frac{\bar{n}u}{KP(0)}\right)^2}}$$

and for the phase shift relative to T_g

$$\phi = \arctan\left(\frac{\bar{n}u}{KP(0)}\right).$$

Since K, $P(0)$, u, $\bar{n} > 0$, ϕ is small for long waves ($\bar{n}$ small), and increases towards $\frac{\pi}{2}$ for short waves (compare with Fig.3).

The solutions forced by a prescribed T_g, in the presence of friction, are now considered. Instead of (22) there is

$$\frac{\delta^2}{dz^2}\Psi_n - 2\delta\frac{d}{dz}\Psi_n + \sigma\left(\frac{\beta}{u} - \bar{n}^2\right)\Psi_n = 2\delta\frac{K}{i\bar{n}u}\left[\frac{d\Psi_n}{dz}(0) - T_g\right] \tag{25}$$

with solutions

$$\Psi_n = e^{\delta z}(c_1 e^{\alpha z} + c_2 e^{-\alpha z}) + 2\delta\frac{K}{i\bar{n}\sigma(\beta - \bar{n}^2 u)}\left[\frac{d\Psi_n}{dz}(0) - T_g\right]$$

implying

$$\Psi_n = c_1\left\{e^{(\delta+\alpha)z} + \frac{2\delta(\delta+\alpha)\kappa}{\sigma i\bar{n}(\beta-\bar{n}^2U)}\right\} + c_2\left\{e^{(\delta-\alpha)z} + \frac{2\delta(\delta-\alpha)\kappa}{\sigma i\bar{n}(\beta-\bar{n}^2U)}\right\} - \frac{2\delta\kappa}{\sigma i\bar{n}(\beta-\bar{n}^2U)}T_g$$

Application of the boundary conditions

$$(\kappa + i\bar{n}U)\frac{d\Psi_n}{dz}(0) - \sigma\mathcal{F}\bar{n}^2\Psi_n(0) = \kappa T_g \quad \text{and}$$
$$i\bar{n}U\frac{d\Psi_n}{dz}(1) + \kappa\frac{\partial\Psi_n}{dz}(0) = \kappa T_g$$

give the following system for c_1 and c_2

$$\begin{pmatrix} (\kappa+i\bar{n}U)(\delta+\alpha)-\sigma\bar{n}^2\mathcal{F}\left[1+\frac{2\delta(\delta+\alpha)\kappa}{\sigma i\bar{n}(\beta-\bar{n}^2U)}\right] & (\kappa+i\bar{n}U)(\delta-\alpha)-\sigma\bar{n}^2\mathcal{F}\left[1+\frac{2\delta(\delta-\alpha)\kappa}{\sigma i\bar{n}(\beta-\bar{n}^2U)}\right] \\ (\delta+\alpha)(i\bar{n}Ue^{\delta+\alpha}+\kappa) & (\delta-\alpha)(i\bar{n}Ue^{\delta-\alpha}+\kappa) \end{pmatrix}\begin{pmatrix} c_1 \\ c_2 \end{pmatrix} = \begin{pmatrix} \kappa\left[1+\bar{n}\sigma\mathcal{F}\frac{2\delta i}{\beta-\bar{n}^2U}\right]T_g \\ \kappa T_g \end{pmatrix}.$$

The forced response for $T_g = 1$, $\kappa = \frac{3}{4}$, $\mathcal{F} = \frac{1}{2}$ and the other parameters as in section II, is shown in Fig.3, for n = 1,2,3,5,7. The left-hand figure shows the 'ridges' (solid lines) and 'troughs' (dotted lines) of Ψ, T and W as a function of height. The right-hand figures are amplitudes as functions of height. In the frictionless case there is a resonance at $\bar{n} = \sqrt{\frac{\beta}{U}}$. Even in the frictional case, there is a finite 'quasi-resonance' at this point. For the given parameters, n = 4 is the resonant wavenumber. The shifts in phase associated with passing through n = 4 are evident in the figure.

Suppose the underlying surface maintains some temperature distribution, but has topographic variations. The topography induces a zonal perturbation in the vorticity,and a temperature perturbation must accompany it to keep the flow geostrophic. The distribution of surface air temperature ($T(0)$) will interact with the ground distribution (T_g) introducing a heating. The forced flow pattern that results will now be considered.

Figure 4 shows the response of the model equations to topography alone, with no feedback heating effect ($\mathcal{H}_n = 1$, $\kappa = 0$). At low wavenumbers the response of Ψ is nearly 180° out of phase with the topographic height, and as the wavenumber increases, friction becomes increasingly important and the phases change. There are of course no phase changes with height. The quasiresonance phenomena is apparent at n = 3 and 5. $W(0)$ increases with increasing wavenumber, while the amplitudes of Ψ and T go to 0 as $n \to \infty$.

The next figure (5) shows the same situation, but with $\kappa = \frac{3}{4}$ and $T_g = 0$. The phase changes of T with height are noticeable at all wavenumbers, whereas the amplitude characteristics of Ψ, T and W are all similar to the previous case. Addition of the diabatic heating feedback introduces little change in the phase of Ψ_n and W_n relative to $\mathcal{H}_n$, and for large n (friction becoming important) the overall response is quite similar.

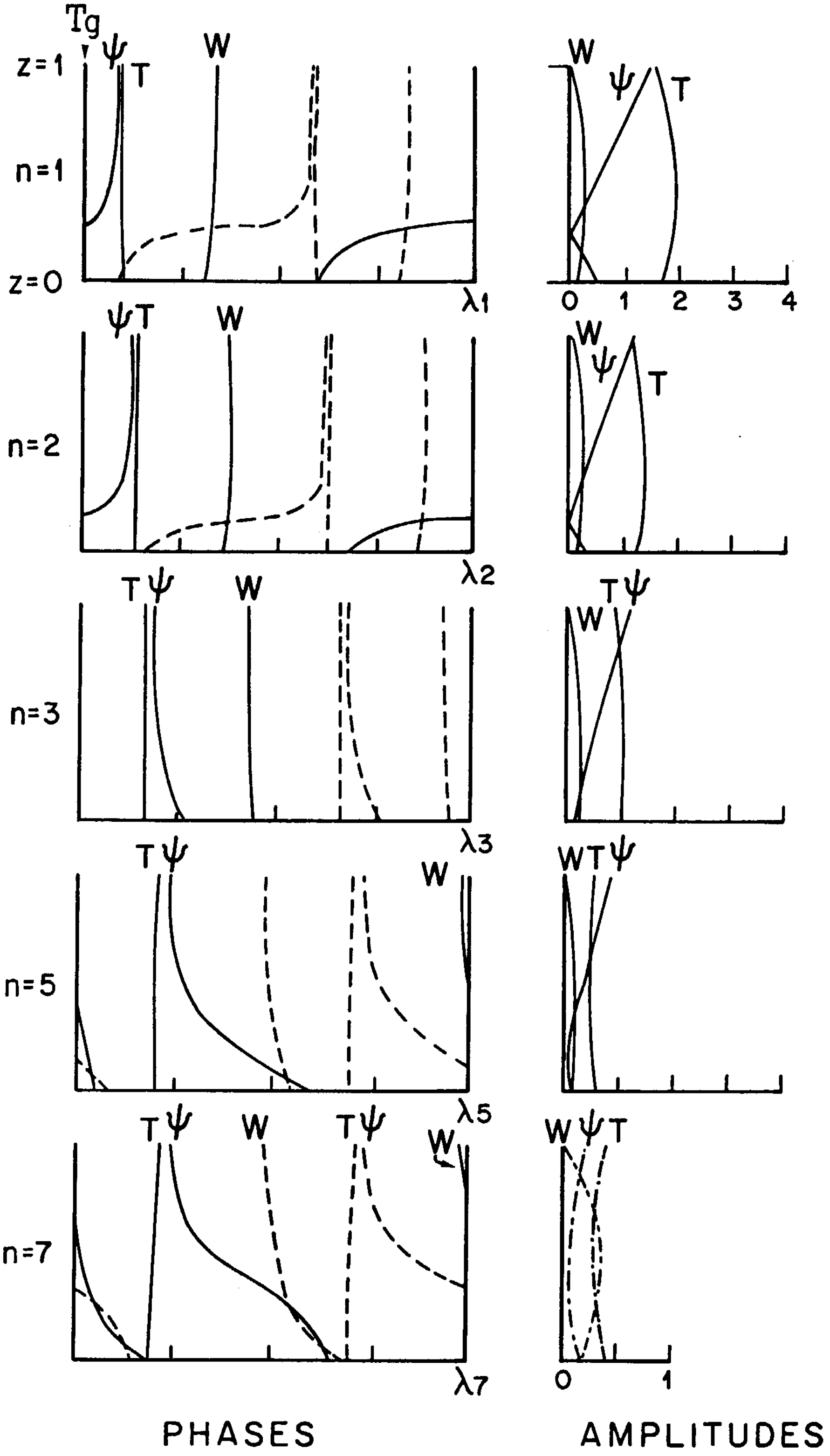
Tg
ψ
T
W
z=1
n=1
z=0
λ1
0
1
2
3
4
W
ψ
T
n=2
λ2
T
ψ
W
n=3
λ3
T
ψ
W
n=5
λ5
W
T
ψ
T
ψ
W
T
ψ
W
n=7
λ7
W
ψ
T
0
1
PHASES
AMPLITUDES

Fig.3

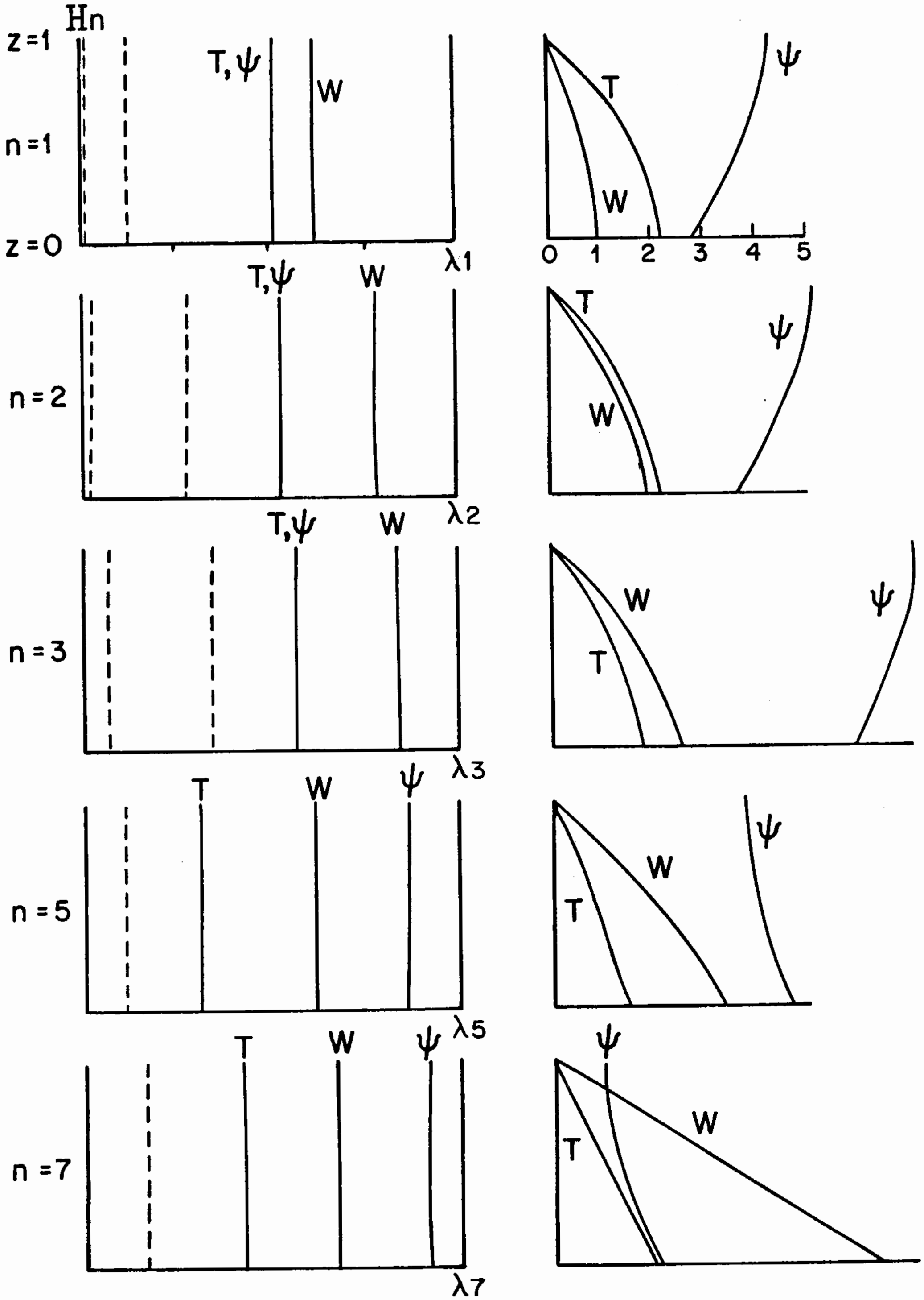
z=1
Hn
n=1
z=0
T,ψ
W
λ1
T
W
ψ
0
1
2
3
4
5
n=2
T,ψ
W
λ2
T
W
ψ
n=3
T,ψ
W
λ3
W
T
ψ
n=5
T
W
ψ
λ5
W
T
ψ
n=7
T
W
ψ
λ7
ψ
W
T

Fig.4

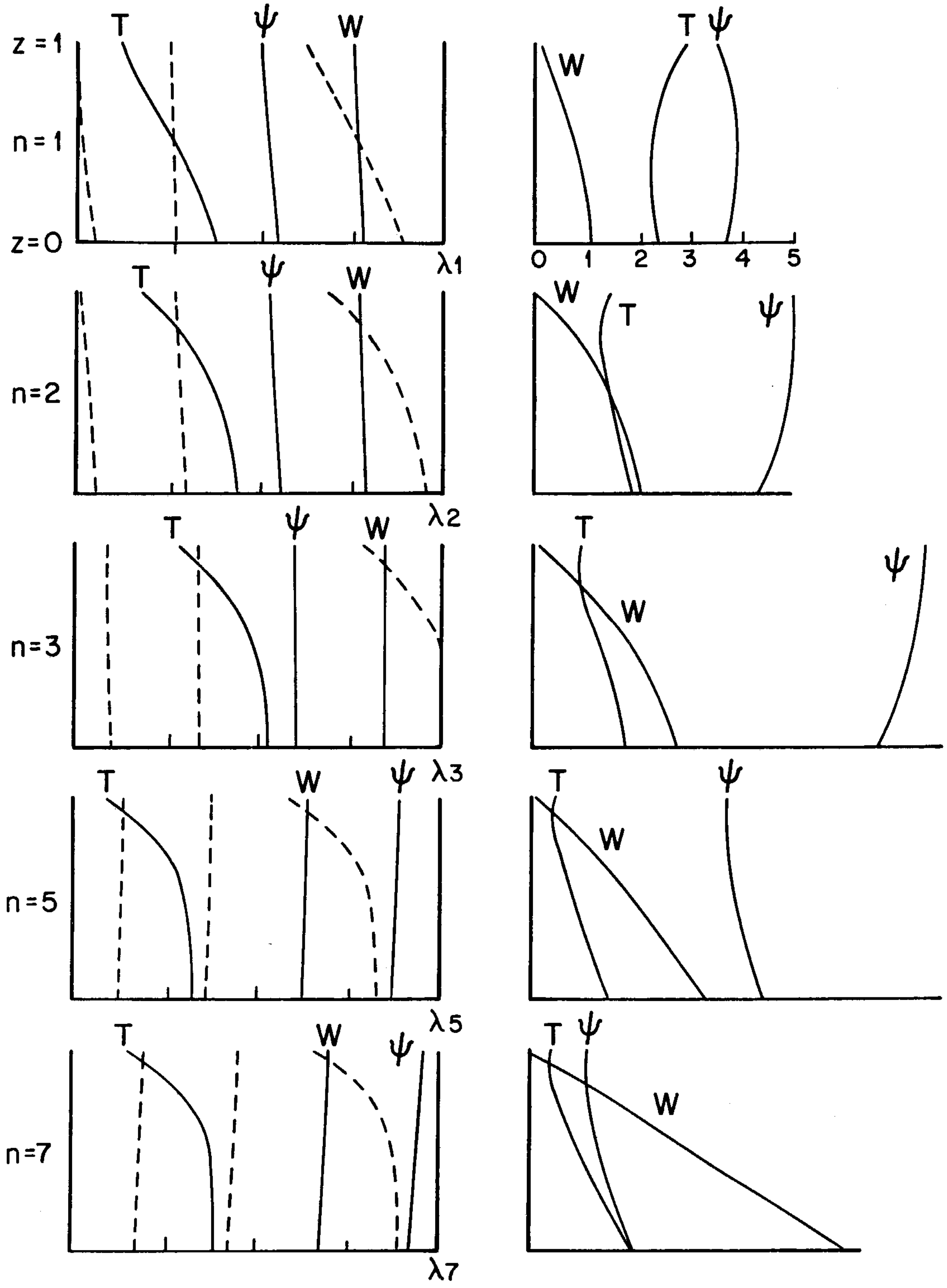

Fig.5

IX. NEWTONIAN COOLING TO EQUILIBRIUM

Suppose there is some equilibrium temperature, T_e, towards which the atmosphere tends, in the sense that at each point there is diabatic cooling proportional to how much warmer than T_e the fluid is at that point. This process, known as 'Newtonian Cooling' can be expressed as

$$q = -K\left[T(z) - T_e(z)\right],$$

and will be the next heating form considered. In the above formula, Te, which is of course, a function of x , can also have height dependence. In the following discussion, however, Te = constant in z , so that

$$Q_n = -\tfrac{1}{2}\left[T_n(z) - T_e\right]. \tag{26}$$

The stability of steady-state solutions follows immediately from the integral constraint equation (14), which takes the form

$$\lambda = \frac{-\bar{n}^2\mathcal{F}(\rho_s|\Psi_n|^2)\big|_{z=0} - \frac{K}{\sigma}\int \rho_s\left|\frac{d\Psi_n}{dz}\right|^2 dz}{\hat{A}_n + \hat{K}_n}$$

From the above it is evident that for frictionless motion, Newtonian cooling $(K>0)$ corresponds to a decaying mode, hence the steady state solution is stable. It also seems evident that some solutions with $K<0$ might also be stable in the presence of friction.

More information about the modes of the frictionless problem is now obtained. Differentiation of the vorticity equation (6) with respect to z gives an equation in T_n $\frac{d^2 W_n}{dz^2}$, and $\frac{dW_n}{dz}$. Expressions for the latter two W_n derivatives gotten by differentiation of the thermocynamic equation. Since $\frac{dQ_n}{dz}$ and $\frac{d^2Q_n}{dz^2}$, but not Q_n now appear, T_e , which is constant in z , will enter only the boundary conditions. Hence:

$$\frac{d^2}{dz^2}T_n - 2\delta\frac{d}{dz}T_n + \sigma i\bar{n}\,\frac{\beta - \bar{n}^2(U-c)}{i\bar{n}(U-c)+K}\,T_n = 0 \tag{27}$$

whose solution is

$$\left.\begin{aligned} &T_n = e^{\delta z}(c_1\cosh\alpha z + c_2\sinh\alpha z) \quad \text{where now} \\ &\alpha^2 \equiv \delta^2 - \sigma i\bar{n}\,\frac{\beta-\bar{n}^2(U-c)}{i\bar{n}(U-c)+K}\,. \end{aligned}\right\} \tag{28}$$

The upper and lower boundary conditions require that W_n vanish, so

$$[i\bar{n}(U-c)+K]\,T_n(1) = K T_e$$

$$[i\bar{n}(U-c)+K]\,T_n(0) = K T_e.$$

To obtain the modes of the systems, set $T_e = 0$; the determinant of resulting homogeneous equations (as before) must vanish for nontrivial solutions. Two possibilities arise: 1) $i\bar{n}(U-c)+K=0$, for which the growth rate is $\lambda = -K$. This agrees with the integral result that Newtonian cooling $(K>0)$ corresponds to a stable mode. 2) $\sinh\alpha = 0$. In the previous cases, this mode corresponded to oscillatory solutions exclusively which were independent of any feedback. In this problem, however, K appears in α and the modes implied by $\sinh\alpha = 0$ must be investigated anew. As before, the solutions are

$$\mathrm{Re}\{\alpha\} = 0$$
$$\mathrm{Im}\{\alpha\} = j\pi,\ j = \text{any integer} \neq 0.$$

Solving for c gives

$$c = U - \frac{\beta^2}{\bar{n}^2+\delta^2+j^2\pi^2} - i\,\frac{K}{\bar{n}}\,\frac{\delta^2+j^2\pi^2}{\bar{n}^2+\delta^2+j^2\pi^2}$$

The growth rate is $\lambda = -\frac{\delta^2+j^2\pi^2}{\bar{n}^2+\delta^2+j^2\pi^2}K$. Since $\delta^2+j^2\pi^2 > 1$ for all j, the mode of 1) above is the most unstable.

Newtonian cooling will now be considered for the two-level model. Its form is $q_2 = -K(T_2 - T_\ell)$. Friction will be included, and as the two-level 'integral' constraint implied, the stability may depend on the extrapolation scheme used for obtaining the surface vorticity (i.e. for obtaining Ψ_0). The system becomes

$$i\bar{n}\left[\beta - \bar{n}^2(U-c)\right]\Psi_3 = -2\frac{\rho_2}{\rho_3}W_2$$
$$i\bar{n}\left[\beta - \bar{n}^2(U-c)\right]\Psi_1 = 2\frac{\rho_2}{\rho_0}W_2 + 2\frac{\rho_0}{\rho_1}\mathcal{F}\bar{n}^2\Psi_0$$
$$2\left[K - i\bar{n}(U-c)\right](\Psi_3 - \Psi_1) = \sigma W_2.$$

Let $\Psi_0 = r\Psi_1 + s\Psi_3$.

For nontrivial solutions, the above system requires

$$(U-c)^2 - \left[\frac{2i\mathcal{F}\frac{\rho_0}{\rho_1}\left(4\frac{\rho_2}{\rho_3} + \bar{n}^2 r\right)}{\bar{n}\left(\bar{n}^2+4\left(\frac{\rho_2}{\rho_3}+\frac{\rho_2}{\rho_1}\right)\right)} + \frac{\beta}{\bar{n}^2} + \frac{\beta - 4\left(\frac{\rho_2}{\rho_3}+\frac{\rho_2}{\rho_1}\right)\frac{iK}{\bar{n}}}{\bar{n}^2+4\left(\frac{\rho_2}{\rho_3}+\frac{\rho_2}{\rho_1}\right)}\right](U-c)$$
$$+\left[-\frac{2i\mathcal{F}\frac{\rho_0}{\rho_1}\left(4\frac{\rho_2}{\rho_3}\frac{iK}{\bar{n}} - \beta r\right)}{\bar{n}(\bar{n}^2+4(\frac{\rho_2}{\rho_3}+\frac{\rho_2}{\rho_1}} + \frac{\beta}{\bar{n}^2}\,\frac{\left(\beta - 4\left(\frac{\rho_2}{\rho_3}+\frac{\rho_2}{\rho_1}\right)\frac{iK}{\bar{n}}\right)}{\left(\bar{n}^2+4\left(\frac{\rho_2}{\rho_3}+\frac{\rho_2}{\rho_1}\right)\right)}\right] = 0$$

where it is presumed the extrapolation is linear $(r + s = 1)$. In the frictionless case, the above gives

$$c = U - \frac{\beta}{\bar{n}^2+4\left(\frac{\rho_2}{\rho_3}+\frac{\rho_2}{\rho_3}\right)} - i\,\frac{K}{\bar{n}}\,\frac{4\left(\frac{\rho_2}{\rho_1}+\frac{\rho_2}{\rho_3}\right)}{\bar{n}^2+4\left(\frac{\rho_2}{\rho_1}+\frac{\rho_2}{\rho_3}\right)}$$

or $c = U - \frac{\beta}{\bar{n}^2}$. The two-layer model gives only the unstable mode corresponding to j = 1 in the continuous case. As was shown, this was not the most unstable mode, so that the two-level model has underestimated the growth rate of the least stable mode. (Note, however, that in the limit $\bar{n} \to 0$, $\lambda = -K$, which is the 'true' most unstable mode.)

Now for the frictional case. In the limit $\bar{n} \to 0$, the effect of friction goes to zero, and the growth rate

$$\lambda = -K + O(\bar{n}) \text{ as } \bar{n} \to 0.$$

In the short wave limit, the fastest growing mode goes to zero as $\bar{n} \to \infty$.

The phase speeds were computed numerically for the case with no extrapolation (r = 1, s = 0) which is stable by integral constraints, and the case r = 1.5, s = -0.5. For $K > 0$, Newtonian cooling, all modes in both cases where stable for all wavenumber. Figure 6 shows the growth rate versus wavenumber for $K = -0.2$ and $K = -0.4$ (Newtonian heating) in the nonextrapolated case (solid line) and extrapolated (dotted line). The longwave limit $\lambda \rightarrow -K$ as $\bar{n} \rightarrow 0$ is evident. While the extrapolation introduced no 'error' into the basic stability, the growth rates do differ, and there is a suggestion that friction is stabilizing at $\bar{n} \sim 1.5$. Any effects due to extrapolation should be more evident in a model with a baroclinic zonal state.

The forced response to a prescribed T_e is shown in Fig.7. The computations and display are exactly analogous to those for the response to prescribed T_g shown in Fig.3.

X. CONCLUSIONS

The inclusion of simple dynamic feedback effects in a zonally asymmetric model does not appreciably alter the general response characteristics of the model atmosphere. In general, processes that introduced some form of negative feedback are stable; positive feedback is destabilizing.

Additionally, the two-level model should be approached cautiously for studying the types of parameterizations considered herein. The association of a quantity at some level should not be taken too literally.

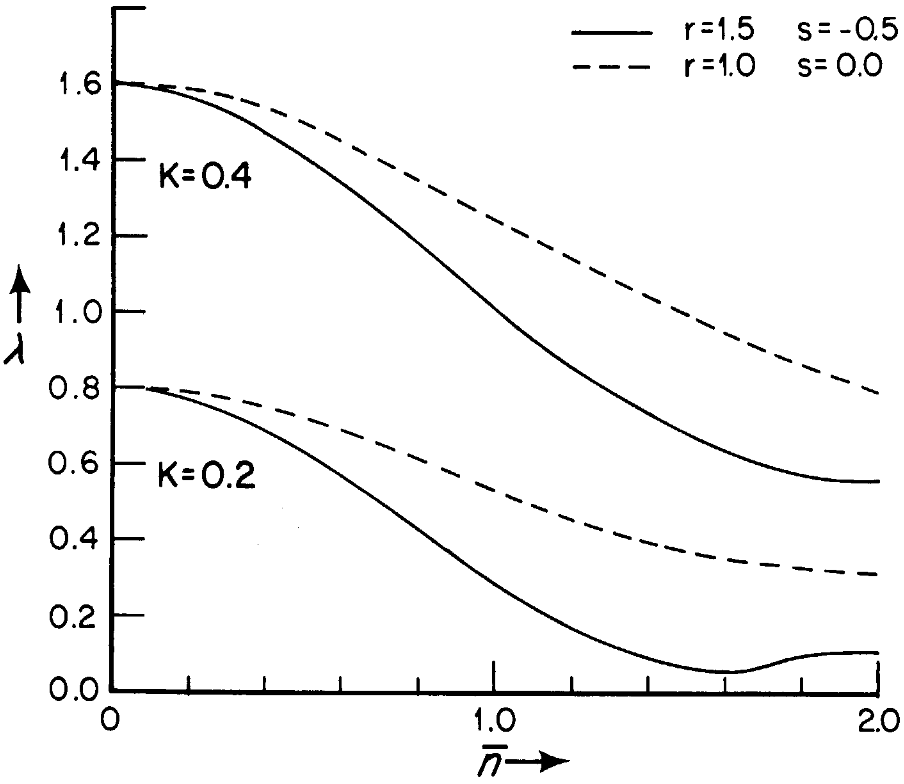

Fig.6

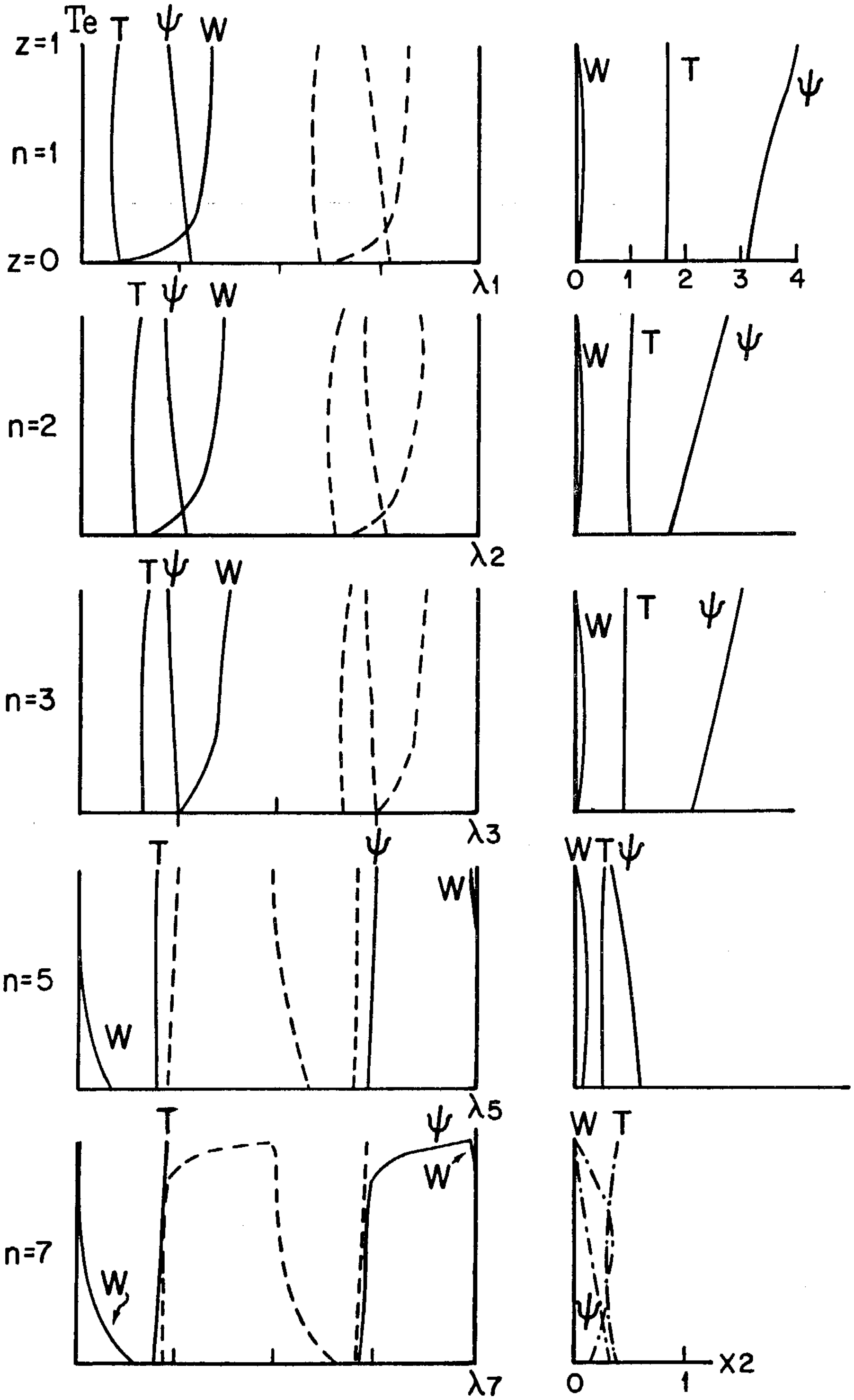

Fig.7

Further investigations might consider a variety of refinements. For one, better dynamics: inclusion of a baroclinic zonal state, meridional variations, stratospheric coupling, interaction with a symmetric regime model, and abondonment of the β -plane (i.e. scale $L \sim a$ rather than $L/a = O(R_O)$). Second, improved parameterizations: use of a horizontally inhomogeneous k reflecting the different thermodynamic properties of land and ocean, treatment of the transient eddy convergences (stochastic properties of weather systems) and their interaction with the diabatic heating processes, and inclusion of a water-vapor cycle, for instance. Third are miscellaneous considerations: what are the nonlinear effects, how can the finite amplitude effects of orography be included, and how important are the vertical distributions of the diabatic heating processes?

XI References

Doos, Bo 1962 The influence of exchange of sensible heat with the earth's surface on the planetary flow. Tellus 14(2): 133.

Saltzman, B. 1968 Surface boundary effects on the general circulation and macroclimate: a review of the theory of the quasi-stationary perturbations in the atmosphere. Met.Monogr. 8(30): 4-19.

Saltzman, B. and S.Ashe 1976 Parameterization of the monthly mean vertical heat transfer at the earth's surface. Tellus 28(4).

XII Acknowledgements

My thanks to Dr. Andrew Ingersoll for his assistance and advice during the summer, and to Dr. Barry Saltzman for his continuing interest and support.

GEOSTROPHIC BAROCLINIC INSTABILITY IN A FLUID WITH THREE LAYERS

Michael H. Davey

Many analytical models have been developed to study the phenomenon of baroclinic instability, and to investigate the effects on it of conditions such as dissipation, varying bottom topography and the β-effect. The models that are able to resolve the structure of the unstable waves analytically require the use of either linear vertical profiles of velocity and static stability (Eady (1969)), or a two-layer system (Phillips (1954)). The aim of the three-layer system presented here is to look at the effect of allowing curvature in the vertical velocity profile. To simplify the necessary algebra, and to isolate the curvature effect, a simple basic state is chosen, with no dissipation and no β -effect.

First the governing equations are established, then the linear stability analysis and its finite-amplitude extension are described. Finally, the linear stability of a special case with an infinitely deep bottom layer is studied.

Description of the model

The basic system is shown in diagram 1. The layers are stably stratified and immiscible, and have equal depth H in the absence of relative motion. Each layer has constant density, ahd the density differences $\rho_2 - \rho_1$, and $\rho_3 - \rho_2$ are

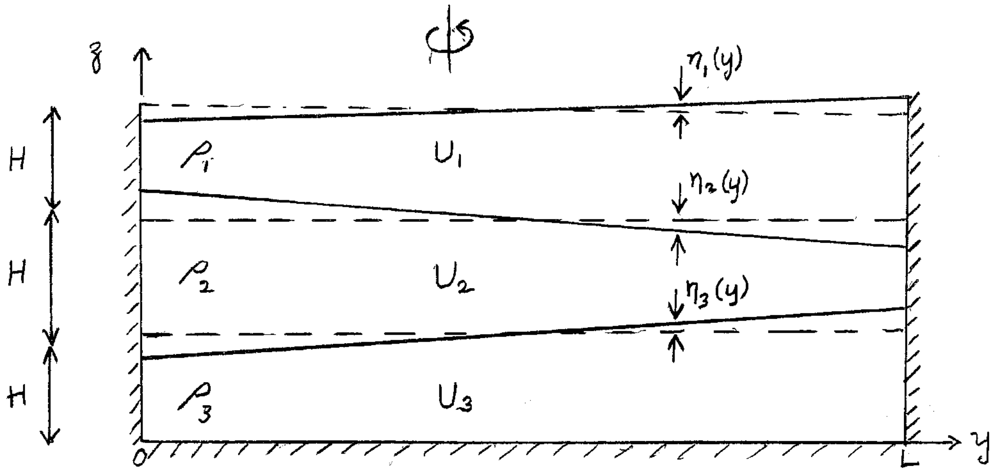

Diagram 1. The basic three-layer system.

both equal to $\Delta\rho$, with $\Delta\rho << \rho_2$ there are vertical sidewalls at y = 0, L, and the system is unbounded in x . The basic state has constant velocities $(U_i, 0, 0)$. (i = 1,2,3). For geostrophic and hydrostatic balance, the following interface displacements are required, in the basic state.

$$\eta_1 = -\frac{fU_1}{g}\left(y-\frac{L}{2}\right)$$

$$\eta_2 = \frac{f}{\Delta\rho g}(\rho_1 U_1 - \rho_2 U_2)\left(y-\frac{L}{2}\right)$$

$$\eta_3 = \frac{f}{\Delta\rho g}(\rho_2 U_2 - \rho_3 U_3)\left(y-\frac{L}{2}\right)$$

f is the coriolis parameter, taken as constant. The Rossby number $\varepsilon = \frac{U}{fL} << 1$, where U is the basic velocity scale. The internal rotational Froude number $F = \frac{f^2L^2}{\left(\frac{\Delta\rho}{\rho_2}\right)gH}$ is chosen to be 0(1), so the length scale L is comparable to the radius of deformation. L under these conditions, $\frac{\eta_2}{H_1}$ and $\frac{\eta_3}{H}$ are $0(\varepsilon)$, and η_1 is negligibly small. The Richardson number $R_i = \frac{g\frac{\Delta\rho}{\rho}\frac{1}{H}}{(U/H)^2} >> 1$ is prescribed, so perturbations to the basic state which have $0(L_D)$ length scale will be geostrophic.

The potential vorticity in each layer is

$$q_1 = \frac{\zeta_1 + f}{H+\eta_1-\eta_2} = \frac{1}{H}\left(f+\zeta_1+f\frac{\eta_2}{H}\right) + 0\left(\varepsilon^2\frac{f}{H}\right)$$

$$q_2 = \frac{\zeta_2 + f}{H+\eta_2-\eta_3} = \frac{1}{H}\left(f+\zeta_2+f\frac{\eta_3-\eta_2}{H}\right) + 0\left(\varepsilon^2\frac{f}{H}\right)$$

$$q_3 = \frac{\zeta_3 + f}{H+\eta_3} = \frac{1}{H}\left(f+\zeta_3-f\frac{\eta_3}{H}\right) + 0\left(\varepsilon^2\frac{f}{H}\right)$$

ζ_i is the vertical vorticity component. In the absence of dissipation, potential vorticity is conserved in each layer

$$\frac{Dq_i}{Dt} = 0$$

it is convenient to use

$$\eta_2 = \frac{P_2 - P_1}{g\Delta\rho}$$
$$\eta_3 = \frac{P_3 - P_2}{g\Delta\rho}$$

where P_i = reduced pressure
= hydrostatic pressure - pressure in absence of relative motion.

The variables are then nondimensionalized as follows: (* denotes a dimensional quantity)

$$(x, y^*) = L(x,y)$$
$$(u^*, v^*) = U(u,v)$$
$$t^* = \frac{L}{U}t \qquad \text{(advective time scale)}$$
$$P_i^* = P_i^* \rho_i U L f \qquad \text{(geostrophic balance)}$$

The governing equations are

$$\frac{D}{Dt}\left[\zeta_1 + F(P_2 - P_1)\right] = 0 \qquad (a)$$
$$\frac{D}{Dt}\left[\zeta_2 + F(P_1 + P_3 - 2P_2)\right] = 0 \qquad (b) \qquad (1)$$
$$\frac{D}{Dt}\left[\zeta_3 + F(P_2 - P_3)\right] = 0 \qquad (c)$$

$\zeta_i = \nabla^2 P_i$ since the P_i are streamfunctions for the horizontal velocity in the respective layers.

The boundary conditions to be used with these equations are

$$P_{ix} = v_i = 0 \qquad \text{at} \qquad y = 0,1 \qquad (a)$$

and

$$\lim_{X \to \infty} \frac{1}{2X}\int_{-X}^{X} P_{iyt}\, dx = 0 \qquad \text{at} \qquad y = 0,1 \qquad (b) \qquad (2)$$

The latter condition is obtained by integrating

$$\varepsilon(u_t + u u_x + v u_y) - v + P_x = 0$$

on the sidewalls (Phillips, (1956)).

Linear Stability Analysis

The stability of the system to small perturbations is investigated by substituting

$$P_i = -U_i y + \phi_i \qquad (3)$$

into (1), and neglecting terms quadratic in ϕ_i. This gives

$$\left(\frac{\partial}{\partial t} + U_1 \frac{\partial}{\partial x}\right)\left[\nabla^2 \phi_1 + F(\phi_2 - \phi_1)\right] + \phi_{1x} F(U_1 - U_2) = 0 \qquad (a)$$

$$\left(\frac{\partial}{\partial t} + U_2 \frac{\partial}{\partial x}\right)\left[\nabla^2\phi_2 + F(\phi_1 - 2\phi_2 + \phi_3)\right] - \phi_{2x} F(U_1 - 2U_2 + U_3) = 0 \qquad (b) \quad (4)$$

$$\left(\frac{\partial}{\partial t} + U_3 \frac{\partial}{\partial x}\right)\left[\nabla^2\phi_3 + F(\phi_2 - \phi_3)\right] - \phi_{3x} F(U_2 - U_3) = 0 \qquad (c)$$

For later reference, the linear operators are denoted L_1, L_2 and L_3 respectively, (i.e. Eqs.(4) (a),(b),(c) are $L_1(\phi_1, \phi_2) = 0$, $L_2(\phi_1, \phi_2, \phi_3) = 0$, and $L_3(\phi_2, \phi_3) = 0$). The shear $U_1 - U_2$ between the upper layers is denoted S_1, and similarly $S_2 = U_2 - U_3$.

Wave solutions satisfying the boundary conditions are

$$\phi_1 = R_e A e^{ik(x-ct)} \sin m\pi y$$

$$\phi_2 = R_e \gamma_2 A e^{ik(x-ct)} \sin m\pi y$$

$$\phi_3 = R_e \gamma_2 \gamma_3 A e^{ik(x-ct)} \sin m\pi y$$

A, c, γ_2 and γ_3 may be complex. c, γ_2 and γ_3 are determined from (4), which leads to

$$(s_1 - a)\left[\gamma_2 - (1+\mu)\right] + S_1 = 0 \qquad (a)$$

$$-a\left[\gamma_2\gamma_3 + 1 - \gamma_2(2+\mu)\right] - \gamma_2(s_1 - S_2) = 0 \qquad (b) \quad (5)$$

$$-(a + S_2)\left[\gamma_2 - \gamma_2\gamma_3(1+\mu)\right] - \gamma_2\gamma_3 S_2 = 0 \qquad (c)$$

where $a = c - U_2$ and $\mu = \frac{m^2\pi^2 + k^2}{F}$. A cubic equation for a is found by eliminating γ_2 and γ_3.

$$a^3 + Pa^2 + Qa + R = 0 \qquad (6)$$

where

$$P = -\frac{(S_1 - S_2)(\mu^2 + 4\mu + 2)}{(1+\mu)(3+\mu)} \quad --$$

$$Q = \frac{(S_1 - S_2)^2(1+\mu) - S_1 S_2(\mu^2 + 2\mu - 2)}{(1+\mu)(3+\mu)}$$

$$R = \frac{\mu(S_1 - S_2)S_1 S_2}{(1+\mu)(3+\mu)}$$

The coefficients of (6) are real, so there will be an exponentially growing wave and an exponentially decaying wave if (b) has complex roots. The criterion for complex roots is

$$q^3 + r^2 > 0 \qquad (7)$$

where $q = \frac{Q}{3} - \left(\frac{P}{3}\right)^2$ and $r = \frac{Q}{2}\frac{P}{3} - \frac{R}{2} - \left(\frac{P}{3}\right)^3$. If $q^3 + r^2 \leq 0$, then all three roots are real and the corresponding waves are neutral. (Note that there is always at least one neutral solution.) If $q^3 + r^2 = 0$, then there is a double root and the system is marginally stable.

To examine the effects of varying the curvature $S_1 - S_2$, it was decided to parameterize the basic state by the curvature and the net shear $S_1 + S_2$. Only $(S_1 - S_2)^2$ and $(S_1 + S_2)^2$ appear in (7), and putting $|S_1 - S_2| = \lambda |S_1 + S_2|$ leads to an equation involving just λ and μ . The structure of the marginal stability curve can then be expressed as two diagrams.

DIAGRAM 2 STABILITY DIAGRAM FOR $|S_1 - S_2| = 1$

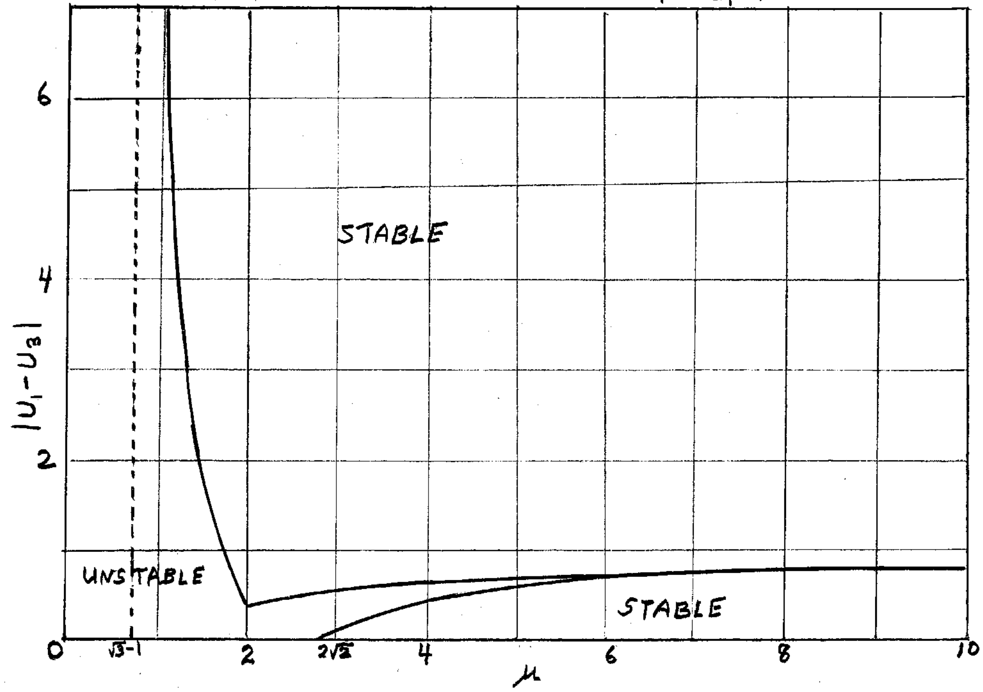

DIAGRAM 3 STABILITY DIAGRAM FOR $|U_1 - U_3| = 1$

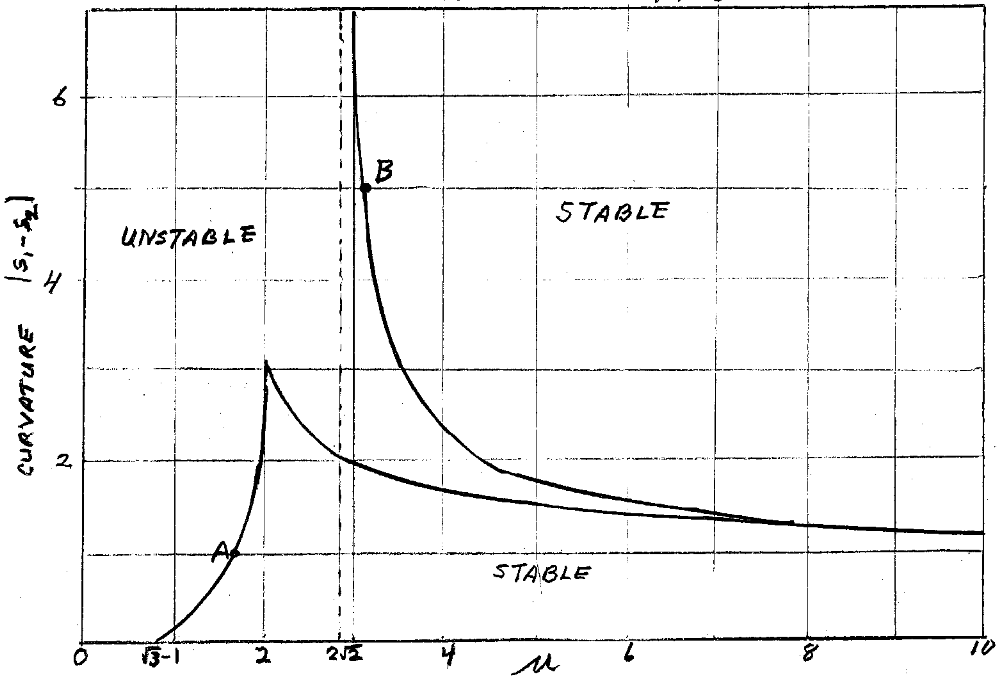

Diagram 2 shows the marginal stability curve with $S_1 + S_2$ fixed and $S_1 - S_2$ and μ varying, and Diagram 3 has $S_1 - S_2$ fixed with $S_1 - S_2$ and μ varying. Four points on these diagrams were found as special simple cases.

(i) $S_1 + S_2 = 0$ leads to $\mu_{\text{crit}} = 2\sqrt{2}$ for all $S_i - S_2$.

(ii) $|S_1 + S_2| = |S_1 - S_2|$ gives a cubic equation for μ_{crit}, with one positive root $\mu_{\text{crit}} = 1{\cdot}709$.

(iii) $S_1 - S_2 = 0$ leads to $\mu_{\text{crit}} = \sqrt{3} - 1$ for all $S_1 + S_2$.

(iv) $|S_1 - S_2| = 3\,|S_1 + S_2|$ leads to $\mu_{\text{crit}} = 2$.

The diagrams show that the system is unstable to conditions with sufficiently small μ. The velocity profile with the smallest μ_{crit} is the one with zero curvature. The addition of any curvature increases μ_{crit}, so curvature has a destabilizing effect compared to zero curvature. The unexpected feature of the diagrams is the appearance of two branches. At present, it has not been determined whether the two branches coalesce or not.

Diagram 3 shows that the effect of curvature on stability is different on the two branches. For small curvature, on the lower branch with $\mu < 2$, μ_{crit} increases as $S_1 - S_2$ increases; but for large $S_1 - S_2$, on the upper branch, μ_{crit} decreases with increasing curvature. It is interesting to note that the peak in Diagram 3 occurs when $\mu_{\text{crit}} = 2$ (case (iv) above), which is the critical value for instability if only two of the three layers were present.

The result for zero curvature (case (iii) can be compared with the stability criteria for the equivalent two-layer and continuous (linear density and velocity profile) systems. Consider a continuous system with total depth H_0 and density difference $\Delta\rho_0$ between the top and bottom surfaces. The system is marginally stable for $\mu_0 = \frac{K^2}{F_0} = 5.76$, where $F_0 = \frac{f^2L^2}{g\frac{\Delta\rho_0}{\rho}H_0}$ and $K^2 = k^2 + m^2\pi^2$. One possible two-level representation of this is a model with two layers of depth $\frac{H_0}{2}$ and density difference $\frac{\Delta\rho_0}{2}$. In this case, $\mu_{2\,\text{crit}} = \frac{K^2}{F_2} + 2$ where $F_2 = \frac{f^2L^2}{g\frac{\Delta\rho_0}{2\rho}\frac{H_0}{2}} = 4F_0$. The three-layer model has layers of depth $\frac{H_0}{3}$ and density differences $\frac{\Delta\rho_0}{3}$. It has been found that $\mu_{3\,\text{crit}} = \frac{K^2}{F_3} = \sqrt{3} + 1$, where $F_3 = \frac{f^2L^2}{g\frac{\Delta\rho_0}{3\rho}\frac{H_0}{3}} = 9F_0$. Hence the two-layer approximation has critical $\frac{K^2}{F_0} = 8$, and the three-layer model has critical $\frac{K^2}{F_0} = 6.6$. Thus, as one would expect, the three-layer system gives a better representation.

Finite-Amplitude Analysis

The dynamics of a disturbance in a two-layer system which is barely unstable (and hence is growing on a time scale much less than the advective time scale) has been extensively studied by Pedlosky (1970, 1971). The same type of analysis can be applied to the three-layer fluid; the present situation with no dissipation or β-effect is the simplest. The development of one growing mode is followed.

Given K^2 and $F = F_c + \Delta$. (Where $K^2/F_c = \mu_{crit}$ and $|\Delta| << F_c$, the growth rate is $O(|\Delta|^{1/2})$. (The situation is comparable to that in the two-layer system - increasing F from R_c causes two neutral modes to change to one growing and one decaying mode.) A new time scale $T = |\Delta|^{1/2} t$ is introduced, and the disturbance $\phi_n(x,y,t,T)$ is expanded as

$$\phi_n = |\Delta|^{1/2}\phi_n^{(1)} + |\Delta|\,\phi_n^{(2)} + \ldots$$

The vorticity equations are written

$$\left(\frac{\partial}{\partial t} + U_1\frac{\partial}{\partial x} + |\Delta|^{1/2}\frac{\partial}{\partial t}\right)\left[\nabla^2\phi_1 + (F_c+\Delta)(\phi_2-\phi_1)\right] + \qquad (a)$$

$$+ \phi_{1x}(F_c+\Delta)s_1 + J\left[\phi_1, \nabla^2\phi_1 + (F_c+\Delta)(\phi_2-\phi_1)\right] = 0$$

$$\left(\frac{\partial}{\partial t} + U_2\frac{\partial}{\partial x} + |\Delta|^{1/2}\frac{\partial}{\partial t}\right)\left[\nabla^2\phi_2 + (F_c+\Delta)(\phi_1-2\phi_2+\phi_3)\right] - \qquad (b) \qquad (8)$$

$$-\phi_{2x}(F_c+\Delta)(s_1-s_2) + J\left[\phi_2, \nabla^2\phi_2 + (F_c+\Delta)(\phi_1+\phi_2-2\phi_2)\right] = 0$$

$$\left(\frac{\partial}{\partial t} + U_3\frac{\partial}{\partial x} + |\Delta|^{1/2}\frac{\partial}{\partial T}\right)\left[\nabla^2\phi_3 + (F_c+\Delta)(\phi_2-\phi_3)\right] - \qquad (c)$$

$$-\phi_{3x}s_2 + J\left[\phi_3, \nabla^2\phi_3 + (F_c+\Delta)(\phi_2-\phi_3)\right] = 0$$

J is the Jacobian operator; $J(f_1, f_2) = f_{1x} f_{2y} - f_{1y} f_{2x}$.

The terms in the above equations represent potential vorticity (p.v.) change due to advection of perturbation p.v. by the basic flow, advection of basic p.v. by the perturbation, growth of perturbation amplitudes, and self-interaction of the perturbations.

To $O(|\Delta|^{1/2})$ (8) gives

$$L_{1c}(\phi_1^{(1)}, \phi_2^{(1)}) = 0$$

$$L_{2c}(\phi_1^{(1)}, \phi_2^{(1)}, \phi_3^{(1)}) = 0$$

$$L_{3c}(\phi_2^{(1)}, \phi_3^{(1)}) = 0$$

where the L_{ic} are the linear operators L_i defined previously, with $F = F_e$. As before, these equations have wave solutions

$$\phi_1^{(1)} = \mathrm{Re}\, A(T) e^{ik(x-ct)} \sin m\pi y$$

$$\phi_2^{(1)} = \gamma_2 \phi_1^{(1)}$$

$$\phi_3^{(1)} = \gamma_2 \gamma_3 \phi_1^{(1)}$$

where c, γ_2 and γ_3 are real and are the solutions of the linear problem with $\mu = \mu_{crit}$. The $O(|\Delta|)$ problem gives

$$L_{1c}(\phi_1^{(2)},\phi_2^{(2)}) = -\frac{\partial}{\partial T}\left[\nabla^2\phi_1^{(1)} + F_c(\phi_2^{(1)}-\phi_1^{(1)})\right] - J\left[\phi_1^{(1)}, \nabla^2\phi_1^{(1)} + F_c(\phi_2^{(1)}-\phi_1^{(1)})\right]$$

$$L_{2c}(\phi_1^{(2)},\phi_2^{(2)},\phi_3^{(2)}) = -\frac{\partial}{\partial T}\left[\nabla^2\phi_2^{(1)} + F_c(\phi_1^{(1)}+\phi_3^{(1)}-2\phi_2^{(1)})\right] - J\left[\phi_2^{(1)}, \nabla^2\phi_2^{(2)} + F_c(\phi_1^{(1)}+\phi_3^{(1)}-2\phi_2^{(1)})\right]$$

$$L_{3c}(\phi_2^{(2)},\phi_3^{(2)}) = -\frac{\partial}{\partial T}\left[\nabla^2\phi_3^{(1)} + F_c(\phi_2^{(1)}-\phi_3^{(1)}) - J\left[\phi_3^{(1)}, \nabla^2\phi_2^{(1)} + F_c(\phi_2^{(1)}-\phi_3^{(1)})\right]\right.$$

The Jacobian terms are all zero because there are no phase shifts between layers to $O(|\Delta|^{1/2})$. The $\frac{\partial}{\partial T}[\cdot\ \cdot\ \cdot]$ inhomogeneities lead to particular solutions of the form

$$\phi_i^{(2)} = \operatorname{Re} A_i^{(2)}(T)e^{ik(x-ct)} \sin m\pi y.$$

The amplitudes $A_i^{(2)}$ must satisfy the matrix equation

$$\begin{bmatrix} \gamma & -1 & 0 \\ 1 & -(\gamma_3+\frac{1}{\gamma_2}) & 1 \\ 0 & -1 & \frac{1}{\gamma_3} \end{bmatrix} \begin{bmatrix} A_1^{(2)} \\ A_2^{(2)} \\ A_3^{(2)} \end{bmatrix} = \frac{1}{ik}\frac{dA}{dT} \begin{bmatrix} -\frac{S_1}{(a-S_1)^2} \\ -\frac{\gamma_2(S_1-S_2)}{a^2} \\ \frac{\gamma_2\gamma_3 S_2}{(a+S_2)^2} \end{bmatrix}$$

(note that c - U_1, c - U_2 and c - U_3 must be non-zero. If one of these is zero (e.g. $S_1 = S_2 \Longrightarrow c = U_2$) then a separate analysis is required). The determinant of the matrix is zero, so the condition for a solution is

$$\frac{dA}{dT}\left[\frac{S_1}{(a-S_1)^2} - \frac{\gamma_2^2(S_1-S_2)}{a^2} - \frac{(\gamma_2\gamma_3)^2 S_2}{(a+S_2)^2}\right] = 0$$

from the linear results. (Equations (5))

It is found that, when $\mu = \mu_{crit.}$,

$$\frac{S_1}{(a-S_1)^2} - \frac{\gamma_2^2(S_1-S_2)}{a^2} - \frac{(\gamma_2\gamma_3)^2 S_2}{(a+S_2)^2} = 0 \tag{9}$$

Hence solutions can be found, with $\frac{dA}{dT}$ not necessarily zero.

The quantities $A_i^{(2)}$ determine the phase shifts between the layers. $A_2^{(2)}$ is arbitrarily set to zero, so the structure of the phase shifts is in the top and bottom layers.

$$A_1^{(2)} = -\frac{1}{\gamma_2}\frac{1}{ik}\frac{S_1}{(a-S_1)^2}\frac{dA}{dT}$$

$$A_3^{(2)} = \frac{\gamma_3}{ik}\frac{(\gamma_3\gamma_2)S_2}{(a+S_2)^2}\frac{dA}{dT}$$

Homogeneous solutions $\Phi_i(y,T)$ must also be included in $\phi_i^{(2)}$. To determine the Φ_i and $A(T)$ the $O(|\Delta|^{3/2})$ analysis is needed. From (8)

$$L_{1c}(\phi_1^{(3)}, \phi_2^{(3)}) = -\frac{\partial}{\partial T}\left[\nabla^2\phi_1^{(2)} + F_c(\phi_2^{(2)} - \phi_1^{(2)})\right] - \frac{\Delta}{|\Delta|}\left(\frac{\partial}{\partial t} + U_1\frac{\partial}{\partial x}\right)(\phi_2^{(1)} - \phi_1^{(1)}) -$$

$$-\frac{\Delta}{|\Delta|}\phi_{1x}^{(1)} S_1 - J\left[\phi_1^{(1)}, \nabla^2\phi_1^{(2)} + F_c(\phi^{(2)}_{(2)} - \phi_1^{(2)})\right] - J\left[\phi_1^{(2)}, \nabla^2\phi_1^{(1)} + F_c(\phi_2^{(1)} - \phi_1^{(1)})\right]$$

$$L_{2c}(\phi_1^{(3)}, \phi_2^{(3)}, \phi_3^{(3)}) = -\frac{\partial}{\partial T}\left[\nabla^2\phi_2^{(2)} + F_c(\phi_1^{(2)} - 2\phi_2^{(2)} + \phi_3^{(2)})\right] - \frac{\Delta}{|\Delta|}\left(\frac{\partial}{\partial t} + U_2\frac{\partial}{\partial x}\right)(\phi_1^{(1)} - 2\phi_2^{(1)} + \phi_3^{(1)}) +$$

$$+\frac{\Delta}{|\Delta|}\phi_{2x}^{(1)}(S_1 - S_2) - J\left[\phi_2^{(1)}, \nabla^2\phi_2^{(2)} + F_c(\phi_1^{(2)} - 2\phi_2^{(2)} + \phi_3^{(2)})\right] - J\left[\phi_2^{(2)}, \nabla^2\phi_2^{(1)} + F_c(\phi_1^{(1)} - 2\phi_2^{(1)} + \phi_3^{(1)})\right]$$

$$L_{3c}(\phi_2^{(3)}, \phi_3^{(3)}) = -\frac{\partial}{\partial T}\left[\nabla^2\phi_3^{(2)} + F_c(\phi_2^{(2)} - \phi_3^{(2)})\right] - \frac{\Delta}{|\Delta|}\left(\frac{\partial}{\partial t} + U_3\frac{\partial}{\partial x}\right)(\phi_2^{(1)} - \phi_3^{(1)}) +$$

$$+\frac{\Delta}{|\Delta|}\phi_{3x}^{(1)} S_2 - J\left[\phi_3^{(1)}, \nabla^2\phi_3^{(2)} + F_c(\phi_2^{(2)} - \phi_3^{(2)})\right] - J\left[\phi_3^{(2)}, \nabla^2\phi_3^{(1)} + F_c(\phi_2^{(1)} - \phi_3^{(1)})\right]$$

The Jacobians contain some inhomogeneities which are independent of x and t, e.g.

$$\mathrm{Re}\, J\left[A e^{ik(x-ct)} \sin m\pi y,\ A_1^{(2)} e^{ik(x-ct)} \sin m\pi y\right]$$

$$= \frac{m\pi}{4} \sin m\pi y \cos m\pi y\, 2ik(AA_1^* - A_1A^*)$$

$$= \frac{m\pi}{4} \sin 2m\pi y\, \frac{1}{\gamma^2}\, \frac{S_1}{(a-S_1)^2}\, \frac{d|A|^2}{dT}$$

(* denotes complex conjugate)

All the inhomogeneities independent of x and t must vanish, because the L_{ic} are operators involving x and t only. This requirement gives differential equations for the Φ_i.

$$\frac{\partial}{\partial T}\left[\Phi_{1yy} + F_c(\Phi_2 - \Phi_1)\right] = \frac{F_c m\pi}{4} \sin 2m\pi y \cdot \frac{S_1}{(a-S_1)^2}\, \frac{d|A|^2}{dT}$$

$$\frac{\partial}{\partial T}\left[\Phi_{2yy} + F_c(\Phi_1 - 2\Phi_2 + \Phi_3)\right] = -\frac{F_c m\pi}{4} \sin 2m\pi y \cdot \gamma_2^2\, \frac{(S_1 - S_2)}{a^2}\, \frac{d|A|^2}{dT}$$

$$\frac{\partial}{\partial T}\left[\Phi_{3yy} + F_c(\Phi_2 - \Phi_3)\right] = -\frac{F_c m\pi}{4} \sin 2m\pi y \cdot \frac{(\gamma_2\gamma_3)^2 S_2}{(a+S_2)^2}\, \frac{d|A|^2}{dT}$$

Solutions which satisfy the boundary conditions (2) are

$$\Phi_1 = \delta A^2\left[D_1 \sin 2m\pi y + m\pi(D_3 - D_1)\frac{\sinh\sqrt{F}(y-\tfrac{1}{2})}{\sqrt{F}\cosh\frac{\sqrt{F}}{2}} + m\pi D_2 \frac{\sinh\sqrt{3F}(y-\tfrac{1}{2})}{\sqrt{3F}\cosh\frac{\sqrt{2F}}{2}}\right]$$

$$\Phi_2 = \delta A^2\left[D_2 \sin 2m\pi y - 2m\pi D_2 \frac{\sinh\sqrt{3F}(y-\tfrac{1}{2})}{\sqrt{3F}\cosh\frac{\sqrt{3F}}{2}}\right]$$

$$\Phi_3 = \delta A^2\left[D_3 \sin 2m\pi y - m\pi(D_3 - D_1)\frac{\sinh\sqrt{F}(y-\tfrac{1}{2})}{\sqrt{F}\cosh\frac{\sqrt{F}}{2}} + m\pi D_2 \frac{\sinh\sqrt{3F}(y-\tfrac{1}{2})}{\sqrt{3F}\cosh\frac{\sqrt{3F}}{2}}\right]$$

where $\delta A^2 = (A(T)^2 - |A(0)|^2)$

$$D_1 = \frac{FD_2}{(4m^2\pi^2+F)} - \frac{Fm\pi}{4}\,\frac{1}{(4m^2\pi^2+F)}\,\frac{S_1}{(a-S_1)^2}$$

$$D_2 = \frac{Fm\pi}{4(4m^2\pi^2+3F)}\,\frac{\gamma_2^2(S_1-S_2)}{a^2}$$

$$D_3 = \frac{FD_2}{(4m^2\pi^2+F)} + \frac{Fm\pi}{4}\,\frac{1}{(4m^2\pi^2+F)}\,\frac{(\gamma_2\gamma_3)^2 S_2}{(a+S_2)^2}$$

Note that $\Phi_1 + \Phi_2 + \Phi_3 = 0$. The Φ_i give the $O(|\Delta|)$ corrections to the basic flow induced by the nonlinear interactions.

$$U_i^{(2)} = -\Phi_{iy}$$

The curvature adjustment is

$$S_1^{(2)} - S_2^{(2)} = (S_1 - S_2)\,\delta A^2\,\frac{3Fm^2\pi^2\gamma_2^2}{2(4m^2\pi^2+3F)a^2}\cdot\left(\cos 2m\pi y - \frac{\cosh\sqrt{3F}(y-\frac{1}{2})}{\cosh\frac{\sqrt{3F}}{2}}\right)$$

This means that where the wave amplitude is largest, | curvature| is decreased if $\delta A^2 > 0$. This is a stabilizing effect for small curvature, but a destabilizing effect for large curvature.

The correction to the net shear is

$$S_1^{(2)} + S_2^{(2)} = U_1^{(2)} - U_2^{(2)} = \delta A^2\left[\frac{S_1}{(a-S_1)^2} + \frac{(\gamma_2\gamma_3)^2 S_2}{(a+S_2)^2}\right]\frac{Fm^2\pi^2}{2(4m^2\pi^2+F)}\left(\cos 2m\pi y - \frac{\cosh\sqrt{F}(y-\frac{1}{2})}{\cosh\frac{\sqrt{F}}{2}}\right)$$

when the wavelike inhomogeneities are written as a Fourier series in $\sin m\pi y$. Terms of the form $\mathrm{Re}\, M_i\, ik e^{ik(x-ct)} \sin m\pi y$ appear. The linear operators give the usual homogeneous solutions $\phi_i^{(3)} = \mathrm{Re}\, A_i^{(3)} e^{ik(x-ct)} \sin m\pi y$. To prevent secular terms appearing (which would make the time scaling invalid), the equation

$$\begin{bmatrix} \gamma^2 & -1 & 0 \\ 1 & -(\gamma_3 + \frac{1}{\gamma_3}) & 1 \\ 0 & -1 & \frac{1}{\gamma^3} \end{bmatrix}\begin{bmatrix} A_1^{(3)} \\ A_2^{(3)} \\ A_3^{(3)} \end{bmatrix} = \begin{bmatrix} \frac{M_1}{F(a-S_1)} \\ -\frac{M_2}{Fa} \\ \frac{M_3}{F(a+S_2)} \end{bmatrix}$$

must have a solution. This requires

$$\frac{M_1}{a-S_1} + \frac{M_2\gamma_2}{a} + \frac{M_3\gamma_2\gamma_3}{a+S_2} = 0$$

An amplitude equation is thus found.

$$\frac{d^2A}{dT^2} = \sigma^2 A - k^2 NA\left(|A|^2 - |A(0)|^2\right) \qquad (10)$$

where $\sigma^2 = \frac{k^2}{F_c} \frac{\Delta}{|\Delta|}\left(1+\gamma_2^2+(\gamma_2\gamma_3)^2\right)\left[\frac{S_1^2}{(a-S_1)^3} + \frac{(\gamma_2\gamma_3)^3 S_2^2}{(a+S_2)^3}\right]$

and
$$N\left[\frac{-a\gamma_2}{\frac{S_1^2}{(a-S_1)^3}+\frac{(\gamma_2\gamma_3)^3 S_2^2}{(a+S_2)^3}}\right]\cdot\frac{1}{(K^2+m^2\pi^2)}\left\{\frac{Fm^2\pi^2}{S_1-S_2}\left(\frac{aS_1S_2}{S_1-S_2}\right)\left(\frac{1}{(a-S_1)^2}-\left(\frac{\gamma_2\gamma_3}{a+S_2}\right)\right)^2+\right.$$
$$+\frac{2Fm^4\pi^4}{4m^2\pi^2+F}\left(\frac{S_1}{(a-S_1)^2}+\frac{(\gamma_2\gamma_3)^2 S_2}{(a+S_2)^2}\right)^2\cdot\left(\frac{1}{4}-\frac{\sqrt{F}\tanh\frac{\sqrt{F}}{2}}{4m^2\pi^2+F}\right)+$$
$$\left.+\frac{2Fm^4\pi^4}{4m^2\pi^2+3F}\,\frac{\gamma_2^4(S_1-S_2)^2}{a^4}\left(\frac{1}{4}-\frac{\sqrt{3F}\tanh\frac{\sqrt{3F}}{2}}{4m^2\pi^2+F}\right)\right\}$$

σ is the growth rate on the time scale T which follows from linear theory. Equation (10) has the same form as one given by Pedlosky (1970) for two layers, and its properties are discussed in detail in that paper. If $N > 0$, then nonlinear effects limit the amplitude growth. If $N < 0$ however, the growth is limited by higher-order interactions. Since $\frac{1}{4} - \frac{\sqrt{X}\tanh\frac{\sqrt{X}}{2}}{4m^2\pi^2+X} > 0$ $(X = F \text{ or } 3F)$

and $\frac{-a\gamma_2}{\left[\frac{S_1^2}{(a-S_1)^3}+\frac{(\gamma_2\gamma_3)^3 S_2}{(a+S_2)^3}\right]} > 0$, then N is certainly positive if $\frac{aS_1S_2}{S_1-S_2} > 0$.

The sign of $\frac{aS_1S_2}{S_1-S_2}$ can be found from the cubic equation for a, by using Descartes rule.

Two particular cases are used to illustrate these results, for marginal stability points on each branch of Diagram 3.

First consider $S_1 = 1$ and $S_2 = 0$. (Point A on Diagram 3).One finds from the linear theory $\mu_{crit} = 1.7$, $a_{crit} = .46$, $\gamma_2 = .85$ and $\gamma_2\gamma_3 = .31$. For a square wave, $(k^2+m^2\pi^2 = 2\pi^2)$ the basic flow changes at $y = \frac{1}{2}$ are

$$U_1^{(2)} = -5.1\,\delta A^2$$
$$U_2^{(2)} = 4.1\,\delta A^2$$
$$U_3^{(2)} = 1.0\,\delta A^2$$

The curvature decreases and the net shear decreases. For $S_2 = 0$, $N > 0$ so the net effect of the interactions is to limit the wave growth. Note that a shear between the bottom two layers has been induced.

The second case is $S_1 = 3$ and $S_2 = -2$. (Point B on Diagram 3.) In this case $\frac{aS_1S_2}{S_1-S_2} < 0$ so N <u>may</u> be negative. One finds $\mu_{crit} = 3.1$, $a_{crit} = 1.3$, $\gamma_2 = 2.3$ and $\gamma_3 = .83$. The mid-channel basic velocity changes for a square wave give

$$S_1^{(2)} - S_2^{(2)} = -31\,\delta A^2$$
$$S_1^{(2)} + S_2^{(2)} = 15\,\delta A^2$$

The evaluation of N yields N = 1.2, so this case also has finite-amplitude stability.

In this finite-amplitude analysis, the possible presence of a neutral mode was ignored. If the neutral mode is included, it is seen that its chance via interactions is very slow compared to the growing mode.

Infinite Depth Bottom Layer

Consider a system with two layers of equal depth H and an infinitely deep third layer, $\rho_2 - \rho_1 = \Delta\rho_1$ and $\rho_3 - \rho_2 = \Delta\rho_2$, and $\Delta\rho$, may be different from $\Delta\rho_2$. The lower shear S_2 is zero. (A more general system is easy to establish, but this special case gives simple algabraic solutions.) Under these conditions, the vorticity equations are

$$\frac{D}{Dt}\left[\nabla^2\phi_1 + F(\phi_2 - \phi_1) + F S_1 y\right] = 0$$

$$\frac{D}{Dt}\left[\nabla^2\phi_2 + F_2(\phi_3 - \phi_2) + F(\phi - \phi_2) - F S_1 y\right] = 0$$

$$\frac{D}{Dt}\nabla^2\phi_3 = 0$$

where

$$F = \frac{f^2 L^2}{g \frac{\Delta\rho_1}{\rho} H} \qquad F_2 = \frac{f^2 L^2}{g \frac{\Delta\rho_2}{\rho} H}$$

The linearized equations have solutions of the usual form

$$\phi_1 = \mathrm{Re}\, A e^{ik(x-ct)} \sin m\pi y$$

$$\phi_2 = \mathrm{Re}\, \gamma_2 A e^{ik(x-ct)} \sin m\pi y$$

$$\phi_3 = \mathrm{Re}\, \gamma_2 \gamma_3 A e^{ik(x-ct)} \sin m\pi y$$

It is found that $\phi_3 = 0$ or $c = U_3$. Hence the interesting unstable modes have $\phi_3 = 0$. The resulting quadratic equation for $a = c - U_2$ is

$$a^2\left[(\mu + \gamma)(\mu + 1) + \mu\right] - S_1 a \mu(\mu + \gamma + 2) + \mu S_1^2 = 0$$

where $\mu = \dfrac{k^2 + m^2\pi^2}{F}$ and $\gamma = \dfrac{\Delta\rho_1}{\Delta\rho_2}$.

This equation has complex roots if

$$\mu^2 + \mu\gamma - 4 < 0 .$$

The critical value for μ is $\frac{\sqrt{\gamma^2 + 16} - \gamma}{2} = \mu_{crit}$ and the system is unstable for

$\mu < \mu_{crit}$. The effect of varying the density differences can be seen. Intuitively one might expect μ_{crit} to decrease as γ decreases, since the lower interface tilts less as $\Delta\rho_2$ is increased. However, $U_2 = U_3$ was specified so the lower interface is always horizontal in the linear theory. The stability criterion shows that μ_{crit} actually increases as γ decreases. In the limit $\gamma \rightarrow 0$, corresponding to $\Delta\rho_2 \rightarrow \infty$, $\mu_{crit} \rightarrow 2$ (the two-layer result). The other limit, $\Delta\rho_2 \rightarrow 0$ gives $\mu_{crit} \rightarrow 0$. This limit models a two-layer system with infinitely deep lower layer, and such a system is always stable.

Conclusions

The effect of curvature in the vertical velocity profile has been studied. A linear stability analysis showed that curvature has a destabilizing influence, and also revealed features that merit further study to find their physical significance. From the analysis of finite-amplitude effects it was found that the basic flow changes produced by nonlinear interactions reduced the magnitude of the curvature. An equation for the amplitude of the unstable mode was derived, and in all cases investigated nonlinear effects limited its growth.

Acknowledgments

I would like to thank Professor Joseph Pedlosky for his enthusiastic help and several discussions. I also wish to thank Professors Melvin Stern and Andrew Ingersoll for their advice on this problem.

References

Eady, E.T. 1949 Long waves and cyclone waves. Tellus 1: 3.

Pedlosky, J. 1970 Finite-amplitude baroclinic waves. J.A.S. 27: 1.

Pedlosky, J. 1971 Finite-amplitude baroblinic waves with small dissipation. J.A.S. 28.

Phillips, N.A. 1956 Energy transformations and meridional circulations associated with simple baroclinic waves in a two-level quasi-geostrophic model. Tellus 6: 3.

STOCHASTIC ANALOGIES TO DIFFUSIVE CLIMATE MODELS

Lawrence C. Kells

1. The Models

In recent years much attention has been given to Budyko-Sellers type radiative-diffusive climate models involving the first few spectral modes (Budyko 1969, Sellers 1969). The prototypical equation is

$$C\frac{\partial\langle I\rangle}{\partial t}+\langle I\rangle-D\nabla^2\langle I\rangle=H$$

where $\langle I(\underline{x},t)\rangle\equiv a+b\langle T\rangle$ is the radiation ensemble averaged over many realizations; $H(\underline{x},t)$ the solar heat source, C the climatic response time to solar heating and D an empirical diffusion coefficient. (We ignore ice feedback and atmospheric-ocean coupling.) The solution in Fourier components is

$$\langle I_{\underline{k}\omega}\rangle=\frac{H_{\underline{k}\omega}}{1+i\omega C+k^2D}.$$

This is found to give accurate results for low-order spectral approximations but it is not improved when high-order modes are included. (North 1975). There is no direct physical basis for assuming a diffusion process. This paper seeks to discover a mathematical analogy to determine the extent of validity of this approximation.

The model we will explore assumes advection by a random atmospheric velocity:

$$C\frac{\partial I}{\partial t}+C\underline{v}\cdot\nabla I+I=H \qquad (1)$$

$\underline{v}(x,t)$ is a Gaussian zero-mean stationary, homogeneous field with auto-correlation time and length scales typical of vertically-averaged large scale weather patterns. (The mean zonal wind velocity is subtracted out.) If these scales are much smaller than those of the source and response terms, then advective transport of I by v is analogous to transport by molecular Brownian motion, leading to diffusive behavior. The key question is, how small can the scales of I become before v no longer behaves like diffusion?

2. The Basic Solution.[1]

We Fourier analyze Eq.(1):

$$(1+i\omega C)I_{\underline{k}\omega}+C\iint i\underline{p}\cdot\underline{V}_{\substack{\underline{k}-\underline{p}\\ \omega-\omega_1}}I_{\underline{p}\omega_1}\,d\underline{p}\,d\omega_1=H_{\underline{k}\omega}$$

or

$$(1+i\omega C)I_{\underline{k}\omega}+m_{\substack{\underline{k}\underline{p}\\ \omega\omega_1}}I_{\underline{p}\omega_1}=H_{\underline{k}\omega} \qquad (2)$$

Thus $\underline{I}=S_0(\underline{H}-\underline{\underline{m}}\,\underline{I})$

where $m_{\substack{\underline{k}\underline{p}\\ \omega\omega_1}}=Ci\underline{p}\cdot\underline{V}_{\substack{\underline{k}-\underline{p}\\ \omega-\omega_1}}$ and $S_0=(1+i\omega C)^{-1}$. (3)

The convolution in (2) precludes a closed-form solution. The task of this paper is to expand the solution into a (divergent) power series and to sum suita-

---

[1] This section is a summary of North (1976).

ble subsets of this series to approximate the solution and compare it to the solution of (1). (For background from the theory of ordinary turbulent diffusion see Kraichnan 1970a, b.)

Iterating (3) gives

$$\underline{\underline{I}} = S_0 H - S_0 \underline{\underline{m}} S_0 \underline{H} + S_0 \underline{\underline{m}} S_0 \underline{\underline{m}} S_0 H - \dots$$

From now on we will be interested only in ensemble averages, not individual realizations, so, using the fact that $\underline{\underline{m}}$ has zero mean,

$$\langle \underline{\underline{I}} \rangle = S_0 \underline{H} + S_0 \langle \underline{\underline{m}} S_0 \underline{\underline{m}} \rangle S_0 \underline{H} + S_0 \langle \underline{\underline{m}} S_0 \underline{\underline{m}} S_0 \underline{\underline{m}} S_0 \underline{\underline{m}} \rangle S_0 \underline{H} + \dots$$

We can develop a Feynman diagram notation as follows (Orszag 1974):

$$\langle \underline{\underline{I}} \rangle = —\chi + —\langle o—o \rangle —\chi + —\langle o—o—o—o \rangle —\chi + \dots$$

where —— $= S_0$, $o = \underline{\underline{m}}$ and $\chi = H$. We also introduce $\langle o—o \rangle \equiv$ 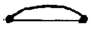 .
By a standard property of Gaussian fields then

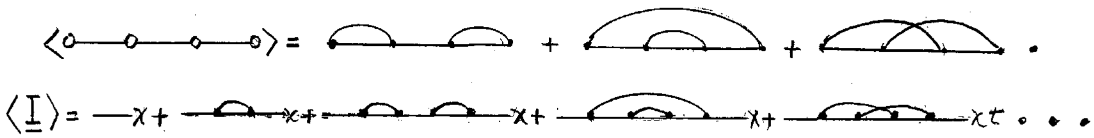

Our purpose is to sum subsets of this series consisting of terms which factor into the terms shown here (as  factors to ( $)^2$).

The first step is to find $S_2 \equiv$  for a twoOdimensional incompressible flow. In longhand

$$S_2 = \iint \langle m_{\substack{\underline{k}\underline{k}_1 \\ \omega\omega_1}} \frac{1}{1+i\omega_1 C} m_{\substack{\underline{k}_1\underline{k}_2 \\ \omega_1\omega_2}} \rangle \, d\underline{k}_1 \, d\omega_1$$

$$= -C^2 \iint \underline{k} \cdot \langle \underline{V}_{\substack{\underline{k}-\underline{k}_1 \\ \omega-\omega_1}} \underline{V}_{\substack{\underline{k}_1\underline{k}_2 \\ \omega_1-\omega_2}} \rangle \cdot \underline{k}_2 \frac{d\underline{k}_1 \, d\omega_1}{1+i\omega_1 C}$$

where we have used the incompressibility condition $(\underline{k}-\underline{k}_1)\cdot\underline{V}_{\substack{k-k_1 \\ \omega-\omega_1}} = 0$.

We must examine the quantity $\langle \underline{V}_{\substack{\underline{k} \\ \omega}} \underline{V}_{\substack{\underline{k}' \\ \omega'}} \rangle$. This must be an isotropic, incompressible, stationary homogeneous tensor. It can be shown from the properties of $\underline{v}$ that the only possible form is $V_r^2 R_{\substack{\underline{k} \\ \omega}} \delta(\underline{k}+\underline{k}') \, \delta(\omega+\omega')(\delta_{ij} - \frac{k_i k_j}{k^2})$ where V_r is the root mean square fluctuating velocity. $R_{\substack{\underline{k} \\ \omega}}$ is the Fourier transform of $\rho(\underline{x}, t)$ which is an empirical estimate of the magnitude of $\langle \underline{V}(\underline{x}', \underline{t}') \underline{V}(\underline{x}+\underline{x}', t+t') \rangle$.

Through Section 4 we will use only δ_{ij} in the tensor part of $\underline{\underline{R}}$, in order to simplify the calculations, as did North. This will change the results by a numerical factor which is inconsequential here. When we specify $R_{\substack{\underline{k} \\ \omega}}$ explicitly we will reinstate $-\frac{k_i k_j}{k^2}$ in order to get the correct numerical results.

Thus

$$S_2 = -K^2 V_r^2 C^2 \delta_{\underline{k}\underline{k}_2} \delta_{\omega\omega_2} \frac{1}{8\pi^3} \iint \rho(\underline{x},t) e^{-i(\underline{k}-\underline{k}_1)\cdot\underline{x} - i(\omega,\omega_1)t} \, d\underline{x} \, d\underline{k}_1 \, \partial t \, \frac{\partial\omega_1}{1+i\omega_1 C}$$

(where δxy is shorthand for $\partial(x-y)$)

$$= -K^2 V_r^2 C \partial_{\underline{k}\underline{k}_2} d_{\omega\omega_2} \int_0^\infty \rho(\underline{0},t) e^{-t(i\omega+\frac{1}{\tau})} dt$$

$$\equiv -K^2 \delta_{\underline{k}\underline{k}_2} d_{\omega\omega_2} D_0(\omega).$$

This result permits us to sum the "bubble subset"

$$\Sigma_2 \equiv \left(\cdots + \cdot \cdot \cdot \right)_{\underline{k}\omega} = \frac{1}{1+i\omega C + K^2 D_0(\omega)}$$

a diffusion-like operator which is a function of ω . Now suppose

$$\rho(0,t) = e^{-\frac{t}{\tau}} \qquad \tau \left| i\omega + \frac{1}{c} \right| << 1 .$$

$$D_0(\omega) = V_r^2 C \left(\frac{1}{\tau} + i\omega + \frac{1}{c} \right)^{-1} \approx V_r^2 C \tau .$$

Thus if the autocorrelation time τ is small enough, $D_0(\omega)$ becomes the classical Taylor diffusion coefficient D.

3. Ond Dimensional Compressible Flow.

Before proceeding further down this line we shall generalize this result - first to those one-dimensional climate models, where the incompressibility assumption would be too restrictive. So

$$S_2 = -V_r^2 C^2 \delta_{kk_2} \delta_{\omega\omega_2} \iint K_1 R_{\substack{k-k_1 \\ \omega-\omega_1}} K_2 \frac{d_{k_1} d\omega_1}{1+i\omega_1 C}$$

(where K_1 remains inside the integral)

$$= -\frac{k V_r^2 C^2 \partial_{kk_2} \partial_{\omega\omega_2}}{2\pi i} \iint \rho(x,t) e^{-ikx - i(\omega-\omega_1)t} \frac{d}{dx} \delta(x) \, dx \, dt \, \frac{d\omega_1}{1+i\omega_1 C}$$

The x integral is $-\frac{\partial\rho}{\partial x} \big\rangle_{x=0} + ik\rho(0,t)$. If $\frac{\partial\rho}{\partial x}$ exists and is equal to zero at x = 0 then this reduces to the incompressible result.

4. Spherical Geometry

Since most climate models are framed in spherical coordinates, it is reassuring to know that analogous results can be found for a sphere. The coordinates are (r, θ, φ), however, we will use the surface of the sphere where r = 1. θ is the colatitude and φ the longitude. We will expand in spherical harmonics $Y_\ell^m(\theta,\varphi) = p_\ell^m(\cos\theta) e^{im\varphi}$ where $\ell \geq 0, |m| \leq \ell$, and p_ℓ^m is the associated Legendre function. These functions have the following useful properties:

$$\oint Y_\ell^m(\hat{r}) Y_{\ell'}^{m'*}(\hat{r}) \, d\Omega = \delta_{\ell\ell'} \delta_{mm'}$$

$$\sum_{\ell,m} Y_\ell^m(\hat{r}) Y_\ell^{m*}(\hat{r}_1) = \frac{d_{\hat{r}\hat{r}_1}}{\sin\theta}$$

$$\nabla^2 Y_\ell^m = -\ell(\ell+1) Y_\ell^m$$

So expanding I and H in $Y_{\ell'}^{m'}$, Fourier transforming in ω', multiplying by $Y_\ell^{m*}(\hat{\underline{r}})e^{-i\omega t}$ and integrating yields

$$(1+i\omega C)I_{\ell m \omega} + C\sum_{\ell' m'} \oint \int \underline{V}_{\omega-\omega'}(\hat{\underline{r}}) I_{\ell' m' \omega'} \cdot (\nabla Y_{\ell'}^{m'}(\hat{\underline{r}})) Y_\ell^{m*}(\hat{\underline{r}})\, d\omega' d\Omega = H_{\ell m \omega}$$

Thus $\mathcal{M}_{\substack{\ell m \omega \\ \ell' m' \omega'}} = C \oint \underline{V}_{\omega-\omega'}(\hat{\underline{r}}) - (\nabla Y_\ell^{m'}(\hat{\underline{r}})) Y_\ell^{m*}(\hat{\underline{r}})\, d\Omega$

where $d\Omega = \sin\theta\, d\theta\, d\varphi$

and (again using the simplified, incompressible $\underline{\underline{R}}$),

$$S_2 = C^2 V r^2 \delta_{\omega\omega_2} \sum_{\ell' m'} \int \oint\oint \nabla\left(Y_{\ell_1}^{m_1}(\hat{\underline{r}}) Y_{\ell_1}^{m_1 *}(\hat{\underline{r}}_1)\right) \cdot \underline{\underline{R}}_{\omega-\omega_1}(\hat{\underline{r}}-\hat{\underline{r}}_1) \cdot \nabla_1 Y_{\ell_2}^{m_2}(\hat{r}_1)\, Y_\ell^{m*}(\hat{\underline{r}}) \frac{d\Omega\, d\Omega_1\, d\omega_1}{1+i\omega_1 C}$$

$$= -\ell(\ell+1) C V_r^2 \delta_{\ell\ell_2} \partial_{mm_2} \partial_{\omega\omega_2} \int_0^\infty \rho(0,t) e^{-t(i\omega+\frac{1}{c})} dt$$

and $\Sigma_2 = \dfrac{1}{1+i\omega C + \ell(\ell+1) D_0(\omega)}$

From this result it seems reasonable that all computations in Cartesian coordinates have their spherical analogues through replacing K^2 by $\ell(\ell+1)$, and this assumption is implicit as we return to the simpler rectangular coordinates for the remainder of this paper.

5. Integral of a Gaussian Distribution.

Let $\rho(\underline{x},t) = e^{-\frac{x^2}{\ell^2} - \frac{t^2}{\tau_a^2}}$ where $\frac{\sqrt{\pi}}{2}\ell$ and $\frac{\sqrt{\pi}}{2}\tau_a$ represent autocorrelation length and time scales. Then $\underline{\underline{R}}_{\underline{K}\omega} = \frac{1}{8\pi^{3/2}} \ell^2 \tau_a e^{-\frac{1}{4}(K^2\ell^2+\omega^2\tau_a^2)} (\delta_{ij} - \frac{K_i K_j}{K^2})$

and

$$S_2 = -V_r^2 C^2 \partial_{\underline{K}\underline{K}_2} \partial_{\omega\omega_2} \frac{\ell^2\tau_a}{8\pi^{3/2}} \iint e^{-\frac{1}{4}(p^2\ell^2+(\omega-\omega_1)^2\tau_a^2)} K_i (\delta_{ij} - \frac{p_i p_j}{p_2}) K_j \frac{d\underline{p}\, d\omega_1}{1+i\omega_1 C}$$

$$= -K^2 V_r^2 c^2 \delta_{\underline{K}\underline{K}_2} \delta_{\omega\omega_2} \frac{\ell^2\tau_a}{8\pi^{3/2}} \iint_{\theta=0}^{2\pi} e^{-\frac{1}{4}(p^2\ell^2+(\omega+\omega_1)^2\tau_a^2)} p \sin^2\theta \frac{d\theta\, dp\, d\omega_1}{1+i\omega_1 C}$$

$$= -K^2 V_r^2 c\, \delta_{\underline{K}\underline{K}_2} \delta_{\omega\omega_2} \frac{1}{2} \int_0^\infty e^{-t^2/\tau_a^2 - (i\omega+\frac{1}{c})t} dt$$

(where we used $e^{-\frac{1}{4}(\omega-\omega_1)^2\tau_a^2} = \frac{1}{\sqrt{\pi}\,\tau_a} \int e^{-t^2/\tau_a^2 - i(\omega-\omega_1)t} dt$)

$$= -K^2 V_r^2 c\, \delta_{\underline{K}\underline{K}_2} \partial_{\omega\omega_2} \frac{\sqrt{\pi}}{4} \tau_a e^{\frac{A^2}{4}} \operatorname{erfc} \frac{A}{2} \text{ where } A = \tau_a(i\omega + \tfrac{1}{c}).$$

(Note that keeping $-\frac{K_i K_j}{K_2}$ resulted in an extra factor of ½). Expanding in A,

$$D_0(\omega) = V_r^2 C \frac{\sqrt{\pi}}{y} \tau_a (1 - \frac{1}{\sqrt{\pi}} A + \frac{1}{4} A^2 + \ldots).$$

If A is small then D_0 is relatively independent of ω , in accord with the remarks ending Section 2.

6. Fourth Order Contributions.

To include a larger subset of the series in our sum, we may compute the fourth order contributions $S_{4,2} \equiv$  and $S_{4,3} \equiv$  and thus the series consisting of all possible chains formed from these and S_2. We will find a renormalization $D_2(\ )$ to the k^2 term as well as a k^4 term $D_2^{(2)}(\omega)$. The result will look like

$$\Sigma_4 = \frac{1}{1 + i\omega C + K^2\left(D_0(\omega) - D_2(\omega)\right) - K^4 D_2^{(2)}(\omega)}$$

The fourth order graphs yield to the same method as the second order; the manipulations are slightly trickier and considerably more tedious, but require no new techniques. The results:

$$S_{4,2} = \left(K^4 + \frac{4K^2}{\ell^2}\right) V_r^4 C\, \delta_{\underline{k}\underline{k}_4} \delta_{\omega\omega_4} \tau_a^3 \frac{\sqrt{\pi}}{8\sqrt{2}} e^{\frac{1}{8}A^2} \int_0^\infty t\, e^{-\frac{1}{2}t^2 - \frac{1}{2}At}\, \mathrm{erfc}\left(\frac{t}{\sqrt{2}} + \frac{A}{2\sqrt{2}}\right) dt$$

$$= \left(K^4 + \frac{4K^2}{\ell^2}\right) V_r^4 C\, \delta_{\underline{k}\underline{k}_4} \delta_{\omega\omega_4} \tau_a^3 \frac{\sqrt{\pi}}{16} \left(\sqrt{2} - 1 - \frac{\sqrt{\pi}}{4} A + \ldots\right)$$

$$S_{4,3} = K^4 V_r^4 C\, \delta_{\underline{k}\underline{k}_4} \delta_{\omega\omega_4} \tau_a^3 \frac{\sqrt{\pi}}{4} e^{\frac{1}{4}A^2} \frac{1}{A} \int_0^\infty e^{-t^2}\left(1 - e^{-At}\right) \mathrm{erfc}\left(t + \tfrac{1}{2}A\right) \partial t$$

$$= K^4 V_r^4 C\, \delta_{\underline{k}\underline{k}_4} \delta_{\omega\omega_4} \tau_a^3 \frac{\sqrt{\pi}}{16} \left(2 - \sqrt{2} - \left(\frac{1}{2\sqrt{\pi}} + \frac{\sqrt{\pi}}{4}\right) A + \ldots\right)$$

Note that the entire renormalization to k^2 comes from

On a scale where $D_0(0) = 1$

$$D_2(0) = \left(\sqrt{2} - 1\right) V_r^2 \frac{\tau_a^2}{\ell^2}$$

$$K^2 D_2^{(2)}(0) = \frac{1}{4} K^2 V_r^2 \tau_a^2 \quad (\text{from } S_{4,2} + S_{4,3})$$

For diffusion to be valid the first requirement is that $|A| \ll 1$ so that $D_0(\omega)$ is constant. That is, the autocorrelation time of $\underline{V}$ must be much shorter than the time scales of the forcing function H and climatic response C. The second requirement is that $\frac{1}{K} \gg \frac{1}{2} V_r \tau_a$ so that the k^4 form is small. Physically this means that the spectral mode must have a much larger length scale than the distance the r.m.s.-velocity wind would travel in one autocorrelation time. If this fails then the diffusion equation must have added terms such as $\nabla^4 \langle I \rangle$.

One might take interest as to whether the k^2 remormalization is small, $D_2 \ll D_0$. This requires $V_r \ll \frac{\ell}{\tau_a}$ but in fact there is no reason this should be the case; it is much more plausible that $V_r \sim \frac{\ell}{\tau_a}$. Thus D_0 is not a good approximation to D. (This is not as detrimental as it seems, because in practice is determined empirically to give the best fit, automatically including every possible renormalization from graphs of all orders.) Note that the ratio $\frac{D_2}{D_0}$ is determined solely by the given properties of $\underline{V}$, independent of K, ω and $\mathcal{C}$.

7. Geophysical Significance.

We now come to the place of inserting actual numbers into the equations. Despite the simplifications and approximations, not the least of which is truncating the series at fourth-order graphs, we will obtain a result (using values) chosen *a priori*) which corresponds in a satisfying way with observations.

We are primarily interested in meridional diffusion even in a two-dimensional model. This is the basis for our choices:

$\sqrt{\frac{\pi}{2}}\,\tau_a$ = three days (period of typical Rossby wave)
$\sqrt{\frac{\pi}{2}}\,\ell$ = 1000 km (meridional extent of typical Rossby wave)
V_r = 10 m $\sec^{-1}$ (typical meridional wind speed)
C = 30 days (standard value)
ω^{-1} = 60 days (annual cycle)

This yields $|A| = .11$, the first desirable result. Now the value of k chosen should be the largest considered in the model, to get the largest contribution to k^4. In a two-mode model, the highest has a cycle corresponding to the earth's diameter; $k^{-1} \doteq 2000$ km. In a four-mode model, $k^{-1} = 1000$ km. In the first case, with $D_0(0)$ scaled as unity, $D_2(0) = 2.8$, $K^2 D_2^{(2)}(0) = .53$ and the crucial ratio $\frac{K^2 D_2^{(2)}}{D_2 - D_0} = .30$. This means that we satisfy the condition for a small K^4 term, but not by much. If we use K from the four-mode model, this ratio becomes 1.2 and it is no longer possible to absorb the k^4 term into the diffusion coefficient, which is also observed to occur in practice.

It should be noted that this conclusion is highly speculative inasmuch as the renormalization is larger than the original diffusion, thus causing D to change sign. (Of course this does not imply that the stochastic model is equivalent to backwards diffusion; it merely says that it is not useful for determining the size of D.) One can however conjecture that this order of magnitude estimate of the ratio of the k^4 to k^2 terms will stand up upon inclusion of contributions from higher-order graphs, and indeed the entire series. (Our choices of numbers were on the pessimistic side already, and renormalizations involve more derivatives of ρ - which are larger in magnitude - than do higher powers of k.)

8. Further Research.

Besides the endless refinements which can be made in these calculations, there are further topics which more time would make worthwhile investigating. First would be an evaluation of the Direct Interaction Approximation for this equation. (See Kraichnan 1970a, b; Orszag (1974)). This would include every nested bubble like $S_{4,2}$ and possibly every contribution to k^2. Still another approach would be to add and subtract $D\nabla^2 I$ from Eq.(1) and expand the perturbation series in $D\nabla^2 I + \underline{V}\cdot\nabla I$ which would be a smaller parameter than $\underline{\underline{\mathcal{M}}}$, containing only the departure from diffusion.

Another interesting extension of the problem would be to evaluate $\langle I(x,t)I(x't')\rangle$, and thus the variance of the climate, by using similar methods on the equation for I^2 as we used for I.

Acknowledgments

I am indebted to Gerald R. North for introducing me to this problem and providing many valuable discussions, and to Joseph B. Keller for his helpful comments and suggestions. My thanks also to Mary Thayer for her typing and editing, and to the other nine Geophysical Fluid Dynamics students for their warm friendship.

References

Budyko, M.I. 1969.The Effect of Solar Radiation Variations on the Climate of the Earth. *Tellus* *21*: 611.

Kraichnan, R.H. 1970a. Turbulent Diffusion: Evaluation of Primitive and Renormalized Perturbation Series by Padé Approximants. *The Padé Approximent in Theoretical Physics*. G.A.Baker and J.L.Gammel, eds. N.Y.Acad.Press. p.129.

Kraichnan, R.H. 1970b. Diffusion by a Random Velocity Field. *Phys.Flu.* *13*: 22.

North, G.R. 1975 Theory of Energy-Balance Climate Models. *J.Atmos.Sci.* *32*: 2033.

North, G.R. 1976 Analytical Behavior of Climate Models. 1976 G.F.D. Lectures. (to be published).

Orszag, S.A. 1974 Flow Research Report No.31. *Lectures on the Statistical Theory of Turbulence*. Cambridge, Mass., Flow Research Inc.

Sellers, W.D. 1967 A Climate Model Based on the Energy Balance of the Earth-Atmosphere System. *J.Appl.Meteor.* *8*: 392.

SOME ASPECTS OF ROTATING WEIR FLOWS

Trevor J. McDougall

The behavior of a flow over a weir in a wide, rotating channel is examined and criteria are developed for (i), stagnation on either of the walls, and (ii), the height on the left wall going to zero (called "bottoming"). The conditions are derived under which a flow which wets both walls upstream, may develop into a bottomed flow downstream. These conditions imply that bottoming cannot occur before the crest of the weir, and noting this solubility constraint, together with the principle of maximum discharge gives an extra relation between the flow variables. The nature of "critical flow" in a very narrow channel, and also over a weir without boundaries is also discussed.

Flow over a Weir in a Wide Channel

Let us consider the flow of a fluid down a channel in which the floor rises to form a broad-crested weir as shown in Fig.1. (The fluid comes from a reservoir into the channel in some complicated way as shown in Fig.1. Farther down the channel cu-position (B), where the cross-stream velocities are small, the motion will be in geostrophic balance across the channel.) We will restrict our concern

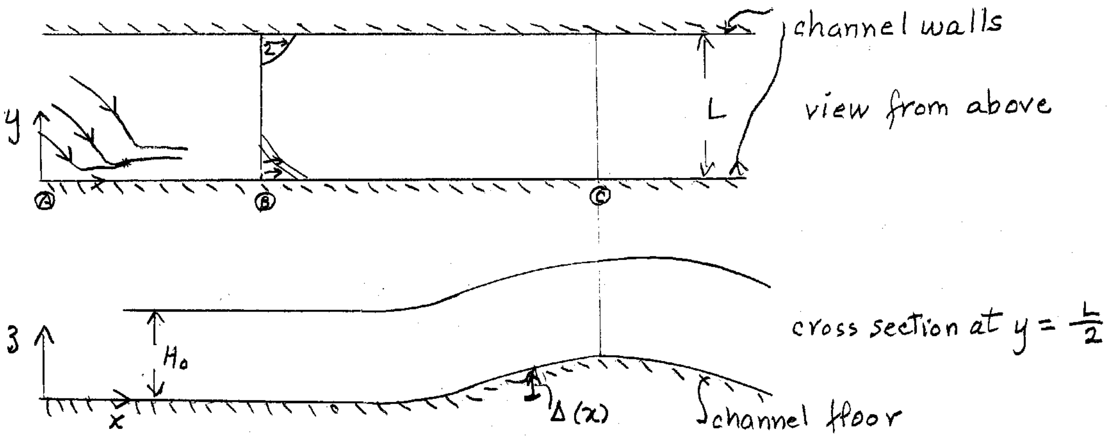

FIG. 1.

to the case where the channel width L is much larger than the upstream radius of deformation.

In our discussion we will assume that all the flow has originated from upstream and that at no position do we have negative downchannel velocities. We further assume that all the streamlines have the same potential vorticity and so the equation of conservation of potential vorticity reduces to

$$\frac{f+\xi}{h} = \frac{f-u_y}{h} = \frac{f}{H_o} \tag{1}$$

We have neglected the v_x term in the relative vorticity here because we assume that the channel depth varies very slowly in the downstream direction (i.e. $\Delta_x \ll 1$). Because of this the cross-stream momentum equation reduces to the geostrophic balance.

$$u = \frac{-g}{f}(h+\Delta)_y = \frac{-g}{f}h_y \tag{2}$$

where we restrict Δ to be a function of x only.

The volume flow rate, Q, must be the same at each cross section.

$$Q = \int_0^L hu\,dy = \frac{-g}{f}\int_0^L h h_y\,dy \quad (\text{from } (2))$$

Therefore

$$h_r^2 - h_\ell^2 = 2\frac{fQ}{g} \equiv H_Q^2 \tag{3}$$

where h_r and h_ℓ are the heights above the channel floor of the fluid on the right and left walls respectively, and we have introduced the constant H_Q for convenience.

The Bernoulli equation is $\frac{1}{2}u^2 + g(h+\Delta) = B(\Psi)$

but we introduce alternate Bernoulli constants H_r and H_e on the right and left-hand walls, respectively, defined by

$$\begin{aligned} \frac{1}{2}u_\ell^2 + g(h_e+\Delta) &= gH_e \\ \frac{1}{2}u_r^2 + g(h_r+\Delta) &= gH_r \end{aligned} \tag{4}$$

Now the four constants H_r, H_e, H_0 and H_Q which describe the flow at position (B) (Fig.1) are not independent. Fofonoff (1974) has shown that if $-\psi$ is the mass flux stream function, $B(\psi)$ is the Benoulli function and $F(\psi)$ is the potential vorticity (both of which are conserved along streamlines), then these are related by

$$F(\psi) = \frac{dB}{d\psi} \tag{5}$$

In our case $F(\psi)$ = constant = $\frac{f}{H_0}$ and so we can integrate (5) to obtain

$$B(\psi) = \frac{f}{H_0}\psi + B(0) \text{ where } B(0) = gH_r . \tag{6}$$

Let $\psi = 0$ at $y = 0$. From the definition of ψ , we have $hu = -\psi_y$; and integrating this across the channel, we have

$$\psi(L) - \psi(0) = \psi(L) = \frac{g}{2f}\left(h_e^2 - h_r^2\right) \text{ or } \psi(L) = -Q$$

Hence we have a relation between the four constants, namely

$$H_e = H_r - \frac{fQ}{gH_0} \text{ or } \frac{H_e}{H_0} = \frac{H_r}{H_0} - \frac{1}{2}\left(\frac{H_Q}{H_0}\right)^2 \tag{7}$$

Now from (1) and (2) we have

$$h_{yy} - \frac{1}{\lambda^2}h = \frac{-f^2}{g} \quad \text{where } \lambda = \frac{\sqrt{gH_0}}{f}$$

$$\text{i.e.} \quad (h - H_0)_{yy} - \frac{1}{\lambda^2}(h - H_0) = 0 \tag{8}$$

This equation has solutions

$$h - H_0 = A\cosh\left(\frac{y}{\lambda}\right) + B\sinh\left(\frac{y}{\lambda}\right)$$

The constants A and B can be found in terms of h_r and h_e and we then obtain

$$h - H_0 = (h_r - H_0)\frac{\sinh\left(\frac{L-y}{\lambda}\right)}{\sinh\frac{L}{\lambda}} - (H_0 - h_e)\frac{\sinh\frac{y}{\lambda}}{\sinh\frac{L}{\lambda}} \tag{9}$$

From (2) and (9) we obtain the velocity

$$u = \sqrt{gH_0}\left\{\left(\frac{h_r}{H_0} - 1\right)\frac{\cosh\left(\frac{L-y}{\lambda}\right)}{\sinh\frac{L}{\lambda}} + \left(1 - \frac{h_e}{H_0}\right)\frac{\cosh\frac{y}{\lambda}}{\sinh\frac{L}{\lambda}}\right\} \tag{10}$$

Now for $L >> \lambda$, Eqs. (9) and (10) describe a flow which is almost quiescent in the middle of the channel, with boundary layers on the left and right walls. From (10) we see that for $L >> \lambda$

$$u_r \rightarrow \sqrt{gH_0}\left(\frac{h_r}{H_0} - 1\right) \text{ and } u_e \rightarrow \sqrt{gH_0}\left(1 - \frac{h_e}{H_0}\right) \tag{11}$$

In this limit we can use these values for the velocity in the Benoulli relations to obtain h_r and h_e as functions of the flow constants and $\Delta(x)$.

$$\frac{h_r}{H_0} = \sqrt{\frac{2(H_r - \Delta)}{H_0} + 1} \text{ and } \frac{h_e}{H_0} = \sqrt{\frac{2H_r - \Delta}{H_0} - 1 - \left(\frac{H_Q}{H_0}\right)^2} = \sqrt{2\frac{H_e - \Delta}{H_0} - 1} \tag{12}$$

The complete solutions for $h(y)$ and $u(y)$ in terms of the flow constants and are given by Eqs. (9) and (10) in conjunction with Eq. (2).

$$h-H_0=H_0\left\{\sqrt{\frac{2(H_r-\Delta)}{H_0}-1}\qquad -1\right\}\frac{\sinh\frac{L-y}{\lambda}}{\sinh\frac{L}{\lambda}}-H_0\left\{1-\sqrt{\frac{2H_r-\Delta}{H_0}-1-\left(\frac{H_Q}{H_0}\right)^2}\right\}\frac{\sinh\frac{y}{\lambda}}{\sinh\frac{L}{\lambda}}$$

Consider now what happens as the flow proceeds down the channel from point (B), and has started to rise up the bump. Equations (12) show that both H_r and H_e decrease as Δ increases, while from (9) and (10) we see that in the middle of the channel, the fluid's height is still H_0 and the down-channel velocity is vanishingly small. Some of the streamlines that were in the right wall boundary layer have now moved across the channel and this explains how the fluid in the middle of the channel now has a larger Benouilli head than before (by an amount Δ). This veering of the streamlines to the left as the fluid rises over the bump is shown diagrammatically in Fig.2.

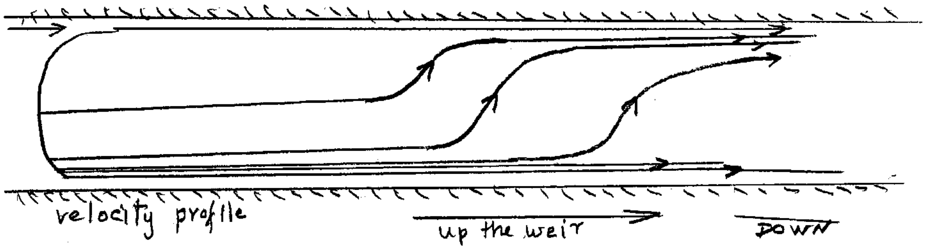

FIG. 2.

In the middle of the channel, u, u_x and u_y are all very small and so the cross-stream velocity can be obtained by the geostrophic relation $-f v=-g(h+\Delta)_x$ and since $h \approx H_0$ = constant here, then $v=\frac{g}{f}\Delta x$.

Conditions necessary to have both walls wetted.

We require that there be no reverse flow in the down-channel direction and Eqs.(11) show that this implies that $h_r \geqslant H_0$ and $h_e \leqslant H_0$. From (10) we can see that two criteria imply that u(y) will not be negative at any y. Those two conditions give (from (12))

$$\frac{H_r}{H_0}-\frac{1}{2}\left(\frac{H_Q}{H_0}\right)^2-1\leq\frac{\Delta}{H_0}\leq\frac{H_r}{H_0}-1 \text{ i.e. } \frac{H_e}{H_0}-1\leq\frac{\Delta}{H_0}\leq\frac{H_r}{H_0}-1 \qquad (13)$$

A third restriction comes from requiring both walls to be wetted (i.e., requiring $h_e \geqslant 0$). From (3) this implies that

$$\left(\frac{h_r}{H_0}\right)^2\geq\left(\frac{H_Q}{H_0}\right)^2 \text{ i.e. } \frac{\Delta}{H_0}\leq\frac{H_r}{H_0}-\frac{1}{2}\left(\frac{H_Q}{H_0}\right)^2-\frac{1}{2}=\frac{H_e}{H_0}-\frac{1}{2} \qquad (14)$$

The left-hand sides of the inequalities in (13) have to apply at all x , and so the most stringent condition to avoid reverse flow on the left wall occurs upstream where $\Delta = 0$, namely

$$\frac{H_r}{H_0}\leq 1+\frac{1}{2}\left(\frac{H_Q}{H_0}\right)^2 \quad \text{or} \quad \frac{H_e}{H_0}\leq 1 \qquad (15)$$

The most crucial position for satisfying the other two conditions will occur at the top of the weir, where $\Delta=\Delta m$. If $\frac{H_Q}{H_0}<1$ then the right-hand inequalities in (13) are more stringent than (14) and vice versa - and so we have

$$\text{if } \frac{H_Q}{H_0}<1 \qquad \frac{\Delta m}{H_0}\leq\frac{H_r}{H_0}-1 \qquad (16)$$

$$\text{if } \frac{H_Q}{H_0} > 1 \qquad \frac{\Delta m}{H_0} \le \frac{H_r}{H_0} - \frac{1}{2}\left(\frac{H_Q}{H_0}\right)^2 - \frac{1}{2} = \frac{H_e}{H_0} - \frac{1}{2} \tag{17}$$

The last two inequalities can be interpreted in the following way. Consider a thought experiment with a channel flow with fixed H_r, H_Q, and H_0 in which we can vary Δm. Then if $\frac{H_Q}{H_0} < 1$ the flow at the right wall will stagnate at the weir crest when $\Delta m = H_r - H_0$ before the flow can have $h_e = 0$, but if $\frac{H_Q}{H_0} > 1$, then the height on the left-hand wall will go to zero when $\Delta m = H_e - \frac{1}{2}H_0$ before the fluid stagnates at the right wall.

Let us consider the two cases $\frac{H_Q}{H_0} > 1$ and $\frac{H_Q}{H_0} < 1$ separately, and combine the two appropriate inequalities from (15), (16) and (17).

If $\frac{H_Q}{H_0} < 1$ we have

$$\frac{\Delta m}{H_0} + 1 \le \frac{H_r}{H_0} \le 1 + \frac{1}{2}\left(\frac{H_Q}{H_0}\right)^2 \tag{18}$$

Therefore for a valid solution we at least need $\frac{\Delta m}{H_0} \le \frac{1}{2}\left(\frac{H_Q}{H_0}\right)^2 < \frac{1}{2}$ (19)

For $\frac{H_Q}{H_0} > 1$ we have

$$\frac{\Delta m - \frac{1}{2}H_0}{H_0} + 1 + \frac{1}{2}\left(\frac{H_Q}{H_0}\right)^2 \le \frac{H_r}{H_0} \le 1 + \frac{1}{2}\left(\frac{H_Q}{H_0}\right)^2 \tag{20}$$

Therefore, for a valid solution we must have

$$\frac{\Delta m}{H_0} \le \frac{1}{2} \tag{21}$$

Solutions for the Flow with $h_e = 0$.

So far we have only considered the restrictions on the flow which ensure that both walls are wetted and no reverse flow occurs; but consider what may happen downstream of the position where h_e first equals zero. The flow will tend to separate from the left wall and therefore the width of the flow will no longer be set by the channel width L.

The analysis of the previous section is valid here up to the derivation of Eq.(8). Solving this equation in a similar way we obtain (writing $h_r = H_Q$ from (3) and $h_e = 0$)

$$h - H_0 = (H_Q - H_0)\frac{\sinh \frac{w-y}{\lambda}}{\sinh \frac{w}{\lambda}} - H_0 \frac{\sinh \frac{y}{\lambda}}{\sinh \frac{w}{\lambda}} \tag{22}$$

$$u = \sqrt{g H_0}\left\{\left(\frac{H_Q}{H_0} - 1\right)\frac{\cosh\left(\frac{w-y}{\lambda}\right)}{\sinh \frac{w}{\lambda}} + \frac{\cosh \frac{y}{\lambda}}{\sinh \frac{w}{\lambda}}\right. \tag{23}$$

In particular, the velocity on the right-hand wall is

$$u_r = \frac{\sqrt{g H_0}}{\sinh \frac{w}{\lambda}}\left\{\left(\frac{H_Q}{H_0} - 1\right)\cosh \frac{w}{\lambda} + 1\right\} \tag{24}$$

Now we will require that the velocity $u \ge 0$ at all $0 \le y \le w$.

For $\frac{H_Q}{H_0} > 1$, we can see from (23) that $u > 0$ for all $0 \le y \le w$.

For $\frac{H_Q}{H_0} < 1$ we now write (23) as

$$u = \frac{\sqrt{g H_o}}{\sinh \frac{w}{\lambda}} \left\{ \left[\left(\frac{H_\ell}{H_o} - 1 \right) \cosh \frac{w}{\lambda} + 1 \right] \cosh \frac{y}{\lambda} + \left(1 - \frac{H_\ell}{H_o} \right) \sinh \frac{w}{\lambda} \sinh \frac{y}{\lambda} \right\}$$

This will certainly be positive everywhere if the expression in square brackets is positive. This is also the condition that $u_r > 0$ (from (24)) and as for $\frac{H_\ell}{H_o}$ we have the constraint that

$$\cosh \frac{w}{\lambda} < \frac{1}{1 - \frac{H_\ell}{H_o}} \tag{25}$$

Now substituting (24) in the expression for the right wall Benoulli function, we obtain

$$\left[\left(\frac{H_\ell}{H_o} - 1 \right) \cosh \frac{w}{\lambda} + 1 \right]^2 = 2 \, \frac{(H_r H_\ell - \Delta)}{H_o} \left(\sinh^2 \frac{w}{\lambda} \right)$$

Putting

$$x = \cosh \frac{w}{\lambda} - 1$$

$$B = \frac{H_\ell}{H_o} - 1$$

$$A = \frac{2(H_r - H_\ell - \Delta)}{H_o}$$

where $A \geq 0$ ($A = 0$ implies flow stagnation at the right wall)

$$x^2(B^2 - A) + 2x(B^2 - A + B) + (B+1)^2 = 0 \tag{26}$$

with solution

$$x = -1 - \frac{B}{B^2 - A} \pm \frac{\sqrt{A(1 - (B^2 - A))}}{B^2 - A} \tag{27}$$

Now let me investigate the solutions to this quadratic. $(B+1)^2$ will always be positive, but the coefficients of x and x^2 in (26) can be of either sign. Now $\cosh \frac{w}{\lambda} > 1$ and so must be positive; hence we are looking for the positive root of Eq.(20) subject to the restriction (25). Descarte's rule can be used to obtain the numbers in the table below. (The entries in the table indicate the sign of the terms.)

	$(B^2 - A)$	$B^2 - A + B$	$(B + 1)^2$	No. of positive solutions
case (a)	+	-	+	2 or more
case (b)	-	-	+	1
case (c)	-	+	+	1
case (d)	+	+	+	0

Table 1.

From Eq.(27) we can see that in order for the radicand to be positive we need $B^2 - A < 1$ (or $H_e > \Delta$). With this restriction, case (a) has two positive solutions, but a simple analysis based on (25) implies that the only allowable solution is the one with the negative sign in (27). Cases (b) and (c) also require the negative sign in (27) and condition (25) in their wet automatically. Case (d) implies both $(B^2 - A)$ and $(B^2 - A + B)$ cannot both be positive. Now we know that $\frac{H_\ell}{H_o} > 0$ i.e. $B > -1$ and so it can be shown that the condition due to case (d) is only relevant for $B > 0$ and is that $B^2 - A < 0$, or for $\frac{H_\ell}{H_o} > 1$,

$$\frac{\Delta}{H_o} < \frac{H_r}{H_o} - \frac{1}{2}\left(\frac{H_Q}{H_o}\right)^2 - \frac{1}{2} \quad \text{or} \quad \frac{\Delta}{H_o} < \frac{H_\ell}{H_o} - \frac{1}{2} \tag{28}$$

The meaning of this restriction can be seen from considering the case when $W \gg \lambda$. From (23) $u_\ell \to \sqrt{gH_o}$ and the left-hand Bernoulli equation (4) yields $\frac{\Delta}{H_o} \to \frac{H_\ell}{H_o} - \frac{1}{2}$. Therefore as the inequality (28) becomes closer and closer to an equality, the required $\frac{W}{\lambda}$ becomes longer and longer.

The required parameter regime for solutions can be shown graphically, as below:

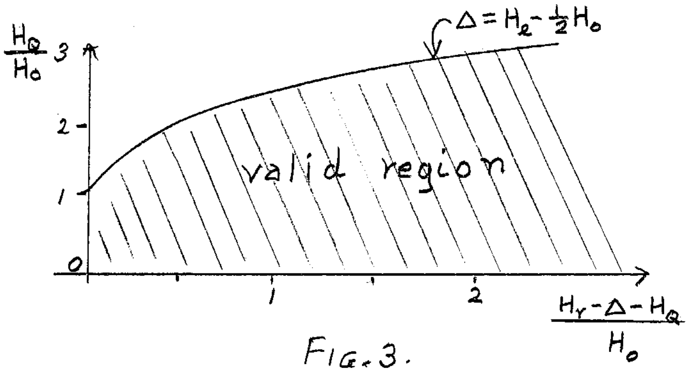

FIG. 3.

The Evolution of Bottomed Flow from a Flow which Wets Both Walls Upstream

Consider a flow which wets both walls upstream, and which has h_e go to zero at some position on the bump before the crest. This implies that $\frac{H_Q}{H_o} \geq 1$ because otherwise the flow would have stagnated previously on the right wall (see the discussion following (16) and (17)). At this position we have from (14) $\frac{\Delta}{H_o} = \frac{H_\ell}{H_o} - \frac{1}{2}$. Now what can happen downstream of this position as Δ continues to increase towards the weir crest? The flow cannot rewet the left wall and so we may expect that the flow may swing to the right, leaving a part of the channel floor dry. If this were to happen, then (28) says that $\frac{\Delta}{H_o}$ must be less than $\frac{H_\ell}{H_o} - \frac{1}{2}$, but in fact $\frac{\Delta}{H_o}$ will be greater than this, and so we must draw the conclusion that $h_\ell = 0$ cannot occur upstream of the weir crest. Now, rewriting Eq. (17) as

$$\frac{1}{2}\left(\frac{H_Q}{H_o}\right)^2 \leq \frac{H_r - \Delta_m}{H_o} - \frac{1}{2} \quad \text{or} \quad Q \leq \frac{gH_o^2}{f}\left[\frac{H_r - \Delta_m}{H_o} - \frac{1}{2}\right] \tag{29}$$

we can see that the maximum discharge recurs when h_e does equal zero at the weir crest (i.e., the equality in (29)). In this way we see that the solubility condition on the weir crest, together with the principle of maximum discharge (if this is applicable in rotating hydraulics), has given a flow which is controlled by the weir crest. Of course, the complete channel flow is still a forced problem, because the discharge which has been obtained above, is in terms of H_r as well as H_o, and this Benoulli head must in practice be set in some complicated way by a combination of the flow upstream of position (B) in Fig.1. Because $B > 0$ for this flow, we can have only cases (b) and (c) of Table 1, and so we know that $B^2 - A < 0$. Therefore

$$\cosh\frac{w}{\lambda}=\frac{B}{A-B^2}+\frac{\sqrt{A\,(1+(A-B^2))}}{A-B^2} \tag{30}$$

and it is easy to show that $\frac{d}{dA}\left(\cosh\frac{w}{\lambda}\right)<0$. Now as the flow proceeds from the crest, $A\left(=2\left(\frac{H_r-H_0-B}{H_0}\right)\right)$ increases and from the above result, we see that $\frac{w}{\lambda}$ will decrease, as we might have expected. In some way, the flow must be supercritical and it may be possible for a hydrolic jump to occur, upon which the flow would lose energy and would probably wet both walls.

Now consider the evolution of the flow over the bump when $\frac{H_\ell}{H_0}<1$. If (16) becomes an equality at some position then the flow will stagnate at y = 0, and beyond this location there would possibly be reverse flow on the right wall. If H_r is such that this never occurs, then in the meaning of this section, the flow must be "subcritical" everywhere. It seems impossible then to establish a flow with $\frac{H_\ell}{H_0}<1$ and $h_\ell=0$, from an upstream flow which has both walls wetted, and yet there are solutions for $\frac{w}{\lambda}$ in this case.

Flow over a Weir in a Narrow Channel

Let us now consider another limiting case of flow in a rotating channel, namely a channel which has $L \ll \lambda$, i.e. $f^2L^2 \ll gH_0$. We can now approximate the sinh and cosh functions (9) by putting $\sinh x \simeq x+\frac{x^3}{6}$ and $\cosh x = 1+\frac{x^2}{2}$. These equations then become

$$h(y)=h_r-(h_r-h_\ell)\frac{y}{L}+\frac{1}{6}\left(\frac{L}{\lambda}\right)^2\frac{y}{L}\cdot\left(1-\frac{y}{L}\right)\left[(h_r-h_\ell)\left(\frac{y}{L}\right)+(3H_0-2h_r-h_\ell)\right] \tag{31}$$

$$u(y)=\frac{g}{fL}(h_r-h_\ell)+\frac{g}{2FL}\left(\frac{L}{\lambda}\right)^2\left[(h_r-h_\ell)\left(\frac{y}{L}\right)^2+2(H_0-h_r)\left(\frac{y}{L}\right)+\left(\frac{2}{3}h_r+\frac{1}{3}h_\ell-H_0\right)\right] \tag{32}$$

These approximate solutions satisfy the potential vorticity Eq.(1) and the Benoulli relation (7); and apart from terms of order $\left(\frac{L}{\lambda}\right)^2$, the height profile is linear and the velocity uniform across the channel. Let us see the constant part of the velocity to be $U_m=\frac{g}{fL}(h_r-h_\ell)$ and the mean height $h_m=\frac{h_r+h_\ell}{2}$, then from Eq.(3) we have

$$\frac{Q}{L}=U_m h_m \tag{33}$$

Substituting U_ℓ from Eq.(32) into the left wall Benoulli relation (4), we obtain

$$H_\ell-\Delta=\frac{U_m^2}{2g}+\frac{Q}{L}\cdot\frac{1}{U_m}-\frac{fQ}{3gH_0}\left(1+\frac{1}{2}\frac{h_\ell}{h_m}\right) \tag{34}$$

Using Eq.(7) we can express this cubic for U_m in terms of the average Benoulli driving head $\frac{1}{2}\left[(H_r-\Delta)+(H_\ell-\Delta)\right]$

$$\frac{1}{2}\left[(H_r-\Delta)+(H_\ell-\Delta)\right]=\frac{U_m^2}{2g}+\frac{Q}{L}\frac{1}{U_m}+\frac{fQ}{6gH_0}\left(1-\frac{h_\ell}{h_m}\right) \tag{35}$$

As f → 0, this equation reduces to the familiar cubic which determines critically in the non-rotating channel problem, from which we obtain

$$U_m^2=g\,h_m \quad \text{and} \quad h_m=\frac{2}{3}\left[\frac{1}{2}(H_r-\Delta)+\frac{1}{2}(H_\ell-\Delta)\right]$$

at the critical section. Now as long as the last term in (35) remains small, then this solution should be approximately true. Let us consider the extreme case where the slope of the critical section is so long that $h_{\ell}\,X\,0$ and $(h_r - h_{\ell}) \approx 2\,h_m$. Then $U_m \sim \frac{2g h_m}{fL} \sim \sqrt{g h_m}$ i.e. $4\,g h_m \sim f^2 L^2$, and combining this with the condition that $f^2 L^2 << g H_o$, we obtain $4\,g h_m \ll H_o$. Now the ratio of the last term in (35) to the other terms in the equation is at most

$$\frac{fQ}{6gH_o} \cdot \frac{1}{h_m} = \frac{fLU_m}{6gH_o} \sim \frac{1}{3}\,\frac{h_m}{H_o}$$

and so we can see that the nonrotating results for criticality will be applicable even for large slopes of the free surface.

Flow Over a Wide, Broad Crested Weir, with No Side Walls.

Consider also flow from a very deep reservoir, of depth H_O, over a weir, as shown in the figure.

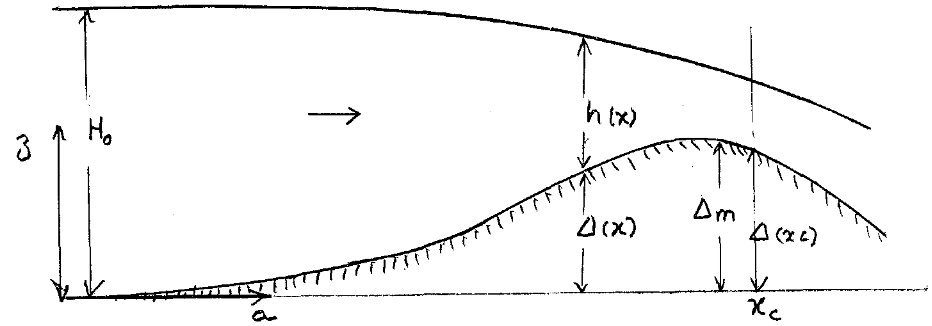

The weir is assumed to be very long in the y direction and because there are no side walls constraining the flow, the mass flux per unit width (= Q = hu), must be independent of y, (i.e. we cannot have any boundary layers in the walls). Saunders and Whitehead (1976) have considered this problem, but we will be in a physical interpretation of the critical condition in terms of the speed of small disturbances. Imposing uniformity in the y direction leads to the following form for the momentum and continuity equations.

$$u u_x - f v = -g(h+\Delta)_x \tag{36}$$

$$u v_x + f u = 0 \tag{37}$$

$$h u_x + u h_x = 0 \tag{38}$$

Assuming $v = 0$ or $x = 0$ Eq.(37) leads to $v(x) = -fx$ (i.e. the flow veers to the right) (39)

Solving (36) and (38) for u_x and h_u, and using (4) we obtain

$$u_x = \frac{u(-g\Delta_x - f^2 x)}{(u^2 - gh)}\;; \quad h_x = h\,\frac{(g\Delta x + f^2 x)}{(u^2 - gh)} \tag{40}$$

Bernoulli's equation for the flow can be derived by integrating (36)

$$\tfrac{1}{2}u^2 + gh = g(H_o - \Delta_G) - \frac{f^2 x^2}{2g} \tag{41}$$

where we have assumed that u is very small at $X = 0$, where $h_{(0)} = H_0$.

We are interested in investigating what "controlled flow" means in this very specialized rotating flow. The non-rotating results can be obtained from (41) by putting $f = 0$ and integrating Q with respect to h or u, while coinciding $H_0 - \Delta_m$ a constant. We thus obtain for critical flow at the weir crest $u_c^2 = gh_c; h_c = \frac{2}{3}(H_0 - \Delta_m)$. Now in the rotating case, (5) says that if u_x and h_x are to be regular where $u^2 = gh$, then Δx must be equal to $-\frac{f^2}{g}x$. The control point $(x = x_c)$ will again be located at the point where $u_c^2 = gh_c$, but now at this point $\Delta_x \Big|_{x=x_c} = -\frac{f^2}{g}x_c$, and (6) now gives

$$h_c = \frac{2}{3}\left\{H_0 - \Delta(x_c) - \frac{f^2 x_c^2}{2g}\right\}.$$

In non-rotating flow, $u = \sqrt{gh}$ in the group velocity of long gravity waves and any small disturbance which originates in the specified region of the flow can now be felt upstream. But what interpretation can we give to $u_c^2 = gh_c$ in this rotating flow problem in the absence of walls along which Kelvin waves would propogate?

The dispersion relation of long inertia-gravity waves in a rotating system is

$$\omega^2 = gH(K^2 + \ell^2) + f^2 \tag{42}$$

where ω is the circular frequency of the disturbance, and $\underset{\sim}{K} = (K, \ell)$ is its wavenumber vector. Let $\mathcal{K} = K^2 + \ell^2$, then the phase velocity is

$$\underline{c} = \frac{\omega \hat{k}}{|\underset{\sim}{K}|} = \sqrt{gh + \left(\frac{f}{\mathcal{K}}\right)^2}\,\frac{(K,\ell)}{\mathcal{K}} \tag{43}$$

and the group velocity is

$$\underset{\sim}{C}g = \left(\frac{\partial\omega}{\partial K}, \frac{\partial\omega}{\partial \ell}\right) = \frac{\sqrt{gh}}{\sqrt{1 + \frac{f^2}{\mathcal{K}^2} - \frac{1}{gh}}}\;\frac{(K,\ell)}{\mathcal{K}} \tag{44}$$

The group velocity approaches $\sqrt{gh} \cdot \frac{(k,\ell)}{\mathcal{K}}$ for very large wave numbers, i.e. for very small wavelengths. This limit is approached if $\frac{f^2}{gh} << \mathcal{K}^2$. Now the condition for the shallow water equations (from which (7) was derived) to be applicable is $\frac{1}{\mathcal{K}} >> h$. Combining these two inequities we obtain

$$\frac{f^2}{gh} << \mathcal{K}^2 << \frac{1}{h^2} \quad \text{and so if } h << \frac{\sqrt{gh}}{f} = \text{radius of deformation then}$$

a range of wavenumbers will exist which will give rise to group velocities approaching $\sqrt{gh}$. This gives a plausible explanation for this critical condition in terms of the more familiar non-rotating argument about disturbance information speeds.

Acknowledgments

I wish to thank Prof. George Veronis for suggesting this problem to me, and also his extremely helpful guidance during the summer. Many helpful discussions with Prof. Melvin Stern, Prof. Joseph Keller and Lars Rød are also very gratefully acknowledged.

References

Fofonoff, N.P. 1954 J.Mar.Res.

Spimbuco, E. and J.A.Whitehead 1976 Hydraulic Control by a Wide Weir in a Rotating Fluid. J.F.M. 73: 521-528.

A FUNCTIONAL FOR ENERGY BALANCE CLIMATE MODELS

David Pollard

This paper presents some mathematical properties of the energy balance equation (Eq.(3) below) used by North (1975) as a simple climate model. In particular, properties of a Lagrangian-like functional which contains complete information on solutions to the equation are investigated. The hope is that these properties will turn out to be common to, and form useful principles for, whole classes of climate models, e.g. for theories of the ice ages. First, as an introduction, we outline a point of view and attempt to define explicitly the assumptions that must be true for equations as simple as Eqs.(2) and (3) to be relevant to the real climate.

(1) Observed scaling of energy equation, and approach to ice-age theories.

The energy equation for the whole atmosphere-ocean-land-ice system, integrated over height, averaged around latitude circles, and averaged over time intervals of $\sim$1000 years and north-south distances of $\sim$ 1000 km, is of the form

$$\overset{(\sim .1\ \text{watts/m}^2)}{\text{"ice-age-related" terms}} + \overset{(\sim 50\ \text{w/m}^2)}{\text{divergence of poleward energy transport}} + \overset{(\sim 100\ \text{w/m}^2)}{\text{I.R. radiation emitted}} = \overset{(\sim 100\ \text{w/m}^2)}{\text{sunlight absorbed}} \quad (1)$$

The 'ice ages' are the global Pleistocene ice ages that have caused major fluctuations on geologic records with time scales of $\sim$10 K years to $\sim$100 K years for the last few million years (Broecker and Von Donk (1970)). One assumes that the smaller climatic fluctuations between 1000 years and 10 K years are not essential mechanisms for the main ice ages. Typical orders of magnitude of the individual terms in (1) are shown; the $\sim$.1 w/m^2 energy flux associated with the ice ages is implied both by a $\sim$ 2°K change in mean total ocean temperature in 10 K years, and by the melting of enough ice cap to raise mean sea level by $\sim$100 m in 10 K years. Present models, even general circulation models, of the 'current budget' (i.e. the last three terms in Eq.(1))cannot hope to give the residual "ice age-related terms" as a function of the current weather, since they would have to be correct (in the above averages) to one part in 1000.

Because of this 'scale separation' in the energy equation, the energy-balance effect of the ice age-related terms can (should?) be neglected. Therefore, one approach to formulating an ice age theory is as follows:-

Given values of various 'long-term' land-ocean-ice parameters (such as surface albedo $a(\phi)$ as a function of latitude ϕ), the current budget equation is solved for the current weather parameters, (e.g. the surface temperature, $T(\phi)$, as a function of latitude). Several models have indicated that any significant departure from this current quasi-equilibrium would decay within $\sim$ 1000 years. Then, another equation is used for the slow changes of the long term parameters, (e.g. $\frac{\partial a}{\partial t}$ as a function of the current a and T). This equation described mechanisms with insignificant energy flows (equivalent to $\sim .1$ w/m^2) but which slowly alter the long term parameters "by other means", (e.g. the accumulation and advance of ice sheets as a function of their current shape and the current water cycle).

The 'current energy budget' used can include many mechanisms such as variations in cloudiness, seasonal correlations, land-ocean asymmetries, atmospheric stationary eddy patterns, etc.; in simple models, these are parameterized as a function of the current $T(\phi)$ and $a(\phi)$. The current energy equation used by North (1975), with his numerical values for reference, is:-

$$-\frac{\partial}{\partial x}\left(D\frac{\partial I}{\partial x}(x)\right) + I(x) = Q\cdot S(x)\cdot a(I) \qquad (2)$$

where x is sin (latitude).

I is the I.R. flux emitted; $I(\mathrm{w/m^2}) \approx 211.2 + 1.55\,T$; T is the surface temperature in °C.

D is a diffusion coefficient describing poleward heat transport.

Q is the solar constant/4; $Q \approx 334.4$ w/m^2.

$S(x)$ is the latitudinal distribution of sunlight; $S(x) \approx 1.0 - .482\,P_2(x)$.

$a(I)$ is 1 - surface albedo; $a(I) \approx .697 - .0779\,P_2(x)$ if $T > -10°C$, for land/ocean;

$a(1) \approx .38$ if $T < -10°C$, for ice.

$P_2(x) = \frac{1}{2}(3x^2 - 1)$.

Many possibly important mechanisms are omitted from this equation. One mechanism, the ice-line feedback on the surface albedo is thus isolated for study. North's equation describes the earth's dynamics as a diffusion of heat polewards. This keeps the equation simple enough to handle analytically, preserving intuitive understanding of what is going on, (in the equation, at least) which is usually lost in even slightly more complicated numerical models. Also Eq.(2) does predict the gross shape of the earth's present surface temperature distribution surprisingly well, using a constant D of 0.382 (North (1975)).

This "current balance" equation can be used in simple theories of the ice ages. Because no asymmetric mechanisms are included, one would be studying the hypothesis that ice ages happen on billiard-ball planets with longitudinally uniform distributions of their condensable substance and that all the earth's asymmetries (Robbins (1976)) only distort this process. However, according to the above "one approach" scheme, one should now use an additional equation for the slow time variation of a due to other processes, so that a would not really be an explicit function of I. This is being done and will be described, I hope, in a later paper.

Apart from the above phenomenological uses of Eq.(2), its mathematical properties can be investigated for possible useful generalizations and insights. In this paper, properties of a Lagrangian-like functional are presented, and its use as a practical description of solutions to Eqs.(2), (3), (8) and (9) and as a 'theoretical insight tool' are illustrated. Also, a stability criterion is derived for two types of additional time-dependent terms (see Eqs.(8) and (9)), which bears out the generally unproven stability principle that the sign of $\frac{dQ}{d}$ determines the stability of a climate model. (d = equilibrium mean temperature.) (c.f. Budyko (1972, Held and Suarez (1974).)

(2) "Equilibrium" Property of the Functional

Adding a time-dependent thermal inertia term, Eq.(2) becomes:-

$$\frac{\partial I(x,t)}{\partial t} - \frac{\partial}{\partial x}\left(D\,\frac{\partial I}{\partial x}\right) + I = Q\cdot S(x)\cdot a(I) \tag{3}$$

Boundary conditions are that $\frac{\partial I}{\partial x} = 0$ at $x = 0$ and 1.

The time scale represented by the nondimensional t is probably on the order of ~1000 years; this value does not affect the mathematics below. Here and in the next section, $a(I)$ can be any function of I, and D can be any well-behaved function of x.

Equation (3) and the functional theory below can be written either in continuous form I(x,t), or expanded in x in the eigenfunctions of the left-hand side of Eq.(2), as $\sum_n I_n(t)\cdot f_n(x)$ (North (1975)). Both forms are mathematically equivalent; one or the other may be more convenient for different applications. The section below is written in continuous form and a later section uses the spectral form.

Define the functional

$$F(I(x)) \equiv \int_0^1 \left\{ \frac{D}{2}\left(\frac{dI}{dx}\right)^2 + \frac{I^2}{2} - Q.\,S(x)\cdot\int_{I_s}^{I(x)} a(I').\,dI' \right\}.\,dx \tag{4}$$

(Here, I_s is an arbitrary constant)

$$= \int_0^1 \left\{ \mathcal{L}(I, I_x) \right\}.\,dx, \text{ say} \quad \left(\text{writing } I_x = \frac{dI}{dx}\right)$$

For small variations $\Delta I(x)$ from $I(x)$,

$$\Delta F \equiv F(I+\Delta I) - F(I) = \int_0^1 \left\{ \frac{\partial \mathcal{L}}{\partial I} - \frac{d}{dx}\left(\frac{\partial \mathcal{L}}{\partial I_x}\right) \right\}.\,\Delta I\cdot dx + O(\Delta I^2)$$

by the standard variational argument (e.g. Whitham (1974), p.391). In this step an integration by parts uses $\frac{dI}{dx} = 0$ at $x = 0$ and 1, which are the boundary conditions of Eq.(3).

Hence,

$$\left\{ \Delta F = 0 \ \underset{\text{for all } \Delta I(x)}{\text{to first order in } \Delta I} \right\} \Longleftrightarrow \left\{ -\frac{d}{dx}\left(D\,\frac{dI}{dx}\right) + I - Q\cdot S(x)\cdot a(I) = 0 \right\}$$

i.e. I(x) is a solution to the equilibrium Eq.(2) if and only if it is an extremum in "I-space" of the functional F(I(x)).

Note that the functional does not contain the time dependence of Eq.(3) directly; it is a true 'Lagrangian' only for the steady state Eq.(2). We looked for a complete (x,t) functional for Eq.(3) without success; perhaps Lagrangian formulations are only possible for purely wave-like equations (which have constants of the motion), and not for combined wave-dissipative equations like (3).

(3) Linear Stability Property of the Functional

As well as "finding" all the steady state solutions as its extrema in I-space, the form of the functional around each extremum determines whether that solution is linearly stable or unstable to infinitesimal perturbations obeying Eq. (3). This is shown as follows:-

At an equilibrium point $I = \phi(x)$, the variation F to a small perturbation $\Delta I(x)$ is zero to first order in ΔI, from above.

To second order, the standard variational argument gives

$$\Delta F = \int_0^1 dx \left\{ \frac{1}{2} \frac{\partial^2 \mathcal{L}}{\partial I^2} \Delta I^2 - \frac{1}{2} \Delta I \cdot \frac{d}{dx}\left(\frac{\partial^2 \mathcal{L}}{\partial I_x^2} \cdot \left(\frac{d\Delta I}{dx} \right) \right) + \Delta I \cdot \left(\frac{d\Delta I}{dx} \right) \cdot \frac{\partial^2 \mathcal{L}}{\partial I \partial I_x} \right\}$$

$$\Rightarrow \Delta F = \frac{1}{2} \int_0^1 dx \cdot \Delta I_{(x)} \cdot \left\{ -\frac{d}{dx}\left(D \frac{d\Delta I}{dx} \right) + \Delta I - Q \cdot S_{(x)} \cdot \frac{da}{dI}(\phi(x)) \cdot \Delta I \right\} \tag{5}$$

(An integration by parts in this step requires $\frac{d\Delta}{dx} I(x) = 0$ at $x = 0$ or 1.

For small perturbations $\psi(x,t)$ from $\phi(x)$, Eq. (3) gives directly, to first order in ψ.

$$-\frac{\partial \psi}{\partial t}(x,t) = \left\{ -\frac{\partial}{\partial x}\left(D \frac{\partial \psi}{\partial x} \right) + \psi - Q \cdot S(x) \cdot \frac{d}{dI} a(\phi(x)) \cdot \psi \right\} \tag{6}$$

Note that the expressions in curly brackets $\{\ldots\}$ in Eqs. (5) and (6) are the same. It is a Sturm-Liouville operator acting on ΔI and ψ; thus, solutions to Eq. (6) are $\hat{\psi}_n(x) \cdot e^{-\lambda_n t}$ where the $\hat{\psi}_n(x)$, $n = 1, 2, \ldots$, form a complete set of orthonormal eigenfunctions with corresponding eigenvalues λ_n. Therefore, all perturbations $\Delta I(x)$ can be expressed as $\sum_n C_n \cdot \hat{\psi}_n(x)$. Substituting this into (5), we get

$$\Delta F = \frac{1}{2} \sum_n \lambda_n C_n^2 \tag{7}$$

Therefore, all $\lambda_n \geq 0 \Leftrightarrow \Delta F \geq 0$ for all small $\Delta I(x)$

i.e. F is a minimum at $I = \phi(x) \Longleftrightarrow \phi(x)$ is stable to Eq. (3)
F is a maximum or saddle " " unstable "

If the I-space is parameterized somehow (e.g. as legendre polynomial modes; see below) then the eigenfunctions $\hat{\psi}_n(x)$ can be regarded as eigenvectors in parameter space. Then, because the same Sturm-Liouville operator occurs in Eqs. (5) and (6), these eigenvectors are the principal axes of the F surface at $I = \phi(x)$. Also, Eq. (7) shows that the radius of curvature $2 \times \frac{\partial F}{\partial (c_n^2)}$ for each principal axis is equal to 1/the corresponding eigenvalue. This is illustrated for a particular case in a later section.

(4) Spectral (in x) Form, Ice-line Lag Case; and General Stability Principle.

For the rest of this paper we use the "step function" albedo; the ice-line

$x = x_s$ is specified so that the albedos north and south of it correspond to ice and land respectively. Equation (3), with this albedo, becomes for the nth mode (North (1975)):-

$$\frac{d}{dt} I_n(t) + L_n \cdot I_n = Q \cdot h_n(x_s) \, , \quad n = 0, 2, 4, \ldots \tag{8}$$

where

$$h_n(x_s) \equiv \int_0^1 S(x) \cdot a(x ; x_s) \cdot f_n(x) \, dx$$

$$I_n(t) \equiv \int_0^1 I(x, t) \cdot f_n(x) \cdot dx$$

For D constant, the f_n are normalized legendre polynomials $\sqrt{2n+1} \times P_n(x)$ and the L_n are their eigenvalues $n \times (n+1) \times D + 1$. (This section generalizes immediately for D any given positive function of latitude.)

In North (1975), the ice-line x_s was fixed to the -10°C isotherm. In this section, we incorporate a crude ice-line lag to represent the thermal inertia of the latent heat associated with the icecaps by:-

$$\ell \cdot \frac{d}{dt} x_s(t) = I(x_s, t) - I_s \tag{9}$$

where I_s (watts/m^2) = 211.2 + 1.55$_x$

The only physical basis for Eq.(9) is the general idea that the ice-line will advance if the weather is "too cold" in its vicinity, and will retreat if "too warm". This concept is itself debatable, since ice accumulation depends strongly on the current water cycle. However, Eqs.(8) and (9) do present another possible instability mechanism to which the present climate as described by Eq.(2) should be stable. Also, this section illustrates how the functional and the general stability principle mentioned above generalize naturally to this two-equation scheme.

The functional, as defined by Eq.(4), translates in the spectral form to:-

$$F(I_0, I_2, \ldots, x_s) = \sum_n L_n \frac{I_n^2}{2} - Q\left(\sum_n h_n(x_s) \cdot I_n - I_s(h_0(x_s) - a_I)\right) \tag{10}$$

I_0, I_2, . . . and x_s are all independent variables, where a_I is the ice albedo. As discussed in North (1975), the description of the earth's dynamics as poleward diffusion is only meaningful for the first two (largest x scale) modes I_0 and I_2, so in what follows we consider just three independent variables I_0, I_2 and x_s, (although the mathematics generalizes naturally to infinite modes).

As before, the extreme of F in (I_0, I_2, x_s) space are steady state solutions to (8) and (9), since $\frac{\partial F}{\partial I_n} = 0$, $n = 0, 2$ is identical to Eq.(2), and since

$$\frac{\partial F}{\partial x_s} = -Q \sum_n \left(h_n'(x_s) \cdot I_n - h_0' \cdot I_s \right)$$

(writing $\frac{dh_n}{dx_s}$ as h_n')

$$= -Q \cdot b \cdot S(x_s) \cdot \left(\sum_n I_n \cdot f_n(x_s) - I_s\right) \text{ since } \frac{dh_n}{dx_s} = b \cdot S(x_s) \cdot f_n(x_s)$$

where b = the discontinuous increase of albedo across the ice-line.

$$= -Q b . S(x) . \left(I(x,t) - I_s \right) .$$

For small perturbations $(\partial_0(t), \delta_2(t), \varepsilon(t))$ from a steady state (ϕ_0, ϕ_2, x_0), Eqs.(8) and (9) give

$$\begin{pmatrix} \dot{\delta}_0 \\ \dot{\delta}_2 \\ \dot{\varepsilon} \end{pmatrix} \begin{pmatrix} L_0 & 0 & -Q.bS.f_0 \\ 0 & L_2 & -Q.bS.f_2 \\ \frac{-f_0}{\ell} & \frac{-f_2}{\ell} & -\sum_n \frac{Q h_n . f_n'}{\ell . L_n} \end{pmatrix} . \begin{pmatrix} \delta_0 \\ \delta_2 \\ \varepsilon \end{pmatrix} = O(\delta^2, \varepsilon^2) \tag{11}$$

where b, S, f_n, h_n, mean their values at $x = x_0$. For the same variation $(\delta_0, \delta_2, \varepsilon)$, the second order Taylor expansion gives:-

$$\Delta F = \frac{1}{2}(\delta_0, \delta_2, \varepsilon) . \begin{pmatrix} L_0 & 0 & -Q.bS.f_0 \\ 0 & L_2 & -QbS.f_2 \\ -Q.bS.f_0 & -Q.bS.f_2 & -Q.bS.\sum_n Q \frac{h_n f_n'}{L_n} \end{pmatrix} . \begin{pmatrix} \delta_0 \\ \delta_2 \\ \varepsilon \end{pmatrix} + O(\delta^3, \varepsilon^3) \tag{12}$$

Comparing these two matrices, one sees that the principal axes and radii of curvature of the local F surface no longer coincide with the eigenvectors and values of the stability problem, unless $1/\ell = Q . b . S(x_0)$. But, surprisingly the previous result that the minimums of F are stable, and its maxima and saddles are unstable, is still true. To prove this, consider perturbations proportional to $e^{-\lambda, t}$; then Eq.(11) requires, for non-trivial solutions, to exist,

$$\ell . \lambda + \sum_n Q . \frac{h_n . f_n'}{L_n} + \sum_n Q \frac{h_n' . f_n}{L_n - \lambda} = 0 \tag{13}$$

Note the eigenvalues from Eq.(12) obey this equation with ℓ replaced by $1/Q.b.S(x_0)$, a positive number for all x_0. It is instructive to rearrange (13) further, before considering actual solutions for λ.

Consider the local slope of the equilibrium curve $x_0(Q)$ which is defined by the steady state solutions for different values of Q. This curve is shown in Fig.1 for North's (1975) model.

Several other models have given similar curves with the same typical shape, and showing multiple values of x_0 for some Q. (Budyko (1972); Held and Suarez (1974))

Along this equilibrium curve,

$$I_s = \sum_n \phi_n(x_0) . f_n(x_0) = \sum_n \frac{Q . h_n(x_0)}{L_n} f_n(x_0) \Rightarrow \frac{I_s}{Q} \frac{dQ}{dx_0} = -\left(\sum_n Q \frac{h_n . f_n'}{L_n} + \sum Q \frac{h_n' . f_n}{L_n} \right) \tag{14}$$

Combining (13) and (14) we get

$$\frac{I_s}{Q^2} . \frac{dQ}{dx_0} = \sum_n \left(\frac{b . S(x_0) . f_n^2(x_0)}{L_n(L_n - \lambda)} \right) . \lambda + \frac{\ell}{Q} . \lambda \tag{15}$$

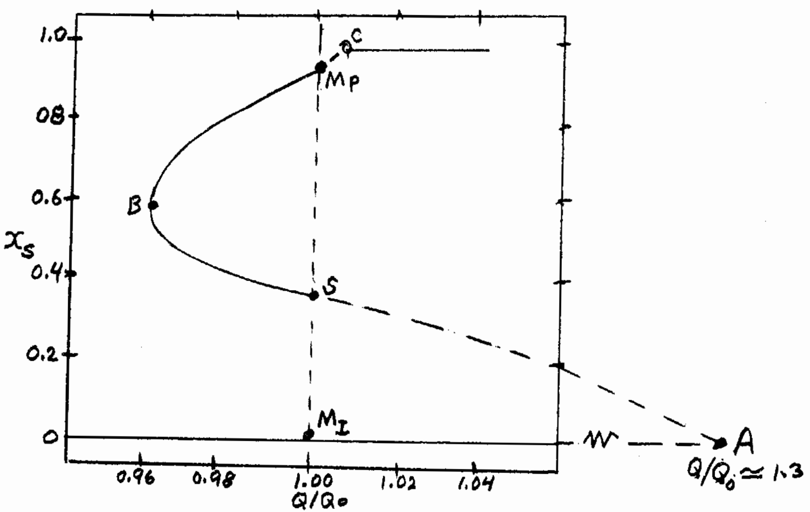

Fig.1 x_s versus Q/Q_0 equilibrium solution curve, for the two-mode case, from North (1975). Q_0 = present mean solar radiation $\simeq$ 334.4 w/m^2.

Noting that $\dot{b} \cdot S(x_0) \cdot f_n^2(x_0)$ and L_n are always positive, one can sketch the right-hand side of (15) as a function of λ :-

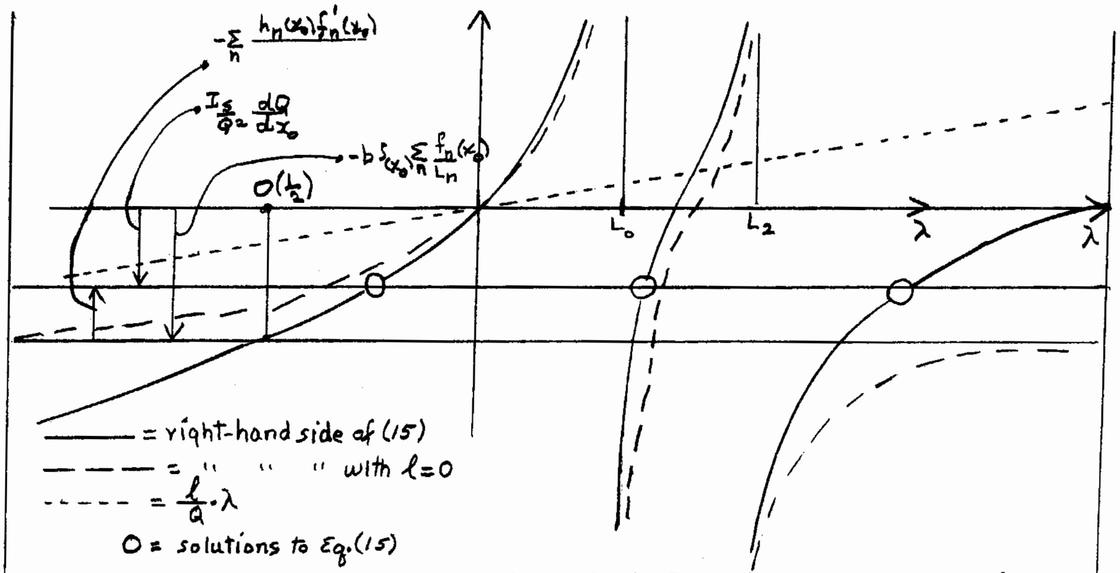

Fig.2 Sketch of behavior of Eq.(15) for eigenvalues to the linear stability problem.

The function looks qualitatively the same for all (positive) values of ℓ due to the singularities under the Σ in (15). Solutions λ to (15) are given by intersections (circled in Fig.2) of the right-hand side function with $\frac{I_s}{Q^2} \cdot \frac{dQ}{dx_0}$. There is a negative root of λ ($\Longleftrightarrow$ instability) if and only if $\frac{I_s}{Q^2} \cdot \frac{dQ}{dx_0} < 0$ whatever (positive) value of ℓ. Since from above, the F-surface eigenvalues from Eq.(12) obey Eq.(15) with ℓ replaced by $1/Q \cdot b \cdot S(x_0)$, we have:-

$$\begin{tikzcd}
\boxed{\text{F is at a minimum (maximum or saddle)}} \arrow[r, Leftrightarrow, "\text{by Eq.(15) with } \ell \text{ replaced by } 1/QbS(x_0) \text{ and Fig.(2)}"'] & \boxed{\frac{dQ}{dx_0} \underset{(<)}{>} 0} \arrow[r, Leftrightarrow, "\text{by Eq.(15) and Fig.2.}"'] & \boxed{\text{The equilibrium solution is stable (unstable) to small perturbations obeying (8) and (9)}}
\end{tikzcd}$$

Thus, points on the part of the equilibrium curve $x_0(Q)$ from A to B in Fig.1 are unstable, and points from B to C, (which include the present climate), are stable.

This bears out the general stability principle discussed by Budyko (1972). It is surprising that the two different instability mechanisms individually lead to the same principle: (the above analysis does go through omitting the I_n term in (8)). The principle can be rephrased in the present model, since

$$\frac{d\phi_0}{dQ} = Q \cdot S(x_0) \cdot b \frac{dx_0}{dQ} + h_0(x_0).$$

It becomes

> "If the climate sensitivity coefficient $Q \cdot \frac{d\phi_0}{dQ}$ is positive, the climate is stable to internal perturbations, and if negative it is unstable."

We have not been able yet to prove it for this paper's continuous $a(I)$ case, but have found no indication that it is not true.

Note that for the $\ell = 0$ case, Fig.2 indicates stability if $\frac{dQ}{dx_0} < 0$ and

$$\left| \frac{I_s}{Q^2} \cdot \frac{dQ}{dx_0} \right| > \left| b \cdot S(x_0) \cdot \sum_n \frac{f_n^2}{L_n} \right|$$

This corresponds to an earth with ice equatorward of x_0, ice-free poleward of x_0, and with heat diffusing equatorward from the poles. For the present distribution of sunlight S(x) and North's (1975) model parameter values, this is an impossible equilibrium state since $\phi_2(x_0) < 0$ for all x_0. (Strictly, one needs to use this fact in the rephrasing of the stability principle above.)

5. "Nonlinearised Behaviour" Property of the Functional

So far, we have only dealt with small perturbations from equilibrium states. In fact, the functional F can be used to describe the full nonlinear time behavior of solutions (I(x,t). We illustrate this below for the two-mode case, Eqs. (8) and (9), with $\ell = 0$ (i.e. no ice-line lag; the North (1975) case).

Clearly, substituting $\frac{\partial F}{\partial I_n}$ back into (8),

$$\frac{dI_n}{dt} = \frac{\partial F}{\partial I_n}, \quad n = 0, 2 \tag{16}$$

This means that the solution points to the differential equation in (I_0, I_2) space moves down-gradient with respect to the surface $F(I_0, I_2)$, following the steepest path downwards and with a "speed" $\sqrt{\dot{I}_0^2 + \dot{I}_2^2}$ equal to the magnitude of this gradient.

Using the chain rule, (16) implies

$$\left.\frac{dF}{dt}\right|_{\text{'along solution path'}} = -\sum_n \left(\frac{dI_n}{dt}\right)^2$$

The continuous I(x,t) form can easily be shown to be

$$\frac{dF}{dt} = -\int_0^1 \left(\frac{\partial I}{\partial t}\right)^2 \cdot dx$$

This agrees intuitively with, (but is not a vigorous proof of) the previous result that minimums of F are stable states, and with the concept that the higher order modes decay to equilibrium faster.

Maps of F versus (I_0, I_2) for different values of Q are shown in Figs.3 and 4, using North's (1975) model parameter values. Actually Eq.(10) has first been non-dimensionalized by Q^2; the plotted quantity is

$$\frac{F(I_0/Q, I_2/Q)}{Q^2} = \frac{1}{2}\left[\left(\frac{I_0}{Q}\right)^2 + L_2\left(\frac{I_2}{Q}\right)^2\right] - \left[h_0\frac{I_0}{Q} + h_2\cdot\frac{I_2}{Q} - \frac{I_s}{Q}(h_0 - a_I)\right]$$

h_0 and h_2 are functions of I_0 and I_2 since the ice-line is defined by I_0 and I_2. Contours of x_s are also indicated in the figures as dashed straight lines.

For the present value of Q, Fig.3 shows two minima M_I and M_p, and a saddle S. These correspond to the three equilibrium solutions in Fig.1, indicated by the same letters. Larger regions of (I_0, I_2) and Q space, not shown in Figs. 3 or 4, were searched (by computer) for other extrema, and none were found. All regions outside the figures' area just slope down into the area.

As Q is reduced below the present value, the F-surface alters continuously. The ice-covered minimum M_I remains and the 'present-earth' minimum M_p shallows and starts to get washed out, until, at $Q/Q_0 \simeq .96$, the M_p minimum and the saddle S simultaneously coalesce and just fade away (Fig.4) into the regional slope coming up from the ice-covered minimum. This corresponds to point B in Fig.1.

If Q is increased above the present value, the M_p minimum deepens and becomes ice free, and at $Q/Q_0 \simeq 1.3$, the M_I minimum fades away into the slope coming up from the deepening M_p minimum.

Whether the depth of M_I changes or not (when scaled by $1/Q^2$) as Q varies is determined by the arbitrary constant in the $\int a$ term in the definition of F, Eq.(4). F/Q^2 remains the same at M_I for $\int_{I_s}^{I} a(I')\,dI'$, as above; for $\int_0^{I} a(I')\,dI'$, the M_I depth changes and the depth of M_p remains the same once it becomes ice-free (i.e. $x_0 = 1.0$).

The behavior of the F surface as Q varies can be "explained" as follows: Split F into two parts, F = T - Q.J where

$$T = \frac{1}{2}\cdot I_0^2 + L_2\cdot\frac{I_2^2}{2}$$ (which is the integrated outgoing and internal energy fluxes)

$$J = h_0 I_0 + h_2 I_2 - I_s\cdot(h_0 - a_I)$$ (which is the correlation of the incoming energy flux and the temperature, plus a term representing the ice effect shoehow).

Sketches of T and J are drawn in Fig.5. The J surface was found numerically, and is approximately planar with a break in slope in the region between $x_s = 0$ and $x_s = 1$.

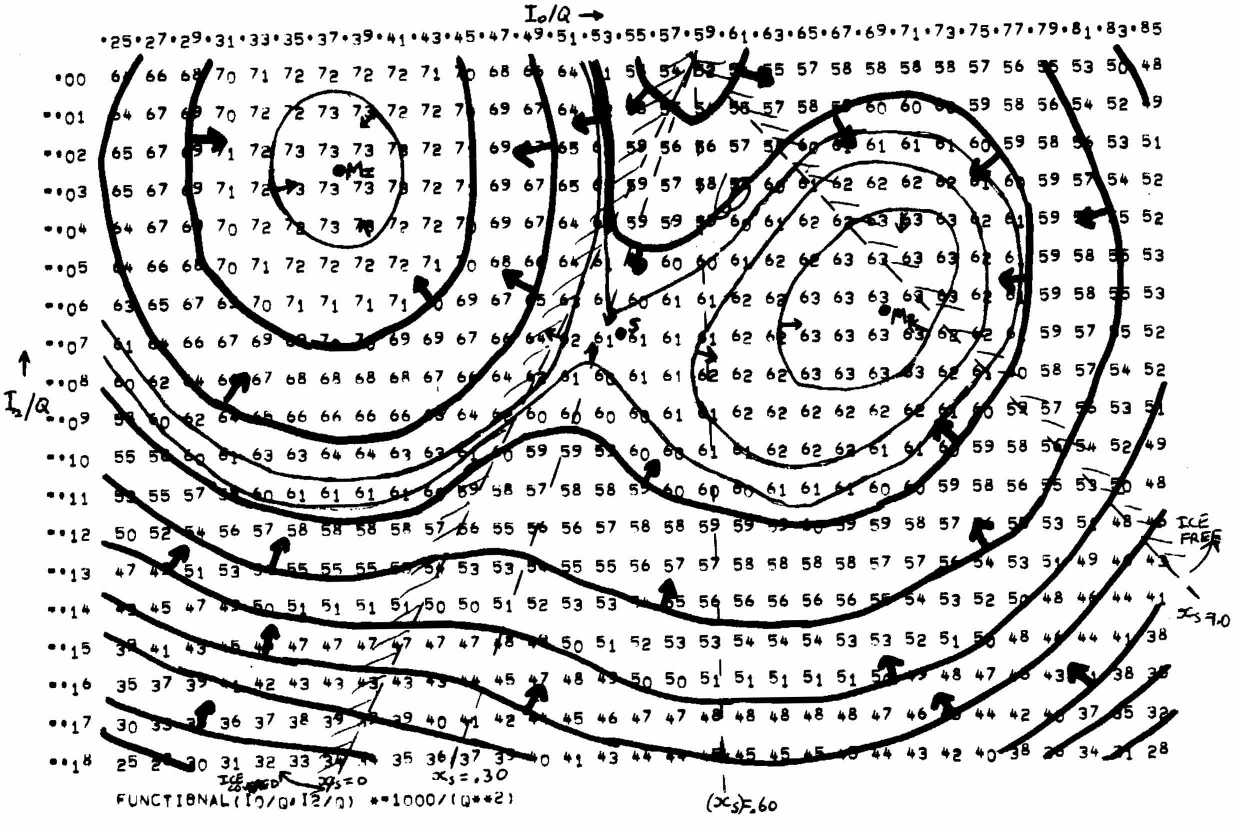

Figure 3

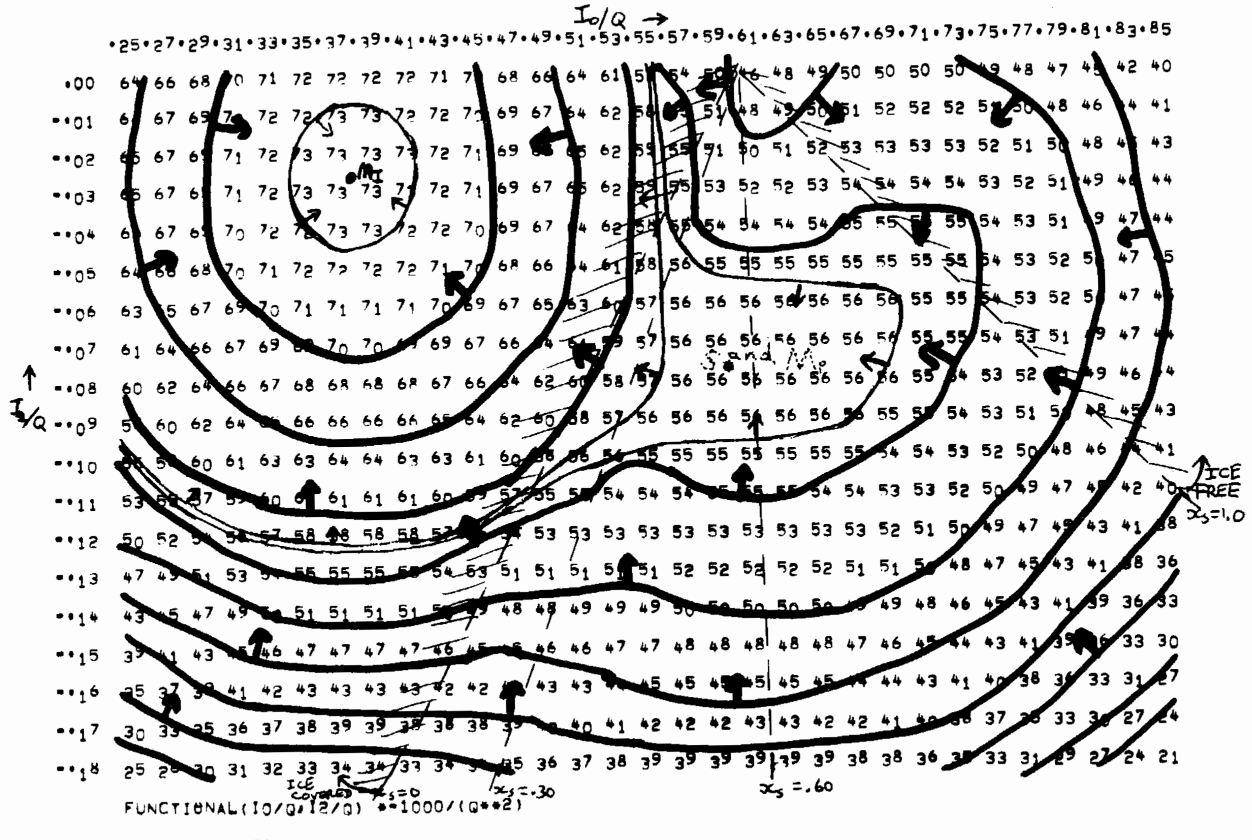

Figure 4

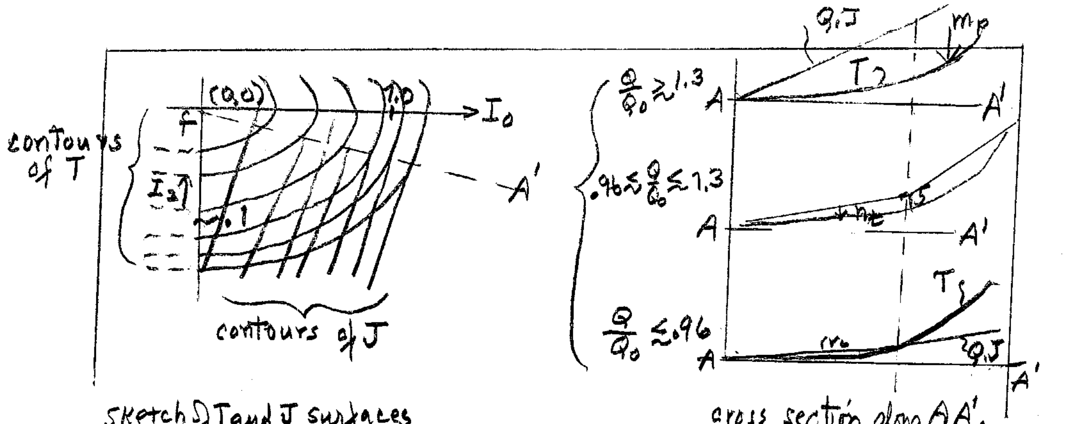

Sketch of T and J surfaces

cross section along AA'.

FIG. 5

The cross sections, also in Fig. 5, show how the two minima and the saddle come about for a certain range of Q, and how, outside this range, just one minimum occurs. Perhaps it is significant that the equilibrium points occur where the gradient of the $T(I_0,I_2)$ surface is equal to Q times the $J(I_0,I_2)$ surface's gradient, with T and J interpreted as above.

(6) "Speculation inducing" Property of the Functional.

For fixed solar conditions, the earth's adjustment in Figs. 3 and 4 to equilibrium (with a time scale perhaps of ~ 1000 years) can be thought of as a fast relaxation, analogous to the return of a parcel of gas molecules back to a Bolzmann distribution after encountering a shock. (This maximizes a certain quantity:- F for the earth, entropy for the gas.) Then, the movement of the earth along the $x_0(Q)$ equilibrium curve of Fig. 1 due to changing solar input (time scale 10's K years) can be thought of as a slow reversible change maintaining equilibrium, as in non-shock changes of a gas parcel, with the internal energy fluxes of the earth being analogous to the intermolecular collisions. But as Malkus (private communication) points out, there is a definite latitudinal structure to these supposedly random fluxes, and also to their net change if S_2 varies, so that perhaps a thermodynamic interpretation is not valid, but some non-equilibrium statistical mechanical analogy, like a minimum entropy principle, (Paltridge, (1975)).

Nevertheless, equations describing the variation of the equilibrium (M_p) value of F along the $x_0(Q)$ curve are easily derived:-

Since, for fixed S_2,

$$\left.\frac{dF_{M_p}}{dQ}\right|_{\text{equil. curve}} = \frac{\partial F_{M_p}}{\partial Q} + \sum_n \frac{\partial F}{\partial I_n} \cdot \frac{d\phi_n(Q)}{dQ}$$

$$= 0 \text{ on equilibrium curve}$$

$$= -J = -\left[\sum_n \left(h_n \phi_n(Q) - I_s(h_0(Q) - a_I)\right)\right]$$

$$= -\frac{1}{2}\sum_n . L_n \frac{\phi_n^2}{Q} + I_s(h_0(Q) - a_I)$$

one can combine these expressions with the definition of F to derive various equations, for instance:-

$$\frac{d}{dQ}\left(-\frac{F}{Q^2}\right) = \frac{I_s}{Q^2}(h_0(Q) - a_I)$$

$$\frac{d}{dQ}\left(\frac{-F}{Q}\right)=\frac{1}{Q_2}\cdot\sum_n\left(\frac{L_n\phi_n^2}{2}\right)$$

Perhaps these or similar equations have useful interpretations, thermodynamic or otherwise.

(7) Concluding Remarks.

The functional as written above applies only to the zonally averaged energy equations of this paper which do incorporate thermal storage, ice-line lag, albedo as a general function of temperature $a(I)$, and a latitude-dependent diffusion coefficient, but which are limited to a diffusive description of the poleward energy transport. North (1975) shows that the form of Eq.(2) can cover systematic circulation effects $v(x)\cdot\partial I/\partial x$, and specified non-homogeneous cloudiness, so these are easily incorporated into the functional. However, for the functional approach to be useful, it must be generalizable to other more complex forms of energy equations, with, for instance, more complex transport terms than linear diffusion. (The present functional definition does extend immediately to the case where the I.R. flux is a general function of the local temperature, f(A + B.T). The corresponding functional term is then $\int^I f(I')\,dI'$.

If a functional with the above properties could be defined for a complex model as a function $F(\alpha_1,\alpha_2,\ldots\alpha_n)$ of N internal variables of the system, then the equilibrium problem becomes just a system of N algebraic equations for $\alpha_1\ldots\alpha_n$:-

$$\frac{\partial F}{\partial\alpha_n}=0,\quad n=1,\ldots N$$

As above, the form of the F surface would determine the linear stability and the nonlinear behavior too. This could be a useful systematic way of dealing with large numerical general circulation models with numerous independent internal variables.

Acknowledgments

I would like to thank Gerald North for an enjoyable and scientifically stimulating summer's work. It should be noted that the initial ideas and impetus for this work were his, and that a lot of this paper is presenting his work and also that of Louis Howard, who formulated the continuous form of the functional. Bruce Wielicki, especially in the initial stages of looking for a functional, also worked on the project, so the write-up here is an amalgamation of several peoples' contributions, and we hope to get a joint paper published shortly.

Also I would like to thank everyone in the Geophysical Fluid Dynamics program for a scientifically positive and exciting summer.

References

Broecker, W.S. and J. VanDonk 1970 Isolation Changes, Ice-Volumes, and the 0^{18} record in deep sea cores. Rev.Geophys.& Sp.Phys., 8: 169-197.

Budyko, M.I. 1972 The Future Climate. Trans.Amer.Geophys.Union 53:868-874.

Held, I. and M. Suarez 1974 Simple Albedo Feedback Models of the Ice Caps. Tellus, 36: 613-629.

North, G.R. 1975 Theory of Energy-Balance Climate Models. J.Atmos.Sci. 32: (11); 2033-2043.

Paltridge, G.W. 1975 Global Dynamics and Climate - a System of Minimum Entropy Exchange. Quart.J.Roy.Met.Soc., 101: 475-484.

Robbins, T. 1976 Even Cowgirls get the Blues. Houghton Mifflin Co.,Boston.365 pp.

Whitham, G.B. 1974 Linear and Nonlinear Waves. Wiley, 636 pp.

SOME ASPECTS OF STEADY, ROTATING CHANNEL FLOW

Lars Petter Røed

1. Introduction

This study is motivated by observations of both actual stream configuration in the ocean and experiments of flow through a channel into an 'infinite' region (Porter, 1976). The Yucatan stream entering the Gulf of Mexico separates from the left bank and makes a swift movement into the Gulf before heading for the Strait of Florida, as shown schematically in Fig.(1.1).

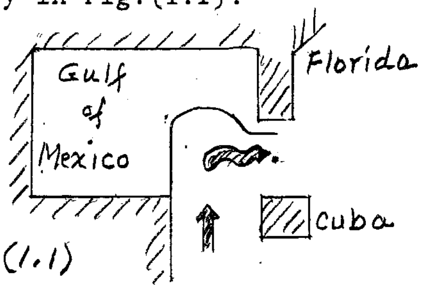

Fig. (1.1)

From the experiments are shown two pictures which have very different flow patterns, Fig.(1.2a) and (1.2b). The first, Fig.(1.2a) shows a flow pattern similar to that drawn in Fig.(1.1) and is nice and smooth, whereas the second shows a formation of an anticyclonic gyre. The present model offers an explanation of the mechanisms involved in the two different flow patterns. Furthermore, the two pictures exhibit a downstream state in the form of a jet current along the wall. The dynamics of such a jet when the wall is curved, is therefore analyzed.

2. Mathematical Setup

To be considered is a non-viscous steady flow of a homogeneous, incompressible fluid down a channel of varying width on a rotating plane, Fig.(2.1). The hydrostatic approximation will be assumed to be valid. The equations of motion and continuity consistent with these assumptions are

$$\underset{\sim}{V}\cdot\nabla\underset{\sim}{V}+f\,\underset{\sim}{k}\times\underset{\sim}{V}=-g\nabla h \tag{2.1}$$

$$\nabla\cdot h\underset{\sim}{V}=0 \tag{2.2}$$

where f is Coriolis parameter, h the height of the free surface, V the horizontal component of the velocity and g the acceleration due to gravity. From these equations one may derive the potential vorticity equation

$$\frac{\zeta+f}{h}=F(\Psi), \tag{2.3}$$

where $\zeta=\underset{\sim}{k}\cdot\nabla\times\underset{\sim}{V}$ is the vertical component of the vorticity and F is a function

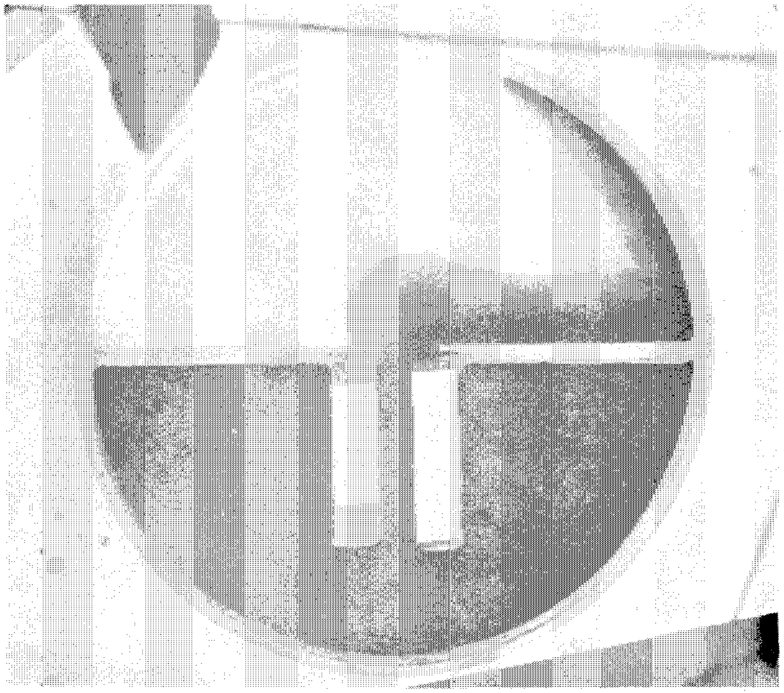

Fig.1.2a. Light fluid (dark) above heavy fluid (light), each fluid initially fitting the two halves of the tank. The reduced gravity g' 3-4cgs units, initial height 3cgs units, width of channel 2cgs units. Rotation rate $T=\frac{4\pi}{f}=9.6$.

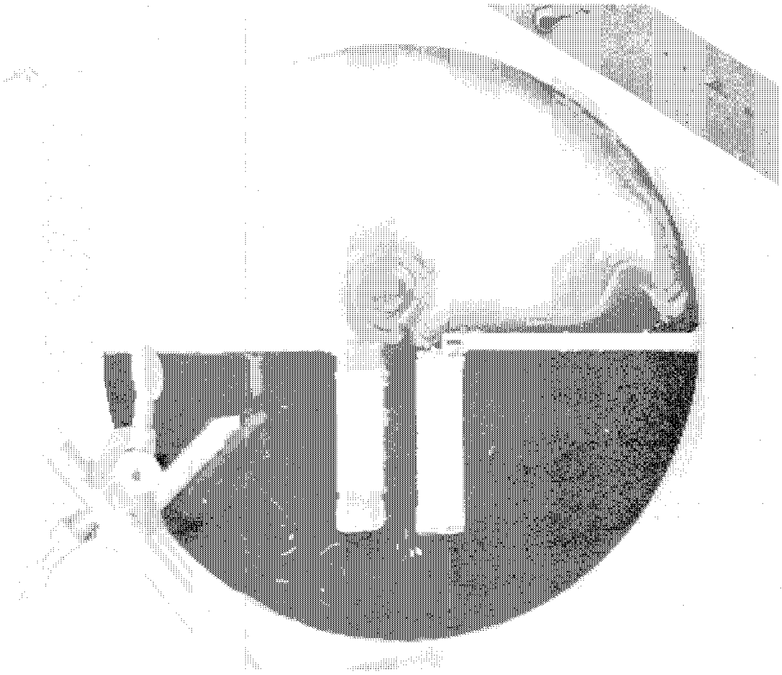

Fig.1.2b. Same as Fig.1.2a but $T=1,115$.

Fig.2.1 Sketch of model shows chosen coordinate system.Note: x is downstream. Flow supposed to be forced to left (!); flow downstream is marked (?).

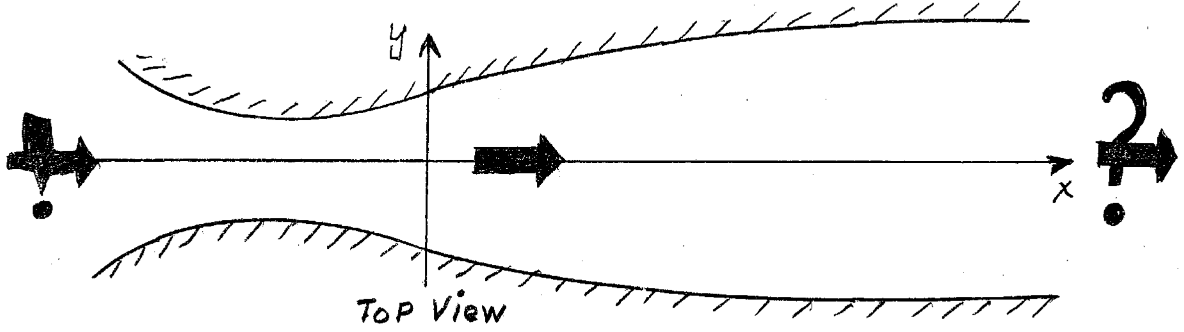

FIG. 2.1

dependent on the stream-function, ψ , only. Thus the potential vorticity (= the absolute vorticity divided by the height) is conserved along streamlines. Moreover, one may derive the Bernouilli equation:

$$\frac{1}{2}\underset{\sim}{v}^2 + gh = B(\psi), \tag{2.4}$$

where the total head, B, is conserved along streamlines. The existence of the stream-function is assured by Eq.(2.2) and may be defined by

$$h\underset{\sim}{v} = \underset{\sim}{k} \times \nabla\psi. \tag{2.5}$$

With this definition of the stream-function the relationship between F and B may be found to be

$$F(\psi) = \frac{dB}{d\psi} \tag{2.6}$$

Furthermore, the discharge, Q, or the volume flux becomes

$$Q = \int_{\sigma} \underset{\sim}{v} \cdot \delta\underset{\sim}{\sigma} = \psi_r - \psi_l . \tag{2.7}$$

Here σ is the surface normal to the flow, ψ_r is the value of the stream-function on a streamline to the right and ψ_l the value on a streamline to the left, looking downstream. Now if the potential vorticity is assumed uniform and defined such that

$$F(\psi) = \frac{f}{H_0} \tag{2.8}$$

where H_0 is dubbed the potential vorticity height, B becomes a linear function of the stream-function, viz:

$$B(\psi) = \frac{f}{H_0}\psi + B(\psi)=0 \tag{2.9}$$

Thus defining

$$B(\psi) = gH(\psi) \tag{2.10}$$

where, H, is dubbed the Bernouilli height, and putting $\psi = 0$ on the left bank of the channel, $(\psi_l = 0)$ it follows that

$$\psi_r = Q \tag{2.11}$$

and

$$H_r = H_l + \frac{fQ}{gH_0} \tag{2.12}$$

(Subscripts r and l will be used throughout this analysis to denote evaluation on right and left bank looking downstream, respectively.

Hence H_r is always greater than or equal to H_ℓ. Only in two cases will $H_r = H_\ell$, namely when $f = 0$ or $H_0 \longrightarrow \infty$. The first corresponds to the concomitant problem of a non-rotating channel flow, whereas the other corresponds to a special case with zero potential vorticity as considered in Whitehead *et al.* (1974).

3. One Aspect of Non-rotating Channel Flow

There is one aspect of non-rotating channel flow which is retained in the rotating channel flow, which is worth discussing. Neglecting rotation, the equation for the height of the free surface is the cubic equation,

$$h^3 - H_\ell h^2 + \frac{Q^2}{2gL^2} = 0 \tag{3.1}$$

where L is the width of the channel. This equation tells us that h, besides being a function of the geometry of the channel, L, is a ~~function~~ function of two parameters, the discharge, Q, and the Bernouilli height on the left wall, H_ℓ. The dependency may be displayed in graphs showing h, scaled by H_ℓ, as a function of L scale by some typical width, L_0. (Fig.3.1).

Fig.3.1 Height of free surface as function of width. Numbers on curves correspond to different discharges.
$Q/L_o H_2 \sqrt{g h_e} = 0.5, 1.0$.

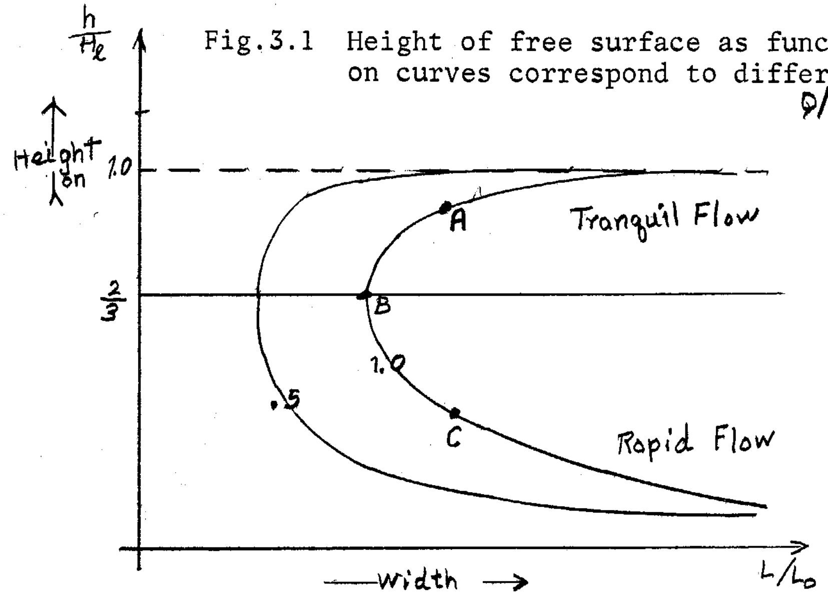

FIG 3.1

Height as function of width. Numbers on curves refer to discharges scaled by $L_0 H_e \sqrt{g H_e}$.

As a thought experiment, consider an upstream flow forced to correspond to point A of Fig.3.1. Furthermore, consider that the channel width is monotonically decreased downstream. Thus as the fluid flows down the channel it reaches at some point downstream the point B, where something is bound to happen if the channel is contracted further downstream. On the other hand, if the minimum width of the channel corresponds to point B, the fluid may, if the channel is widened again, reach the point C corresponding to a rapid flow in contrast to the tranquil flow of the upwtream state. In this sense and for this reason the point B will be referred to as a critical point.

4. Flow in a Rotating Channel*

Consider a rotating channel flow with no flow across the channel ($v = 0$) and no changes downstream ($\frac{\partial}{\partial(x)} = 0$). Moreover, if one scales as follows:

$$u^* \sim \sqrt{gH_\ell^*}\ ;\ h^* \sim H_\ell^*\ ;\ Q^* \sim L_0 H_\ell^* \sqrt{gH_\ell^*}\ ;\ y^*,\ L^* \sim L_0 \tag{4.1}$$

the equation of section 2 may be written

$$\left(\frac{L_0}{\lambda}\right) u = -h_y \qquad \text{(Eq.of motion)} \tag{4.2}$$

$$h_{yy} - \epsilon^2 \left(\frac{L_0}{\lambda}\right)^2 h = -\left(\frac{L_0}{\lambda}\right)^2 . \qquad \text{(Pot.vort.equation)} \tag{4.3}$$

Here $\epsilon^2 = H_\ell^* / H_0^*$ is the nondimensional potential vorticity and $\lambda = \sqrt{gH_\ell^*}/f$ is the radius of deformation. Now if $L_0/\lambda \ll 1$ it follows that to zero order there are no variations across the channel and that the non-rotating cubic equation, Eq.(3.1), is reproduced. On the other hand if $L_0/\lambda \gg 1$ the height is, apart from layers close to the walls where h_{yy} might become large, governed by the equation,

$$\epsilon^2 \left(\frac{L_0}{\lambda}\right)^2 h = \left(\frac{L_0}{\lambda}\right)^2 \tag{4.4}$$

which simply entails that the height is equal to the potential vorticity height in the interior, and that the flow takes place in boundary layers along the walls of width equal to the radius of deformation, λ . (c.f. McDougall (1976)). If the potential vorticity, ϵ^2, is very small Eq.(4.3) reduces to

$$h_{yy} = -\left(\frac{L_0}{\lambda}\right)^2 \tag{4.5}$$

which has been analyzed by Whitehead *et al.* (1974).

In the present analysis, flows with L_0 of order λ will be considered and one may as well put $L_0 = \lambda$. Thus Eqs.(4.2) and (4.3) become

$$u = -h_y \tag{4.6}$$

$$h_{yy} - \epsilon^2 h = -1 . \tag{4.7}$$

Defining a nondimensional discharge height, H_Q , by

$$H_Q = \frac{1}{H_\ell^*} \sqrt{\frac{2fQ}{g}} \tag{4.8}$$

Eq.(2.7) may be evaluated by means of Eq.(4.6) to give

$$H_Q^2 = h_r^2 - h_\ell^2 , \tag{4.9}$$

whereas the Bernouilli equation on the left wall takes the form

$$\frac{1}{2} u_\ell^2 + h_\ell = 1 \tag{4.10}$$

The solution to Eq.(4.7) is straightforward and expressed in terms of the height and the velocity on the left wall, h_ℓ and u_ℓ , respectively, it may be written

$$h = \frac{1}{\epsilon^2} - \frac{1}{\epsilon^2}\left(1 - \epsilon^2 h_\ell\right) \cosh \epsilon (L-y) + \frac{u_\ell}{\epsilon} \sinh \epsilon (L-y) \tag{4.11}$$

---

* In this and the next section, if not otherwise stated, starred quantities entail dimentional quantities.

u_ℓ is a function of h_ℓ through Eq.(4.10). Thus Eq.(4.9) provides an equation for h_ℓ in terms of the geometry, L, namely

$$1-(1-\epsilon^2 h_\ell)\cos h_\ell L+\epsilon\sqrt{2(1-h_\ell)}\,\sin h_\ell L=\epsilon^2\sqrt{H_Q^2+h_\ell^2} \tag{4.12}$$

This equation is the rotating version of the non-rotating cubic equation, Eq.(3.1). Different from the non-rotating case, h_ℓ^* depends, besides the geometry, not only on H_ℓ^* and Q^* but also on the potential vorticity height H_0^*. So, to study a forced rotating channel flow, three parameters need to be fixed. Figures (4.1) and (4.2) show h_e as a function of L for $\epsilon^2 = 1.0$ and $\epsilon^2 = .5$, respectively, and the curves drawn correspond to the curves drawn on Fig.(3.1) for different discharges. The aspect of non-rotating channel flow discussed in section 3 still applies for points where $\partial h_\ell/\partial L=0$, although this line is changed from the straight line $h_e = \frac{2}{3}$ in Fig.(3.1) to a curved one when rotation is present. More important, however, are two other aspects of the flow, namely:

(1) the possibility of stagnation (u = 0) at the right wall (y = 0) when $\epsilon^2 < 1.0$ in the tranquil flow state and

(2) the possibility that the height on the left wall may go to zero in the rapid flow state.

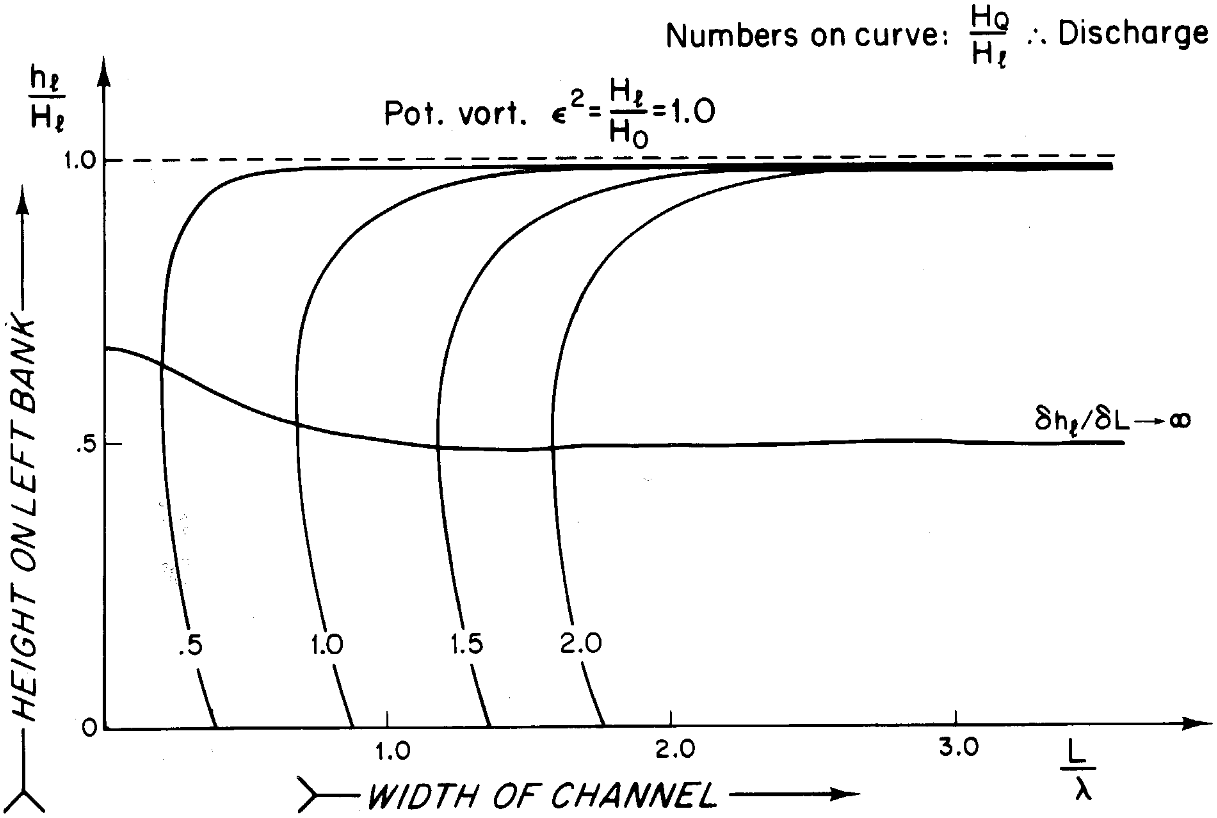

Fig.4.1 Same as Fig.3.1. Note additional features due to rotation. ϵ^2=1.0. See text.

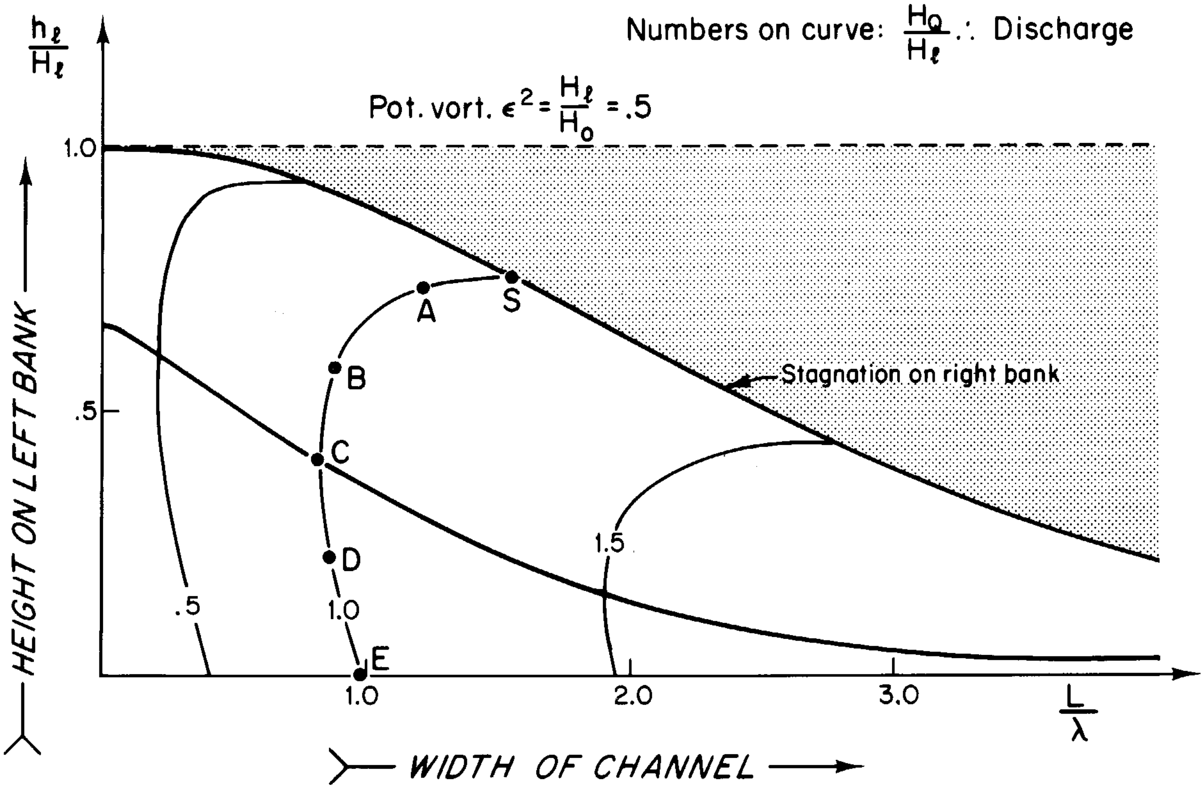

Fig.4.2,same as Fig.4.1. ϵ^2=.5 Note line called stagnation corresponding to zero velocity on right bank. See text.

These two aspects of the rotating flow may offer an explanation or be the main mechanism for the features shown by the experiments. The strikingly different flow pattern in the first and second experiment may be achieved by letting the parameters be in favor of either of the two different possibilities. Thus the first possibility with stagnation on the right wall necessarily entails that a streamline is leaving the wall, i.e. separation occurs on the right wall and may give rise to the anticyclonic gyre, whereas the second possibility entails that the height of the fluid goes to zero on the left wall, i.e. the flow separates from the left wall and may be turned around the sharp bend more easily.

5. Separated Flow Along a Curved Wall.

Even if the flow stagnates on the right-hand wall, the flow downstream is seen to be a jet along the wall with a free streamline on its outer edge where h = 0. However, in this case the downstream state cannot be connected with the upstream state by means of conservation of energy, which may be accomplished if the flow separates on the left-hand wall.

It may therefore be worthwhile to consider the problem of a "free" jet along a curved wall (Fig.5.1). It is convenient to introduce a new system of coordinates (S*,n*) with S^* always tangent to the wall, thus measuring the arc length, and n* to the wall (see Fig.(5.1)). If at the same time one scales such that

$$s^* = \rho_0 x,\ n^* = \lambda y,\ \rho^* = \rho_0\, \rho(x),\ h^* = H_\ell^* h,\ v_s^* = \sqrt{g H_\ell^*}\, u, \qquad (5.1)$$
$$v_n = V v$$

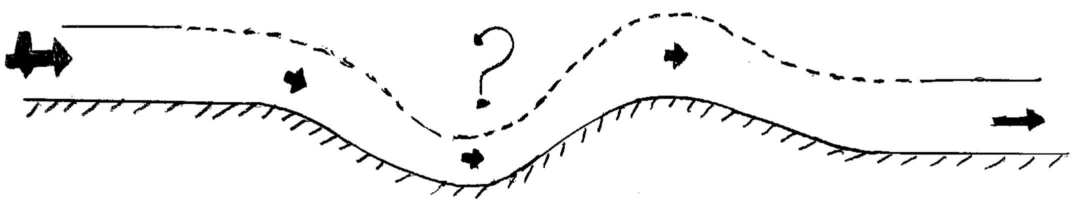

FIG. 5.1

Forced separated flow along a curved wall.

and note that due to continuity

$$\lambda\sqrt{gH_x} = \rho_0 V \tag{5.2}$$

where ρ_0 is the minimum radius of curvature, the equations of section 2 may be written

$$uu_x + vu_y - \frac{1}{R}\frac{uv}{\rho+(y/R)} - v = -h_x \tag{5.3}$$

$$\frac{1}{R^2}(uv_x + vv_y) + \frac{1}{R}\frac{u^2}{\rho+(y/R)} + u = -h_y \tag{5.4}$$

Equations of motion (5.3), (5.4)

$$(hu)_x + (hv)_y - \frac{1}{R}\frac{v}{\rho+(y/R)} = 0 \qquad \text{Continuity} \tag{5.5}$$

$$-u_y + \frac{1}{R^2}v_x + \frac{1}{R}\frac{u}{\rho+(y/R)} - \epsilon^2 h = -1 \; ; \qquad \text{Potential vorticity} \tag{5.6}$$

$$\frac{1}{2}\left(u^2 + \frac{1}{R^2}v^2\right) + h = H(\psi) \; ; \qquad \text{Bernouilli} \tag{5.7}$$

A new parameter, $\frac{1}{R} = \frac{\lambda}{\rho_0}$, is introduced which is the ratio between the radius of deformation, λ, and the radius of curvature, ρ_0. The new terms in the equations due to the curvature are the terms with $\frac{1}{R}$ in front. The nondimensional radius of curvature, $\rho(x)$, has a sign attached to it such that ρ is negative on capes and positive at bays. (Fig.5.1). The position of the free streamline where h = 0, is defined by the line

$$y = w(x) \tag{5.8}$$

where the dimensional width is scaled by the radius of deformation, λ, to form w. Thus at the free streamline, y = w,

$$h = 0, \; \frac{1}{2}\left(u^2 + \frac{1}{R^2}v^2\right) = 1 \tag{5.9}$$

whereas on the wall y = 0

$$\frac{1}{2}\left(u^2 + \frac{1}{R^2}v^2\right) + h = H_r \, . \tag{5.10}$$

When the radius of curvature is very large compared to the radius of deformation, the system is seen to zero order to be reduced to the system discussed in section 4. However, the introduction of a free streamline imposes a new constraint on the flow. This may be seen by expanding the dependent variables as follows:

$$(u, v, h, w) = (u^{(0)}, v^{(0)}, h^{(0)}, w^{(0)}) + \frac{1}{R}(u^{(1)}, v^{(1)}, h^{(1)}, w^{(1)}) + \dots \tag{5.11}$$

where to zero order the equations are

$$u^{(0)} = -h_y^{(0)}, \quad -u_y^{(0)} - \epsilon^2 h^{(0)} = -1 \tag{5.12}$$

with the boundary conditions

$$h^{(0)} = 0, \quad \tfrac{1}{2}u^{(0)2} = 1; \quad y = w^{(0)} \tag{5.13}$$

and

$$h^{(0)} = H_Q \text{ or } \tfrac{1}{2}u^{(0)2} + h^{(0)} = H_r \quad ; y = 0 \tag{5.14}$$

The solutions are

$$h^{(0)} = \frac{1}{\epsilon^2} - \frac{1}{\epsilon^2}\cosh\epsilon(w^{(0)}-y) + \frac{\sqrt{2}}{\epsilon}\sinh\epsilon(w^{(0)}-y) \tag{5.15}$$

where $w^{(0)}$ is determined by Eq.(5.14), viz.

$$1-\cosh\epsilon w^{(0)} + \epsilon\sqrt{2}\,\sinh\epsilon w^{(0)} = \epsilon^2 H_Q. \tag{5.16}$$

In Fig. 5.2 isolines are shown for $w^{(0)}$ i.e. the width of the jet scaled by λ, in the parameter space made up by the potential vorticity, ϵ^2, and the discharge height, H_Q. The heavy drawn line called stagnation entails that those isolines ending on this curve have $u^{(0)} = 0$ at the right wall for this value of ϵ^2 and H_Q. It is interesting to note that for $\epsilon^2 = 1/2$ all height profiles are exponential whereas for $\epsilon^2 = 0$ all height profiles are parabolic. (Whitehead *et al.*,loc.cit.).

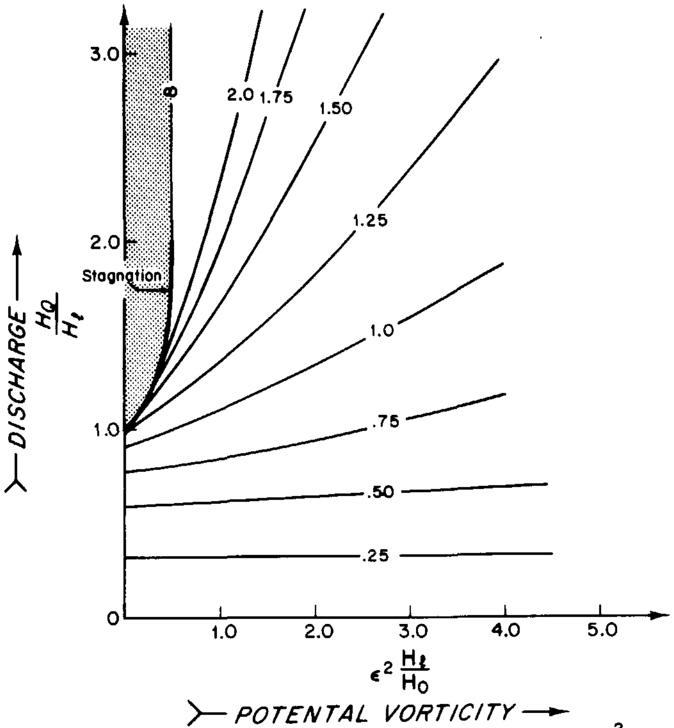

THE ZEROTH ORDER WIDTH AS FUNCTION OF ϵ^2, H_Q.

Fig.5.2 Isolines in ϵ^2, H_Q space for perpendicular distance from wall of streamline where h=0($w^{(0)}$) to zeroth order. See text.

Also it is evident that for discharge heights greater than two (i.e. $H_Q \geq 2$) ϵ^2 has to be greater than 1/2 to have solutions, i.e. the potential vorticity height has to be less than two times the Bernouilli height on the left wall $(H_0^* \leq 2 H_\ell^*)$, which corresponds to large widths compared to the radius of deformation.

Furthermore, $w^{(0)}$ is a constant once the parameters are fixed and is not changed when the radius of curvature is changed. Thus to zero order the free streamline is parallel to the wall Fig.(5.3).

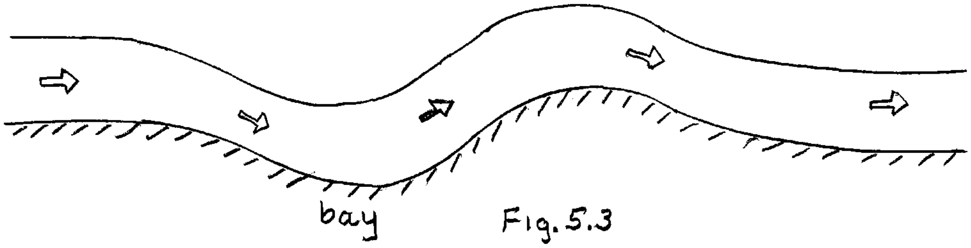

Fig.5.3

To obtain information about the effect of curvature one has to solve the first order problem. The governing equations to first order are

$$\rho u^{(1)} = -\rho h^{(1)}{}_y - u^{(0)2} \tag{5.17}$$

$$-\rho u^{(1)}{}_y - \epsilon^2 \rho h^{(1)} = -u^{(0)} \tag{5.18}$$

with the boundary conditions

$$\rho h^{(1)} - \rho w^{(1)} u^{(0)} = 0 \; ; \; y = w^{(0)} \tag{5.19}$$

$$\rho u^{(1)} + \rho w^{(1)} = 0 \; ; \; y = w^{(0)} \tag{5.20}$$

$$u^{(0)} \rho u^{(1)} + \rho h^{(1)} = 0 \; ; \; y = 0 \tag{5.21}$$

The solution for the height times the radius of curvature is

$$\rho h^{(1)} = (\rho w^{(1)} + \tfrac{2}{3}) u^{(0)} + \frac{4\epsilon^2 - 3}{6\epsilon^3} \sinh \epsilon (w^{(0)} - y) + \frac{1}{2}(w^{(0)} - y)\left(\frac{1 - \epsilon^2 h^{(0)}}{\epsilon^2}\right) - \frac{2u^{(0)}}{3\epsilon^2}(1 - \epsilon^2 h^{(0)}) \tag{5.22}$$

where use has been made of Eqs.(5.19) and (5.20). Equation (5.21) thus gives an equation for the correction to first order in the width, $w^{(1)}$, times the radius of curvature, viz:

$$\rho w^{(1)} = -\frac{2}{3\epsilon^2} - \frac{P(\epsilon, H_Q)}{\epsilon^2 H_Q u_r^{(0)}} \tag{5.23}$$

where the subscript r entails evaluation at the right wall y = 0. The function P is

$$P = \frac{4\epsilon^2 - 3}{6\epsilon^2}\left[u_r^{(0)} \cosh \epsilon w^{(0)} + \frac{1}{\epsilon} \sinh \epsilon w^{(0)}\right] + \frac{w^{(0)}}{2\epsilon^2}\left[1 - \epsilon^2 (H_Q + u_r^{(0)2})\right] + \frac{2u_r^{(0)}}{3\epsilon^2}(1 - \epsilon^2 H_Q)\left[(1 - \epsilon^2 H_Q) - \frac{1}{4}\right] - \frac{1}{3} u_r^{(0)3} \tag{5.24}$$

The solution for $\rho w^{(1)}$ may be presented in the same way as the zeroth order, $w^{(0)}$, and is demonstrated in Fig.(5.4) which shows isolines for $\rho w^{(1)}$ in the ϵ^2, H_Q space. Dashed lines correspond to negative values of $\rho w^{(1)}$. If $\rho w^{(1)} < 0$ then $w^{(1)}$ is positive at capes and negative at bays as shown in Fig.(5.5).

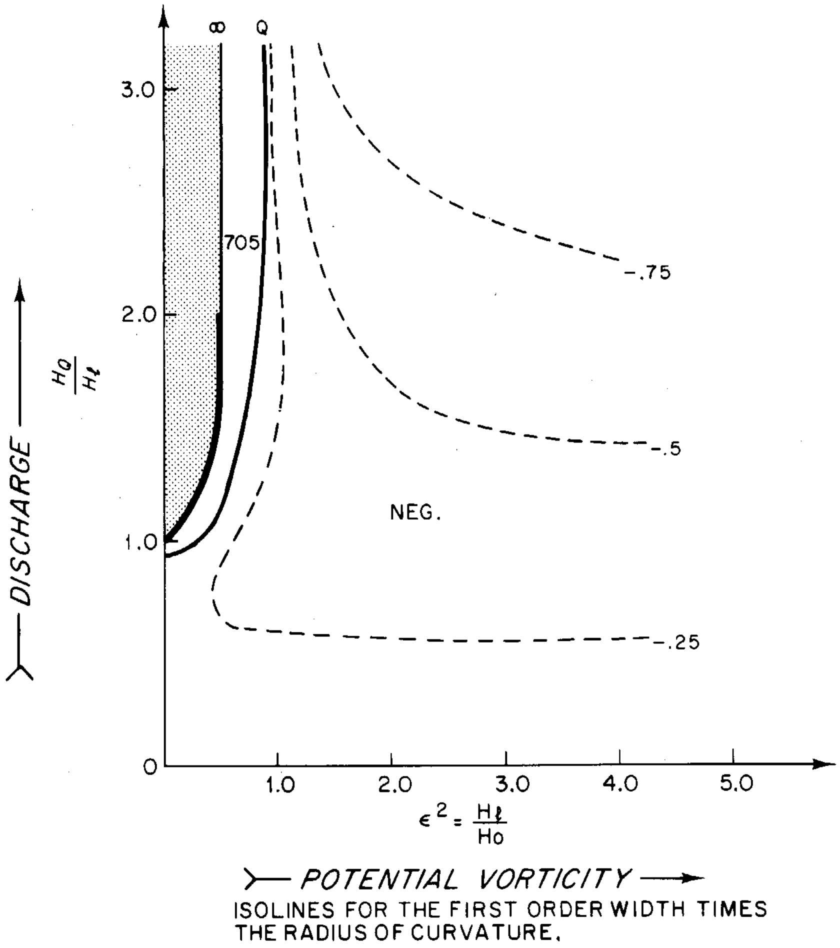

Fig.5.4 Isolines in ϵ^2, H_Q space for $\rho w^{(1)}$ i.e. first order correction to distance from wall of streamline where h=0 times radius of curvature. See text.

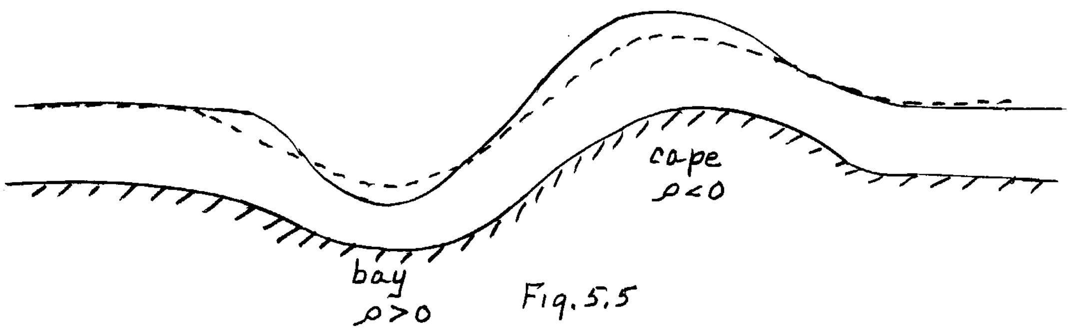

Fig. 5.5

Heavy lines: $y = w^{(0)} + \frac{1}{R} w^{(1)}$. Dashed line: $y = w^{(0)}$.

However, for a certain choice of parameters $\rho w^{(1)}$ attains positive values which have the opposite effect, i.e., $w^{(1)}$ is positive at bays and negative at capes. Note that in this case one is normally close to stagnation on the right wall.

Acknowledgment

It has been a most enjoyable and stimulating summer and I would like to express my gratitude to Dr. Melvin Stern for his suggestion of the problem. I would also like to acknowledge the valuable discussions I have had with him, Dr. George Veronis, Dr. Joseph Keller and Trevor McDougall.

References

Porter, D.L. 1976 Independent Research Exercise in Partial Fulfillment of Ph.D. at Massachusetts Institute of Technology - Woods Hole Oceanographic Institution, June 1976.

McDougall, T.J. 1976 Fellow lecturer, Geophysical Fluid Dynamics Program, Summer.

Whitehead, J.A., A.Leetmaa and R.A.Knox 1974 Rotating Hydraulics of Straits and Sill Flows. Geoph.Fluid Dyn. 6: 101-125.

A STUDY OF THE FORMATION OF BOTTOM WATER IN THE WESTERN MEDITERRANEAN SEA

Richard D. Romea

Introduction

The formation of bottom waters in the world oceans has been an elusive subject for many years. Oceans are generally strongly stratified and deep vertical mixing rarely occurs. The process seems to be quite catastrophic and short-lived, and could be easily missed in many places. Recently, much concentrated effort has gone into observing the process in the northwestern Mediterranean Sea, 100 km south of the coast of France. The area was accessible to research vessels and was observed in great detail during the winter of 1968-1969. Bottom water formation was observed only in one place during this winter, in a patch about 50 km wide and 100 km long. Directly under this patch is the Rhone deep sea fan, a topographic feature with a scale of the order of 50 km.

The event was short-lived, with vertical mixing lasting only two weeks, during the Mistral, a cold wind which blows from the north, between the Alps and the Pyranees. Wind speeds during the Mistral are typically 30 knots, with 50 knots recorded. Temperatures of 6°C are typical.

During the winter of 1968-1969, the Mistral began on the night of February 3, and lasted about 10 days. It was preceded by a month of cold weather. The cooling at the surface was uniform over the whole region and was typically 100 joules/m^2 sec. for the Mistral period.

The normal stratification of the northwest Mediterranean is weak, with a characteristic three-layer system. From the surface to about 200 m, the water is of Atlantic origin, with a typical temperature of 13.1°C and salinity of

38 - 38.4 °/oo. The intermediate water, extending from 200 m to 500 m, has high temperature ($>$ 13.1°C) and salinity (38.5 °/oo). Below 500 m is the cold bottom water, with temperature 12.7°C and salinity 38.4 °/oo.

A three-stage process was observed by the MEDOC group; the preconditioning phase, lasting about 30 days (January), the violent mixing phase, which starts with the onset of the Mistral, and the sinking and spreading phase, which can last until the middle of March. During the beginning of January, a dense patch of water is observed at the surface. Sections across this patch indicate a doming of the isopycnal surfaces towards the surface, and the formation of fronts of density and salinity surfaces. At the end of this preconditioning phase, horizontal variations of density, temperature, and salinity are of the same order as vertical variations.

The violent mixing stage is marked by a strong reduction of vertical density and salinity gradients, accompanied by deep vertical mixing almost to the bottom.

The remainder of this study will be an attempt to understand the process that was observed by the MEDOC group. In particular, the extreme locality of the region of bottom water formation will have to be explained, given the uniform meteorological conditions at the surface.

Mixed Layer Dynamics

We can look at the hydrographic situation as a two-layer system, with an interface at 500 m depth. The total depth of the sea is 2.5 km. A typical value for $\Delta \rho$, the density difference between the two layers, is 2×10^{-4}. A simple calculation shows that it would take 150-200 days to cool the upper layer so that $\Delta \rho = 0$. Even in the fierce Mistral conditions, the process would take about 50 days. Since there are only about 30 preconditioning days and 10 Mistral days, simple static cooling of the upper layer is not sufficient to cause strong vertical mixing.

The next obvious process to consider is the deepening of a surface mixed layer by entrainment. There are three effects which may contribute to the deepening of the mixed layer: mechanical stirring by the wind, cooling, and evaporation. If the latent heat associated with evaporation is included in the cooling effect, the salinity change due to the excess of evaporation over precipitation is minimal and does not contribute significantly to the mixed layer deepening.

Mechanical stirring is unimportant below the surface layers (100 m). The deepening goes like $t^{1/3}$ (Turner, 1973) and is also presumably limited by rotational effects, whereas the deepening due to cooling is not.

Turner's model of mixed layer deepening in the presence of a linear stable salt gradient and a constant temperature, with a constant heat flux from the top, gives the relation

$$d = \left(\frac{2B}{N_s^2}\right)^{1/2} t^{1/2}$$

$$N_s^2 = -g\beta \frac{ds}{dz} \qquad \text{(salt gradient)}$$

$$B = -g\frac{\alpha Q}{\rho c} \qquad \text{(buoyancy flux)}$$

Where d is the depth of the mixed layer, Q is the heat flux, C is the heat capacity, S is the salinity, and the equation of state has been used:

$$\rho = \rho_0 (1 - \alpha \Delta T + \beta \Delta S) .$$

Using typical values for ΔS, ΔT, and Q, it becomes clear that the mixed layer alone will not get much below 500 meters, even in Mistral conditions. At 500 meters, the mixed layer deepens at a rate of about one meter per day.

Two Layer Model with Uniform Potential Vorticity: (Shelf Model)

A new mechanism which might be relevant to the Mediterranean Sea in winter is the non-adiabatic geostrophic adjustment process. A simple two-layer model illustrates the physics:

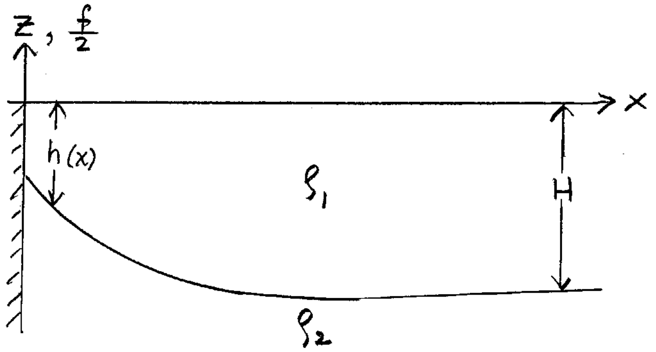

In this model, the lower layer, with density: $\rho_2 = \rho_1 + \Delta\rho$, is infinitely deep, and hence is dynamically passive. The interface is assumed to behave so that there is a uniform potential vorticity in the upper layer. Variations in y are zero. The relevant equations are:

$$\frac{f}{H} = \frac{f + \frac{\partial v}{\partial x}}{h} ; \qquad \text{conservation of potential vorticity}$$

$$f v = g^* \frac{\partial h}{\partial x} ; \qquad \text{geostrophic relation}$$

g^* is the reduced gravity:

$$g^* = \frac{\Delta\rho}{\rho_2} g$$

v is the geostrophic velocity in the y-direction.

These equations can be combined to yield:

$$\frac{\partial^2 h}{\partial x^2} - \frac{f^2}{g^* H} h = \frac{-f^2}{g^*} ,$$

with boundary conditions:

$$h(x) \longrightarrow H \quad \text{as} \quad x \longrightarrow \infty$$

$$V(0) = V_0 \quad \text{(velocity at the coast)}$$

The solution is:

$$h(x) = H - V_0 \sqrt{\frac{H}{g^*}}\, e^{-\frac{f}{\sqrt{g^* H}} x} .$$

The decay distance, or e- folding time, $\frac{\sqrt{g^* H}}{f}$, is the deformation radius.

If we vary g^* quasi-statically, by changing the density of the upper layer uniformly and allowing the system to adjust geostrophically to the new deformation radius, we can deduce the effect of cooling the upper layer on the interface height. With

$$g^* = \left(\frac{\Delta\rho - \delta\rho(t)}{\rho_0}\right) g ,$$

the interface will surface at $x = 0$ when

$$\delta\rho = \Delta\rho - \frac{\rho_0 V_0^2}{gH} .$$

In other words, when the density of the upper layer is lowered slightly, the interface will rise slightly, until the interface eventually breaks the surface.

At a depth of 500 meters, with typical parameters ($V_0 \sim 10$ cm/sec, $\Delta\rho \sim 2\text{x}10^{-4}$), the growth rate of the interface is 1 - 5 m/day. This means that, during the 30-day preconditioning phase, the initial topographic disturbance could amplify up to 100 meters upwards.

Of course this model is not really relevant to the Mediterranean problem, but it is an indication that we should investigate further. In fact, the model might be relevant for bottom water production along coasts and on shelves.

Isolated Vortex

The case of an isolated cyclonic vortex is more related to our problem. Obvious questions are: Will the interface rise with cooling at the surface, and will the interface break the surface?

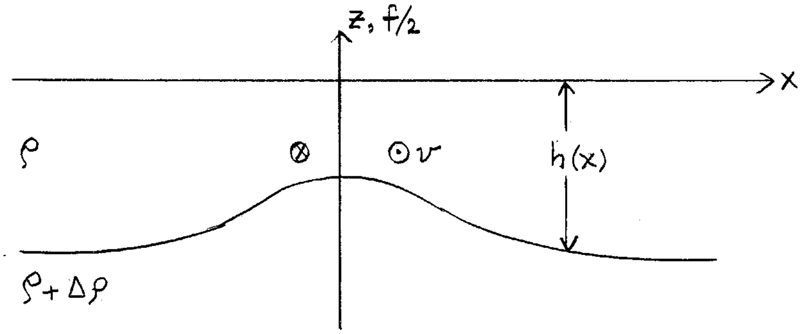

The potential vorticity equation is:

$$\frac{\partial}{\partial t}\left[\frac{f + \frac{g^*}{f} h_{xx}}{h}\right] = 0$$

When $g^* \longrightarrow 0$ (i.e., the density of the two layers becomes the same), $v \longrightarrow 0$ in the upper layer. This implies:

$$\frac{f + g_0^* h_{0xx}}{h_0} = \frac{f}{h_f}$$

where the subscript o indicates initial values, and the subscript f indicates final values. The equation can be rewritten:

$$\frac{h_f}{h_0} = \frac{f}{f + \frac{g_0^*}{f} h_{0xx}}$$

This quantity is less than one, for an initially cyclonic vortex, i.e., the interface rises. However, the interface does not reach the surface.

Another way of thinking about this process is to look at columns. As v goes to zero, columns move outward from the center of the gyre to conserve angular momentum. The interface rise follows as a consequence of the conservation of mass. However, the column which is sitting directly over the center of the gyre cannot go anywhere. Hence the limitation on h_f.

A nonlinear potential vorticity equation can be derived using the geostrophic relation, the potential vorticity equation, and the nonlinear y-momentum equation:

$$v = \frac{g^*}{f}\frac{\partial h}{\partial x}$$

$$\frac{D}{Dt}\left[\frac{f + \frac{g^*}{f}h_{xx}}{h}\right] = 0$$

$$\frac{\partial v}{\partial t} + u\left(\frac{\partial v}{\partial x} + f\right) = 0 \quad ;$$

$$\left(\frac{f + \frac{g^*}{f}h_{xx}}{h}\right)_t - \frac{(g^* h_x)_t}{(f^2 + g^* h_{xx})}\left(\frac{f + \frac{g^*}{f}h_{xx}}{h}\right)_x = 0$$

If $\frac{\partial}{\partial t}$ is expressed in terms of $\frac{\partial}{\partial g^*}$ (the two are simply related) and the substitution

$$I = \frac{g^*}{f^2}$$

is made, the equation becomes:

$$\left(\frac{1 + I h_{xx}}{h}\right)_I - \frac{(I h_x)_I}{(I h_{xx} + 1)}\left(\frac{1 + I h_{xx}}{h}\right)_x = 0$$

In the limit $I \rightarrow 0$ $(g^* \rightarrow 0)$, the equation reduces to

$$\frac{\partial h^2}{\partial t} = -h\frac{\partial^2 h^2}{\partial x^2} .$$

This is a negative diffusion equation, and tells us several things.

1. An initially flat interface will not do anything.
2. As $h \rightarrow 0$, the rising slows down; the sides of the bump will catch up to the center.
3. Fronts may form, with large horizontal gradients.

This kind of behavior is very suggestive of some of the MEDOC sections.

Two-Layer Model with Uniform Cooling

All the previous models have assumed that the density changes uniformly in the upper layer, as a result of the cooling. In fact, this is not such a bad assumption, but one would like to be sure that the effect of non-uniform density variations in the upper layer still yields the same qualitative results. There is reason to believe that a more realistic model would actually increase the amplification effect.

The same two-layer formulation is used, except that Q, the heat flux, is now specified. ΔT is the temperature difference between the two layers: the lower

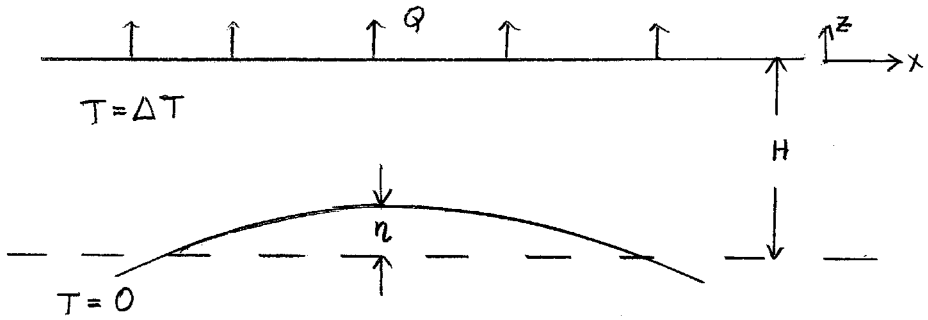

layer is assumed infinite in depth and passive.

A consistent model could be formulated when $\frac{\eta}{H} << 1$ and $\frac{U}{fL} << 1$. The equations are:

Momentum:

$$f v = \frac{1}{\rho_0}\frac{\partial P}{\partial x}$$

$$\frac{\partial v}{\partial t} + f u = 0$$

$$\frac{\partial}{\partial z}\left(\frac{P}{\rho_0}\right) = -g\frac{\rho}{\rho_0}$$

Continuity:

$$\frac{\partial u}{\partial x} + \frac{\partial w}{\partial z} = 0$$

State:

$$\rho = \rho_0(1-\alpha T)$$

Heat:

$$(H-\eta)\frac{dT}{dt} = -\frac{Q}{\rho_0 C}$$

Pressure Condition:

$$\frac{\partial P}{\partial x} = -\rho_0 g \alpha T\frac{\partial \eta}{\partial x} \quad \text{at } z=-H+\eta$$

Boundary Conditions:

$$w = 0 \quad \text{at } z = 0$$

$$w = \frac{\partial \eta}{\partial t} \quad \text{at } z=-H+\eta$$

The temperature T can be written:

$$T = \Delta T - Ft + T'(x,t),$$

where $T' << \Delta T$

$$F = \frac{Q}{\rho_0 C H}$$

In this representation, $\Delta T - Ft$ is the cooling of the layer with no motion, and T' is the perturbation due to the interface deformation.

This formulation works if: (in the upper layer)

$$u = u(x,z,t)$$
$$v = v(x,z,t)$$
$$w = w(x,z,t)$$
$$P = P(x,z,t)$$
$$\rho = \rho(x,t)$$
$$T = T(x,t)$$
$$\eta = \eta(x,t)$$

The linearized equations become:

momentum: $$fv = \frac{1}{\rho_0}\frac{\partial p}{\partial x}$$

$$\frac{\partial v}{\partial t} + fu = 0$$

$$\frac{\partial p}{\partial z} = \rho_0 g \alpha (\Delta T - Ft + T')$$

continuity: $$\frac{\partial u}{\partial x} + \frac{\partial w}{\partial z} = 0$$

heat: $$\frac{\partial T'}{\partial t} = -\frac{F}{H}\eta$$

Boundary Conditions : $$\frac{\partial p}{\partial x} = -\rho_0 g \alpha (\Delta T - Ft)\frac{\partial \eta}{\partial x} \quad \text{at } z = -H$$

$$w = 0 \quad \text{at} \quad z = 0$$

$$w = \frac{\partial \eta}{\partial t} \quad \text{at} \quad z = -H$$

Of course, this model is restricted to the initial displacements by the linearization.

The equations can be combined to yield one (nondimensional) equation:

$$\frac{1}{2}\eta_{xx} - (1-t)\eta_{xxt} + \eta_t = 0$$

The equation can be Fourier transformed in x , with the result that, initially, η grows like t .

If an initial perturbation $$\eta(x,0) = A_0 \cos kx$$

is assumed, $A(t)$ can be found:

$$A(t) = A_0 \left[\frac{1+k^2}{1+k^2(1-t)}\right]^{1/2}$$

$$\eta(x,t) = A(t)\cos kx .$$

For small time: $$A(t) = A_0 \left[1 + \frac{1}{2}\left(\frac{k^2 t}{1+k^2}\right)\right]$$

Typical values (a small bump was used) give an interface rise on the order of two meters a day. This initial growth rate is smaller than that for the shelf model, but the growth will presumably speed up as the feedback becomes important.

T can be calculated from the heat equation. For a small bump $(k \to \infty)$

$$A(t) \sim A_0 \left(\frac{1}{1-t}\right)^{1/2}$$

$$T = (1-t) + 2A_0\left[(1-t)^{1/2} - 1\right]$$

When T goes to zero, there is no longer a difference between the two layers. T = 0 when:

$$(1-t_c) = -2A_0\left[(1-t_c)^{1/2}-1\right]$$

Solving for t_c shows that the effect of the rising interface is to decrease the vertical stability right in the center of the gyre faster than it would decrease due to the cooling alone. The effect on the regions outside the center of the gyre is minimal.

Conclusion

In this study, various models have been investigated to try to understand the mechanism of bottom water formation. The bump, which has its genesis in the topographic relief of the bottom, amplifies due to the non-adiabatic geostrophic adjustment of pycnoclines to the surface cooling. In this region, the topography, the cooling, and the cyclonic circulation are essential ingrediants in the process. The rising interface prevents the deepening of the cooling layer due to entrainment. This mixed layer alone will not deepen fast enough, even during Mistral forcing, to form bottom water. The deepening process will slow down as the surface cooling affects a larger body of fluid.

However, there is a region which has been preconditioned. Here the vertical stability has been drastically reduced, even though the cooling has been uniform at the surface. At the onset of the Mistral, the mixed layer can break through in the center of the gyre. The violent mixing phase, which involves the mixing of the intermediate water with the surface water, allows vertical mixing all the way to the bottom.

Acknowledgments

Many thanks to Prof. Melvin E. Stern for suggesting this problem to me, and especially for his excellent guidance throughout the summer program.

References

Anati, D. and H. Stommel 1970 The initial phase of deep water formation in the Northwest Mediterranean during MEDOC '69. Cah.Oceanogr. 23: 343.

Anati, D. 1971 On the mechanics of the deep mixed layer formation during MEDOC '69. Cah.Oceanogr. 23: 427-443.

Bunker, A.F. 1972 Wintertime interactions of the atmosphere with the Mediterranean Sea. J.P.O. 2: 225-238.

Hogg, N. 1973 The preconditioning phase of MEDOC 1969 - II, Topographic effects. Deep-Sea Res. 20: 449.

Lacombe, H. and P. Tchernia 1972 Évolution hydrologique dans la zone de formation d'eau profonde au large de la cote Méditerranée Française par hiver très froid (1962-1963). Colloques Internationaux du CNRS, No.215. La Formation des Eaux Profondes.

MEDOC Group 1970 Observation of formation of deep water in the Mediterranean Sea - 1969. Nature 227: 1037-1040.

Sankey, T. 1971 The formation of deep water in the northwest Mediterranean. Prog.Oceanogr. 6: 159.

Saint-Guily, B. 1963 Remarques sur le mecanisme de formation des eaux profondes. *Rapp.Comm.Int.Mer.Medit.* *17*(3): 929-932.

Stommel, H. 1972 Deep winter time convection in the western Mediterranean Sea, in: *Studies in Physical Oceanography*. Al Gordon, ed., Gordon and Breach *2*: 207-218.

Swallow, J. and G. Caston 1972 MEDOC 1969, the preconditioning phase. *Colloques Internationaux du CNRS*. No.*215*, Processus de formation des eaux profondes. p.139-145.

Turner, J. 1973 *Buoyancy Effects in Fluids*, Cambridge Univ.Press. pp.251-287.

CLIMATIC FEEDBACKS CALCULATED FROM SATELLITE OBSERVATIONS

Glenn H. White

This work is dedicated to Dr. Grace Feng who informed me this spring that global climatology had nothing to do with geophysical fluid dynamics. This summer has proven her correct.

1. Introduction

Of the various types of climate models, energy balance models have received the widest attention due to the relative ease in understanding and interpreting them. They generally focus on the surface temperature's response to changes in the components of the Earth's radiation budget and commonly relate the outgoing infrared flux and albedo to the surface temperature by means of empirical formulas.

Table 1.

Parameterization of infrared flux and albedo in some energy balance climate models. (F is the outgoing infrared flux at the top of the atmosphere in watts/m^2. T is the surface temperature in $^{\circ}$C, n is the amount of cloudiness, m is an atmospheric attenuation coefficient, α is the albedo, and b(x) and c(x) are constants varying only with latitude x.)

Infrared flux

Budyko (1969)	$F = 226.1 + 2.26T - (48.4 + 1.61T)n$
$n = .5 \Longrightarrow$	$F = 201.9 + 1.46T$
Sellers (1969)	$F = \sigma T^4 (1 - m \tanh (19\, T^6 \times 10^{-16}))$
linearized by North (1975)	$F = 211.2 + 1.55T$

Albedo

Budyko (1969)	$\alpha = .62$	if	$T < -10^{\circ}C$
	$\alpha = .32$		$T > -10^{\circ}C$
Sellers (1969)	$\alpha = b(x) - .009T$	T+	$T \angle 10^{\circ}C$
	$\alpha = c(x)$		$T > 10^{\circ}C$
Faegre (1972)	$\alpha = .486 - .009T$		

Table 1 shows the parameterization of albedo and temperature in some energy balance models. Budyko (1969) parameterized the outgoing infrared radiation as a function of surface temperature and cloudiness based on mean monthly data at surface stations, but in his actual model held the cloudiness constant. He parameterized the albedo in terms of a temperature-dependent step function, letting the edge of the ice cap be represented by the -10°C isotherm. Sellers (1969) used a more complex infrared flux involving an atmospheric attenuation coefficient. North (1975) approximated Sellers' expression by a linear function of temperature. Sellers expressed the albedo as a linear function of temperature in latitudes where snow and ice would be present at least part of the year and as a latitudinally dependent constant elsewhere. Faegre (1972) expressed albedo as a linear function of temperature everywhere. Schneider and Gal-Chen (1973) investigated different parameterizations employed in energy balance climate models and concluded that the albedo parameterization in the tropics was particularly important. A subsequent paper (Gal-Chen and Schneider, 1976) concluded that different albedo parameterizations affected the results of energy balance climate models much more drastically than did different parameterizations of the dynamics.

This paper attempts to determine the accuracy of the above parameterizations of albedo and infrared flux by correlating satellite observations of mean monthly zonally averaged infrared fluxes and albedos (Ellis and Vonder Haar, 1976) with mean monthly 1000 mb temperatures (Van Loon, 1975) by means of linear least squares fits. The limited number and accuracy of satellite observations precludes for many years the use of mean annual values for such correlations.

II. The Data

The twelve mean monthly sets of zonal albedo and infrared flux were compiled by Ellis and Vonder Haar (1976) from 29 months of satellite observations by six different satellites during the period July 1964 to May 1971. They estimated the experimental error as ± 5% of the observed albedo or infrared flux.

These 29 months include three months of observations by ITOS 1 in April, May, and June 1970 and one month by NOAA 1 in May 1971. Table 2 contrasts the the observations of globally averaged albedo and infrared flux by these satellites with others for April, May, June in other years by other satellites. Numbus 2's global infrared flux was calculated from Vonder Haar's data and the other three satellites' observations. The variation may be partly explained by the time of observation. The infrared flux observed by satellites is larger in the afternoon and smaller in the morning. Flanders and Smith (1975) attribute the large albedos observed by ITOS 1 and NOAA 1 to more convective cloudiness in the afternoon. There is also the possibility that some experimental error is present, affecting Ellis and Vonder Haar's data for April, May, and June.

Mean monthly zonal cloudiness from 30°N to 30°S was calculated from data compiled by Sadler (1969) from nephanalyses from TIROS IX and X and ESSA 1 and 3 between February 1965 and January 1967.

III. Infrared Flux

Table 3 shows the results of attempting linear least square fits of zonal mean monthly outgoing infrared radiation fluxes with zonal mean monthly 1000 mb temperatures. The correlation coefficient used is:

Table 2

Globally averaged albedo and infrared radiation as observed in April, May, and June of different years by different satellites.

Satellite		albedo	TR	net radiation
ITOS 1	April	.348	254.6	-26.2
1970	May	.341	254.5	-32.9
observation time	June	.333	254.1	-35.4
15:00				
(Flanders and Smith, 1975)				
NOAA 1	Feb.-March	.351	247.1	-12.1
1971				
observation time	June	.344	246.9	-26.2
15:00				
(Flanders and Smith,1975)				
NIMBUS 3	April 16-30	.288	241.4	-1.4
1969	May 1-15	.291	242.1	-6.3
observation time	May 16-31	.298	244.2	-11.2
11:30	June 1-15	.296	244.9	-12.6
(Raschke *et al.*)	June 16-30	.291	245.6	-12.6
NIMBUS 2	May		236.25	(calculated)
1966	June		237.15	
observation time				
11.30				

$$1 - \frac{(\sigma yx)^2}{(\sigma y)^2}, \qquad (1)$$

where $(\sigma yx)^2$ is the estimate of the variance of the linear least squares fit and $(\sigma y)^2$ is the variance of the observed infrared fluxes about their mean. Range is the difference between the maximum and minimum monthly values in the twelve-month data set. We have listed the ratio of range to the mean annual zonal infrared flux in parentheses when the range is less than twice the experimental uncertainty. The numbers in parentheses following the linear fit coefficients are estimates of the standard deviations of the coefficients. These numbers reflect uncertainty only in the statistical fit and not in the original data. These two standard deviations for A(x) and B(x) are not independent of each other, but any change in B(x) would lead to a change in A(x) such that the outgoing flux at the mean annual zonal temperature would remain the same.

We have also listed the estimated experimental uncertainty (± 5% of the zonal mean infrared flux) and the standard deviation of the least square fit. The standard deviation of the fit is smaller than the experimental uncertainty everywhere except in the polar regions. At 75°S and 85°S, the zonal 1000 mb temperature falls quite rapidly in the fall and much less rapidly in the winter, while the infrared flux drops at an approximately constant rate throughout the fall and winter. The infrared flux observed from outer space comes of course from some dis-

Table 3.

Latitude	Meam Annual infrared flux (watts/m^2)	Linear Function (T in °C) F(x) = A(x) + B(x)T(x)	Correlation	Estimated Experimental Uncertainty(5%)	Standard Deviation of Fit	Annual Range of IR Flux	Annual Range of Temperatire
85°N	174.7	204.5(±6.8)+1.654(±.308)T(x)	.72	8.7	13.5	69.6	35.4
75°N	178.2	202.4(±6.7)+1.903(±.403)T(x)	.66	8.9	14.7	67.7	28.2
65°N	189.1	199.0(± .5)±1.807(±.253)T(x)	.82	9.5	10.9	63.4	34.9
55°N	201.1	196.3(±2.5)±2.205(±.271)T(x)	.86	10.1	8.4	57.7	25.1
45°N	218.3	194.8(±2.6)±2.818(±.235)T(x)	.93	10.9	6.0	58.2	21.1
35°N	239.6	188.6(±5.9)±3.211(±.349)T(x)	.88	12.0	6.6	49.6	15.6
25°N	257.7	203.4(±14.6)±2.341(±.622)T(x)	.54	12.9	7.2	26.7	9.3
15°N	257.1	328.2(±69.1)-2.709(±2.627)T(x)	.01	12.9	11.4	43.3	3.7
5°N	250.0	-42/3(±112.6)+11.092(±4.275)T(x)	.34	12.5	4.8	19.3(7.7%)	1.0
5°S	258.2	430.6(±122.0)-6.574(±4.653)T(x)	.08	12.9	9.3	28.8	1.8
15°S	266.7	464.7(±49.0)-8.042(±1.987)T(x)	.58	13.3	8.0	34.7	3.4
25°S	262.7	276.3(±10.2)-0.635(±.475)T(x)	.07	13.1	3.9	15.0(5.7%)	6.8
35°S	244.4	195.6(±6.2)+2.946(±.370)T(x)	.85	12.2	3.0	24.2(9.9%)	6.5
45°S	224.4	166.6(±8.2)+5.978(±.834)T(x)	.82	11.2	4.9	32.4	4.9
55°S	206.9	185.3(±3.8)+7.688(±1.173)T(x)	.79	10.3	6.6	39.4	4.5
65°S	189.6	216.3(±4.3)+4.465(±.581)T(x)	.84	9.5	8.7	60.0	12.1
75°S	163.3	266.6(±19.4)+3.100(±.560)T(x)	.73	8.2	18.2	106.7	26.0
85°S	154.3	284.9(±28.3)+2.984(±.630)T(x)	.66	7.7	22.6	118.2	28.0

Correlations of Zonal Infrared Radiation and Zonal Surface Temperature.

tance above the ground and there the atmosphere may well cool more gradually over the Antarctic than the ground does in the fall, especially since a strong inversion is often present in the Antarctic during the polar night. The same pattern does not seem to be present in the Northern Hemisphere polar regions.

We found that the variance unexplained by the linear least squares fit could be reduced by a factor of two on the average by removing the months April, May, and June and that this also reduced the standard deviation an average of 32%.

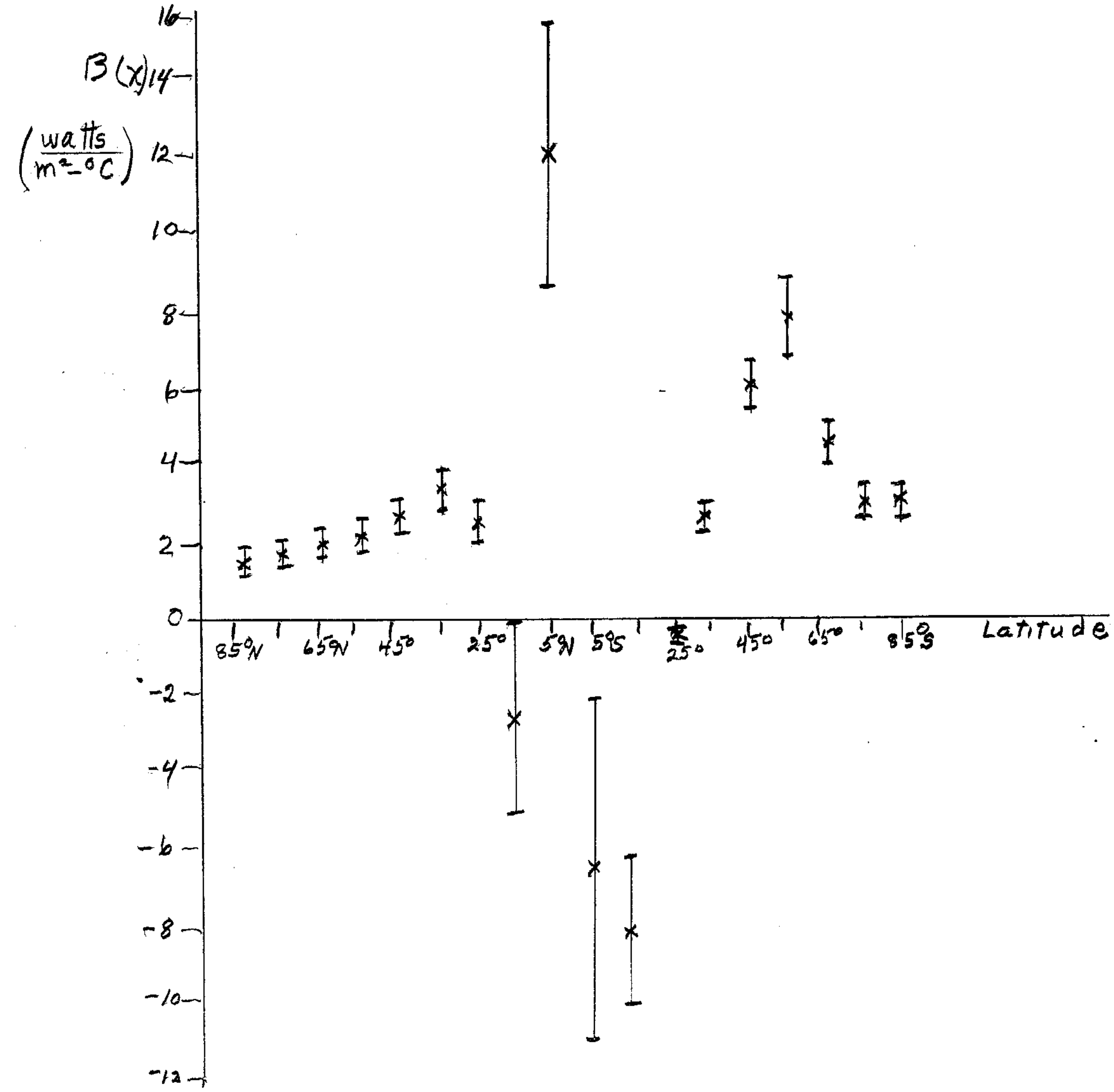

Fig.1. The slope of the zonal infrared flux - temperature relation as a function of latitude.

Figure 1 is a graphical presentation of the slopes of the zonal infrared-temperature relations. The error bars represent the standard deviations as given in Table 3.

Note that the zonal infrared fluxes increase with temperature outside the tropics and are well correlated with temperature.while in the tropics the infrared generally decreases as the temperature increases although the correlations are usually so poor as to be nonexistant. Note that at 5°N the infrared flux and surface temperature both vary by very little.

The slopes outside the tropics seem to be lowest near the poles and higher at lower latitudes. This could be due to the higher temperatures at lower latitudes and therefore greater water vapor content and variability in the atmosphere.

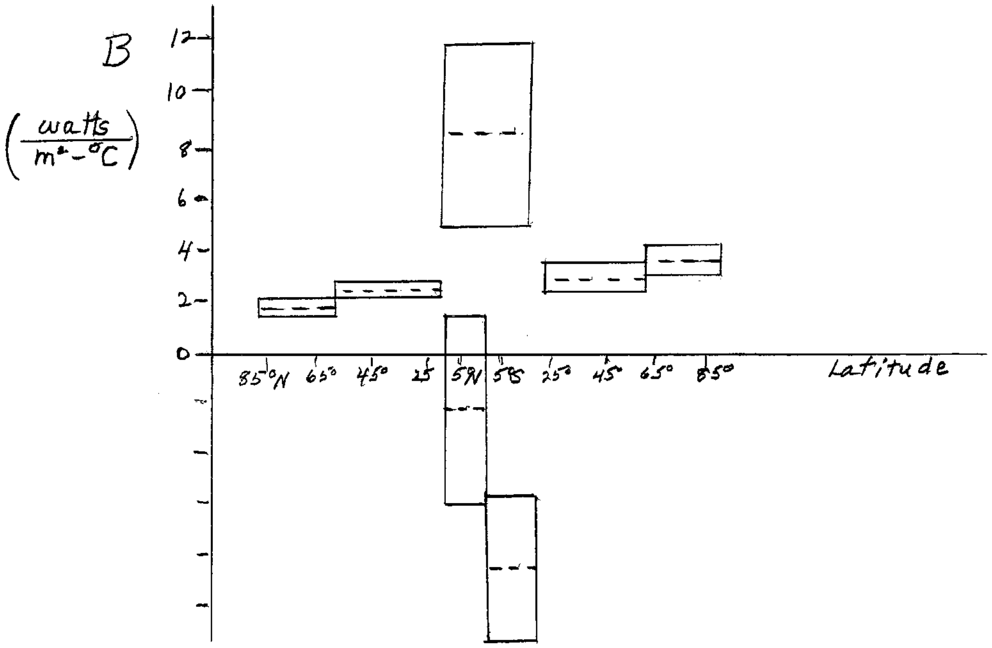

Fig.2. Slope of the regional infrared - temperature relation as a function of latitude. (– – — slope, ——— slope ± standard deviation of slope).

Figure 2 is the graphical representation of the slopes of the regional infrared flux-temperature. The boxes represent the slope (the dashed line) with the standard deviation. To calculate the regional monthly infrared flux, we weighted the zonal fluxes by the cosine of the central latitude of the zone and then summed. The table shows good correlations outside the tropics with positive slopes. Note that while the midlatitudes in the two hemispheres have a same slope to within the standard deviations, the slope in the Antarctic is twice that in the Arctic. Negative slopes are found in the Northern and Southern Hemisphere tropics separately, with an appreciable correlation in the Southern tropics. However, if one looks at the entire tropics (15°N - 15°S), one finds a positive slope. This could mean that the infrared flux is greatly influenced by the Intertropical Convergence Zone and perhaps other bands of cloudiness moving across the equator. In that case the seasonal zonal linear fits in the tropics (as in Table 3) would be quite different from the case of a change in the mean annual temperature. However, note the very small annual ranges in both infrared flux and temperature in the region 15°N - 15°S. In addition, 15°N - 15°S encompasses two regions in which the change of temperature is in opposite directions during the same season. These two facts throw doubt on the validity of the correlation in the region 15°N - 15°S.

The poor correlation for the Southern Hemisphere is partly due to the small change in infrared flux during the year and partly due to the presence of two

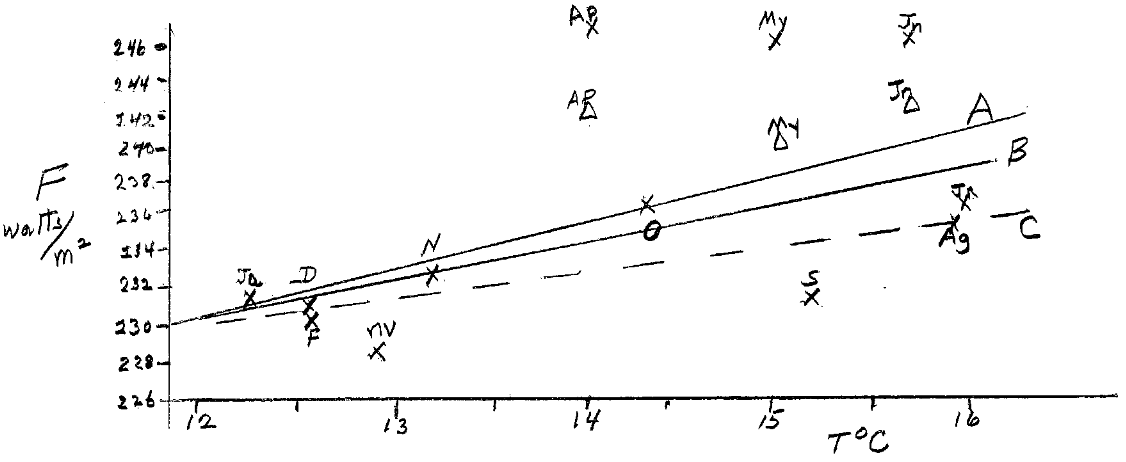

Fig.3 Globally averaged mean monthly infrared flux as a function of globally averaged mean monthly temperature. (x: original data; △: infrared fluxes after removing ITOS 1 and NOAA 1 data) Curve A is the result of a least square fit of the oritinal data (F = 200.3+2.510T; correlation = .24). Curve B is the least squares fit when ITOS 1 and NOAA 1 data is eliminated from April, May, and June; (F = 205.9+ 2.026T, correlation = .34). Curve C is the least squares fit when April, May and June are eliminated altogether. (F = 213.1+1.393T, correlation = .45).

regions which have opposite slopes (5°S - 15°S and 25°S - 85°S).

Note that the standard deviation of the least squares fit is significantly less than the estimated experimental uncertainty for all except the polar regions.

Removing the months of April, May, and June reduces the variance of the infrared flux unexplained by temperature by an average factor of almost three for all regions except 15°N - 15°S (where the slope changes sign when the three months are removed) while the standard deviation of the linear fit in all regions is reduced on the average by 44%.

The dramatic improvement in the fit of a linear relation to the data by removing the months April, May, and June encourages further speculation about the possibility of an experimental error larger than 5% in those three months. Fig.3 is a plot of the globally averaged mean monthly infrared flux against the globally averaged mean monthly temperature. We have computed, using Table 2, the global mean infrared flux in April, May, and June when the ITOS 1 and NOAA 1 data is excluded. Figure 3 shows that excluding the ITOS 1 and NOAA 1 (curve B) improves the fit, but not as much as if the three months are left out altogether (curve C). This suggests that there is some reason other than experimental error why the infrared radiation is higher in April, May, and June than a linear infrared - temperature relation would indicate and that removing the three months altogether may yield a result further from reality than the original correlations.

Table 5 shows the correlation of regional mean monthly infrared radiation with regional mean monthly cloudiness in the tropics. Note that the correlations are considerably higher than for the same regions in Table 4 and the standard deviation is much less.

Table 6 shows the results of a multiple linear regression seeking to relate infrared flux to both temperature and cloudiness in the tropics. Note that for 15°N - 5°N the correlation and standard deviation have not significantly improved

Table 4

Region	Mean Annual IR	Linear Function (T in ^{o}C) $F = A + BT$	Correlation	Est. Experimental Uncertainty (5%)	Standard Deviation of Fit	Annual Range of IR Flux	Annual Range of Temperature
85^{o}N-65^{o}N	183.8	200.9(±4.6)+1.833(±0.304)T	.76	9.2	12.4	65.6	32.5
85^{o}N-25^{o}N	222.8	201.3(±3.6)+2.379(±.310)T	.84	11.1	7.6	47.6	19.9
55^{o}N-25^{o}N	232.7	196.2(±4.8)+2.663(±.322)T	.86	11.6	6.6	43.5	16.7
15^{o}N-5^{o}N	253.5	309.5(±99.2)-2.128(±3.769)T	-.07	12.7	8.7	30.0	2.2
5^{o}S-15^{o}S	262.4	478.9(±73.7)-8.514(±2.896)T	.41	13.1	8.5	31.7	2.5
15^{o}N-15^{o}S	258.0	33.9(±93.8)+8.660(±3.624)T	.30	12.9	4.9	16.3(6.3%)	1.3
25^{o}S-55^{o}S	238.1	196.3(±7.5)+3.026(±.537)T	.74	11.9	3.8	21.0(8.8%)	5.7
25^{o}S-85^{0}S	225.6	201.4(±4.0)+3.442(±.524)T	.79	11.3	5.2	30.9	8.1
65^{o}S-85^{o}S	176.7	248.0(±12.0)+3.660(±0.584)T	.78	8.8	13.3	82.3	18.6
NH	233.3	204.2(±6.5)+1.944(±0.414)T	.66	11.7	7.0	30.2	13.7
SH	238.2	217.1(±8.9)+1.580(±0.657)T	.30	11.9	4.9	17.0(7.1%)	6.0
Globe	235.7	200.3(±16.9)+2.510(±1.191)T	.24	11.8	5.7	18.3(7.8%)	3.8

Correlations of Regional Infrared Flux and Regional Surface Temperature

Table 5

Region	Mean Annual IR	$F = M + N A_c$	Correlation	Est. Error	Standard Deviation	Range in IR Flux	Range in Cloudiness
$15^{o}N-5^{o}N$	253.5	$349.3(\pm 20.0)-197.4(\pm 41.2)A_c$	.67	12.7	4.9	30.0	9.9%
$5^{o}S-15^{o}S$	262,4	$44k,7(\pm 28.6)-355.0(\pm 56.6)A_c$	.78	13.1	5.2	31.7	8.7%
$15^{o}N-15^{o}S$	258.0	$353.4(\pm 39.8)-192.8(\pm 80.4)A_c$	.30	12.9	4.9	16.4(6.3%)	5.8%

Regional infrared radiation as a function of regional cloudiness.

Table 6

Region	Mean Annual IR	$F = S + U^{*}T + V A_c$	Correlation	Est. Error	Standard Deviation	Range in IR Flux	Range in T	Range in Cloudiness
$15^{o}N-5^{o}N$	253.5	$282.6+3.025T-224.1\ A_c$	.69	12.7	4.7	30.0	2.2	9.9%
$5^{o}S-15^{o}S$	262.4	$533.1-4.810T-293.9\ A_c$	.90	13.1	3.4	31.7	2.5	8.7%
$15^{o}N-15^{o}S$	258.0	$192.2+4.540T-104.5\ A_c$	.25	12.9	5.1	16.4(6.3%)	1.3	5.8%

Regional Infrared Flux as a Function of Regional Temperature and Regional Cloudiness.

Table 7

Region	Mean Annual Cloudiness	$A_c = P + RT$	Correlation	Standard Deviation	Range in Cloudiness	Range in Temperature
$15^{o}N-5^{o}N$	.485	$-.120(\pm .380)+.02302(\pm .01446)T$	.12	.034	9.9%	2.2
$5^{o}S-15^{o}S$	.505	$.185(\pm .232)+.01259(\pm .00911)T$	.08	.027	8.7%	2.5
$15^{o}N-15^{o}S$	.495	$1.516(\pm .178)-.03945(\pm .00686)T$	.74	.009	5.8%	1.3

Regional Cloudiness as a Function of Regional Temperature.

over Table 5, but that there has been improvement at 5°S-15°S. This plus Table 4 suggests that infrared flux can be better correlated with cloudiness than with temperature in the tropics, especially in the tropics north of the equator.

Table 6 also shows that in the region 5°S -15°S an increase in temperature would lead to a decrease in infrared flux even if the cloudiness did not vary. An increase in temperature could lead to more water vapor in the air and thus greater infrared opacity or to higher cloud tops. The cloudiness might not vary in either case, but the infrared flux would do so.

Table 7 shows the correlation of regional cloudiness and regional temperature. This suggests that cloudiness cannot be accurately expressed as a linear function of temperature. Figure 4 shows the regional cloudiness for 5°S-15°S plotted as a function of regional temperature. Note that the values for April, May, and June again appear to be quite different than other months and that one can significantly improve the correlation of cloudiness with temperature by removing April, May, and June. Since the cloudiness used here was observed by different satellites at largely different times than those observing the radiation budget, this would imply that there may exist some atmospheric mechanism that produces less cloudiness and greater infrared flux in April, May, and June than would be predicted by linear functions of temperature.

Cloudiness at 25°N and 25°S varies by less than four percent during the year and good correlations with temperature were not obtained. A negative slope was present at both latitudes.

There appears to be a strong possibility that in the tropics an increase in surface temperature would lead to a decrease in infrared flux. Infrared flux appears better correlated to cloudiness in the tropics than to surface temperature, and cloudiness may not be a simple function of temperature. This would considerably complicate the energy balance climate models. It appears that one cannot parameterize the whole globe by one empirical expression giving infrared as a linear function of temperature. It also appears that some satellite data employed by Ellis and Vonder Haar (1976) may be inaccurate.

IV. Albedo

Table 8 shows the linear least-square fits of zonal albedos with zonal 1000 mb temperatures. Figure 5 is the graphical representation of the slopes. In the polar latitudes we have left out the albedos estimated by Ellis and Vonder Haar (1976), the albedo in months when the incident flux was less than 17 watts/m^2 (5% of the solar constant divided by four), and the albedo when the entire zone was not illuminated for the entire month. The mean annual albedos listed are simply the means of the monthly albedos and are slightly different from Ellis and Vonder Haar's (1976) annual zonal albedos, which are weighted by the monthly illumination.

Note the negative slopes everywhere but in the tropics, although the only good correlations are found in the Northern Hemisphere midlatitudes and in the polar regions. There are positive slopes in the tropics, although the only non-negligible correlation is at 15°S. The observed albedos in April, May, and June, particularly in the Southern Hemisphere midlatitudes, seemed anomalously high, perhaps due to the previously mentioned bias in observation time towards the afternoon when convective cloudiness would be a maximum (Flanders and Smith, 1975).

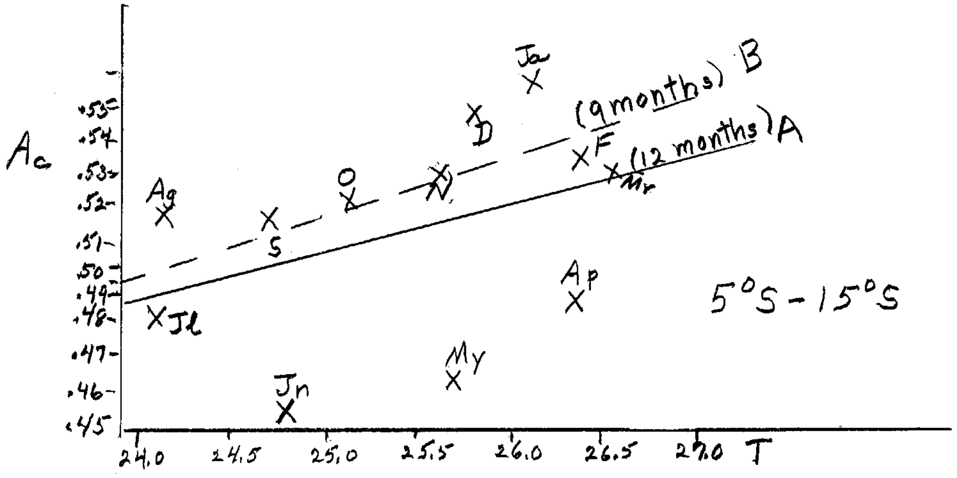

Fig.4. Regional mean monthly cloudiness as a function of regional mean monthly temperature for the region 5°S-15°S. Curve A is the least square fit for 12 months of data (A_c = .185+.01259T, correlation = .08). Curve B is the least square fit excluding April, May, and June. (A_c = .130+.01526T, correlation = .54).

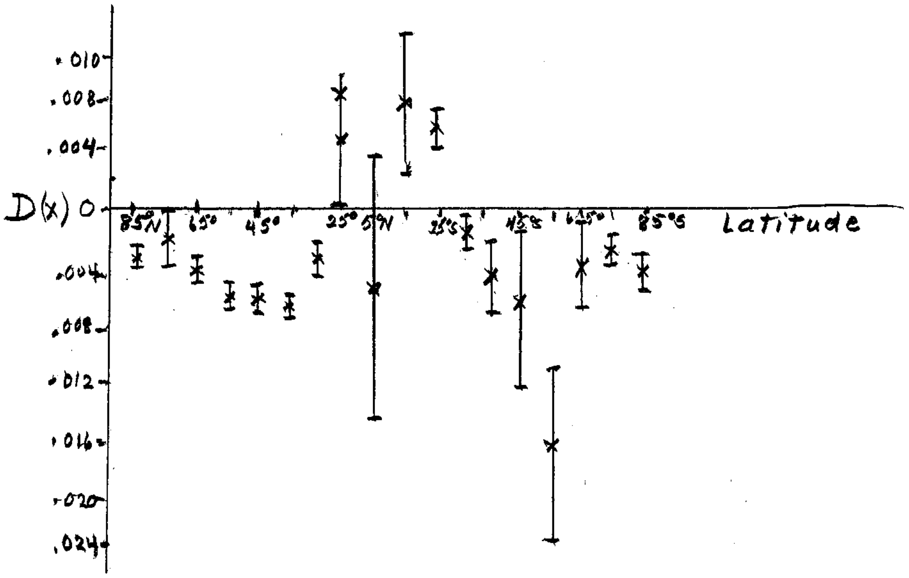

Fig. 5. Slope of the zonal albedo - temperature relation as a function of latitude.

Table 8

Latitude	Mean Annual Albedo	Linear Function (T in $^{\circ}$C) $\alpha(x) = C(x) + D(x)T(x)$	Correlation	Est. Exper. Uncertainty(5%)	Standard Deviation of Fit	Range of Albedo	Range of Temperature
85°N	.592	$.572(\pm.010)-.00274(\pm.00081)T(x)$	.72	.030	.018	.075	26.1 (5 months)
75°N	.544	$.527(\pm.026)-.00212(\pm.00202)T(x)$	.02	.027	.051	.127	27.3 (6 months)
65°N	.462	$.458(\pm.015)-.00428(\pm.00139)T(x)$	.51	.023	.046	.184	33.0 (9 months)
55°N	.432	$.445(\pm.009)-.00593(\pm.00101)T(x)$	.75	.022	.031	.228	25.1
45°N	.371	$.423(\pm.010)-.00622(\pm.00091)T(x)$	.81	.019	.023	.164	21.1
35°N	.317	$.421(\pm.009)-.00653(\pm.00054)T(x)$	.93	.016	.010	.122	15.6
25°N	.274	$.347(\pm.022)-.00316(\pm.00092)T(x)$	.49	.014	.011	.046	9.3
15°N	.248	$.154(\pm.101)+.00361(\pm.00384)T(x)$	-.01	.012	.017	.056	3.7
5°N	.254	$.398(\pm.250)-.00545(\pm.00949)T(x)$	-.06	.013	.011	.034	1.0
5°S	.240	$.079(\pm.115)+.00615(\pm.00438)T(x)$	.08	.012	.009	.028	1.8
15°S	.235	$.106(\pm.034)+.00525(\pm.00140)T(x)$	.54	.012	.006	.026	3.4
25°S	.252	$.283(\pm.025)-.00147(\pm.00117)T(x)$	.05	.013	.010	.036	6.8
35°S	.303	$.379(\pm.045)-.00459(\pm.00270)T(x)$	.15	.015	.022	.073	6.5
45°S	.370	$.443(\pm.051)-.00749(\pm.00579)T(x)$	.09	.019	.031	.087	4.9
55°S	.449	$.500(\pm.021)-.01798(\pm.00638)T(x)$	.39	.022	.036	.143	4.4
65°S	.517	$.501(\pm.015)-.00413(\pm.00287)T(x)$	.13	.026	.029	.106	11.1 (8 months)
75°S	.607	$.535(\pm.023)-.00282(\pm.00087)T(x)$	.65	.030	.015	.072	18.5 (6 months)
85°S	.624	$.487(\pm.029)-.00417(\pm.00088)T(x)$	.84	.031	.014	.085	19.1 (5 months)

Correlations of Zonal Albedo and Zonal Surface Temperature

The standard deviation of the linear fit exceeds the estimated experimental uncertainty at 75°N-45°N, 15°N, and 35°S - 65°S, suggesting that albedo is dependent on another factor than temperature or that the estimated experimental uncertainty is too small. Even if April, May, and June are removed, the standard deviation from 65°N to 45°N and from 45°S to 65°S still exceed the estimated experimental uncertainty.

To obtain Table 9 we weighted each monthly zonal albedo by the mean annual ratio of solar radiation incident at that latitude to the solar constant divided by four, as well as by the cosine of the central latitude. We wished to find albedo as a function of temperature and therefore wanted to exclude changes in albedo which are due to the purely seasonal effect of changing solar zenith angle at a particular latitude. The changing solar zenith angle produces changes in the ratio of illumination of different zones and changes in the albedo and surface which are quite independent of any internal change in the Earth-atmosphere system. To avoid the first, we used the mean annual ratio of locally incident solar radiation to the solar constant divided by four. We also filled in the months of no albedo at polar latitudes with the mean annual zonal albedo from Ellis and Vonder Haar (1976). Figure 6 is the graphical representation of the slopes.

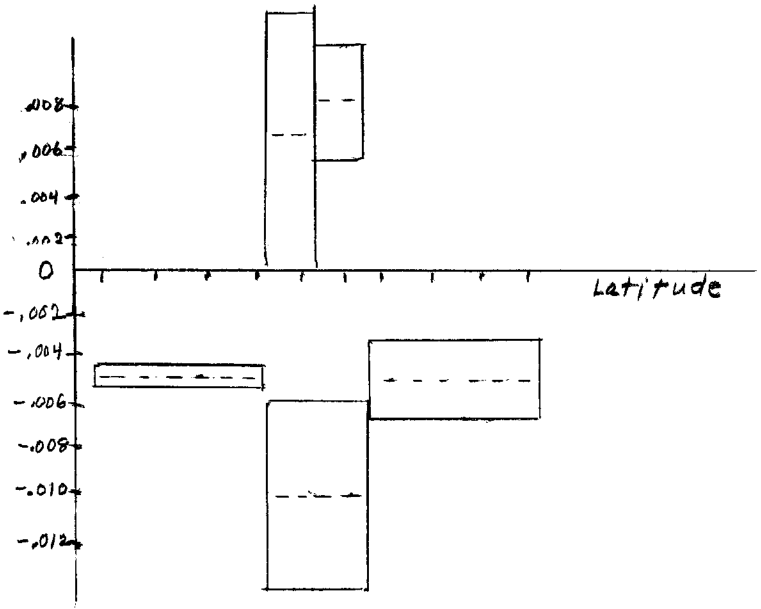

Fig.6. Slope of the regional albedo - temperature relation as a function of latitude.

Good correlations are found only in the Northern Hemisphere outside the tropics. Note that the same regions in opposite hemispheres have roughly the same coefficients, suggesting that the differences between the two hemispheres do not affect the albedo-temperature feedback. Positive slopes are observed in the tropics in each hemisphere separately, but not for the tropics as a whole, suggesting again that there may be clouds shifting back and forth across the equator, creating apparent positive slopes that are purely due to seasonal effects.

The standard deviation of the least squares fit exceeds the estimated experimental uncertainty in the Southern Hemisphere midlatitudes only. If April, May,

Table 9

Region	Mean Annual Albedo	Linear Function (T in ^{o}C) $\alpha = C + DT$	Corre-lation	Est. Exper. Uncertainty	Standard Deviation	Range of Albedo	Range of Temper-ature.
85^{o}N-25^{o}N	.353	.391(±.005)-.00425(±.00042)T	.90	.018	.010	.100	19.9
55^{o}N-25^{o}N	.331	.405(±.009)-.00538(±.00059)T	.88	.017	.012	.106	16.7
15^{o}N-5^{o}N	.251	.113(±.138)+.00524(±.00525)T	-.00	.013	.012	.036	2.2
5^{o}S-15^{o}S	.238	.070(±.058)+.00661(±.00228)T	.40	.012	.007	.025	2.5
25^{o}S-55^{o}S	.322	.402(±.039)-.00579(±.00277)T	.23	.016	.020	.069	5.4
25^{o}S-85^{o}S	.352	.383(±.012)-.00440(±.00159)T	.38	.018	.016	.065	8.1
15^{o}N-15^{o}S	.245	.479(±.096)-.00907(±.00371)T	.31	.012	.005	.020(8.2%)	1.3
NH	.311	.356(±.007)-.00299(±.00045)T	.80	.016	.008	.046	13.7
SH	.305	.332(±.016)-.00201(±.00119)T	.14	.015	.009	.030(9.8%)	6.0
Globe	.308	.354(±.020)-.00327(±.00142)T	.28	.015	.007	.024(7.8%)	3.8

Correlations of Regional Albedo and Regional Surface Temperature

Table 10

Region	Mean Annual Albedo	Linear Function = J + KA_c (A_c - % cloudiness)	Corre-lation	Exper. Uncertainty	Standard Deviation	Range of Albedo	Range of Cloudiness
15^{o}N-5^{o}N	.251	.115(±.030)+.280(±.061)A_c	.65	.013	.007	.036	9.9%
5^{o}S-15^{o}S	.258	.118(±.032)+.238(±.063)A_c	.55	.012	.006	.025	8.7%
15^{o}N-15^{o}S	.245	.150(±.042)+.191(±.085)A_c	.27	.012	.005	.020(8.2%)	5.8%

Regional Albedo as a Function of Regional Cloudiness and June are removed, however, this standard deviation becomes less than the estimated experimental uncertainty. Removing April, May, and June reduces the standard deviation an average of 25% for all regions except 15°N - 15°S.

Table 10 shows the result of attempting a correlation of regional albedo and regional cloudiness in the tropics. A correlation with positive slope is found everywhere and is especially good at 15°N-5°N. Apparently, albedo can be better related to cloudiness than to temperature, since the correlations here at 15°N-5°N and 5°S-15°S are better than Table 8.

Table 11 shows the results of trying to correlate albedo with both temperature and cloudiness. Note that there is no improvement in correlation over Table 10 for 15°N-5°N, suggesting that albedo is related to cloudiness but not temperature there.

The above suggests that Sellers (1969) and Faegre (1972) overestimated the negative slope of the albedo-temperature relation in mid-latitude and polar regions and that albedo may increase with temperature in the tropics. This would act to offset the effect of ice and snow in polar and mid-latitudes and to stabilize the Earth's response to a global cooling or warming. Albedo in the tropics appears to be better related to cloudiness than to temperature.

V. Solar Zenith Angle Effect on Albedo.

The albedo of a surface depends on the angle with which the incident radiation strikes the surface. As the solar zenith angle increases, so does the albedo. Thus, even if exactly the same conditions prevailed at a certain latitude throughout the year, the albedo would still change due to the changing solar zenith angle. Since surface temperature generally increases when the solar zenith angle decreases, this can create an apparent correlation of albedo with surface temperature that bears no relation to what would happen if the surface temperature were to change over a period of years. We therefore sought to change all mean monthly zonal albedos to what they would have been if the sun had been at its mean annual solar zenith angle that month.

To do the above we followed the procedure used by Raschke *et al.* (1973b) to convert the Nimbus 3 observed albedos to what they would have been if the sun had been at its mean daily solar zenith angle. They considered three surfaces: ocean, cloud-land, and snow. In the tropics we used Sadler's (1969) monthly cloudiness and assumed that the cloudiness was the same over ocean and over land. We also assumed that the albedo of cloud-free ocean at the top of the atmosphere would be 0.10 if the sun were directly overhead.

Outside the tropics we used the mean annual cloudiness given by Cess (1976) and assumed it was constant during the year. We assumed the ocean was ice-covered year around at 85° and 75° in both hemispheres and ice-free at 65°N. At 65°S we let the ice vary with the month (Deacon, 1971). At polar latitudes we used Cess' (1976) estimate of cloud albedo which is based on the assumption that surface albedo is less than cloud albedo even in the polar regions.

Thus we divided the albedo in non-polar regions into a cloud-free ocean albedo and a cloud-land albedo and multiplied each by a correction factor taken from Fig.5, p.11, Raschke *et al.* (1973b). In the polar regions, as mentioned before, ice albedo was included as well. The estimate of ice albedo resulting from our calculations was not always reasonable, varying at 65°S from .284 in September to .839 in March.

Table 11

Region	Mean Ann. Albedo	$\alpha = W + XT + YA_c$	Correlation	Est. Error	Stand. Dev.	Range in Albedo	Range in T	Range in Cloudiness
15°N-5°N	.251	$.169-.00152T+.293A_c$	.61	.013	.008	.036	2.2	9.9%
5°S-15°S	.238	$.036+.00429T+.184A_c$	.70	.012	.005	.025	2.5	8.7%
15°N-15°S	.245	$.397-.00694T+.055A_c$	.25	.012	.005	.020(8.2%)	1.3	5.8

Regional Albedo as a Function of Regional Temperature and Regional Cloudiness

Table 12

Latitude	Mean Ann. Albedo	$\alpha(x) = C(x)+D(x)T(x)$	Correlation	Exp. Error	Stand. Dev.	Range of Alb.	Range of Temperature
85°N	.624	.619(±.022)-.00066(±.00180)T(x)	-.28	.031	.040	.084	26.1 (5 months)
75°N	.559	.554(±.032)-.00060(±.00246)T(x)	-.23	.028	.062	.135	27.3 (6 ,pmtjs)
65°N	.475	.473(±.020)-.00242(±.00176)T(x)	.10	.024	.058	.193	35.0 (9 months)
55°N	.435	.440(±.011)-.00227(±.00124)T(x)	.17	.022	.039	.170	25.1
45°N	.366	.385(±.014)-.00237(±.00126)T(x)	.19	.018	.032	.111	21.1
35°N	.311	.353(±.018)-.00260(±.00105)T(x)	.32	.016	.020	.072	15.6
25°N	.269	.252(±.022)+.00074(±.00093)T(x)	-.03	.013	.011	.037	9.3
15°N	.247	-.023(±.095)+.01028(±.00360)T(x)	.39	.012	.016	.068	3.7
5°N	.254	.220(±.289)+.00126(±.01096)T(x)	-.10	.013	.012	.033	1.0
5°S	.239	.012(±.157)+.00866(±.00598)T(x)	.09	.012	.012	.035	1.8
15°S	.234	-.030(±.069)+.01074(±.00281)T(x)	.55	.012	.011	.050	3.4
25°S	.249	.172(±.026)+.00357(±.00121)T(x)	.41	.012	.010	.046	6.8
35°S	.297	.243(±.026)+.00325(±.00158)T(x)	.23	.015	.013	.051	6.5
45°S	.364	.298(±.021)+.00679(±.00215)T(x)	.45	.018	.013	.053	4.9
55°S	.452	.448(±.013)+.00142(±.00395)T(x)	-.09	.023	.022	.077	4.5
65°S	.537	.539(±.017)+.00045(±.00322)T(x)	-.16	.027	.033	.092	11.1 (8 months)
75°S	.623	.594(±.040)-.00115(±.00150)T(x)	-.09	.031	.025	.065	18.5 (6 months)
85°S	.646	.604(±.033)-.00128(±.00098)T(x)	.15	.032	.015	.038(5.9%)	19.1 (5 months)

Correlation of Zonal Albedo with Zonal Temperature with Solar Zenith Angle Dependence Removed.

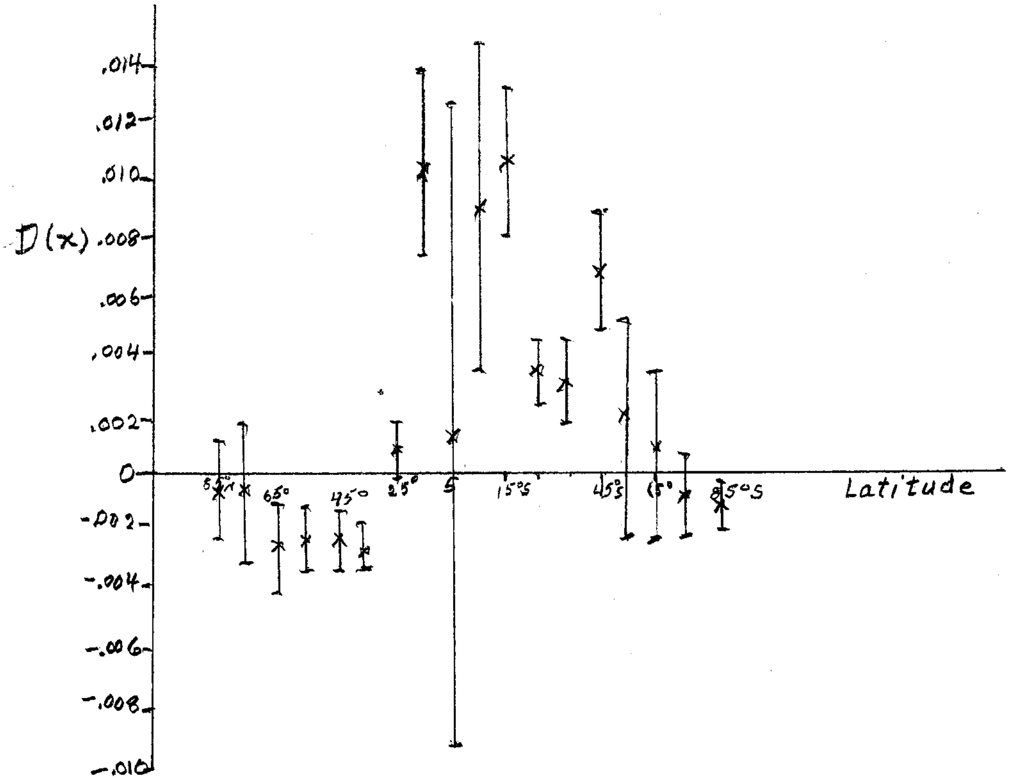

Fig.7. Slopes of the zonal albedo-temperature relation plotted against latitude when albedo has been corrected for solar zenith angle.

Table 12 shows the resulting correlations of zonal albedo and zonal temperature. Figure 7 is the graphical representation of the slopes. Removing the solar zenith angle variation has decreased the correlation with temperature drastically in the Northern Hemisphere while increasing it in the Southern Hemisphere from 5°S to 45°S. The sign of the slope has changed in the Southern Hemisphere midlatitudes, where albedo now increases with temperature. The difference now apparent between the Northern Hemisphere and Southern Hemisphere midlatitudes may be due to the differing ratios of land and ocean. Note that the standard deviation now exceeds the estimated experimental error from 85°N to 35°N, at 15°N, and at 65°S.

Table 13 shows the correlations of regional albedo with regional temperature when we correct for solar zenith angle dependence. Figure 8 is the graphical representation. Correlations are rather poor everywhere. The asymmetry of the hemisphere shows up now in the mid- and polar latitudes where the sign of the slope is not different in the different hemispheres. Note that the standard deviation of the linear fit exceeds the estimated error in the Northern Hemisphere outside the tropics. This may suggest that temperature alone may not explain the albedo variation, that perhaps the albedo may lag the temperature by a few months. Figure 9 shows the regional albedo as a function of regional temperature for the region from 85°N to 25°N. Note that the albedo is higher in May than any other month, which does not seem realistic for these latitudes. Omitting April, May, and June improves the least-squares fit greatly. There is a strong suggestion in the figure that the albedo does lag the surface temperature by about two months, which might be expected if ice and snow cover were an important part of the albedo variation.

Table 13

Region	Mean Ann. Albedo	$\alpha = C + DT$	Corre- lation	Est. Error	Standard Deviation	Range of Albedo	Range of Temperature
85°N-25°N	.352	.365(±.009)-.00140(±.00080)T	.16	.018	.020	.057	19.9
55°N-25°N	.327	.350(±.014)-.00169(±.00092)T	.18	.016	.019	.058	16.7
15°N-5°N	.250	-.127(±.133)+.01434(±.00506)T	.39	.013	.012	.050	2.2
5°S-15°S	.237	-.045(±.099)+.01101(±.00388)T	.39	.012	.011	.042	2.5
25°S-55°S	.318	.266(±.019)+.00382(±.00139)T	.37	.016	.010	.041	5.7
25°S-85°S	.352	.335(±.008)+.00247(±.00100)T	.32	.018	.010	.038	8.1
15°N-15°S	.244	.389(±.103)-.00560(±.00398)T	.08	.012	.005	.014 (5.7%)	1.3
NH	.310	.311(±.010)-.00007(±.00066)T	-.10	.016	.011	.035	13.6
SH	.305	.250(±.015)+.00409(±.00100)T	.54	.015	.008	.039	6.0
Globe	.307	.355(±.014)-.00334(±.00100)T	.48	.015	.005	.018 (5.9%)	3.9

Correlation of Regional Albedo with Regional Temperature with Solar Zenith Angle Removed.

Table 14

Region	Mean Ann. Albedo	Linear Function $\alpha = J + K A_c$	Corre- lation	Exp. Error	Standard Deviation	Range of Albedo (Annual)	Annual Range of A_c
15°N-5°N	.250	.074(±.032)+.363(±.067)A_c	.72	.013	.008	.050	9.9%
5°S-15°S	.237	.008(±.043)+.454(±.085)A_c	.72	.012	.008	.042	8.7%
15°N-15°S	.244	.153(±.038)+.183(±.078)A_c	.29	.012	.005	.014 (5.7%)	5.8%

Correlation of Regional Albedo with Regional Cloudiness with Solar Zenith Angle Dependence Removed.

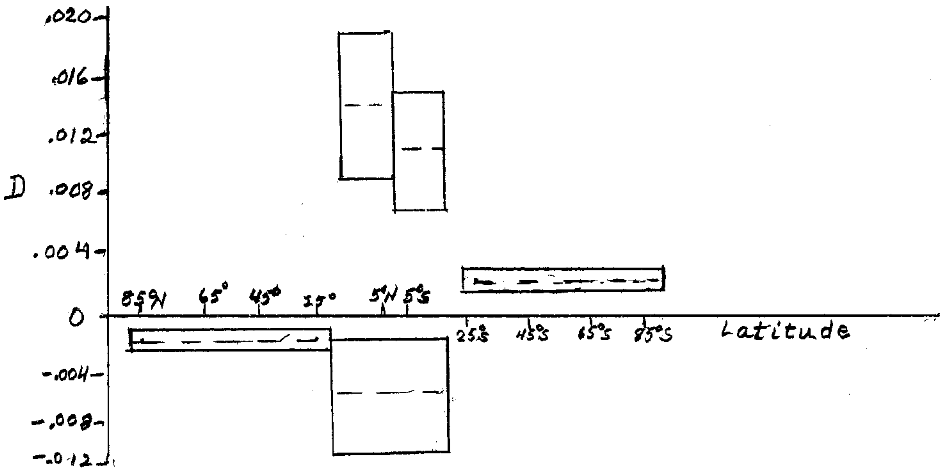

Fig.8. Slopes of the regional albedo-temperature relation plotted against latitude when albedo has been corrected for solar zenith angle.

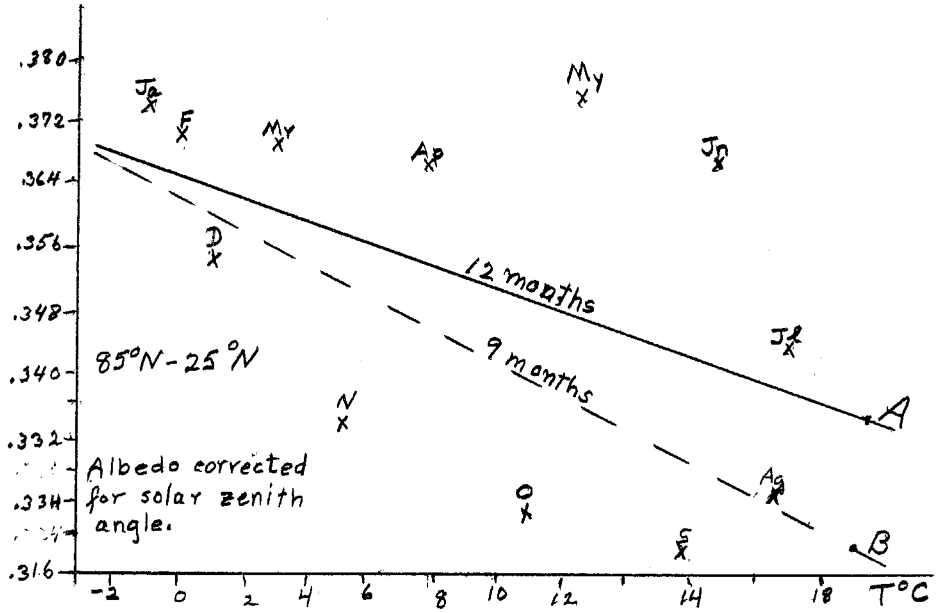

Fig.9. Regional albedo corrected for solar zenith angle as a function of regional surface temperature for the region 85°N-25°N. Curve A is the least-square fit of all twelve months. (α = .365-.00140T, correlation = .16). Curve B is the least-square fit when April, May, and June are omitted. (α = .363-00206T, correlation = .54).

Table 13 and Fig.8 also show that the albedo-temperature relation is the same to within the standard deviation for both 15°N-5°N and 5°S-15°S. The global correlation illustrates one potential fallacy of our original least-square fits. Globally, we have a good correlation with a negative slope that exceeds any negative slope in Table 12. This is due to the globe following the Northern Hemisphere temperature pattern while the largest albedo change is found in the Southern Hemisphere, thus producing a false correlation. The globe encompasses two regions where in the same season temperatures are changing in opposite directions. The same type of false correlation may have occurred when we considered 15°N-15°S.

Removing April, May, and June improves the correlation in the Northern Hemisphere and in the tropics.

Table 14 shows the new correlation of regional albedo with regional cloudiness in the tropics. The correlations here at 15°N-5°N and 5°S-15°S are nearly twice those in Table 12, suggesting again that albedo is more related to cloudiness than to temperature. The slopes here may be too large since Cess (1976) gives the albedo of the surface as .150 at 5°N and .142 at 15°N and the albedo of clouds as .354 at 50°N and .383 at 15°N. Cess's numbers suggest a slope of .2 to .25.

Table 15 shows the correlation of regional albedo corrected for solar zenith angle with regional cloudiness and regional temperature. The correlations are only slightly better than in Table 14, suggesting that cloudiness is more important than temperature in determining albedo.

Our attempt to remove the variation of albedo due to solar zenith angle variation has created a vastly different picture, one in which albedo increasing with temperature, probably due to increasing cloudiness, seems to be dominant. The negative slope in the Northern Hemisphere mid-latitudes has been reduced by a factor of three, while albedo now appears to increase with temperature in the Southern Hemisphere mid-latitudes. The albedo-temperature response now appears quite asymmetric about the equator, probably due to the different land-sea ratios in the two hemispheres. Albedo now definitely appears to increase with temperature in the Northern Hemisphere tropics, but albedo in the tropics appears to be more related to cloudiness than to temperature.

VI. Effect of Cloudiness on the Radiation Balance.

Schneider (1972) stated that an increase in the amount of global cloud cover can have two opposite effects on the global radiation balance: i) an increase in planetary albedo leading to less solar absorption, and ii) a decrease in the infrared radiative loss to space.

It can be expressed in the form:

$$\delta = \left(\frac{\partial Q_{Abs}}{\partial A_c}\right) - \left(\frac{\partial F}{\partial A_c}\right)$$

$$= -\left(Q\,(x)\,\frac{\partial \alpha}{\partial A_c} + \frac{\partial F}{\partial A_c}\right)$$

where δ_l is the net flux difference, A_C is the cloudiness, $Q_{Abs.}$ is the absorbed solar radiation, and Q(x) is the locally incident solar radiation. We have calculated correlations of zonal albedo with zonal cloudiness and zonal infrared flux with zonal cloudiness and can use these to calculate the net flux difference in the tropics. Table 16 shows the result, for the original albedo and for the albedo corrected for solar zenith angle dependence. The numbers in parentheses reflect the uncertainty in the net flux difference from the uncertainty in the slopes of the zonal infrared-cloudiness and albedo-cloudiness linear least-square fits. Our results are not accurate enough to determine even the sign of the effect in some latitudes, but in the southern tropics the dominant effect of increasing cloudiness appears to be a decrease in the infrared radiative loss to space. This is the opposite of Schneider's (1972) result, where he assumed a fixed cloud height. Our empirical infrared flux-cloudiness relation does not hold could height fixed.

Table 15

Region	Mean Annual Albedo	$\alpha = W + XT + YA_c$	Corre-lation	Est. Error	Standard Deviation	Range in Albedo	Range in T	Range in Cloudiness
15°N-5°N	.250	$-.091+.00751T+.297A_c$	.81	.013	.007	.050	2.2	9.9%
5°S-15°S	.237	$-.114+.00642T+.372A_c$	.84	.012	.006	.041	2.5	8.7%
15°N-15°S	.244	$-.090+.00684T+.316A_c$	.28	.012	.005	.014 (5.7%)	1.3	5.8%

Correlation of Regional Albedo with Regional Cloudiness and Regional Temperature with Solar Angle Variation Removed.

Table 16

Latitude	δ (in watts/m^2)
original data	
25°N	184.8(±357.0)
15°N	75.7(±72.9)
5°N	88.4(±74.0)
5°S	221.2(±95.0)
15°S	263.4(±80.7)
25°S	15.3(±212.0)
Albedo corrected for solar zenith angle	
25°N	446.8(±344.8)
15°N	43.5(±74.5)
5°N	59.0(±74.9)
5°S	154.8(±96.3)
15°S	164.4(±96.1)
25°S	53.8(±242.8)

Table 16. Effect of Cloudiness on the Radiation Balance of the Tropics (δ is the change in Net Downward Radiative Flux per Unit Increase in Cloudiness).

VII. Conclusion

We have implicitly assumed that albedo and infrared flux respond immediately to any change in 1000 mb temperature and that therefore each month is statistically independent of the other months. However, in reality lags between temperature and albedo and infrared flux do occur, as at 85°S in the infrared flux. There is also a lag between the minimum temperature and the maximum ice extent. In the Northern Hemisphere the maximum ice extent occurs in April (Kukla and Kukla, 1974) and in the Southern Hemisphere in September (Deacon, 1971).

One must also consider the possibility that albedo, infrared flux, and especially cloudiness, respond quite differently to a gradual cooling or warming of the Earth over several years than they do to seasonal temperature changes, and that therefore the results here might not be applicable to the parameterization of energy - balance climate models. Cloudiness has been shown here to have a great influence on the tropical radiation balance and has not been shown to be correlated to any great extent with surface temperature. The seasonal cycle of cloudiness could be quite different from the response of cloudiness to a gradual cooling or warming of the Earth over several years or to a change in solar constant.

But this work has shown that the observed response of infrared flux and albedo to seasonal changes in surface temperatures do not verify the parameterizations used by Budyko (1969), Sellers (1969), Faegre (1972), and North (1975). The response of infrared flux and albedo to a uniform change in surface temperature appears to vary from region to region over the globe and may even change sign in the tropics. Cloudiness appears to be the important variable in the tropics' seasonal radiation budget and has not been shown to be simply related to surface temperature. This suggests that variable cloudiness must be included in an energy-balance climate model and that parameterizing cloudiness as a linear function of temperature would not be adequate.

Our crude correction for the variation of albedo with solar zenith angle has shown that this correction can considerably alter the estimates of albedo-temperature feedback. Our results also seem to indicate that the Earth can not be treated as symmetric about the equator, that even the sign of the albedo-temperature feedback in the mid-latitudes is different in the two hemispheres.

Our results also show that cloudiness changes, at least on a seasonal basis, may be more important than changes in ice and snow cover and that in the tropics and Southern Hemisphere mid-latitudes albedo increases with temperature, therefore acting to stabilize the climatic response to changes in temperature or solar constant.

Acknowledgments

The author wishes to thank Drs. Chylek, Coakley, Ingersoll, North, Rooth, and Vonder Haar for helpful comments and discussions during various phases of this work.

References

Budyko, M.I. 1969 The Effect of Solar Radiation Variations on the Climate of the Earth. Tellus 21: 611-619.

Cess, R.C. 1976 Climatic Change: An Appraisal of Atmospheric Feedback Mechanisms Employing Zonal Climatology. (Submitted for publication.)

Deacon, George, ed. 1971 Symposium on Antarctic Ice and Water Masses. Scientific Committee on Antarctic Research. W.Heffer & Sons,Ltd.,Cambridge,England. 133 pp.

Ellis, J. and T.H.Vonder Haar 1976 Zonal Average Earth Radiation Budget Measurements from Satellites for Climate Studies. Atmospheric Science paper No. 240, Dept.Atm.Sci., Colorado State Univ.,Fort Collins, Colorado.

Faegre, A. 1972 An Intransitive Model of the Earth-Atmosphere-Ocean System. J.Appl.Meteor., 11: 4-6.

Flanders, D.H. and W.L.Smith 1975 Radiation Budget Data from the Meteorological Satellites, ITOS 1 and NOAA 1. NOAA Technical Memorandum NESS 72, Nat'l. Tech.Information Service, Dept.Commerce, Springfield, Va.

Galchen, T. and S.Schneider 1976 Energy Balance Climate Modeling: Comparison of Radiative and Dynamic Feedback Mechanisms. Tellus 28: 108-121.

Kukla, G.J. and H.J.Kukla 1974 Increased Surface Albedo in the Northern Hemisphere. Science 183: 709-714.

North, G.R. 1975 Theory of Energy-Balance Climate Modesl. J.Atmos.Sci. 32:2033-2043.

Raschke, E., T.H.Vonder Haar, W.R.Bandeen and M.Pasternak 1973 The Annual Radiation Balance of the Earth Atmosphere System during 1969-1970 from Nimbus 3 Measurements. J.Atmos.Sci., 30: 342-364.

Raschke, E., T.H.Vonder Haar, M.Pasternak and W.R.Bandeen 1973 The Radiation Balance of the Earth-Atmosphere System from Nimbus 3 Radiation Measurements. NASA Tech.Note NASA TN D-7249 Nat'l.Tech.Inform.Serv., Springfield, Va.

Sadler, J.S. 1969 Average Cloudiness in the Tropics from Satellite Observations. East-West Center Press, Honolulu, Hawaii. 22 pp.

Schneider, S.H. 1972 Cloudiness as a Global Climatic Feedback Mechanism: The Effects on the Radiation Balance and Surface Temperature of Variations in Cloudiness. J.Atmos.Sci., 29: 1413-1422.

Schneider, S.H. and T.Gal-Chen 1973 Numerical Experiments in Climate Stability. J.Geophys.Res. 78: 6182-6194.

Sellers, W.D. 1969 A Climate Model Based on the Energy Balance of the Earth-Atmosphere System. J.Appl.Meteor. 8: 392-400.

van Loon, H. 1975 Monthly Mean Surface Temperatures. Unpublished.

CLOUDS AND CLIMATE

Bruce A. Wielicki

To date the most productive approaches to long-term climate have utilized some form of a global energy balance equation. On time scales much greater than the response time of the ocean heat reservoir (≈1000 yrs by most estimates) such a global energy balance would seem inescapable. Estimates of glacial climate oscillations over the last one million years indicate climate regime time scales of 10,000 to 100,000 yrs, comfortably above this limit. A single equation admits solution of only a single variable, so atmospheric transport, infrared flux, and any feedbacks are parameterized as functions of surface temperature. The major

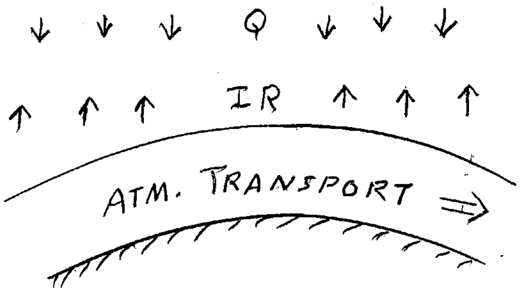

A generalized global energy balance equation might be written

$$\underline{\text{div (Atm Transport)} + \text{IR} = Q}$$

climate variables which can affect such a parameterization are listed below:

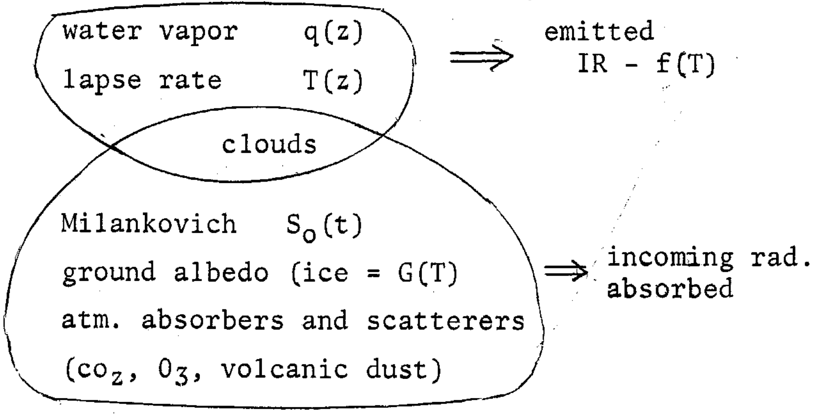

water vapor $q(z)$
lapse rate $T(z)$
$\Longrightarrow$ emitted IR - f(T)

clouds

Milankovich $S_0(t)$
ground albedo (ice = G(T)
atm. absorbers and scatterers
(co_2, O_3, volcanic dust)
$\Longrightarrow$ incoming rad. absorbed

The effects of Milankovich variations in solar constant, ice-albedo feedback, and specified variations of radiatively important atmospheric constituents for incoming solar radiation, have received the lion's share of attention to date: models have been developed by Budyko (1969), Sellers (1969, 1973) and most recently North (1975). Estimates of climate sensitivity ($S_0 \frac{dT}{dS_0}$) are increased three-fold by ice feedback but are still a factor of four or more below the sensitivity necessary to account for glacial oscillations by means of Milankovich forcing alone. Latest studies of paleontological data however are indicating significant response at these astronomical periods, maintaining interest in this mechanism.

Of the remaining terms clouds seem the most likely candidate for strong climate feedback. The moisture-condensation process is extremely sensitive due to its step-function-like nature, and clouds interact with both outgoing infrared (greenhouse effect) and incoming solar (albedo change) radiation. These two processes most often work in opposition, (whenever cloud albedo exceeds ground albedo, typically .5 : .1 for land or sea) but there exists no obvious physical mechanism to couple them in balance. As clouds presently cover ≈ 50% of the globe, and account for a large portion of the planetary albedo, it is not difficult to imagine large effects of mean cloudiness on the Earth's climate. The actual specification of such interactions however is extremely difficult, as a brief review of recent research on this problem will quickly show.

To study the effect of cloud cover fraction (A_c) as a feedback mechanism, both

$$\frac{\partial A_c}{\partial \text{ climate}} \quad \text{and} \quad \frac{\partial \text{ radiation}}{\partial A_c}$$

must be established. (Since temperature is in a very real sense the "measure" of climate in energy balance models, the first of these may then be rewritten as $\frac{\partial A_c}{\partial T}$.) At present even the sign of the above terms is in doubt.

S.H.Schneider (1972), utilizing the approach of Manabe and Weatherald (1967), treated clouds as balck body radiators at height Z_c with temperature $T(Z_c)$. For observed $T(z)$ and $q(z)$, he found that the albedo effect dominated the infrared change due to cloudiness if cloud height is held fixed. For typical cloud albedos of 0.5, increased cloudiness will therefore effect a net cooling over land and sea but a warming over ice or snow. Further, since temperature decreases with increasing altitude, increasing cloud height will also exert a net cooling. For the present global averages, Schneider found that increasing A_c from .50 to .58 was equivalent to increasing cloud height by 600 meters. This established that $\frac{\partial R_{NET}}{\partial A_c}$ is undetermined (even in sign) as long as cloud height remains either unspecified or unknown. At present cloud height can not be determined from satellite data, but may well be in the not too distant future. General circulation models would seem to lack the vertical resolution to handle cloud height changes, however their changes in A_c might conceivably reflect the net effect of A_c and Z_c in the atmosphere. One final note should be added: should the temperature or moisture lapse rates vary with climate, $\frac{\partial R_{NET}}{\partial A_c}$ will also vary with climate, and a highly nonlinear feedback may result.

Estimates of the change in cloud fraction with climate are in basic disagreement. Paltridge (1974), using a somewhat involved energy balance approach, indicates $\frac{\partial A_c}{\partial T} \approx 3\%/^\circ C$. Runs of an NCAR GCM (unpublished data), specifying ±2°C changes in surface temperature, find $\frac{\partial A_c}{\partial T} \approx -1\%/^\circ C$. Since both of these use essentially fixed height cloudiness, (i.e. $\frac{\partial R_{NET}}{\partial A_c}$ typically < 0) the Paltridge result represents a strong negative feedback to climate change, while the NCAR result reflects a strong positive or destabilizing feedback. Weare and Snell (1972) with a unique although somewhat abstract "diffuse cloud" model find a stabilizing effect even larger than that of Paltridge. Finally, in an attempt to examine seasonal and latitudinal "climate" variations Cess (1976 preprint) uses satellite data to correlate surface temperature, A_c, I.R., and albedo, and finds $\frac{\partial A_c}{\partial T} \sim -1\%/^\circ C$ and $\frac{\partial R_{NET}}{\partial A_c} \approx 0$ i.e. no net effect on climate sensitivity.

There exists little other than personal preference to favor one of these results over another, as all include basic assumptions or conditions which are still in question. However we can reverse the problem, asking if a given feedback is hypothesized, what effect is then implied. Utilizing our greater faith in the simple energy balance equation, and present knowledge of past climate, we can then indicate the reasonableness of any initially hypothesized feedback, while gaining an indication of the magnitude of cloud feedback sensitiviey. The most obvious criterion will require that the present climate be stable to small perturbations from equilibrium.

We will choose North's (1975) formulation of the energy balance equation, as it is mathematically the most general and well-defined of those presented to date. A basic familiarity with his results will be assumed, and his notation will be followed wherever possible. Clearly the uncertainties in specifying cloud-climate feedbacks indicate that only the simplest of formulations be studied, i.e.

$$-D\nabla^2 T + (A+BT) + C'(x,x_s)\cdot\Delta T = QS(x)\cdot\{a(x,x_s) + b'(x,x_s)\cdot\Delta T\}$$

These terms are exactly as in North (1975) except for the addition of $c'(x,x_s)\cdot\Delta T$ and $b'(x,x_s)\cdot\Delta T$, which represent the infrared and albedo effects of clouds respectively. $\Delta T(x) = T(x) - T^{\circ}(x)$ where $T^{o}(x)$ is the present climate solution of the model for ice line $x_s = .95$. In this sense $c(x,x_s)$ is a linearization of $\left(\frac{\partial cloud}{\partial T}\cdot\frac{\partial IR}{\partial cloud}\right)$ about the present climate, with a similar interpretation for $b'(x,x_s)$. The possible strong dependence of such a feedback on x and x_s as indicated by Schneider's (1972) results suggests the latitude dependence of c' and b'. The equation can be further simplified to realizing that the sensitivity parameter $S = Q\frac{dT}{dQ}$ is typically of order 100°C and in the unstable regions of special interest approaches infinity, indicating that

$\frac{\Delta T}{T}\Big/\frac{\Delta Q}{Q} \gg 1$ and the albedo effect of clouds becomes:

$$Q^{\circ}S(x)\,b'(x,x_s)\,\Delta T$$

where $Q^{\circ} = Q(x_s = .95)$. Defining

$$c(x,x_s) = c'(x,x_s) - Q_0 S(x)\,b'(x,x_s),$$

we obtain:

$$-D\cdot\nabla^2 T + (A+BT) + C(x,x_s)\cdot\Delta T = Q\cdot S(x)\cdot a(x,x_s) \tag{1}$$

The parameter C now conveniently denotes the net radiational effect (positive for outgoing flux) due to cloud change with climate. To obtain a physical sense of its magnitude, for fixed cloud height

$$C = \frac{\partial A_c}{\partial T}\cdot\frac{\partial RNET}{\partial A_c},$$

Schneider's mean value for $\frac{\partial RNET}{\partial A_c}$ is approximately + 1 w/m^2 outgoing per 1% increase in A_c, for which C = 1 if $\frac{\partial A_c}{\partial T} = 1\,\%/^{\circ}C$.

Such equations, as shown by North (1975), are especially amenable to solution by Legendre polynomial expansion. Taking advantage of $I(x) = A + B\cdot T(x)$:

$$-D\nabla^2 I + I + \left(\frac{c(x,x_s)}{B}\right)\Delta I = Q\cdot S(x)\cdot a(x,x_s)$$

Expanding in Legendre polynomials:

$$-D\sum_n n(n+1)\cdot I_n\cdot P_n(x) + \sum_n I_n\cdot P_n(x) + \sum F_n(x_s)\cdot P_n(x) = Q\sum_n H_n(x_s)\cdot P_n(x) \tag{2}$$

where $$H_n(x_s) = (2n+1)\cdot\int_0^1 s(x)\,a(x,x_s)\cdot P_n(x)\,dx$$

$$F_n(x_s) = \left(\frac{2n+1}{B}\right)\cdot\int_0^1 \Delta I(x)\cdot c(x,x_s)\cdot P_n(x)\,dx$$

Now since $$\Delta I(x) = I(x) - I^{\circ}(x)$$

$$F_n(x_s) = \left(\frac{2n+1}{B}\right)\cdot\int_0^1 c(x,x_s)\cdot\left[\sum_m (I_m - I_m^{\circ})\cdot P_m(x)\right]\cdot P_n(x)\,dx$$

defining

$$F_{nm}(x_s) = \frac{2n+1}{B}\cdot\int_0^1 c(x,x_s)\,P_m(x)\,P_n(x)\,dx$$

then

$$F_n(x_s) = \sum_m (I_m - I_m^o) \cdot F_{nm}(x_s)$$

Multiplying Eq.(2) by $P_n(x)$ and integrating with liberal use of the orthogonality principle leads to:

$$L_n I_n + \big[\sum_m (I_m - I_m^o) \cdot F_{nm}(X_s) = Q H_n(x_s) \tag{3}$$

$$\Sigma I_n P_n(x)_s = I_s \tag{4}$$

where $L_n = n(n+1)D + 1$, and Eq.(4) sets the ice line condition. These two equations differ from North's only by the term in brackets. This term introduces however, a coupling of the linear algebraid equations in I_n.

For the present climate ($I_m = I_m^o$) the equation reduces to North's, which requires the diffusion coefficient D = .382 remains unchanged. Once χ_s is specified, $H_n(X_s)$ and $F_{nm}(x_s)$ are known, and the remaining Q and I_n are determined. Note however that $\frac{dQ}{dx_s}$, the stability, and the sensitivity $(Q \frac{dT_o}{dQ})$ will depend on $G(x, x_s)$ even for $x_s = .95$.

The stability analysis is quite straightforward (see North 1976). Consider the time-dependent equation:

$$\frac{\partial}{\partial t} I_n(t) + L_n I_n + \Big[\sum_m (I_m - I_m^o) F_{nm}(x_s)\Big] = Q \cdot H_n(x_s) \tag{5}$$

let the perturbations from equilibrium I_n^* and X^* be small:

$$I_n(t) = I_n^* + \delta_n(t)$$

$$x_s(t) = x^* + \varepsilon(t)$$

Linearizing:

$$F_{nm}(x_s) = F_{nm}(x^*) + F'_{nm}(x^*) \cdot \varepsilon$$

$$H_n(x_s) = H_n(x^*) + H'(x^*)\, \varepsilon$$

where primes denote the obvious derivatives. Substituting into Eq.(5) and dropping terms of order $\varepsilon \cdot \delta$ leads to:

$$\frac{\partial}{\partial t}(\delta_n) + L_n \delta_n + \Big[\sum_m \delta_m F_{nm}(x^*) + \sum_m (I_m^* - I_m^o) F'_{nm}(x^*) \cdot \varepsilon\Big] = Q H_n(x^*) \cdot \varepsilon \tag{6}$$

Similarly expanding the ice line condition $\Sigma I_n P_n(x_s) = I_s$ leads to a relation between ε and δ:

$$\varepsilon = -\frac{\Sigma \delta_\ell P_\ell(x^*)}{\Sigma I_\ell^* P'_\ell(x^*)}, \quad P' = \frac{dP}{dx_s}(x^*)$$

Now let $\delta_n(t) = D_n e^{-\lambda t}$. Equation (6) then becomes a set of coupled linear homogeneous equations for the D_n:

$$(L_n - \lambda) \cdot D_n + \Big[\sum_m D_m F_{nm}(x^*) - \sum_m (I_m^* - I_m^o) F'_{nm}(x^*) \cdot \Big(\frac{\Sigma D_\ell P_\ell}{\Sigma I_\ell^* P'_\ell}\Big)\Big] = -Q H'_n(x^*) \cdot \Big(\frac{\Sigma D_\ell P_\ell}{\Sigma I_\ell^* P'_\ell}\Big)$$

for which a non-trivial solution exists only if the coefficient determinant = 0. This condition determines the stability parameters λ_n.

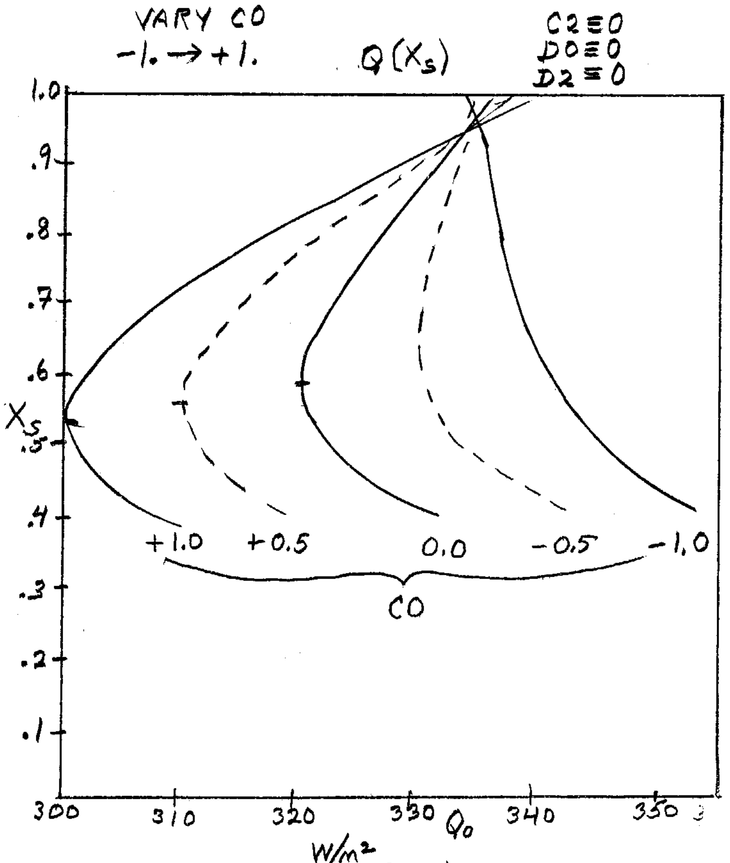

FIG. 1.

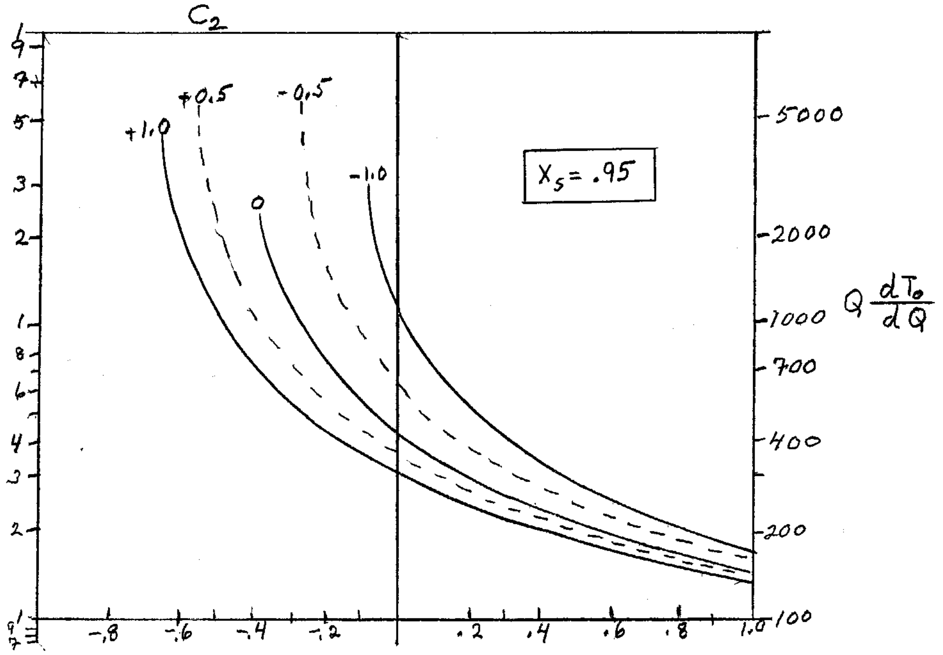

Sensitivity vs. CO for various CZ; (DO ≡ 0)

FIG. 2

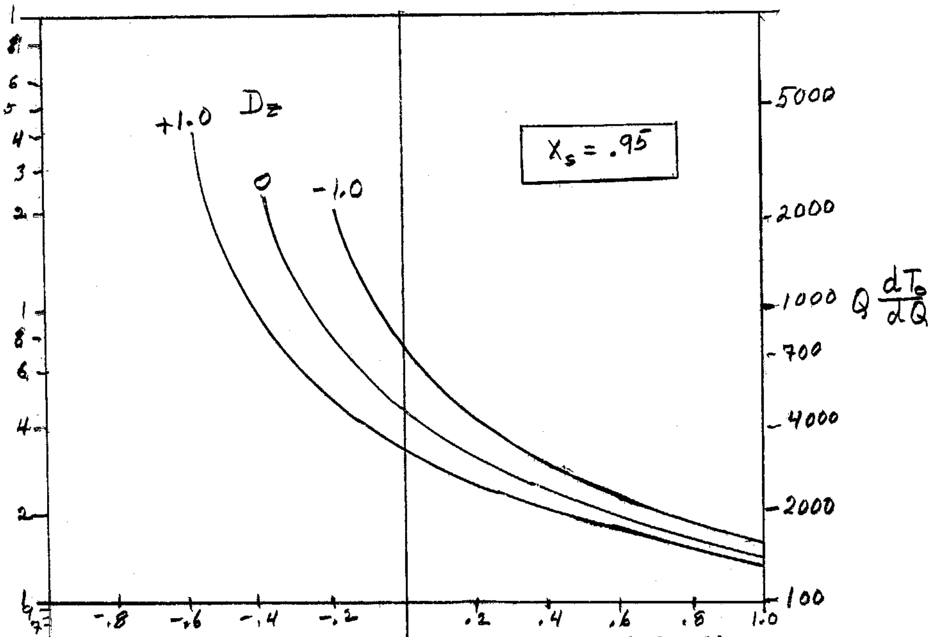

Sensitivity vs. CO for various DO (C2≡0)

F*I*G.3

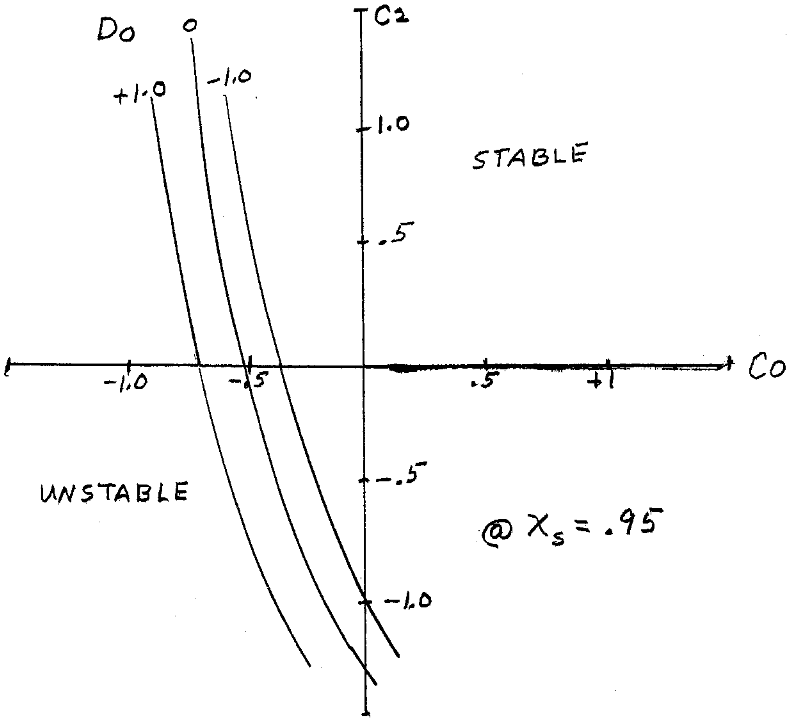

Regions of stability/instability in CO, C2 space for various values of DO.

FIG.4

Solution will be determined for the two-mode case, for which we will let

$$c(x, x_s) = C_0 + C_2 \cdot P_2(x);\ x < x_s$$

$$d_0 + d_2 P_2(x)\ x > x_s .$$

Such a specification greatly aids interpretation of the results; i.e. the variations of stability and sensitivity of the present climate in $c(x, x_s)$ parameter space.

The results are shown in Fig. 1-4 and may be summarized as follows:

1) CO, C2, or DO $>$ 0 indicate a negative feedback, or stabilizing influence of cloudiness on climate. For C) and D) this is obvious, and for C2 it can be shown by noticing that for $[C_0 + C_2 P_2(x)] \cdot [\Delta T_0 + \Delta T_2 P_2(x)$, the integrated effect (0 to X_S) is dominated by the $C_2 \Delta T_2 \int_0^{x_s} P_2(x) \cdot P_2(x) dx$ term for X_S near 1.

C_0, C_2 or $D_0 < 0$ is conversely destabilizing.

2) One can by the same reasoning show that for the present climate a given magnitude of CO will in some sense have roughly five times as much effect on the solution as a similar C_2 or D_0. This is shown in Figs.2 and 3 for climate sensitivity by considering the ratio of ΔC_0 to ΔC_2 between two points of equal sensitivity on two adjacent C_2 curves.

3) Although not rigorously proven, all solutions studied exhibited a similar stability criterion to North's earlier model, i.e.

$$\frac{dQ}{dx_s} > 0 ; \left(Q \frac{dT_0}{dQ} > 0\right) \qquad \text{stable}$$

$$\frac{dQ}{dx_s} < 0 ; \left(Q \frac{dT_0}{dQ} < 0\right) \qquad \text{unstable}$$

4) Figure 1 shows the typical $Q(X_s)$ curves exhibiting the shift of the unstable point due to the stabilizing or destabilizing effect of C_0. Note for $C_0 = -1$ all solutions including the present climate are unstable. Noting that in Figs.2 and 3 the region to the left of the asymptotes of the steeply rising sensitivity curves are unstable, a similar effect is seen for C_2, and D_0.

5) Using Figs.2 and 3, Fig. 4 establishes the range of parameter space for which the current climate is unstable. It does not seem unreasonable to require any realistic feedback to lie outside this region. For fixed height cloudiness this implies

$$\frac{\partial A_c}{\partial T} > -1\%/^\circ C$$

We immediately note that the near ±2°C O.S.T. experiment just violates this constraint. The reason of course is that fixing ocean surface temperatures treats the ocean as an infinite heat source or sink which can control its own global equilibrium - such fluxes violating the assumption of a global energy balance at the top of the atmosphere. Such a model is more useful for climate time scales less than the ocean response time of $\approx$ 1000 yrs. It would seem necessary that any future GCM simulations of glacial time scale climate changes should apply a net energy flux balance at the surface.

(6) As Schneider (1972) indicated, the effect of cloud cover on net radiation fluxes should reverse sense over ice and snow (fixed height) - could this be an important feedback to the ice-line? Due to the C_0 dominance seen earlier such effects will not be evident for the present climate.

(7) Paltridge's (1974) result of +37%/$^{\circ}$C gives a sensitivity of $\approx$ 120, i.e. his cloudiness change more than compensates for the positive ice-albedo feedback.

(8) It is clear that for the present climate, $\chi_s = .95$, we can choose C_0, C_2 or D_0 such that Milandovich sensitivities are obtained. However such regions are very narrow in $C(x, \chi_s)$ parameter space. As it is more than likely that climate feedback due to cloudiness will change at least slightly with changing climate, such a mechanism is too restricted to supply the proper sensitivity over long periods of time. Cloudiness does not seem to be an answer to the Milankovich dilemma.

In conclusion, two "pitches" are clearly appropriate. First, despite its questionable application to long term climate, improved seasonal cloudiness data is called for, with cloud height if possible. Second, GCM responses should be studied, hopefully with some restriction on net ocean heat fluxes.

Acknowledgments

I would like to thank Dr. Gerald North and Dr. Richard Somerville for their guidance, friendship and encouragement.

References

Budyko, M.I. 1969 The Effect of Solar Radiation Variations on the Climate of the Earth. Tellus 21: 611-619.

Manabe, S. and R.T.Wetherald 1967 Thermal Equilibrium of the Atmosphere with a Given Distribution of Relative Humidity. J.A.S. 24: 241-259.

NCAR Data - unpublished, supplied by Drs. R.Chervin and R. Somerville of the National Center for Atmospheric Research, sponsored by the National Science Foundation.

North, Gerald R. 1975 Theory of Energy Balance Climate Models. J.A.S. 32:2033-2043.

North, Gerald R. 1976 Stability Theorem for Energy Balance Climate Models. Submitted for publication.

Paltridge, G.W. 1974 Global Cloud Cover and Earth Surface Temperature. J.A.S. 31: 1571-1576.

Schneider, S.H. 1972 Cloudiness as a Global Climatic Feedback Mechanism: The Effects on the Radiation Balance and Surface Temperature of Variations in Cloudiness. J.A.S. 29: 1413-1422.

Sellers, W.D. 1969 A Global Climatic Model Based on the Energy Balance of the Earth-Atmosphere System. J.A.M. 8: 392-400.

Sellers, W.D. 1973 A New Global Climatic Model. J.A.M. 12: 241-254.

Cess, R.D. 1976 Climate Change: An appraisal of Atmospheric Feedback Mechanisms Employing Zonal Climatology. Submitted for publication.

Weare, B. and F.M.Snell 1974 A Diffuse Thin Cloud Atmospheric Structure as a Feedback Mechanism in Global Climate Modeling. J.A.S. 31: 1725-1734.

A PRELIMINARY STUDY OF FLOWS GENERATED BY A CYLINDER MOVING ON A BETA-PLANE

Toshio Yamagata

1. Introduction

A study of a flow, generated by an obstacle moving steadily through a fluid at rest, is one of the most basic and classical problems in fluid dynamics because it focuses on nonlinear inertial force. However, we do not yet have a complete theory to cover whole range of Reynolds numbers. Therefore, laboratory experiments are an important aid for our understanding of flow behavior, especially in high Reynolds number flow.

The problem has also been extended to stratified fluid, where new aspects of the original problem have been obtained concerning forward wakes, lee waves and recent topics about waves and turbulence.

We shall be concerned here with a rotating fluid on the beta-plane. More than 20 years ago, the problem was investigated in a limited parameter range (moderate local Rossby number) by Fultz and Long (1951), Long (1952), and Fultz and Frenzen (1955), using a hemispherical annulus. They showed some interesting flow behaviors such as Rossby lee waves in a prograde flow (westerly flow), blocking in a retrograde flow (easterly flow), eddy formation near edges of blocking, etc. Their motivation was to examine the effects of large scale mountain barriers such as Himalayas or the effect of blocking high on the zonal current in the atmosphere.

Apparently, the problem has an intimate relation to the Taylor column problem on a beta-plane. The latter problem was investigated by Ingersoll (1969) in connection with Jupitor's Great Red Spot (inviscid, zero local Rossby number) and by McCartney (1975) in connection with oceanic and atmospheric flows over a barrier (inviscid, moderate local Rossby number). McCartney also performed a laboratory experiment using a paraboloidal free surface to simulate beta-effect and confirmed the existence of lee waves for the case of a prograde flow. For the case of a retrograde flow around a tall obstacle, McCartney found blocking with vortices at the edges.

Here, as a preliminary study for a future extensive work covering wide ranges of Rossby number, Ekman number and planetary vorticity factor, I show some drag calculations in § 2. Because of the complexity of the flow regime, and its variation over the parametric regime, the drag may provide a useful means of organizing and discussing the results. In the next § 3, a brief description of the laboratory experiment performed will be given, paying special attention to a forward influence in a prograde flow and a wake in a retrograde flow. Some theoretical calculation for a forward influence will be shown in the Appendix.

2. Drag calculations

2.1 Basic equation

The nondimensional vorticity equation for the stream function ψ on a beta-plane may be written as

$$\nabla^2\psi_t + \epsilon J(\psi, \nabla^2\psi) + B\psi_x - E\delta^{-2}\nabla^4\psi + E^{1/2}\nabla^2\psi = 0 \qquad (2.1.1)$$

All variables in (2.1.1) are nondimensionalized using a diameter L of a cylinder as a horizontal length scale, velocity U of a moving cylinder as a velocity scale and $(2\Omega)^{-1}$ as a time scale. The first term of (2.1.1) means the local time change of vorticity, second term means the advection of vorticity, third term means the beta-effect, fourth term means the lateral diffusion of vorticity and the last term means the Ekman dissipation of vorticity. Nondimensional numbers are defined as follows:

$\epsilon = U/2\Omega L$: Rossby number
$B = \beta L/2\Omega$: planetary vorticity factor
$E = \nu/2\Omega H^2$: Ekman number
$\delta = H/L$: aspect ratio
(2.1.2)

The lateral diffusion of vorticity is small in our experiment and, therefore, neglected throughout the analysis.

2.2 Steady flow on the f-plane

In this case, B = 0 and the vorticity equation is reduced to

$$\epsilon J(\psi, \nabla^2\psi) + E^{1/2}\nabla^2\psi = 0 \qquad (2.2.1)$$

The boundary condition at the cylinder moving in the x-direction (east-west) is written as

$$\left.\begin{aligned} \psi &= \sin\theta \quad \text{at } r = \tfrac{1}{2} \\ \psi &= 0 \quad\quad\;\; \text{at } r \to \infty \end{aligned}\right\}, \qquad (2.2.2)$$

where no circulation around the cylinder is assumed. This system has the irrotational solution:

$$\psi = \frac{\sin\theta}{2r} \qquad (2.2.3)$$

The simplest way to calculate the drag is by means of the conservation of energy. This states that the rate of work done by the external force D_E^* must equal the dissipation rate in the Ekman layer (note lateral friction has been neglected) and, thus, we have

$$D_E^* U = \frac{\rho\nu}{\sqrt{\nu/2\Omega}} \iint |\nabla^*\psi^*|^2 \cdot dS^* \qquad (2.2.4a)$$

$$= -\frac{\rho\nu}{\sqrt{\nu/2\Omega}} U^2 \cdot L^2 \int_{-\pi}^{\pi} \psi \cdot \psi_r \cdot r \Big/_{r=\frac{1}{2}} d\theta, \qquad (2.2.4b)$$

where * denotes dimensional quantities. Using (2.2.3), D_E^* becomes

$$D_E^* = \pi\, 2^{-3/2} \cdot \rho \cdot \Omega^{1/2} \cdot \nu^{1/2} \cdot U \cdot L^2 \,. \qquad (2.2.5)$$

2.3 Steady flow on the beta-plane when $\mathcal{E}$ is small.

The vorticity equation is reduced to

$$B\Psi_x + E^{1/2}\nabla^2\Psi = 0 \qquad (2.3.1)$$

The solution with the boundary condition (2.2.2) is written as

$$\Psi = \rho^{-\frac{B}{2\sqrt{E}}\cdot x}\sum_{n=1}^{\infty} X_n \cdot K_n\left(\frac{B}{2\sqrt{E}}\cdot r\right)\sin n\theta, \qquad (2.3.2)$$

where K_n denotes the modified Bessel function of the second kind and

$$X_n = \pi^{-1}\cdot K_n^{-1}(B/4\sqrt{E})\int_{-\pi}^{\pi}\sin\tau\cdot\sin n\tau\cdot\rho^{\frac{B}{4\sqrt{E}}\cos\tau}\,d\tau. \qquad (2.3.3)$$

The formula to calculate Ekman drag D_E^* is readily seen to be the same as (2.2.4b), so it is sufficient for our purpose to compute Ψ, Ψ_r at $r = 1/2$. First, let us consider the limiting case of $E^{1/2}/B >> 1$. In this case, D_E^* becomes, using (2.3.2),

$$D_E^* = \pi\cdot 2^{-3/2}\cdot\rho\cdot\Omega^{1/2}\cdot\nu^{1/2}\cdot U\cdot L^2\left(1+\frac{1}{128}\frac{B^2}{E}+O\left(\frac{B^4}{E^2}\right)\right). \qquad (2.3.4)$$

To obtain the drag in the other limiting case of $B/E^{1/2} >> 1$, (2.3.2) is not tractable, so let us obtain an approximate solution. After rewriting (2.3.1) with cylindrical coordinates, we get a solution valid for $x > 0$ and $\cos\theta \sim O(1)$ as

$$\psi \sim \sin\theta\cdot e^{-\frac{B}{E^{1/2}}(r-1/2)\cdot\cos\theta} \qquad (2.3.5)$$

which is the well-known Stommel boundary layer solution. For $x < 0$, we have

$$\Psi \sim y \qquad (2.3.6)$$

except thin free shear layers at $y = \pm\frac{1}{2}$. Near $\theta = \pm\pi/2$, (2.3.5) is not valid. Careful examination shows there is another boundary layer whose width is $O(E^{1/6}B^{-1/3})$ in θ-direction and $O(E^{1/3}B^{-2/3})$ in r-direction. However, the contribution to the drag from this boundary layer is $O(E^{1/3}B^{-2/3})$ smaller than that of the Stommel boundary layer, so negligible to the first order of approximation. Thus, D_E^* becomes, to $O(B/E^{1/2})$,

$$D_E^* \sim \frac{1}{12}\cdot\rho\cdot\beta\cdot L^3\cdot H\cdot U. \qquad (2.3.7)$$

Notice that D_E^* is independent of ν to this order of approximation. If we move a cylinder in the direction that makes angle α with the x-axis, D_E^* becomes

$$D_E^* \sim \frac{1}{8}\left(1-\frac{1}{3}\cos 2\alpha\right)\rho\cdot\beta L^3\cdot H\cdot U \qquad (2.3.8)$$

Therefore, the Ekman drag is smallest when a cylinder moves in the east-west direction.

2.4 Steady inviscid flow on the beta-plane.

The vorticity equation becomes

$$\mathcal{E}J(\Psi,\nabla^2\Psi) + B\Psi_x = 0 \qquad (2.4.1)$$

This is rewritten in the form:

$$J(\Psi, \nabla^2\Psi + B/\mathcal{E}\,y) = 0 \qquad (2.4.2)$$

Therefore, potential vorticity $\nabla^2\psi + \beta/\varepsilon\, y$ is conserved along a streamline:

$$\nabla^2\psi + \beta/\varepsilon\, y = F(\psi). \tag{2.4.3}$$

If we adopt Long's hypothesis of no upstream influences, we obtain in a frame of a moving cylinder,

$$\nabla^2\psi - \beta/\varepsilon\, \psi = 0 \tag{2.4.4}$$

with boundary conditions

$$\left.\begin{aligned} \psi &= -\sin\theta \quad \text{at} \quad r = 1/2 \\ \psi &\to 0 \quad \text{at} \quad r \to \infty \end{aligned}\right\} \tag{2.4.5}$$

for a retrograde flow. (No circulation around the cylinder is assumed.) For a prograde flow,

$$\nabla^2\psi + \beta/\varepsilon\, \psi = 0 \tag{2.4.6}$$

with boundary conditions

$$\left.\begin{aligned} \psi &= \sin\theta \quad \text{at} \quad r = \tfrac{1}{2} \\ r^{1/2}\psi &\to 0 \quad \text{at} \quad r \to \infty \left(\tfrac{1}{2}\pi < \theta < \tfrac{3}{2}\pi\right) \end{aligned}\right\} \tag{2.4.7}$$

where no circulation around the cylinder is assumed.

The solution to (2.4.4) and (2.4.5) is

$$\psi = -\frac{K_1\left(\sqrt{\beta/\varepsilon}\, r\right)}{K_1\left(\frac{1}{2}\sqrt{\beta/\varepsilon}\right)} \cdot \sin\theta \tag{2.4.8}$$

This solution does not show blocking, which is incompatible with observations (Long (1952)). Apparently, Long's hypothesis is not good in a circular channel flow of a retrograde case. Anyway, we have no wave drag in a steady state of the retrograde case.

The solution to (2.4.6) and (2.4.7) was obtained by Miles and Huppert (1968). We have steady lee waves on the east side of the cylinder. Following their procedure, the wave drag D_W^* is given by

$$D_W^* \sim 0{,}22\, \rho\, U^{3/2} \beta^{1/2} L^2 H\, Y_1^{-2}\left(\sqrt{\frac{\beta L^2}{4U}}\right), \tag{2.4.9}$$

approximately for $\beta/\varepsilon < 19.4$.

3. Preliminary experiment

3.1 Apparatus

The fluid configuration is shown schematically in Fig. 3.1.

The cylinder was towed around the basin by another motor mounted on the turntable. The beta effect was supplied by the paraboloidal free surface. The flow was observed by using Baker's thymol blue technique, or by using a potassium permanganate dye. The data source is listed in Table 3.1

3.2 Wind-driven current due to resting air.

As we have no cover over the rotating tank, a wind-driven current always exists. The velocity profile of this current is shown in Fig.3.2. The dashed line is a theoretical prediction based on a simple stress balance at an infinite

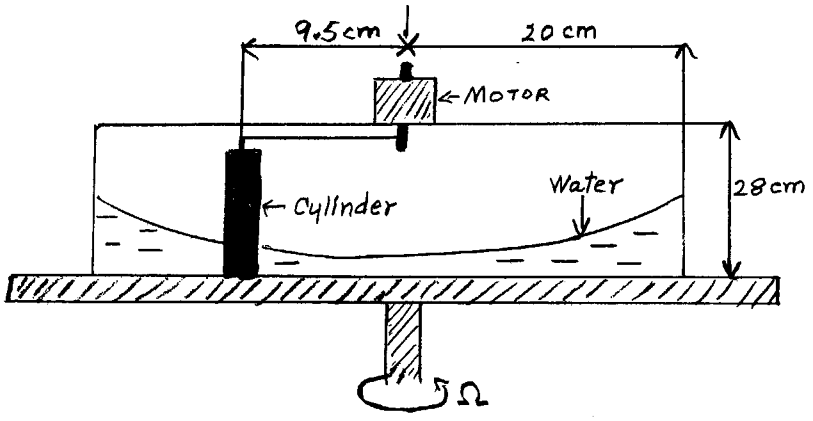

Fig. 3.1

surface (Yamagata and Kimura, 1973). The agreement between theory and experiment is fairly good within $r \leq 4$cm. The discrepancy increases toward the periphery of the basin due to the large height of the side wall. Notice that this weak current is always easterly relative to the rotating tank. In 3.4, we measure the velocity field of this weak easterly flow around the cylinder inserted into the container.

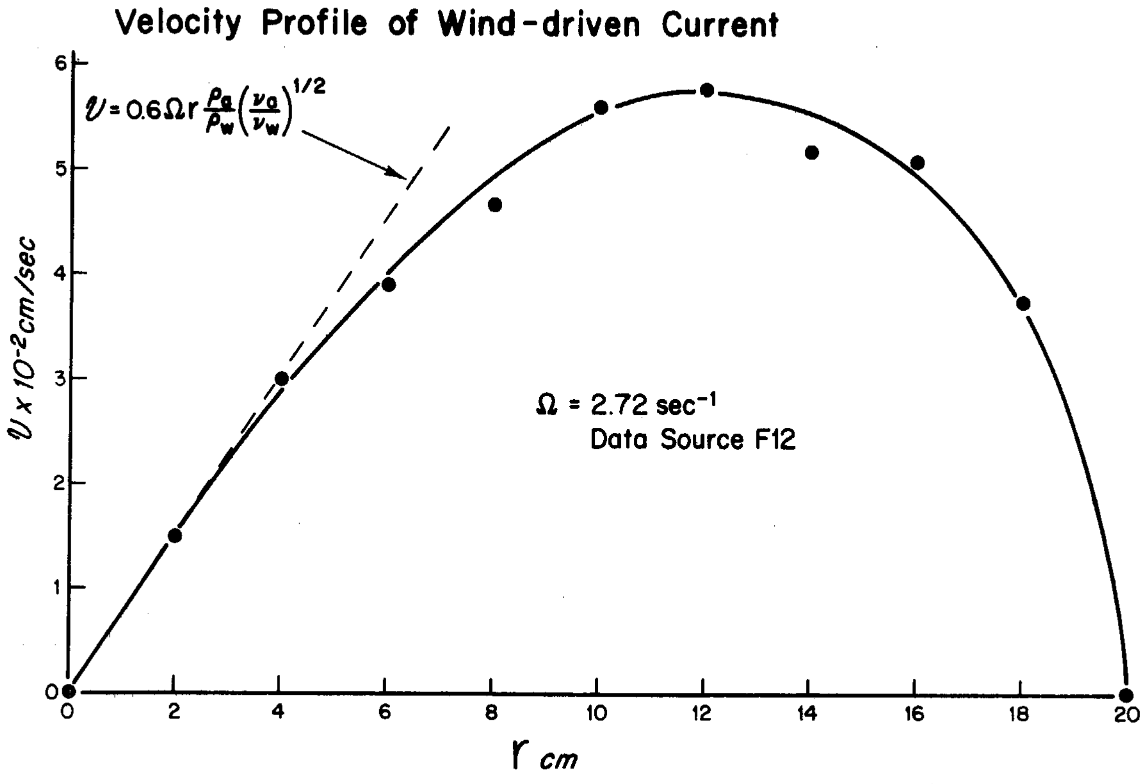

Fig. 3.2

Table 3.1

	Ω	H	L	B	$\sqrt{E}$	ε
	(sec^{-1})	(cm)	(cm)	$(\times 10^{-3})$	$(\times 10^{-3})$	$(\times 10^{-3})$
F12	2.72	10.0	-	-	4.29	-
F17	2.72	10.0	3.8	27.3	4.29	2.61
F18	1.36	10.0	3.8	6.81	6.06	2.61
F19	0.68	10.0	3.8	1.70	8.57	2.61
F23	2.72	10.0	3.8	27.3	4.29	2.61
F27	2.72	10.0	3.8	27.3	4.29	6.53
F35	1.36	10.0	3.8	6.81	6.06	15.8
F36	1.36	10.0	3.8	6.81	6.06	34.1
F37	1.36	10.0	3.8	6.81	6.06	52.5
F38	1.36	10.0	3.8	6.81	6.06	70.9
F39	1.36	10.0	3.8	6.81	6.06	21.0
F40	1.36	10.0	3.8	6.81	6.06	39.4
F41	1.36	10.0	3.8	6.81	6.06	57.8
F42	1.36	10.0	3.8	6.81	6.06	76.1
F48	2.72	5.0	3.8	54.5	8.57	6.53
F49	2.72	10.0	3.8	27.3	4.29	6.53
F50	2.72	15.0	3.8	18.2	2.86	6.53

For the experiment in this section,

$$B/\sqrt{E} \sim 6.36$$
$$0.12 < \varepsilon/B < 0.36$$
$$0.76 < \varepsilon/\sqrt{E} < 2.28$$

From a formal scaling viewpoint, the ratio of the advection term, the beta term and the Ekman friction term is $\varepsilon/B : 1 : 1$, when $x \sim O(B/\sqrt{E}$ and $y \sim O(1))$. On the other hand, the aforementioned ratio is $\varepsilon/\sqrt{E} : 1 : 1$ when $x \sim O(1)$ and $y \sim O(\sqrt{E}/B)^{1/2}$. The data in Fig.3.32 correspond to $|x| \sim 1.3$, which implies that the advection is not negligible. Nevertheless, the agreement between linear theory and experiment is good, in spite of the fact that the formal limit of validity of the linear theory has been exceeded. Apparently, the upstream influence is essentially due to the beta-effect and the Ekman effect.

3.3 Weak westerly flow

We towed a cylinder to the west faster than the wind-driven current to realize a westerly flow in a frame of a moving cylinder. Our special attention was paid to a detection of a forward influence. Figure 3.3.1 (F27) shows a picture

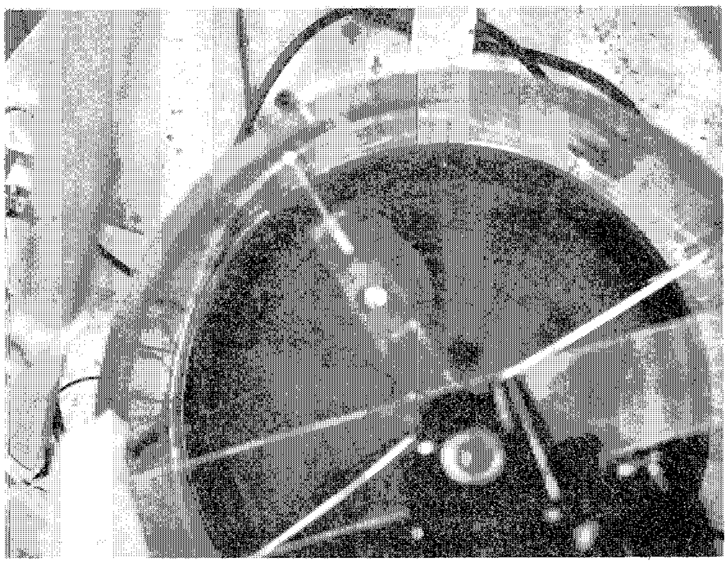

Fig. 3.3.1 (F-27)

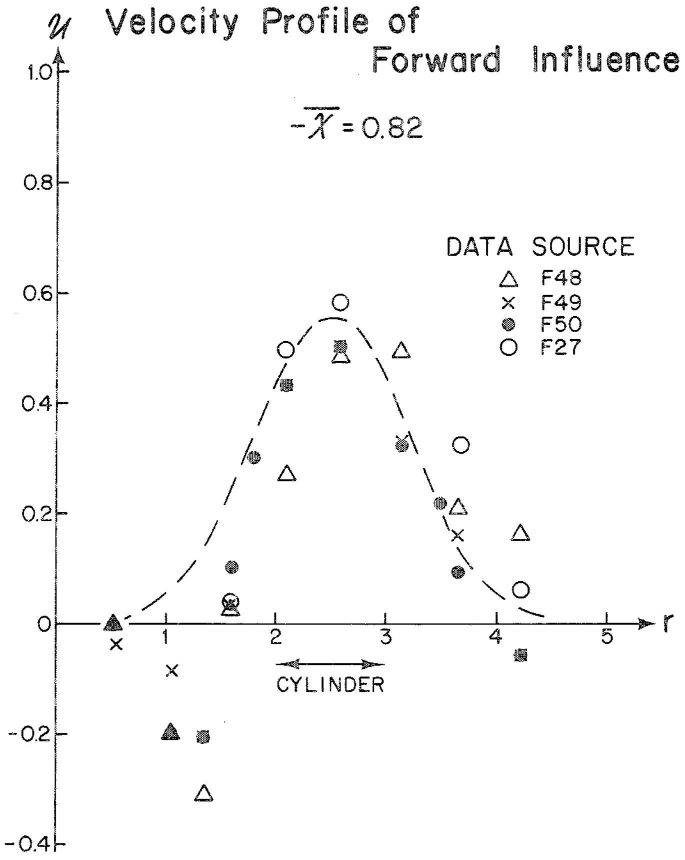

Fig.3.3.2

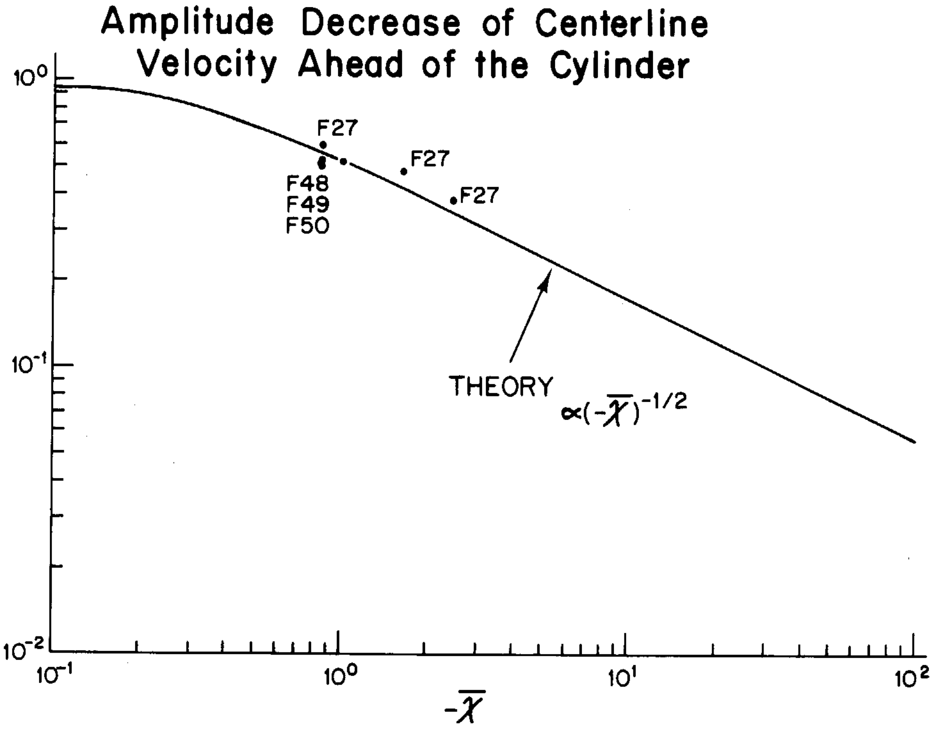

Fig. 3.3.3

of a forward influence taken at 40 sec after the dye was released. In this picture, the wires to produce dye were fixed to the frame of a moving cylinder. Figure 3.3.2 shows perturbed velocity profiles ahead of the cylinder. A dashed line is a theoretical prediction based on the balance between beta-effect and Ekman dissipation (see A-5). Figure 3.3.3 shows the decrease of a centerline velocity ahead of the cylinder. The abscissa denotes the stretched coordinate $\overline{\chi}$ (see A-5).

3.4 Weak easterly flow

We utilized the wind-driven current to realize a weak easterly flow, since the cylinder was fixed to the frame of rotating basin. Figure 3.4.1 is a typical picture taken at 40 sec after the dye was released. We can see a definite blocking behind the cylinder. Figure 3.4.2 (F23) is another illustration of blocking at the same condition. This picture was taken at 30 minutes after a potassium permanganate dye was injected behind the cylinder. We see the dye remains trapped in a blocked region behind the cylinder. It should be noted that the blocking area begins at the northern edge of the cylinder, but not at the southern edge, as observed by Long (1952). This might have some relations to the net circulation observed around the cylinder. Figures 3.4.3 (F17) is the perturbed velocity profiles behind the cylinder. Definite alternating flows are observed, and the y-scale of these flows is smaller than that of a forward wake in a weak westerly flow. We tried to apply the same theory with 3.3, but found it does not work well. Also, the data showing the decrease of a centerline velocity behind the cylinder were highly scattered when we used the stretched coordinate $\overline{\chi}$ (Fig.3.4.4). The parameters of F17 data are:

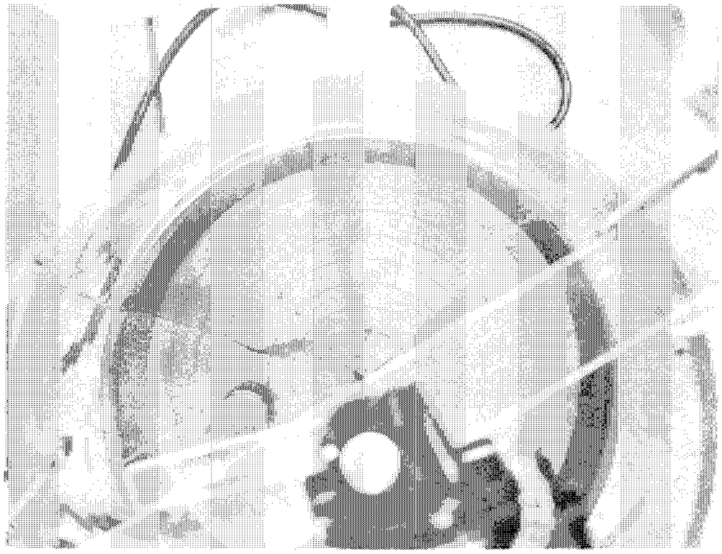

Fig. 3.4.1 (F-17)

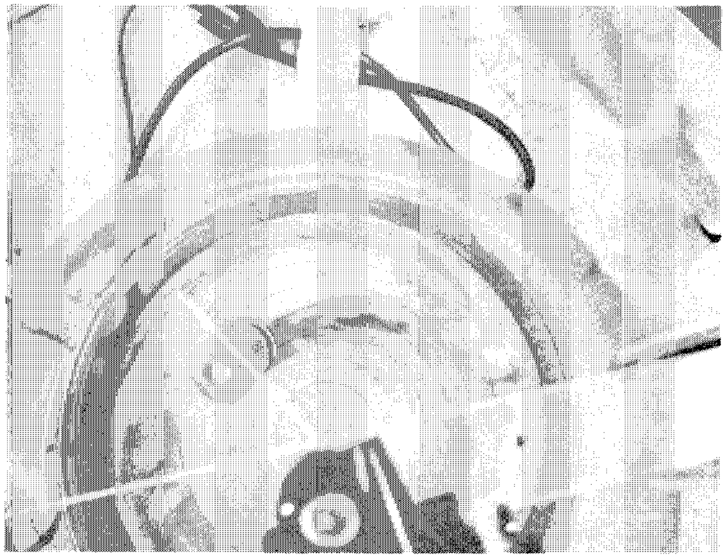

Fig. 3.4.2 (F-23)

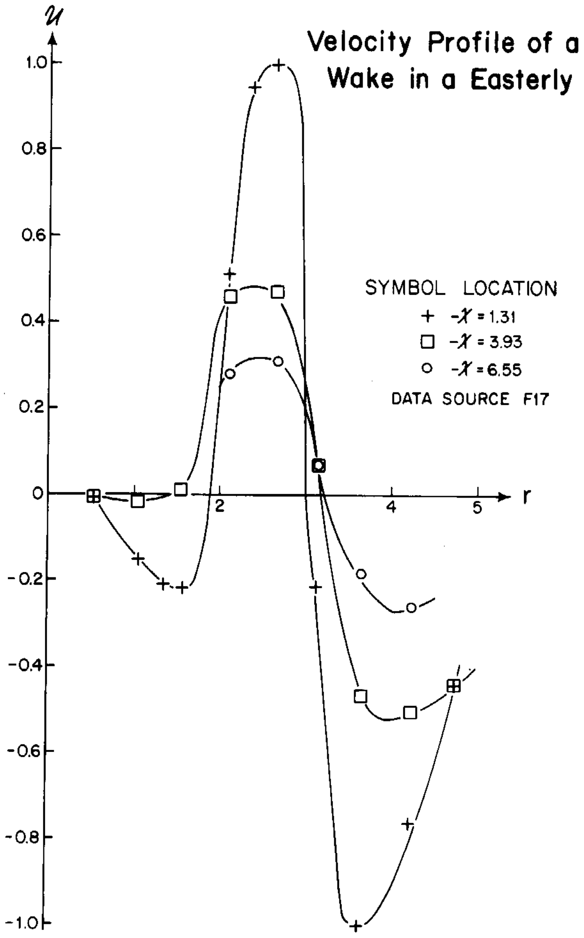

Fig. 3.4.3

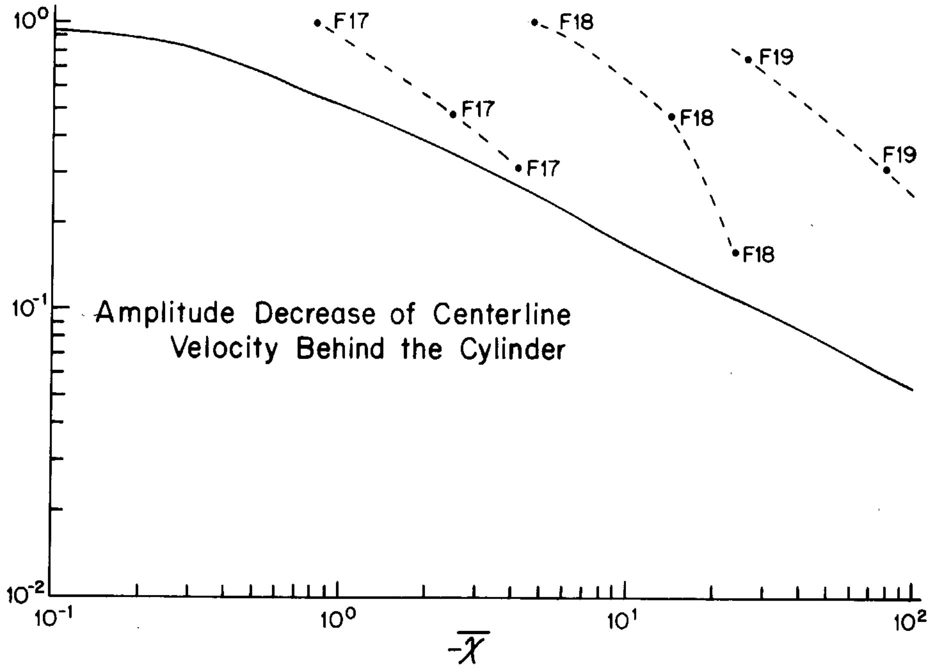

Fig. 3.4.4

$$B/\sqrt{E} \sim 6.36$$
$$\varepsilon/B \sim 0.10$$
$$\varepsilon/\sqrt{E} \sim 0.61$$

For these values, the advection is negligible when $x \sim O(B/\sqrt{E})$ and $y \sim O(1)$. On the other hand, the advection is not negligible when $x \sim O(1)$ and $y \sim (\sqrt{E}/B)^{1/2}$, as previously mentioned. This latter region corresponds to the dotted line (F17) in Fig.3.4.4. But the line approaches the theoretical curve when $|\bar{x}|$ is large, as anticipated.

3.5 Moderate westerly flow.

Figures 3.5.1 (F35), 3.5.2 (F36), 3.5.3 (F37) and 3.5.4 (F38) show the pictures of streak lines behind the cylinder. We see Rossby lee-wave patterns, as observed by Long (1952). As ε increases, the wavelength becomes large, as predicted by a simple lee-wave theory. But at the same time, the wake just behind the cylinder expands and finally leads to the shedding of eddies (Fig. 3.5.4). The critical Rossby number for the shedding of eddies seems to lie between $5.25 \times 10^{-2} < \varepsilon_c < 7.09 \times 10^{-2}$ when $B = 6..8 \times 10^{-3}$, $\sqrt{E} = 6.06 \times 10^{-3}$. Figure 3.5.4 shows a pronounced cyclone, while an anticyclone seems to be suppressed. Also notice that the vortex street is very different from the non-rotating Kármán vortex street*. It will be interesting to correlate the eddy-shedding process with quantitative measurements of drag.

3.6 Moderate easterly flow

Figures 3.6.1 (F39), 3.6.2 (F40), 3.6.3 (F41) and 3.6.4 (F42) show the pictures of streak lines behind the cylinder. Figure 3.6.1 shows the long wake behind the cylinder. The structure, however, seems to be different from that of 3.4, especially just behind the cylinder. In this easterly case, the critical Rossby number to shed eddies ($2.10 \times 10^{-2} < \varepsilon_c < 3.94 \times 10^{-2}$) is apparently smaller than that of a westerly flow. The array of shed vortices looks like a Kármán vortex street in the non-rotating fluid and shows quite a difference from 3.5. This might be due to the existence of blocking area, which will change the form of the boundary layer separation. We also intend to correlate these qualitative observations with drag measurements.

4. Conclusions

The main results of this note are the following three points:

a) The forward influence was observed for a weak westerly flow and the agreement between the linear theory and the experiment is good.

b) For a downstream wake in a weak easterly flow, the theory does not work near the cylinder.

c) Rough critical Rossby numbers for shedding eddies were found for both easterly and westerly flows.

---

*The author is indebted to Dr. R. Hall and Prof. G. Veronis for the information of recent G. Halikas (S.I.O.)'s similar experiment.

We intend to confirm these points by a more precise experiment and correlate the various flow behaviours with quantitative drag measurements.

Appendix

If we consider a far-upstream region of the moving cylinder, the advection term and lateral diffusion term will be negligible. Then (2.1.1) becomes

$$\nabla^2 \Psi_t + B\Psi_x + \sqrt{E}\,\nabla^2 \Psi = 0 \tag{A-1}$$

Adopting the boundary layer type approximation, (A-1) may be reduced to

$$\Psi_{yyt} + B\Psi_x + \sqrt{E}\,\Psi_{yy} = 0 \tag{A-2}$$

and the boundary condition is

$$\left.\begin{array}{ll} u = -\Psi_y = -1 & |y| < \frac{1}{2},\ x = 0, t \geq 0 \\ u = -\Psi_y = 0 & |y| > \frac{1}{2},\ x = 0 \end{array}\right\} \tag{A-3}$$

By taking the Fourier transform in y, we obtain the analytic solution as

$$\Psi = -\frac{2}{\pi}\int_0^{\sqrt{\frac{Bt}{-x}}} \frac{\sin k/2}{k^2} \cdot e^{\frac{\sqrt{E}}{B}k^2 x} \cdot \sin ky\, dk_{(x<0)} \tag{A-4}$$

The final zonal velocity u is given by

$$\begin{aligned} u/_{t=\infty} &= -\Psi_y/_{t=\infty} \\ &= -\frac{1}{2}\left[\operatorname{erf}\left(\frac{\frac{1}{2}+y}{-\sqrt{\bar{x}}}\right) - \operatorname{erf}\left(\frac{-\frac{1}{2}+y}{\sqrt{-\bar{x}}}\right)\right]_{(x<0)} \end{aligned} \tag{A-5}$$

where a stretched coordinate $\bar{x} = \frac{4\sqrt{E}}{B}x$ is adopted. Notice that the amplitude decrease of u ahead of the forcing region is nearly proportional to $(-\bar{x})^{1/2}$ except for a small value of $(\bar{x})$.

Acknowledgements

I am indebted to the staff members of the Geophysical Fluid Dynamics Program, especially to Profs. M.Stern and A. Ingersoll for suggestions and interesting discussions. For the laboratory experiment, I thank Dr. J.Whitehead and especially Mr. R.Frazel. I am also thankful to Hidaka Foundation, whose financial support enabled me to attend this interesting summer seminar.

References

Fultz, D. and P.Frenzen 1955 J.Meteor. 12: 332-338.

Fultz, D. and R.R.Long 1951 Tellus 3: 61-68.

Ingersoll, A.P. 1969 J.Atmos.Sci. 26: 744-752.

Long, R.R. 1952 J.Meteor. 9: 187-199.

McCartney, M.S. 1975 J.Fluid Mech. 68: 71-95.

Miles, J.W. and H.E.Huppert 1968 J.Fluid Mech. 33: 803-914.

Yamagata, T. and R. Kimura 1973 J.Meteor.Soc.Japan 51: 420-434.

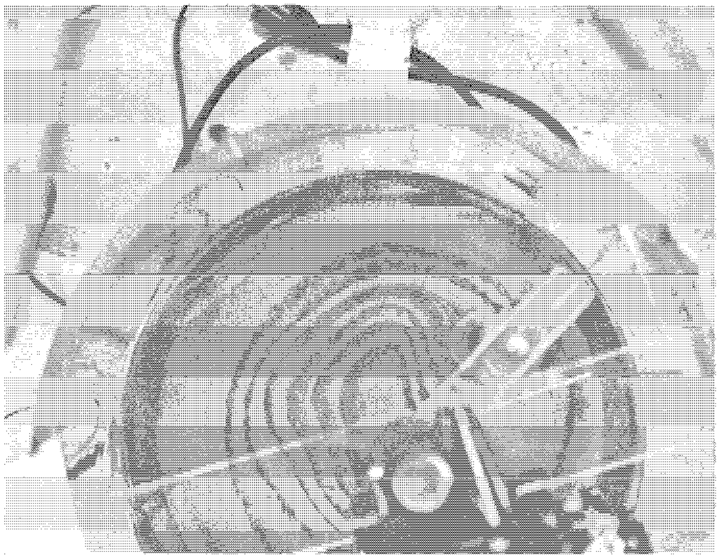

Fig. 3.5.1 (F-35)

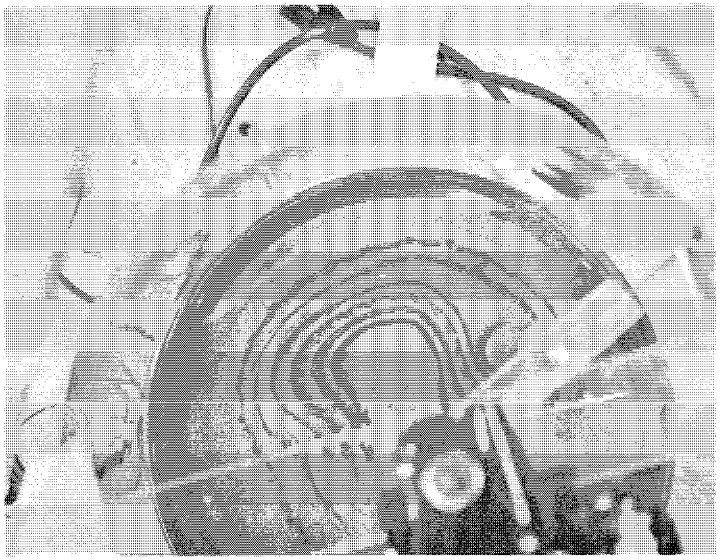

Fig. 3.5.2 (F-36)

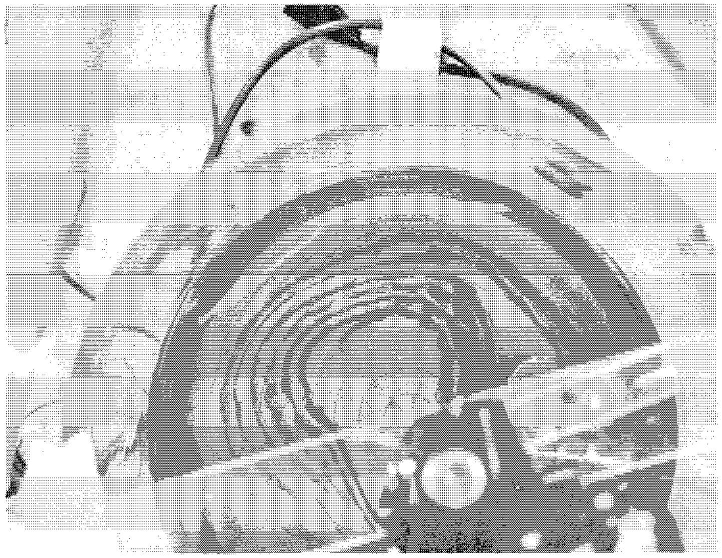

Fig. 3.5.3 (F-37)

Fig. 3.5.4 (F-38)

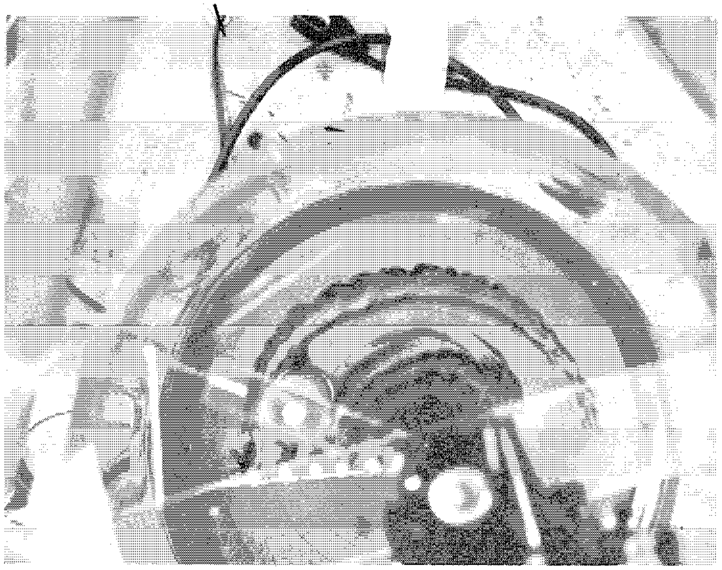

Fig. 3.6.1 (F-39)

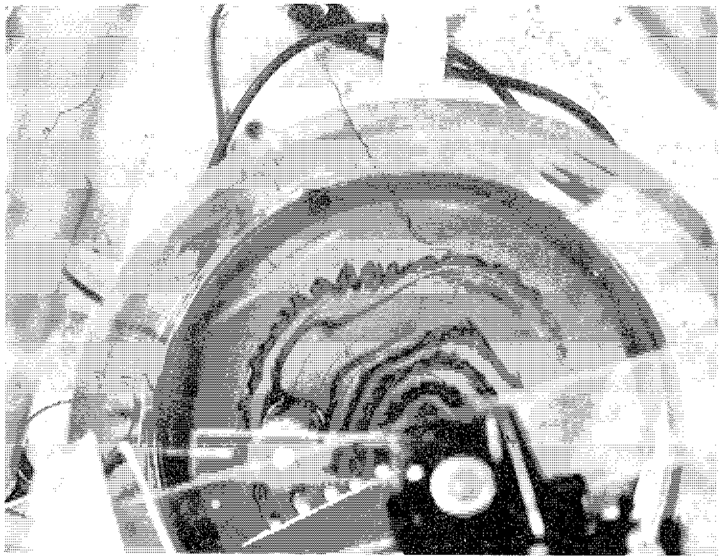

Fig. 3.6.2 (F-40)

Fig. 3.6.3 (F-41)

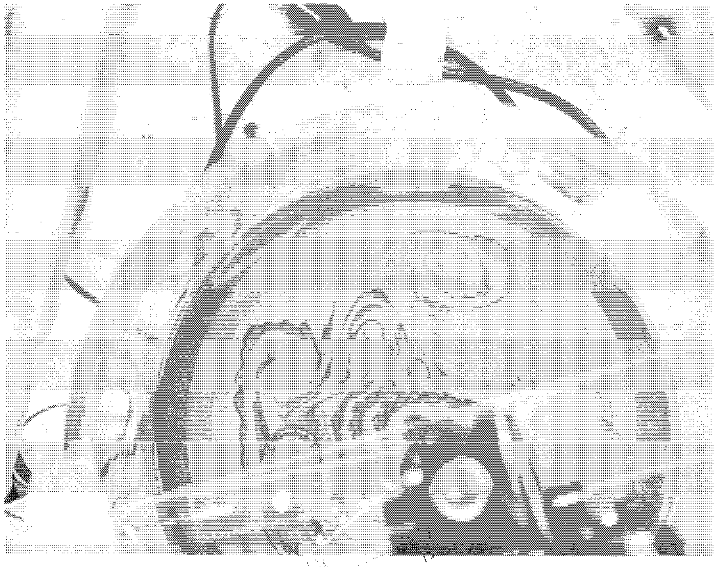

Fig. 3.6.4 (F-42)